

The background of the cover features a photograph of an outdoor swimming pool. In the foreground, a person's arms are raised out of the water. The pool is surrounded by several white lounge chairs. In the background, a large, ornate church with two prominent spires is visible under a blue sky with scattered white clouds. A large, semi-transparent blue oval is overlaid on the top left portion of the image.

Empirical

Multi-band

Characterization of Propagation

with Modelling Aspects for Communications

Diego Dupleich

Dissertation



TECHNISCHE UNIVERSITÄT ILMENAU

Empirical Multi-band Characterization of Propagation with Modelling Aspects for Communications

Dissertation

zur Erlangung des akademischen Grades
Doktoringenieur
(Dr.-Ing.)

vorgelegt der
Fakultät für Elektrotechnik und Informationstechnik
der Technischen Universität Ilmenau

von
M.Sc. Diego Dupleich
geboren am 23. März 1984 in Paraná

Gutachter: Prof. Dr.-Ing. Reiner Thomä
Prof. Dr. Vittorio Degli Esposti
Prof. Dr.-Ing. Thomas Kürner

Vorgelegt am: 22.06.2021

Verteidigt am: 24.08.2022

DOI: 10.22032/dbt.53613
URN: urn:nbn:de:gbv:ilm1-2022000341



Dieses Werk ist lizenziert unter einer
Creative Commons Namensnennung 4.0 International Lizenz.

*Semejante bestia fue encerrada en un laberinto que construyó el artesano Dédalo, un
laberinto del que todo aquel que entraba nunca salía.*

*Gracias mamá y papá por el constante apoyo, fuerza y
libertad cuando más los necesitaba.*

Polvo infinito de Cassiopeia.

*Lo que dejamos
atrás.*

Azizam.

Abstract

This thesis presents an empirical characterization of propagation for wireless communications at mm-waves and sub-THz, taking as a reference the already well known and studied sub-6 GHz band. The large blocks of free spectrum available at these high frequency bands makes them particularly suitable to provide the necessary instantaneous bandwidths to meet the requirements of future wireless technologies (5G, 5G and beyond, and 6G). However, isotropic path-loss and penetration-loss are larger with increasing carrier frequency, hence, coverage is severely reduced. Path-loss can be compensated with the utilization of highly directive radio-interfaces, which increases the resolution in the angular domain. Nonetheless, this emphasizes the need of spacial awareness in systems, making more relevant the question “where does the signal come from?” In addition, larger application bandwidths increase the resolution in the time domain, reducing small-scale fading and allowing to observe inside of clusters of multi-path components (MPCs). Consequently, communication systems have a more deterministic picture of the environment in the angular, time, and polarization domain, characteristics that need to be reflected in channel models for these frequencies. Therefore, in the present work we introduce an extensive characterization of propagation by intensive simultaneous multi-band measurements in the sub-6 GHz, mm-wave, and sub-THz bands. Firstly, the suitability of the simultaneous multi-band measurement procedure to characterize propagation from marginal power profiles and large scale parameters (LSPs) has been evaluated. Then, key propagation aspects for single and multi-band channel modelling in several verticals of 5G have been identified, and extensions to popular spatial channel models (SCMs) covering the aforementioned system aspects have been introduced and evaluated.

Zusammenfassung

Diese Arbeit präsentiert eine empirische Untersuchung der Wellenausbreitung für drahtlose Kommunikation im Millimeterwellen- und sub-THz-Band, wobei als Referenz das bereits bekannte und untersuchte sub-6-GHz-Band verwendet wird. Die großen verfügbaren Bandbreiten in diesen hohen Frequenzbändern erlauben die Verwendung hoher instantaner Bandbreiten zur Erfüllung der wesentlichen Anforderungen zukünftiger Mobilfunktechnologien (5G, "5G and beyond" und 6G). Aufgrund zunehmender Pfad- und Eindringverluste bei zunehmender Trägerfrequenz ist die resultierende Abdeckung dabei jedoch stark reduziert. Die entstehenden Pfadverluste können durch die Verwendung hochdirektiver Funkschnittstellen kompensiert werden, wodurch die resultierende Auflösung im Winkelbereich erhöht wird und die Notwendigkeit einer räumlichen Kenntnis der Systeme mit sich bringt: Woher kommt das Signal? Darüber hinaus erhöhen größere Anwendungsbandbreiten die Auflösung im Zeitbereich, reduzieren das small-scale Fading und ermöglichen die Untersuchung innerhalb von Clustern von Mehrwegekomponenten. Daraus ergibt sich für Kommunikationssysteme ein vorhersehbareres Bild im Winkel-, Zeit- und Polarisationsbereich, welches Eigenschaften sind, die in Kanalmodellen für diese Frequenzen widergespiegelt werden müssen. Aus diesem Grund wurde in der vorliegenden Arbeit eine umfassende Charakterisierung der Wellenausbreitung durch simultane Multibandmessungen in den sub-6 GHz-, Millimeterwellen- und sub-THz-Bändern vorgestellt. Zu Beginn wurde die Eignung des simultanen Multiband-Messverfahrens zur Charakterisierung der Ausbreitung von Grenzwert-Leistungsprofilen und large-scale Parametern bewertet. Anschließend wurden wichtige Wellenausbreitungsaspekte für die Ein- und Multibandkanalmodellierung innerhalb mehrerer Säulen der 5G-Technologie identifiziert und Erweiterungen zu verbreiteten räumlichen Kanalmodellen eingeführt und bewertet, welche die oben genannten Systemaspekte abdecken.

Special thanks to Prof. Reiner Thomä, Prof. Vittorio Degli Esposti, and Prof. Thomas Kürner for the constant teaching in multiple aspects, and for accepting having to read this thesis. To Dr. Wim Kotterman for the very fruitful and interesting conversations in the widest range of topics. To Robert Müller, Stephan Häfner, Niu Han, Sergii Skoblikov, and Gerd Sommerkorn for making possible to accomplish most of the measurements and simulations presented in this work. To Christian Schneider, Navid Iqbal, Dr. Jian Luo, and Dr. Mate Boban for the constant collaborations. To Dr. Markus Landmann for the always compelling ideas. To Prof. Sana Salous, Prof. Katsuyuki Haneda, Prof. Pekka Kyösti, Prof. Claude Oestges, Prof. Fredrik Tufvesson, Prof. Narcís Cardona, Dr. Tommi Jämsä, and all the people from the COST, IRACON, and now INTERACT family, that even if they don't cite my papers, made possible an endless and incredible rich exchange of personal, scientific, and professional experiences. To Alexander Ebert for helping me with the translation of the abstract and providing yerba and whiskey, when necessary. To Prof. Giovanni Del Galdo for his support, to Gitta Weber-Wolf for her patience, and to the EMT/EMS people for being there.

Contents

Contents	vi
List of Figures	xi
List of Tables	xiv
List of Abbreviations	xx
1 Introduction	3
1.1 Does It Work?	4
1.2 Propagation Characteristics, System Aspects, and Channel Modelling at mm-wave and sub-THz	5
1.3 The Massive Idea of MIMO Communications	8
1.4 The Next Generation of Wireless Communications	10
1.5 Thesis Outline and Personal Contribution	12
I mm-Wave, Sub-THz, and Multi-band Characterization of Propagation from Measurements and Simulations	15
2 Multi-band Channel Sounding and Parameter Estimation	17
2.1 Multi-band Ultra-wideband Channel Sounding	18
2.2 Non-parametric Estimation of Marginal Power Profiles and Large Scale Parameters from Directive Scans	21
2.2.1 Measured Signal Model Using Directive Scans	21
Directive Scans and Angular Resolution	22
Band Limited Measurements and Delay Resolution	23
2.2.2 Noise Floor Estimation and Removal	24
2.2.3 Marginal Power Profiles from Directive Scans	25
2.2.4 Time and Angular Spreads from Directive Scans	26
2.2.5 Dynamic Range Limitation for Delay Spread Calculation	28
2.2.6 Multi-band Path-loss from Measurements	29
Multi-band ABG Model	29
Multi-band CI Model	30
2.3 Parametric Estimation of Specular and Dense Multi-path Components	30
2.4 Future of Channel Sounding and Modelling	32
3 Validation of the Multi-band Measurement and Estimation Methodology	35
3.1 Introduction	36
3.2 Characterization of Errors on the Estimation of Multi-band Large Scale Parameters from Directive Scans	37
3.3 Error Quantization by Simulative Analysis using Ray-Tracing	38
3.3.1 Emulated Channel Sounder Equation Model	38

3.3.2	Influence of Bandwidth and Directivity on the Estimation of Large Scale Parameters from Directive Scans	39
3.4	Characterization of Errors from Limited Resolution in the Measurement Equipment	39
3.5	Characterization of the Errors in the Estimation of the Multi-band Large Scale Parameters	40
3.6	Characterization of the Errors in the Estimation of Total Received Power and Multi-band Path-loss	42
3.7	Influence of the Scanning Step on the Estimation of Large Scale Parameters from Directive Scans	43
3.7.1	Synthesis of Antenna Patterns using Directive Measurements	43
3.7.2	Influence on the Marginal Power Profiles and Large Scale Parameters	45
3.8	Conclusions	45
4	Characterization of Propagation from Measurements and Simulations	47
4.1	Item Level Characterization at 70 GHz in Anechoic Chamber	48
4.1.1	Specular and Diffuse Scattering	48
4.1.2	Polarimetric Analysis of the Scattering Process	48
4.1.3	Obstruction Loss	49
4.2	Human Shadowing Loss	50
4.3	Indoor Propagation Analysis and Characterization	52
4.3.1	Introduction	52
4.3.2	Scenarios and Set-up	53
4.3.3	Multi-Store Entrance Hall Scenario at 30 GHz and 60 GHz	54
Environment and Propagation Characterization	55	
Analysis of Large Scale Parameters	55	
4.3.4	Large Corridor Scenario at 6.75 GHz, 30 GHz, and 60 GHz	56
Environment and Propagation Characterization	56	
Analysis of Large Scale Parameters	58	
Polarimetric Power Ratios	60	
Empirical Multi-band Path-loss	61	
Ray-Tracing Comparison	61	
4.3.5	Conference Room at 190 GHz	63
Environment and Propagation Characterization	63	
Analysis of Large Scale Parameters	65	
Polarimetric Power Ratios	66	
Empirical Path-loss	66	
4.4	Outdoor Propagation Analysis and Characterization	67
4.4.1	Introduction	67
4.4.2	Scenarios and Measurement Set-up	68
4.4.3	Environment Characterization from Measurements	70
4.4.4	Analysis of Large Scale Parameters	71
4.4.5	Multi-band Empirical Path-loss	73
4.5	Industry Scenario Propagation Analysis and Characterization	74
4.5.1	Introduction	74
4.5.2	Scenarios and Measurement Set-up	75
4.5.3	Environment Characterization	77
4.5.4	Analysis of Large Scale Parameters	78

4.5.5	Multi-band Empirical Path-loss	80
4.5.6	Specular to Dense Multipath Components Power Ratio	80
4.6	V2V Propagation Analysis and Characterization	83
4.6.1	Introduction	83
4.6.2	Corner scenario	84
	Environment Characterization	84
	Analysis of Large Scale Parameters	86
4.6.3	Overtaking in Urban Scenario	87
	Environment Characterization	87
	Analysis of Large Scale Parameters	88
	Blockage Loss	89
4.6.4	Approach Under Blockage in Urban Scenario	90
	Environment Characterization	91
	Analysis of Large Scale Parameters	92
	Empirical Multi-band Path-loss and Blockage Loss	94
4.6.5	Vehicles in the Environment	94
4.7	Conclusions	95

II Influence of System Aspects and Multi-band Channel Modelling Components 97

5 Influence of System Aspects on Performance and Modelling 99

5.1	Introduction	100
5.2	Influence of mm-Wave System Aspects on Delay Spread	101
5.3	Influence of mm-Wave System Aspects on Small-Scale Parameters	102
5.3.1	Signal Model	103
5.3.2	Influence of Directivity in the Time Variant Channel Impulse Response	104
5.3.3	Fading Depth Estimation	106
5.3.4	Effects of Directivity on Doppler	106
5.3.5	Influence on the Distribution of the Envelope	107
5.4	Conclusions	109

6 mm-Waves, Sub-THz, and Multi-band Channel Modelling Components 111

6.1	Introduction	112
6.2	Preliminaries: Deterministic Vs. Random Location of Clusters	113
6.3	Deterministic Components in Spatial Channel Models	114
6.3.1	Deterministic Components in Spatial Channel Models	114
	Ground Reflection	115
	Side and Back Reflections	116
	Diffuse Scatterers	118
6.3.2	Analysis and Synthesis of Deterministic Components in Measurements	118
6.3.3	Validation of Deterministic Components in Spatial Channel Models	120
6.4	Non-Geometry-Based Multi-band Correlated Spatial Channel Modelling	120
6.4.1	Introduction	120
6.4.2	Modifications in the Channel Coefficient Generation Procedure	121
6.4.3	Analysis of the Frequency Correlation of Large-Scale Parameters	122
6.4.4	Synthesis of Correlated Large-Scale Parameters	123

6.4.5	Synthesis of Correlated Channel Impulse Responses	125
6.4.6	Validation of System-Level Correlated Multi-band Spatial Channel Models	127
6.5	Conclusions	127
7	Polarization in Spatial Channel Models	131
7.1	Introduction	132
7.2	Limitations of the Current Modelling Approach	133
7.3	Novel Methodology: Correlation Based Modelling of the Polarimetric Power Ratios	135
7.4	Analysis and Model Parametrization	136
7.4.1	Ray-Tracing Simulations Set-Up	136
7.4.2	Distribution of the Polarimetric Power Ratios	137
7.4.3	Correlation of the Polarimetric Power Ratios	138
7.4.4	Analysis of Common Paths Over Frequency	139
7.5	Synthesis and Model Validation	140
7.6	Influence of Modelling Aspects on the Analysis of Polarization Diversity . . .	141
7.7	Conclusions and Future Work	143
8	Conclusions and Future Work	147
8.1	Conclusions	148
8.2	Open Discussions and Future Work	151
	Bibliography	153
	Appendix	165
A	The Multipath Propagation and Radio Channel	165
A.1	Propagation Mechanisms	166
A.2	The Multi-path Propagation Channel	168
A.2.1	Deterministic Description of the Propagation Channel: First Set of Bello Equations	169
	Spreading Functions	169
	Marginal Spreading Functions	172
	Full Characterization of the Multi-path Propagation Channel Considering Polarization	173
A.2.2	Stochastic Description of the Propagation Channel: Second Set of Bello Equations	173
	Wide-Sense Stationary (WSS) Process	173
	Uncorrelated Scattering (US)	174
	Wide-Sense Stationary Uncorrelated Scattering (WSSUS)	174
	Marginal Power Profiles and Spreading Factors	174
A.3	The Multi-path Radio Channel	176
A.3.1	Signal Model Considering Single Polarized Antennas	177
A.3.2	Extension to Dual-polarized Antennas	177

A.4	The Multi-path MIMO Propagation and Radio Channel	178
B	Fading in Wireless Mobile Channels	181
B.1	Introduction	182
B.2	Large-Scale Fading	182
B.2.1	Free Space Path-loss	183
B.2.2	Empirical Path-loss and Shadowing Models	184
B.2.3	Empirical Multi-band Path-loss Models	184
B.2.4	Directional and Omni-directional Path-loss	185
B.3	Small-Scale Fading	186
B.3.1	Time Spreading of the Signal and Frequency Selectivity	186
	Frequency Flat Fading	187
	Frequency-selective Fading	188
B.3.2	Time Variance of the Signal and Frequency Spreading	189
	Slow Fading	190
	Fast Fading	190
B.4	Summary	191
C	State of the Art in Physical Channel Models	193
C.1	Introduction	194
C.2	Deterministic vs Stochastic Physical Channel Modelling	195
C.3	Ray-Tracing for mm-wave and Sub-THz Simulations	196
C.4	Review of Stochastic Spatial Channel Models	196
C.4.1	Non-geometry-based Spatial Channel Models: Channel Equation and Channel Impulse Response Generation	198
	Extensions for Large Bandwidths and Large Antenna Arrays: Modi- fication on the Channel Equation	200
	Extensions for Large Bandwidths and Large Antenna Arrays: Model- ling of Intra-cluster Angular and Delay Spreads	200
	Explicit Ground Reflection	201
	Correlation Modelling for Multi-frequency Simulations	201
C.4.2	Quasi-deterministic Spatial Channel Modelling	202
	Channel Impulse Response Equation	202
	Deterministic rays (D-rays)	203
	Random rays (R-rays)	203
	Intra-cluster Properties	203
C.5	Summary of the State of the Art in mm-wave and Multi-band Channel Modelling	203
D	Miscellaneous	205
D.1	Identification of the Channel Impulse Response using M-sequences	206
D.2	Influence of Bandwidth in Band-limited Channels	208
D.3	Analysis of the Influence of Directivity and Bandwidth using the Deterministic Two-rays Ground-reflection Model	209
D.4	Simulative Analysis of the Influence of Directivity and Bandwidth in Small- scale Fading	211
D.5	Parametrization of Ray-Tracing simulations	215
D.6	Validation of RT Model: Zusebau Building	215
D.6.1	Cluster Level Ray-tracing Validation from Measurements	216

D.6.2	Complete Ray-tracing Scenario Validation from Measurements	217
D.7	Parameters for the Deterministic Clusters Simulations	218
D.8	List of Antennas used During the Measurements	221
E	List of Own Publications, Patents, and Recognitions	223
E.1	Publications as First Author	224
E.1.1	Journals and Magazines	224
E.1.2	Conferences	225
E.1.3	White Papers, Temporary Documents, and Technical Documents in Standardization	230
E.2	Contributions	232
E.2.1	Books	232
E.2.2	Journals and Magazines	233
E.2.3	Conferences	237
E.2.4	White Papers and Temporary Documents	241
E.3	Patents	242
F	Declaration of Authorship	243

List of Figures

1.1	Influence of physical size of antennas on directivity	6
1.2	Propagation characteristics, system aspects, and channel models requirements	7
1.3	Propagation, radio channels, and communication channel	8
1.4	Beam-forming and spatial multiplexing capabilities for different MIMO architectures	9
1.5	Service requirements for different applications of several vertical segments . .	11
1.6	Standardization time-lines of the different groups for 5G	11
2.1	Multi-band channel sounder in different environments and set-ups.	19
2.2	Schematic of the multi-band multi-channel sounder.	20
2.3	Schematic of a single band multi-channel sounder.	20
2.4	Estimated noise floor in measured CIR and influence on DS of different thresholds.	24
2.5	Flow chart of the marginal power profiles and LSPs calculation.	27
2.6	RIMAX processing in parameter estimation of diffuse and specular power. . .	31
2.7	Validation of RT from measurements and parametrization of SCMs.	32
3.1	RT and measurement comparison considering the influence of resolution. . . .	36
3.2	Influence of bandwidth and directivity on the estimation of the PDP.	38
3.3	CDF of DS and ASs estimated from emulated measurements and RT for different bandwidths and directivities.	40
3.4	CDF of the error in LSPs in the different bands with the reference RT and difference error between bands.	40
3.5	Comparison of marginal power profiles in different bands.	41
3.6	CDF of the relative error between the total RX power with the emulated sounding process and the reference RT and difference error between the estimated total RX power in the different bands.	42
3.7	PL from synthetic omni-directional profiles and RT	42
3.8	Influence of angular scanning steps on the RX power.	44
3.9	Influence of the angular scanning steps on the marginal power profiles. . . .	45
4.1	Scattering pattern for brick wall and flat screen monitor	48
4.2	Polarimetric decomposition of the scattering pattern for reflection in a wall and in the flat screen monitor	49
4.3	DKED and QKED model using absorbing screen	51
4.4	Measured and modelled human shadowing at 70 GHz	52
4.5	Location of the TX in indoor scenarios	53
4.6	View from RX towards TX in hall scenario	54
4.7	Measured PDPs in hall scenario at 30 GHz and 60 GHz	55
4.8	LSPs in hall scenarios at 30 GHz and 60 GHz	56
4.9	View from the TX in large corridor scenario at 6.75 GHz, 30 GHz, and 60 GHz	57

4.10	Measured PDPs in large corridor scenario at 6.75 GHz, 30 GHz, and 60 GHz	58
4.11	LSPs from measurements in large corridor scenario at 6.75 GHz, 30 GHz, and 60 GHz	59
4.12	Polarimetric synthetic omni-directional RX power in large corridor scenario at 6.75 GHz, 30 GHz, and 60 GHz	60
4.13	CDF of the per-position isotropic PPRs in large corridor scenario at 6.75 GHz, 30 GHz, and 60 GHz	60
4.14	Path-loss from measurements in large corridor scenario at 6.75 GHz, 30 GHz, and 60 GHz	61
4.15	Measured and RT simulated PDP in large corridor scenario at 6.75 GHz, 30 GHz, and 60 GHz	62
4.16	Measured and RT simulated LSPs in large corridor scenario at 6.75 GHz, 30 GHz, and 60 GHz	63
4.17	View from RX and from TX in conference room scenario	63
4.18	RT simulated and measured PAEP and the polarimetric decomposition in conference room scenario at 190 GHz	64
4.19	Measured and RT simulated co-polarized PAAP in conference room scenario at 190 GHz	65
4.20	Measured and RT simulated LSPs in conference room scenario at 190 GHz	65
4.21	CDF of the PPRs in conference room scenario at 190 GHz	66
4.22	Measured and RT simulated path-loss in the conference room scenario at 190 GHz	67
4.23	TX and RX positions in outdoor measurements	68
4.24	View from the TX and RX in street canyon scenario in Ilmenau an Tokyo	69
4.25	Measured PAEP in street canyon scenario at 60 GHz	70
4.26	Measured PDP in street canyon scenarios at 6.75 GHz, 30 GHz, and 60 GHz	71
4.27	Complete set of measured PDPs in street canyon scenarios at 30 GHz and 60 GHz	72
4.28	LSPs in street canyon scenarios at 6.75 GHz, 30 GHz, and 60 GHz	72
4.29	Path-loss in street canyon scenarios at 6.75 GHz, 30 GHz, and 60 GHz	74
4.30	View from the TX in industry scenario	76
4.31	TX and RX positions in industry scenario	76
4.32	Measured PDPs in industry scenario at 6.75 GHz, 30 GHz, and 60 GHz	77
4.33	Measured PAP at TX in industry scenario at 6.75 GHz, 30 GHz, and 60 GHz	78
4.34	LSPs from measurements in industry scenario at 6.75 GHz, 30 GHz, and 60 GHz	79
4.35	Path-loss from measurements in industry scenario at 6.75 GHz, 30 GHz, and 60 GHz	80
4.36	Statistics of the specular to dense power ratio in industry scenario at 6.75 GHz and 30 GHz	81
4.37	CDF of the specular to dense power ratio in industry scenario at 6.75 GHz and 30 GHz	82
4.38	V2V corner scenario with different visibility conditions and parked vehicles in the environment	85
4.39	Measured PDPs in V2V corner scenario at 6.75 GHz and 60 GHz	85
4.40	Measured PAAP in V2V corner scenario at 60 GHz	85
4.41	LSPs from measurements in V2V corner scenario at 6.75 GHz, 30 GHz, and 60 GHz	86
4.42	V2V overtaking scenario in an urban environment	87

4.43	Measured PDP in V2V overtaking scenario at 6.75 GHz, 30 GHz, and 60 GHz	88
4.44	DS from measurements in V2V overtaking scenario at 6.75 GHz, 30 GHz, and 60 GHz	88
4.45	ASA from measurements in V2V overtaking scenario at 6.75 GHz, 30 GHz, and 60 GHz	88
4.46	ASD from measurements in V2V overtaking scenario at 6.75 GHz, 30 GHz, and 60 GHz	89
4.47	Measured PDPs at 60 GHz during blockage with passenger vehicle and pick-up truck	90
4.48	V2V blockage loss at 6.75 GHz, 30 GHz, and 60 GHz with passenger vehicle and pick-up truck.	90
4.49	Approach under blockage in V2V scenario.	91
4.50	Measured PDP in V2V approach under blockage scenario at 6.75 GHz, 30 GHz, and 60 GHz	91
4.51	Measured PDPs in V2V approach under blockage scenario at 6.75 GHz, 30 GHz, and 60 GHz	92
4.52	Measured PAAP in V2V approach under blockage scenario at 60 GHz	93
4.53	LSPs from measurements in V2V approach under blockage scenario at 6.75 GHz, 30 GHz, and 60 GHz	93
4.54	Blockage loss and path-loss in V2V approach under blockage scenario at 6.75 GHz, 30 GHz, and 60 GHz	94
4.55	Measured PDPs with and without parked cars in V2V corner scenario at 6.75 GHz, 30 GHz, and 60 GHz	95
5.1	Effects of directivity on the number of MPCs within the channel	100
5.2	Influence of directivity on the intra-cluster number of receiving paths	101
5.3	Influence of directivity on DS in the measured scenarios and visibilities	102
5.4	Measurement set-up in cluster-level fading investigations at 60 GHz	103
5.5	RX power along the track in cluster-level fading investigations at 60 GHz	104
5.6	Measured PSDs in cluster-level fading investigations at 60 GHz	105
5.7	Influence of bandwidth and directivity in cluster-level fading investigations at 60 GHz	106
5.8	Fade-depth for different bandwidths and directivities in cluster-level fading investigations at 60 GHz	107
5.9	Measured Doppler-delay power spectrum for different directivities in cluster-level fading investigations at 60 GHz	107
5.10	Measured Doppler power spectrum with different directivities in cluster-level fading investigations at 60 GHz	108
5.11	Distribution of the signal level with different bandwidths and directivities in cluster-level fading investigations at 60 GHz	108
6.1	Ground reflection sketch	115
6.2	Measured RX power of the ground reflection and estimated reflection coefficient in street canyon scenarios at 30 GHz	116
6.3	Schematic of the specular components in street canyon scenario with a building at the end	117
6.4	Measured and estimated position of the deterministic components in street canyon scenarios	119

6.5	Measured and estimated positions of the deterministic components in large corridor scenario	119
6.6	Measured and simulated PDP and PAP at RX with deterministic components in large corridor scenario at 30 GHz	120
6.7	Measured and simulated DS and ASA in large corridor scenario at 30 GHz	120
6.8	Modifications on the 3GPP SCM receipt for correlated multi-band simulations	121
6.9	Correlation of LSPs from multi-band measurements	123
6.10	Correlation of LSPs over frequency from multi-band measurements	123
6.11	Synthesized CIR from correlated multi-band simulations	126
6.12	Validation methodology for 3GPP correlated multi-band SCM	127
6.13	Mean of the LSPs in the different steps of the synthesis of correlated multi-band channel impulse responses (CIRs)	128
6.14	Multi-band cross-correlation factor of the different LSPs	128
7.1	Utilization of beams to overcome human-shadowing	132
7.2	Reflection coefficient and CPR in a single layered wall	134
7.3	RT maps and simulations set-up for analysis of polarization	136
7.4	Bivariate histogram of the PPRs and ground and ceiling reflections	137
7.5	Histogram and fit to the Normal distribution of the multi-band PPRs from RT simulations	138
7.6	CDF of the PPRs of the common paths over frequency	139
7.7	CDF of the synthesized and RT simulated PPRs	140
7.8	Bivariate histogram of the PPRs from model and RT simulations	140
7.9	Condition number of different modelling approaches and number of MPCs within the beam	142
A.1	Propagation mechanisms and multi-path channel	166
A.2	Reflection and transmission coefficients for air to concrete interface	167
A.3	Spherical coordinate system and polarization at TX and RX	170
A.4	Fourier relationships between the different Bello functions	171
A.5	MIMO coordinate system at TX and RX	178
B.1	Classification of fading and its relation to the different dimensions	182
B.2	Sketch of multi-path propagation channel, equivalent channel after digitization, and Fourier transform for flat and frequency selective fading	186
B.3	Doppler shift and spread relation to the number of MPCs	190
C.1	Classification of channel models according to their nature	194
C.2	WINNER representation of clusters with sub-paths	197
C.3	Channel generation procedure of the 3GPP SCM	198
C.4	Structure of the CIR in the quasi-deterministic model MIWEBA	202
D.1	Influence of bandwidth on the resolution of MPCs	209
D.2	Components of the two-rays ground-reflection model	210
D.3	Polarimetric ground-reflection coefficients and RX power for the two-rays ground-reflection model	211
D.4	Influence of bandwidth and directivity in the RX power for the two-rays ground-reflection model	211

D.5	Set-up for simulations of effects of bandwidth and directivity on small-scale fading	211
D.6	Simulated single-path channel in the different domains with different bandwidths	213
D.7	Simulated Doppler power spectrum for different bandwidths and number of MPCs within the channel	213
D.8	Simulated MPC channel in the different domains with different bandwidths .	214
D.9	Simulated PSD for different bandwidths and number of MPCs within the channel	214
D.10	Simulated averaged RX power for different bandwidths and number of MPCs within the channel	215
D.11	Indoor hall and large corridor RT model validation set-up	216
D.12	Cluster-level measured and simulated bi-azimuth profile: average over the different positions in the rail	217
D.13	View of the complete hall with the TX and RXs locations in the measurements for the scenario validation	217
D.14	Measured and RT simulated RX power of the specular reflection for the different co-polarized components	217
D.15	Synthetic omni-directional RX power from for the different polarizations: measurements and simulations	218

List of Tables

2.1	False alarm probability for different threshold values with $\nu = 2$	25
3.1	Relative and difference error on the estimation of multi-band LSPs from directive scans.	41
4.1	Scattering parameters and obstruction loss of different tested objects at 70 GHz.	50
4.2	Indoor measurement campaigns	54
4.3	Indoor measurements set-up	54
4.4	LSPs from measurements in hall scenario at 30 GHz and 60 GHz	56
4.5	LSPs from measurements in large corridor scenario at 6.75 GHz, 30 GHz, and 60 GHz	59
4.6	PPRs from measurements in large corridor scenario at 6.75 GHz, 30 GHz, and 60 GHz	61
4.7	Path-loss parameters from measurements in large corridor scenario at 6.75 GHz, 30 GHz, and 60 GHz	62
4.8	LSPs from measurements and RT simulations in conference room scenario at 190 GHz	66
4.9	PPRs and path-loss parameters from measurements and RT simulations in conference room scenario at 190 GHz	67
4.10	Measurement set-ups in street canyon scenarios.	69
4.11	LSPs from measurements in street canyon scenarios at 6.75 GHz, 30 GHz, and 60 GHz	73
4.12	Path-loss parameters from measurements in street canyon scenarios at 6.75 GHz, 30 GHz, and 60 GHz	74
4.13	Industry scenario measurement set-up	76
4.14	LSPs from measurements in industry scenario at 6.75 GHz, 30 GHz, and 60 GHz	79
4.15	Path-loss parameters from measurements in industry scenario at 6.75 GHz, 30 GHz, and 60 GHz	81
4.16	Specular to dense power ratio from measurements in industry scenario at 6.75 GHz and 30 GHz	82
4.17	V2V measurement campaigns	84
4.18	LSPs from measurements in V2V overtaking scenario at 6.75 GHz, 30 GHz, and 60 GHz	89
4.19	Blockage loss in V2V overtaking scenario at 6.75 GHz, 30 GHz, and 60 GHz	90
4.20	LSPs from measurements in V2V approach under blockage scenario at 6.75 GHz, 30 GHz, and 60 GHz	94
4.21	Path-loss parameters and blockage loss from measurements in V2V approach under blockage scenario at 6.75 GHz, 30 GHz, and 60 GHz	95
5.1	Directivities in cluster-level fading investigations at 60 GHz	103

5.2	Estimated K-factor for the different bandwidths and directivities in cluster-level fading investigations at 60 GHz	109
6.1	Model parameters for 3GPP correlated multi-band SCM validation	127
7.1	Statistics of the multi-band PPRs from RT simulations after fitting	138
7.2	Correlation of the multi-band PPRs from RT simulations	139
7.3	Correlation between the PPRs of common paths over frequency from RT simulations	140
A.1	Dispersive/selective relation between the different dimensions.	172
D.1	RT parameters for the simulations in the different scenarios.	216
D.2	Parameter for the deterministic clusters simulations.	220
D.3	List of antennas.	221

Acronyms

4G <i>fourth-generation</i>	9
5G <i>fifth-generation</i>	9, 10
ADC <i>analog-to-digital converter</i>	21
AGC <i>automatic gain control</i>	21, 25
AoA <i>azimuth of arrival</i>	94, 108, 110, 118, 200
AoD <i>azimuth of departure</i>	118
AP <i>access point</i>	48, 49, 128
AS <i>azimuth spread</i>	25, 35, 36, 41, 50, 68, 112, 140, 166, 186
ASA <i>azimuth spread of arrival</i> 25, 48, 53, 54, 56, 57, 60, 68, 81, 82, 87, 108, 113, 115, 120, 140, 166, 189	
ASD <i>azimuth spread of departure</i>	60, 68, 73–75, 81, 87, 115, 120, 140, 189
AWGN <i>additive white Gaussian noise</i>	20–22, 133, 195
BER <i>bit error rate</i>	178, 179
BF <i>beam-forming</i>	7–9
BR <i>back reflection</i>	107, 110–112
BS <i>base station</i>	49
BW <i>bandwidth</i>	68
CBSCM <i>correlation-based stochastic channel model</i>	182
CDF <i>cumulative distribution function</i>	55, 61, 77, 131, 132
CI <i>close-in</i>	27, 56, 61, 75, 89, 173, 174

CIR <i>channel impulse response</i>	x, 15, 17, 19, 21, 22, 27, 28, 33–37, 98, 102, 105, 113, 115, 117, 119–121, 139, 158–160, 165, 175, 182, 183, 187, 190–192, 195–197
COST <i>European cooperation in science and technology</i>	185
CPR <i>co-polarization ratio</i>	55, 61, 115, 125–127, 129, 130, 133, 135, 136, 141, 187
CS <i>channel sounder</i>	48, 56, 57, 59, 60, 63, 71–73
D2D <i>device-to-device</i>	3
DKED <i>double knife-edge diffraction</i>	45, 46
DMC <i>diffuse multipath component</i>	122, 139, 141
DMC <i>dense multipath component</i>	5, 14, 27, 28, 52, 55, 70, 72, 77, 157
DoA <i>direction of arrival</i>	18, 59, 108, 111, 115, 118, 158, 160, 182, 185–187, 189, 191
DoD <i>direction of departure</i>	18, 108, 111, 115, 118, 158, 160, 182, 185, 186, 189, 191
DP-UMCS <i>dual-polarized ultra wide-band multi-channel sounder</i>	15
DR <i>dynamic range</i>	25, 165
DS <i>delay spread</i>	12, 21, 25, 35, 39, 41, 47, 48, 50, 53, 54, 56–58, 60, 62, 66, 68, 73–75, 79, 81, 83, 84, 86, 87, 93–96, 103, 105, 106, 108, 112, 113, 115, 116, 120, 122, 139, 140, 165, 166, 176, 180, 186, 189, 192
DSP <i>digital signal processor</i>	8
ED <i>excess delay</i>	165
EoA <i>elevation of arrival</i>	108, 118, 129, 135
EoD <i>elevation of departure</i>	118, 129, 135
ES <i>elevation spread</i>	25, 36, 37, 166
ESA <i>elevation spread of arrival</i>	25, 60, 166, 189
ESD <i>elevation spread of departure</i>	60, 189
ESPRIT <i>Estimation of Signal Parameters via Rotational Invariance Techniques</i>	18
FI <i>floating-intercept</i>	75, 173
FIR <i>finite impulse response</i>	20

FGPA <i>field programmable gate array</i>	8
FSPL <i>free-space path-loss</i>	26, 75, 105, 171–173, 198
GBSCM <i>geometry-based stochastic channel model</i>	121, 192
GI <i>guard interval</i>	8
GO <i>geometrical optics</i>	184
GPS <i>global positioning system</i>	78
GR <i>ground reflection</i>	65, 108, 109, 189
GTD <i>geometrical theory of diffraction</i>	128, 184
GTP <i>geometrical theory of propagation</i>	184
HPBW <i>half-power beam-width</i> . 33–35, 40, 41, 43, 57, 61, 62, 70, 79, 96, 97, 100, 102, 139, 204, 205	
HRPE <i>high resolution parameter estimation</i>	18, 29, 32, 33, 135, 139, 142, 163
IoT <i>Internet of Things</i>	3, 78
ISI <i>inter-symbol interference</i>	165, 178
LNA <i>low noise amplifier</i>	21
LOS <i>line of sight</i> 5, 10, 47, 49–59, 65, 66, 73, 86, 94, 108, 109, 124, 129, 133, 156, 173, 176, 177, 187, 198	
LSP <i>large scale parameter</i> 4, 7, 12, 24, 29–33, 35, 39, 41, 42, 48, 50, 51, 54, 57, 58, 60, 61, 65, 68, 70, 73, 74, 81, 83, 84, 87, 91, 104–108, 113–122, 139–142, 185, 186, 189, 190	
LTI <i>linear time-invariant</i>	20, 159, 195
M2M <i>machine-to-machine</i>	3
METIS <i>Mobile and wireless communications Enablers for the Twenty-twenty Information Society</i>	45, 107, 183, 192
MIMO <i>multiple-input/multiple-output</i>	7, 8, 168, 182, 187
MiWEBA <i>Millimetre-Wave Evolution for Backhaul and Access</i> 106, 108, 121, 181, 183, 185, 190–192	
mmMAGIC <i>Millimetre-Wave Based Mobile Radio Access Network for Fifth Generation In-</i>	

<i>tegrated Communications</i>	45, 48
MPC <i>multi-path component</i>	4, 6, 8, 15, 18, 19, 25, 27, 34, 35, 39, 40, 44, 47, 48, 52, 60, 70, 79, 87, 93–95, 98, 99, 101, 103, 105, 130, 140–142, 159–161, 164–167, 171, 176, 177, 180, 183–185, 189, 196, 200–204
MUSIC <i>MUltiple SIgnal Classification</i>	18
NF <i>noise floor</i>	21
NLOS <i>non-line of sight</i>	8, 11, 49–58, 94, 95, 133, 141, 156, 158, 173, 176, 177, 184
OFDM <i>orthogonal frequency-division multiplexing</i>	8, 165, 171, 178, 180
OLOS <i>obstructed-line of sight</i>	49–51, 53, 55, 56, 156, 173
OSM <i>orthogonal stochastic measure</i>	165
PAAP <i>power bi-azimuth profile</i>	59, 60
PAEP <i>power azimuth/elevation profile</i>	59, 65, 165
PAP <i>power azimuth profile</i>	72, 73, 113, 165, 192
PDAP <i>power delay/angular profile</i>	22
PDF <i>probability distribution function</i>	176, 177
PDP <i>power delay profile</i>	20–22, 34, 35, 37, 39, 40, 50, 56, 58, 65, 70, 72, 79, 80, 82, 83, 85–87, 89, 90, 105, 109, 111, 113, 164, 165, 174
PEP <i>power elevation profile</i>	165
PL <i>path loss</i>	26, 56, 75
PLE <i>path-loss exponent</i>	27, 47, 56, 61, 68, 69, 75, 89, 171, 173, 174
PN <i>pseudo-noise</i>	15, 194
PPR <i>polarimetric power ratio</i>	55, 56, 61, 62, 125–132, 134, 135, 142
PRBS <i>pseudo-random binary sequence</i>	15, 194
PSD <i>power spectral density</i>	194, 201
QKED <i>quadruple knife-edge diffraction</i>	45, 46

QuaDRiGa <i>Quasi Deterministic Radio Channel Generator</i>	70, 107, 185, 189, 192
RF <i>radio-frequency</i>	15, 17
RMa <i>rural-macro</i>	192
RMS <i>root-mean square</i>	102, 165, 176
RT <i>ray tracing</i> .12, 29, 32–34, 37, 43, 48, 51, 56–62, 125, 128, 139, 142, 159, 163, 182–185, 188, 192, 204–206	
RX <i>receiver</i>	15, 17, 47, 195
SAGE <i>Space-Alternating Generalized Expectation maximization</i>	18
SCM <i>spatial channel model</i> .4, 6, 7, 11, 12, 29, 44, 90, 91, 94, 104, 106, 114, 118, 120–122, 125, 127, 128, 133, 135, 139, 141, 142, 181–186, 189, 192	
SIMO <i>single-input/multiple-output</i>	17
SISO <i>single-input/single-output</i>	159
SM <i>spatial multiplexing</i>	7–9
SMC <i>specular multi-path component</i>	5, 156, 157
SNR <i>signal-to-noise ratio</i>	8, 9, 28, 176, 179, 182, 195
SOS <i>sum-of-sinusoids</i>	107
SR <i>side reflection</i>	110
SSP <i>small scale parameter</i>	186
TDoA <i>time delay of arrival</i>18, 27, 34, 108, 110–112, 115, 158, 185–189
TU Ilmenau <i>Technische Universität Ilmenau</i>	12, 15
TWDP <i>two-wave with diffuse power</i>	95, 177
TX <i>transmitter</i>	15, 17, 47, 195
UE <i>user equipment</i>48–50, 128, 185
UMa <i>urban-macro</i>	192
UMi <i>urban-micro</i>	192

URA <i>uniform rectangular array</i>	168
US <i>uncorrelated scattering</i>	164
UTD <i>uniform theory of diffraction</i>	128
UWB <i>ultra-wideband</i>	16, 17, 135
V2V <i>vehicle-to-vehicle</i>	12, 29
WAVE <i>Wireless Access in Vehicular Environment</i>	78
WINNER <i>Wireless World Initiative New Radio</i>	185
WSS <i>wide-sense stationary</i>	164
WSSUS <i>wide-sense stationary uncorrelated scattering</i>	164
XPD <i>cross-polarization discrimination</i>	167, 206
XPI <i>cross-polarization isolation</i>	61
XPR <i>cross-polarization ratio</i>	61, 115, 126, 127, 129, 133, 135, 136, 141, 187, 206

Introduction and Thesis Outline

1 Introduction

“One of the symptoms of an approaching nervous breakdown is the belief that one’s work is terribly important.”

A British philosopher.

Overview

This introductory chapter establishes the multiple research questions that are investigated along this work. We start by defining the main differences between propagation at mm-wave and sub-6 GHz, the system aspects that need to be implemented to compensate these differences, and their implications in performance and channel modelling. In addition, we also introduce general perspectives and expectations for 5G and beyond wireless networks. Finally, this chapter concludes with the outline and a guideline to read this thesis.

1.1 Does It Work?

“He is not such a genius but he’s quite helpful and enthusiastic.”

An Italian Professor.

In the latest years, there has been an increased interest and research activities involving the characterization of mm-wave propagation for communications. This interest has been boosted mainly by the shortage of spectrum at sub-6 GHz bands to cover the requirements of 1000 times wireless data traffic growth from 2010 to beyond 2020, [1]. Only mobile traffic has grown 18-fold from 2011 to 2016, being mostly boosted by the large volume of data consumption by multimedia services in mobile devices, representing since 2012 more than the half of the mobile traffic, [2]. Moreover, with the exponential growth of the Internet of Things (IoT), device-to-device (D2D), and machine-to-machine (M2M) communications, the number of on-line devices upswings significantly and increases drastically the total data traffic in the networks.

Hence, with a massive number of interconnected devices, and with the demand of huge instantaneous data-rates, saturation becomes a problem. We firstly encounter saturation at the physical layer, which for wireless systems is the spectrum. Furthermore, the capacity of communication systems depends on the spectral efficiency, bandwidth, and cell size (related to signal strength, interference, and noise), being the capacity at the current sub-6 GHz technologies, almost on the Shannon boundaries.

Therefore, the latest release of large chunks of mm-wave spectrum for wireless applications alleviates two problems: the saturation and the availability of instantaneous bandwidth. The mm-wave and sub-THz range offers co-located large bandwidths that can be used to boost data-rates and conform the radio access demands to fulfil the required throughputs for different applications, enabling the implementation of multiple services: from wireless multimedia streaming for home entertainment applications to augmented reality in public networks; and a large diversity of scenarios: from very short range indoor communications to high mobility vehicular applications. Furthermore, in the next generation of wireless communications, it is expected a coexistence of multiple standards operating together, supported by a diverse number of radio-interfaces at different frequencies. Hence, mm-wave and multi-band channel modelling and applications are also gaining more and more interest in the community [3, 4].

While there were several publications covering propagation measurements and communications at mm-wave [5, 6, 7, 8, 9], Rappaport’s paper with the catchy phrase *“It will work”* [10] was the one that convinced the agnostic masses, that it could actually work.

But, some *propagation* characteristics at high frequencies are, in some aspects, different in the lower frequency bands. Hence, communication *systems* have to be shaped in such a way that they match these characteristics. Thus, *channel models* also have to meet these system requirements to be able to accurately and efficiently test different architectures and algorithms.

1.2 Propagation Characteristics, System Aspects, and Channel Modelling at mm-wave and sub-THz

“The propagation channel is the only component that can’t be engineered.”

A Finnish Professor.

Between the main propagation differences resulting from a shorter wavelengths we can mention:

- larger free space path-loss with isotropic antennas,
- relative small size of wavelength to objects and surfaces,
- higher penetration and obstruction loss.

Before the boom of the mm-wave, there was for long a paradigm stating that wireless communications at higher frequencies were arduous, mostly based on the large attenuations that the electromagnetic waves exhibit with increasing frequency. However, this is a misconception from the Friss transmission formula [11] considering isotropic radiators:

$$\frac{P_R}{P_T} = G_R G_T \left(\frac{c}{4\pi f_c d} \right)^2, \quad (1.1)$$

where P_R and P_T are the RX and TX power, respectively, G_R and G_T are the RX and TX antenna gains, respectively, d is the TX-RX distance, c is the propagation speed of light, and f_c is the carrier frequency of the signal. Hence, the P_R/P_T ratio is reduced by a f_c^2 factor.

However, we can clearly see in (1.1) that to achieve the same P_R/P_T ratio that at lower frequencies, the increment on the carrier frequency can be compensated by the gain (directivity) either at TX or RX, or both sides. For example, to have the same P_R/P_T ratio at $f_{c,2} = 60$ GHz than at $f_{c,1} = 3$ GHz, we need to scale the combined TX-RX gain by $M^2 = (f_{c,2}/f_{c,1})^2 = 20^2$. Since the physical size of the antennas is proportional to the wavelength, large number of antennas can be easily integrated in small volumes to achieve the necessary gains. For example, if we consider patch antennas as shown in Fig. 1.1, $M \times M$ antennas can be located in an array increasing the total physical area by M^2 and gain (compared to a single antenna element of the array) to M . However, this gain is obtained only in a given direction (directivity). This single implementation aspect and its subsequent consequences might be the biggest game changer in communications from the sub-6 GHz to the mm-wave, involving multiple facets from system design to channel modelling.

Moreover, the utilization of wideband signals offers a higher resolution in the delay domain, and for instance a more deterministic picture of the environment and electromagnetic properties of the scattering materials. For instance, high gain antennas isolate clusters and a larger bandwidth allow us to “see” inside of them by resolving the multiple paths. The system bandwidths under consideration will play a major role on if those multiple path are resolved

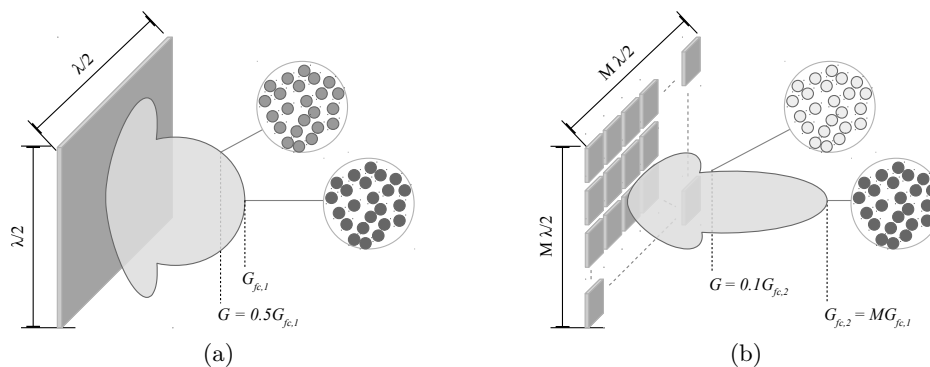


Figure 1.1: (a) Low-gain antenna with wide pattern illuminating multiple clusters, and (b) high-gain array with the same physical size as (a), illuminating a single cluster.

and seen by the receiver as deterministic, or if they are combined stochastically introducing fading. Hence, intra-cluster parameters become more relevant and arises the question of if we can still model them as random processes (as we do at lower frequencies [4, 12, 13]).

The combination of high directive beams and a large bandwidth is expected to reduce small scale fading since channel taps might contain a reduced number of paths (as extreme case, one) and no longer the superposition of multiple uncorrelated paths. For instance, fading modelling has to be revised. Furthermore, with a more deterministic picture, propagation parameters as polarization become more pertinent: a mismatch on the polarization in a scenario of a single path is more severe than a mismatch on the polarization of multiple paths, since the probability that any of those multiple paths carries the polarization of the antenna is higher.

Furthermore, the small size of the wavelength at mm-wave turn small objects into specular reflectors. Since specular reflections only reach the RX if the incident and reflected angles are appropriate, the probability that a scattered path reaches the RX is higher compared to a specular multi-path component (SMC) [14]. Thus, there is an expectation of having a larger amount of dense multipath component (DMC) power at lower frequencies (where scatterers are less specular), but a systematic and quantitative multi-band analysis has not been yet conducted, [15]. Moreover, small objects might be “invisible” at lower frequencies due to their relative size to the wavelength, but visible in the mm-wave range. Examples are pipes, edges, furniture, etc. As shown in measurements in [16], we can also expect to see scatterers at mm-wave that are not present at lower frequencies.

Obstruction loss also becomes more severe and human shadowing is a problem that has to be considered not only in modelling, but also in strategies to overcome its effect. Specially since high directive beams are more affected by human shadowing. The obstruction of the line of sight (LOS) component or main reflected paths might drop considerably the link budget. Therefore, reliable systems at mm-wave and sub-THz need beam-diversity and channel models must accurately model the location of the scatterers to allow the evaluation of such algorithms, and enable their tracking in dynamic scenarios by spatial-consistency.

Penetration losses depend on the material and limits indoor scenarios mostly to intra-room

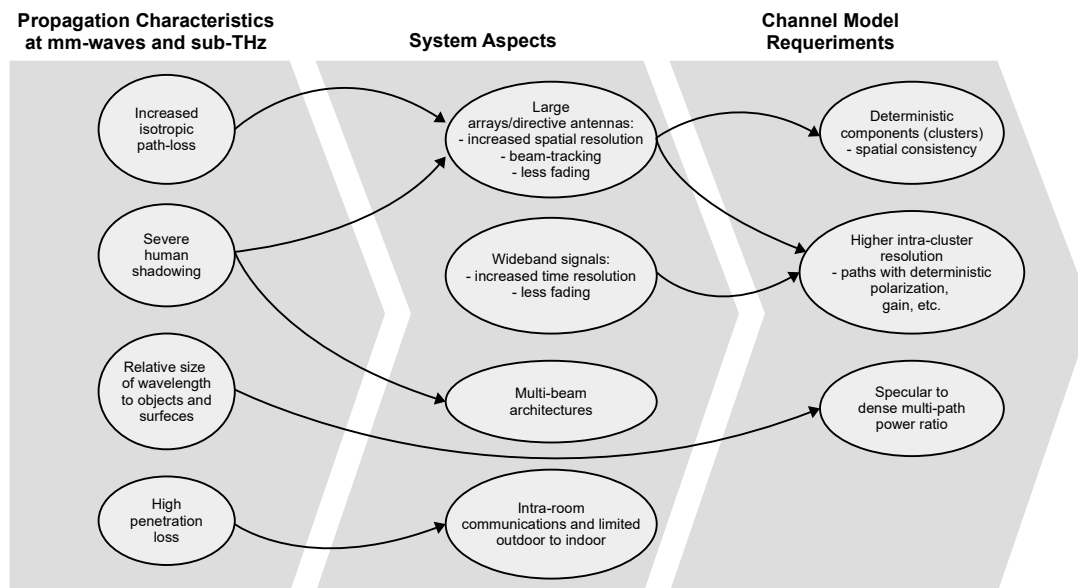


Figure 1.2: Propagation characteristics, system aspects, and channel models requirements.

communications [17], and reduces the outdoor-to-indoor transmission of signal in outdoor scenarios [18]. This scales down interference allowing a more efficient utilization of resources, and confines what is “outdoor” to its environment, and what is “indoor”, to its room.

Consequently, channel models need to adapt to these system requirements. With a higher resolution in the angular domain, clusters in stochastic SCMs can’t be described any more as a completely stochastic summation of MPCs following a random distribution. The isolation of paths in the radio-channel makes more visible properties as polarization, Doppler, and fading. In addition, if we consider mobility, aspects as a consistent location of the scatterers and geometry (propagation distance and angles) need to be more consistent and realistic. Therefore, propagation models must include components following a more deterministic behaviour.

A summary of the main propagation characteristics, their influence on system requirements, and key channel modelling requirements to effectively address those features is presented in Fig. 1.2.

Therefore, in order to study propagation and develop models to test a variety of systems at different frequencies, it is important to isolate the influence of the resolution of the measurement and communication systems in the different domains (angular, Doppler, time-delay, and their counterparts in the Fourier transform). Following the previous analysis, we differentiate between propagation, radio, and digitized channel, accordingly to the amount of system components included in the chain, as shown in Fig. 1.3. Let us define the *propagation channel* by *pure* physical propagation aspects considering only the carrier frequency and isotropic radiators. This assumes no influence of any system component, i.e., an infinite resolution in the different properties of the propagation path (amplitude, delay, angle, polarization, etc.). The propagation channel, as defined here, is an idealization assuming physically impracticable antennas (isotropic). On the other hand, the *radio channel* includes

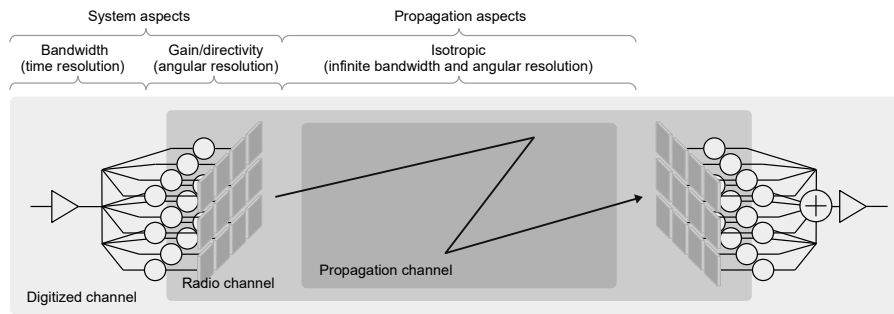


Figure 1.3: Propagation, radio channels, and communication channel.

the first system component: the antenna, which defines the resolution in the angular domain. With extremely high directive antennas, the angular information of a path can be accurately resolved. Finally, under the assumption of a digital communication system, the *digitized channel* introduces the sampling rate of the system (bandwidth). Also, with an extremely large bandwidth, the different paths can be accurately resolved in time-delay. This is the channel that can be used to transmit and receive information and accounts the influence of the antennas (gain/directivity), and the digital interface (bandwidth).

Physical stochastic SCMs¹ based on the WINNER and 3GPP standard [12, 4] are antenna and bandwidth independent², which allows a decoupling between the propagation and system aspects. Different system implementations can be tested by including the antennas and bandwidth in a post-processing step during the simulations. These models are usually described by LSPs, which correspond to the spreads of the marginal power profiles from an isotropic perspective (propagation). Therefore, the characterization of propagation through the study of LSPs in the different frequencies and scenarios is a key feature in this thesis.

1.3 The Massive Idea of MIMO Communications

“Once you go digital, it is hard to come back.”

A Bavarian Professor.

Multiple-input/multiple-output (MIMO) systems involve the utilization of multiple antennas at the TX and RX. Depending on if each antenna is connected to an information signal source (digital interface under a fair assumption that nowadays most of the modems are digital), or to a combiner/splitter, we can differentiate between digital, analog, or hybrid MIMO architectures as seen in Fig. 1.4. While beam-forming (BF) (in its analog implementation) has been utilized for long in different applications from radar to communications, the benefits of spatial multiplexing (SM) and optimum combiners in digital MIMO systems

¹The state of the art in physical SCM can be found in the Appendix C.

²A certain bandwidth dependency is implicitly addressed in the implementation of intra-cluster fading and the antenna dependency on the simplification on the number of clusters.

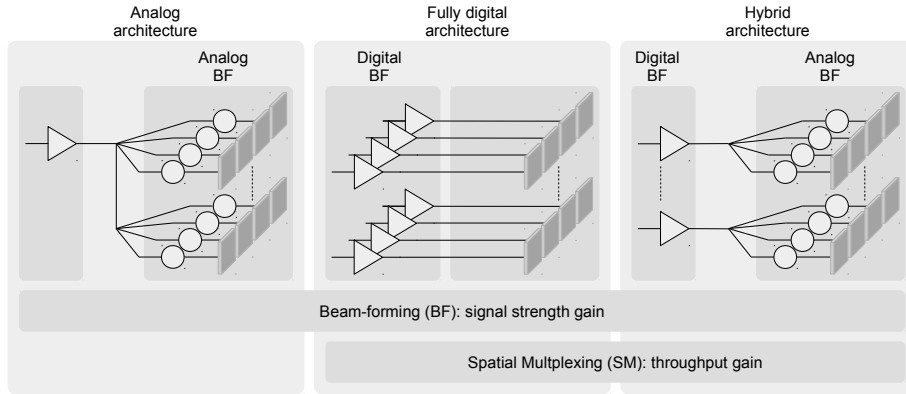


Figure 1.4: Beam-forming and spatial multiplexing capabilities for different MIMO architectures.

have already been introduced in the early 80s in [19]. From there to the recent years, a huge amount of research in the academy and industry has been focused on the development of algorithms to seize the benefits of MIMO systems. The progress on field programmable gate arrays (FPGAs) and digital signal processors (DSPs) enabled high speed computation and large integration volumes in compact surfaces, shifting communications to a paradigm in which we were digitally processing the signals from multiple low gain antennas. Hence, the digital interfaces observe a wider range of the propagation channel, facilitating the condition of rich scattering, which is essential to achieve the necessary decorrelation between the antenna elements to produce orthogonal channels between the TX and RX. Furthermore, the number of antennas and computation requirements compared to the obtained throughput gains was cost effective. On the other hand, the number of antennas at mm-wave scales approximately by a factor of 100 and bandwidths by a factor of 20, making that fully digital architectures become expensive in implementation and energy consumption. Thus, hybrid architectures seem to be a cost/performance compromise between the analog and digital implementations: an analog part in charge of compensating path-loss and a digital part to achieve coding gains, [20]. Differently to the fully digital architecture, in analog and hybrid systems, modulation schemes as orthogonal frequency-division multiplexing (OFDM) take place after spatial filtering. Hence, the digitized signal consists of a few MPCs and OFDM parameters as the needed guard intervals (GIs) are severely reduced.

Furthermore, according to the processing of the signals in the antennas, we can differentiate, as shown in Fig. 1.4, between two applications: SM and BF. In the first case, parallel data-streams are transmitted at the same time and in the same frequency, increasing the spectral efficiency and throughput. In the second case, a single data stream is combined coherently at the antennas to increase the signal strength in a determined direction.

In addition, the use of multiple beams is a promising strategy to supply communication systems with robustness against shadowing and facilitate non-line of sight (NLOS) communications. In the first case, as studied in [21], spare path is used when the main link is interrupted. In the second case, multiple beams are combined coherently to increase the signal-to-noise ratio (SNR), [22].

Moreover, multi-beam systems can be used to implement SM, increasing considerably the

capacity by the transmission of multiple data streams to a single user. However, this needs a rich scattering radio channel, which is not the case with mm-wave and sub-THz systems, in which the number of scatterers is reduced after applying the directivity of the antennas, or the course BF in the array. Since mm-wave systems are expected to operate in *energy limited conditions*, i.e. low SNR, the utilization of multiple antennas might be mostly reduced to increase SNR. Nevertheless, BF and SM can be used together if, after applying BF to achieve a target SNR, there are still degrees of freedom for SM to further increase capacity, [23].

1.4 The Next Generation of Wireless Communications

“In the next generation of wireless communications...”

Every research paper.

There are multiple consortia and groups dealing separately with the different standards and ecosystems of applications. Examples are the IEEE 802.11 family with Wi-Fi and automotive communications, the “dot p” subgroup; the IEEE 802.15.4 family for sensors and home automation; and LTE/LTE-A as standard for the fourth-generation (4G) public cellular communication networks. However, the next generation of mobile communications, the fifth-generation (5G), was outlined as a merging technology, instead of a replacement of the 4G. This will offer the playground in which multiple communication systems interact between each other, creating the largest interconnected network ever seen until now [20].

The progressively digitization and inter-connection of “everything” requires distributed computing, storage, and network access. In the current state of the art, different services and applications have dedicated resources as hardware and networks. However, the envisioned integrated 5G shall flexibly accommodate different use cases from *verticals* into a common logic network, [24, 25, 26]. These vertical sectors with their respective applications can be summarized as:

- factories: time-critical process and remote control, non-critical factory automation, localization, etc.,
- healthcare: remote monitoring, robotics, assets and interventions management in hospital, etc.,
- media and entertainment: ultra high fidelity media, on-site live event experience, immersive and integrated media, cooperative media production, etc.,
- public safety: surveillance, drone detection, etc.,
- automotive: autonomous and automated driving, share view, information society on road, etc.,

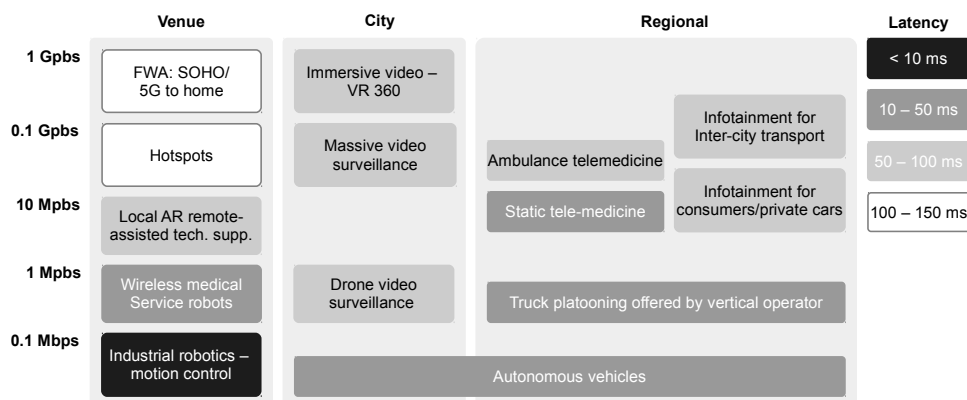


Figure 1.5: Service requirements in terms of data-rate, latency, and centralization level for different applications of several vertical segments.

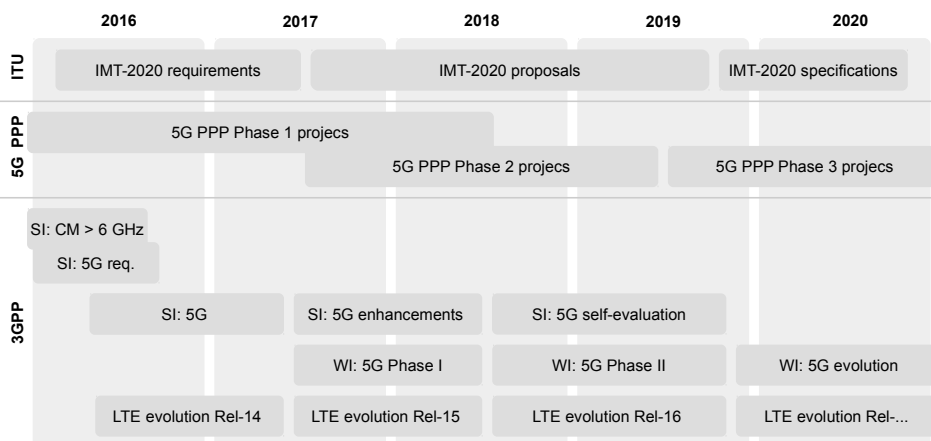


Figure 1.6: Standardization time-lines of the different groups for 5G.

- energy: grid access, back-haul, and back-bone, etc.

These different applications utilize services with diverse requirements in *latency*, *reliability*, *density*, *accuracy in positioning*, *data-rates*, *coverage*, and *mobility*. The data-rate, latency, and centralization level of some of them are summarized in Fig. 1.5.

The first version of standardization for 5G was expected to be ready by 2020 for the main groups and consortia [24], as shown in Fig. 1.6³. This includes mm-wave as one of the radio access technologies and opens an incredible number of research in different areas: from the characterization of propagation in multiple scenarios to system design for a set of diverse applications. However, the closer we got to the date, the more that mm-wave were pushed to the next-next generation of wireless communications (5G and beyond, or 6G), at least, in mobile communications. While back- and front-hauling (fixed links in LOS in most of the cases), and WiFi are already in the market at a certain extent, mobility is still not a mature technology and several aspects need to be resolved.

³Of course, many of these deadlines were not met.

1.5 Thesis Outline and Personal Contribution

“I am not talking to all of you, but to each of you.”

An Argentinian writer.

When I first started working on this topic in 2013, compared to the well known sub-6 GHz, there was a big gap on the characterization of propagation in complex scenarios at mm-wave. At that time, in a very short period, a rich set of measurements at mm-wave were conducted intensively all around the world with the clear objective of characterizing the mm-wave channel for 5G. At the beginning, it was studied independently from the sub-6 GHz and there was a generalised idea of unfavourable or limited propagation conditions, particularly in NLOS. Therefore, mm-wave were relegated to target only short-range indoor applications or fixed back-hauling links with extreme high gain antennas in LOS. This conclusions were also supported by comparisons with previous measurements at sub-6 GHz. However, most of the results were contrasted with measurements carried out with different measurement techniques and characteristics, and at different times and scenarios.

What was also contradictory, is that while the channel was assumed to be different, channel models were still based on the same structure than the sub-6 GHz, and most of the modelling concepts were based on simply scaling the current sub-6 GHz models with parameters from mm-wave measurements. The influence of essential aspects as implementation bandwidths and directivity were minimized or even not considered at all. Only, at some extent, in quasi-deterministic models.

However, still a fair comparison of the mm-wave to the sub-6 GHz propagation channel was missing. Therefore, we have design measurement equipments and set-ups in order to conduct a comparative multi-band analysis of propagation at sub-6 GHz, mm-wave, and sub-THz. The novelty is based on the similarity of the measurement conditions and characteristics, and therefore, on the results from fair comparisons. The results have shown that with the right system characteristics, mm-wave offer similar opportunities than the sub-6 GHz bands. Hence, the biggest challenge now falls into the design of the adequate radio-interface. Thus, proper channel models are required to evaluate their implementations.

A compendium of the theoretical background and state of the art on propagation, fading, and channel modelling is located in the first part of the Appendix. The Appendix A addresses the fundamentals of multi-path propagation and radio-channel modelling. The Appendix B describes the effects of fading in the different domains and how it is modelled. Finally, Appendix C introduces a brief review in SCM, with the state of the art at mm-wave. I also remark the limitations to address the mm-wave system requirements of the different models, which are demonstrated through measurements in the main body of this work.

The rest of this thesis is outlined in two experimental parts, plus this introductory and conclusion chapters. Each chapter is design to be a self-contained piece of work, with an introduction and a conclusion. The Part I introduces the measurement and analysis meth-

odology, and the characterization of multi-band propagation. Part II, analyses the influence of system aspects in the different domain, and channel modelling components.

The Part I, “*mm-wave, Sub-THz, and Multi-band Characterization of Propagation from Measurements and Simulations*”, contains most of the empirical work. In **Chapter 2**, I firstly introduce the measurement equipment used during all the campaigns, which has been developed at the Technische Universität Ilmenau (TU Ilmenau). This chapter also includes the methodology used to analyse the different multi-band propagation parameters from finite resolution measurements. Then, the complete multi-band measurement and analysis methodology is validated in **Chapter 3** by a hybrid measurement/simulation process, showing the achievable accuracy and limitations of this multi-band measurement set-up. Finally, the different measurement campaigns and results in multiple scenarios from several 5G verticals as indoors, street-canyon, industrial, and vehicle-to-vehicle (V2V) are addressed in **Chapter 4**. First, I introduce measurements in controlled environments to study different nature of scatterers: specular and diffuse, based on the dependency of power on the incident angles, polarization, and structure of the scatterer. Later, human blockage at mm-wave is analysed considering the effects of directivity. Finally, complex scenarios are analysed in details, looking for the importance of deterministic components for spatial consistency and the similarities between the mm-wave and sub-6 GHz bands.

Finally, Part II, “*Influence of System Aspects and Multi-band Channel Modelling Components*” addresses different system and modelling aspects indicated in Fig. 1.2. The influence of system aspects such as bandwidth and directivity on delay spreads (DSs) and fading, and the deterministic/stochastic description of the fading process in the channel is addressed in **Chapter 5**. Next, **Chapter 6** opens the discussion between two well known stochastic SCMs approaches: geometry-based and non-geometry-based. According to the simulation requirements (spatial consistency, deterministic location of clusters, generalization of results, etc.), models with deterministic components or completely stochastic ones can be chosen. In addition, the implementation of deterministic components in stochastic SCMs is addressed also in this chapter: the different deterministic clusters found in the measurements are synthesized in a model, and the results show that these clusters are the ones that control the dynamics of the LSPs. On the other hand, Chapter 6.4 extends the non-geometry-based stochastic 3GPP SCM for correlated multi-band simulations with the parameters extracted from the simultaneous multi-band measurements presented in Chapter 4. Finally, **Chapter 7** deals with polarization, introducing analysis and a new modelling approach for stochastic SCMs based on measurements and measurement-validated ray tracing (RT) simulations.

Last, but not least, this thesis concludes in **Chapter 8**, with a final summary of all the contributions and the main results from my work.

This thesis is an empirical work trying to introduce ideas supported by measurements, but also trying to generate a wide range of open points for future work. I personally hope that the reader can find in this document answers and new questions for future research.

Part I

mm-Wave, Sub-THz, and Multi-band Characterization of Propagation from Measurements and Simulations

2 Multi-band Channel Sounding and Parameter Estimation

“You are only coming through in waves, your lips move but I can’t hear what you’re saying.”

A British musician.

Overview

This chapter introduces the multi-band channel sounder used during the different measurement campaigns addressed in this work, showing its architecture, principle of operation, and limitations. We analyse the pre- and post-processing of the measurements and calculation of the different non-parametric power profiles, spreads, and other channel parameters from directive scan measurements, analysing the influence of the finite resolution in the different domains. All these parameters are key modelling aspects for the models addressed in Part II. In addition, we introduce the calculation of specular to DMC power ratio from RiMAX. Theoretical aspects on multipath propagation, analysis and modelling are addressed in Appendix A.

2.1 Multi-band Ultra-wideband Channel Sounding

Channel sounding consists, as the name explicitly depicts, of “sounding” the environment with radio-frequency (RF) signals, and analysing the received echoes to characterize the propagation of electromagnetic waves. Accordingly to the nature of the sounding signals, channel sounder architectures can be classified, between others, into two categories: narrowband and wideband. The first one utilises a narrowband test signal, e.g. a single tone, measuring the frequency response of the channel in a single frequency. On the other hand, the latter utilizes broadband signals with specific properties, e.g. pseudo-noise (PN) sequences in the time domain, measuring instantaneously the complete bandwidth of the CIR in the time domain. Examples of the most frequently used channel sounder architectures are the following¹:

- **Vector network analysers (VNAs)** are narrowband commercial off-the-shelf solutions based on sweeping a carrier over different stepped frequencies. The advantage is the simplicity of the architecture and the possibility of adjusting the bandwidth for different applications. On the other hand, the environment has to remain static during the frequency sweep, reducing flexibility and Doppler resolution due to the increased scanning time. The frequency response of the sounding signal is flat, facilitating between others, the deconvolution of the measurement system response during calibration. In addition, non-linearities and the impairments of inter-band products are also minimized. The CIR is later obtained by the inverse Fourier transform of the recorded frequency response of the channel.
- **Correlation-based channel sounders** modulates a carrier with a known wideband binary sequence such as pseudo-random binary sequences (PRBSs), which is later correlated with a copy of the transmitter (TX) signal at the receiver (RX). The correlation peaks denotes the different MPCs. The properties of the PRBS defines also the ratio between the correlation peaks and the side-lobes (more details can be found in Appendix D.1). This is a time domain architecture, since the CIR is directly recorded during the sounding process. The frequency response of the channel is obtained by means of the Fourier transform. The frequency domain sounding signal has a “sinc” shape. There are two different architectures for correlation at the RX: *sliding-correlator* and *direct-correlator*. The first one allows bandwidth compression, but introduces a delay that reduces performance and Doppler resolution. The latter, offers real-time correlation by down-converting and digitizing the RX signal, and performing the correlation in a later post-processing step. This enables higher time and Doppler resolution. On the other hand, wideband signals are more susceptible to non-linearities introduced by the operating hardware.

The dual-polarized ultra wide-band multi-channel sounder (DP-UMCS) utilized throughout this work is an in-house development of the Electronic Measurements and Signal Processing (EMS) research lab (former Elektronische Messtechnik) at the TU Ilmenau, with financial support, between others, from HUAWEI, [28]. This is a correlation-based channel sounder consisting of TX and RX units with 3D positioners mounted on tripods as shown in the

¹A complete summary on the different architectures can be found in [27].

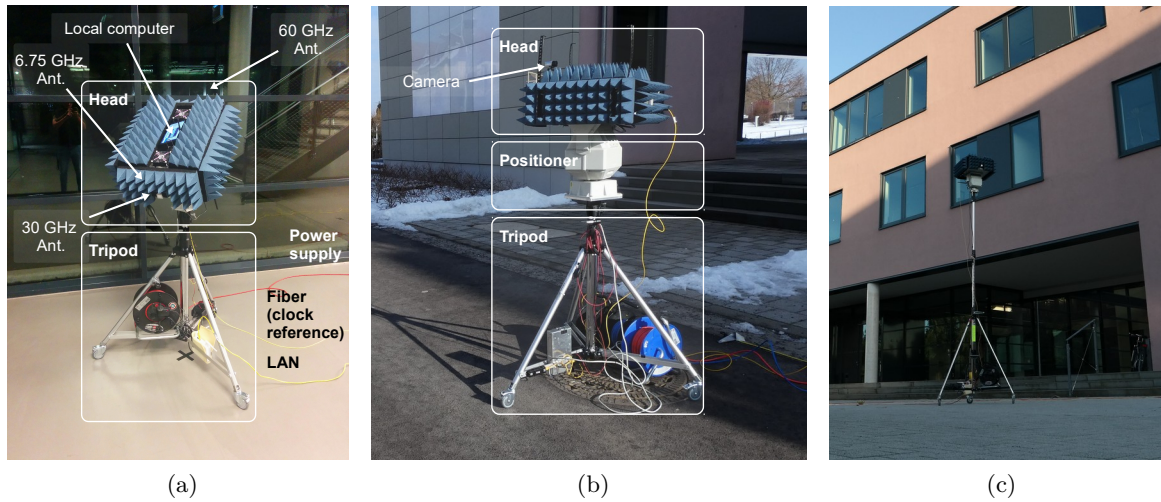


Figure 2.1: Multi-band channel sounder in different environments and set-ups: (a) indoor, (b) outdoors in V2V scenarios, and (c) outdoor with elevation emulating an access point in front-hauling scenarios.

pictures in Fig. 2.1. The tripods allow to regulate the height of the channel sounder and to scan the environment in different directions using dual-polarized directive antennas. Each head has multiple ultra-wideband (UWB) units connected to up- and down-converters as shown in Fig. 2.2. The up and down-converters multiply the clock frequency $f_0 = 6.75$ GHz by an integer number², resulting the target carrier frequencies f_c in the mm-wave bands $f_c = 5 \cdot f_0 = 33.75$ GHz at 30 GHz band, $f_c = 9 \cdot f_0 = 60.75$ GHz at 60 GHz band, and $f_c = 11 \cdot f_0 = 74.75$ GHz at 70 GHz band. The sub-THz band has a different up and down-converter architecture, in which the clock frequency $f_0 = 7.5$ GHz is up- and down-scaled in three stages of $\times 2 \times 6 \times 2 = 24$, being $f_c = 24 \cdot f_0 = 180$ GHz.

Each antenna is pointing in different directions, which allows to scan the environment in the different frequencies at the same time³. However, while the measurements are concurrent in the different bands, the antennas are capturing the channel from different directions. After a complete rotation in azimuth, the channel is measured quasi-simultaneously at the different frequencies in all the directions. This reduces the chances of variations on the environment or differences on the location of the channel sounder units, easing channel comparisons.

The schematic of a single band chain is displayed in Fig. 2.3. The UWB baseband units at TX and RX are synchronized using a 10 MHz clock reference signal distributed over optical fiber in order to achieve a higher stability and reduce clock drifting. Moreover, each TX and RX unit has a local computer to control the UWB baseband units, positioners, and store the raw measurement data. These computers are connected and synchronized via LAN cables.

²The hardware implementation of the multiplier is a factor of 2, but odd numbers can be obtained by taking the lower or upper bands.

³In case of performing elevation scans, the TX and RX units at 6.75 GHz in Fig. 2.2 are stacked under the 33.75 GHz units. This is because with El./Az. positioners, the units on the sides (e.g. the 6.75 GHz in Fig. 2.2) are unable to scan in elevation since they are located in the rotation axis. In such a case, the antennas at 6.75 GHz would be only rotated over their polarization axis.

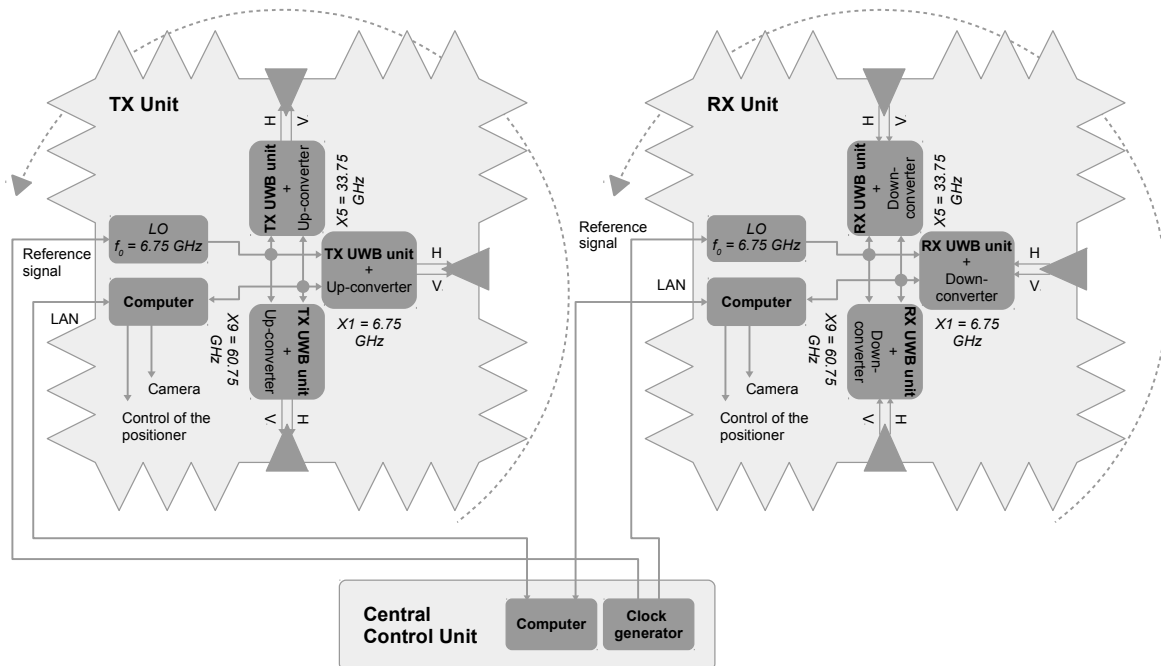


Figure 2.2: Schematic of the multi-band multi-channel sounder.

The UWB baseband units, developed at Ilmsens, are based on a M-sequence chip-set⁴. Most of the measurements presented in this work have been conducted using a $M = 12$ bit sequence with $N = 4095$ samples. Nevertheless, some measurements were conducted using a $M = 15$ bit device with $N = 32767$ samples. For simplifications, otherwise indicated the contrary, we assume that the measurements are conducted with $M = 12$ bit. These modules were originally developed for mono-static single-input/multiple-output (SIMO) UWB radar and for biomedical applications, [29, 30], but later adapted to UWB RF channel measurements [31]. These units consist of 1 TX + 2 RX ports, offering at each of them an instantaneous null-to-null bandwidth equal to f_0 . While the TX port is connected to a switch for the different polarizations, the RX ports are used simultaneously to capture the orthogonal polarizations.

⁴The theoretical background on the identification of the CIR using M-sequences is addressed in Appendix D.1.

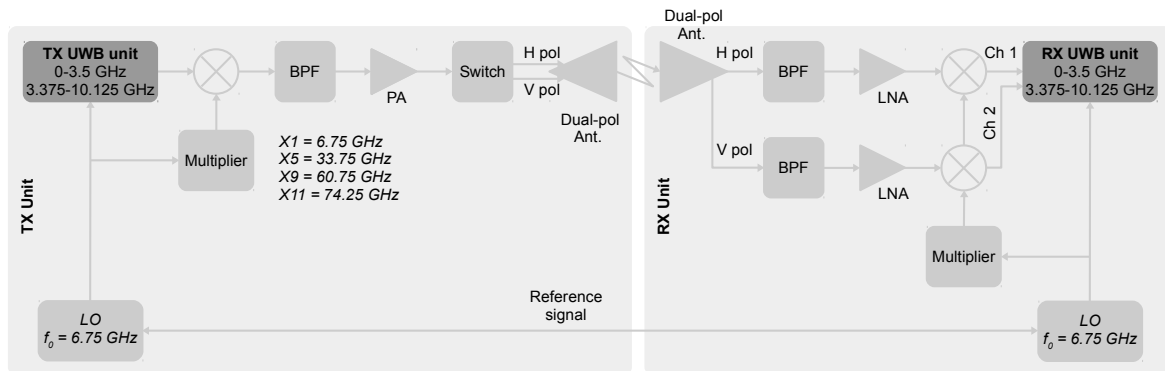


Figure 2.3: Schematic of a single band multi-channel sounder.

2.2 Non-parametric Estimation of Marginal Power Profiles and Large Scale Parameters from Directive Scans

2.2.1 Measured Signal Model Using Directive Scans

Under the assumption of a static channel between the TX and RX, the multi-path *isotropic propagation channel* $h(\tau, \mathbf{\Omega}_D, \mathbf{\Omega}_A)$ equation can be defined as

$$h(\tau, \mathbf{\Omega}_D, \mathbf{\Omega}_A) = \sum_{l=0}^{L-1} \gamma_l^p \delta(\tau - \tau_l) \delta(\mathbf{\Omega}_D - \mathbf{\Omega}_{D,l}) \delta(\mathbf{\Omega}_A - \mathbf{\Omega}_{A,l}), \quad (2.1)$$

where $\gamma^p = |\gamma^p| e^{j\Phi^p}$ is the complex channel coefficient in the TX/RX polarization defined by the tuple $p = \{\phi\phi, \theta\phi, \phi\theta, \theta\theta\}$, τ_l is the time delay of arrival (TDoA), $\mathbf{\Omega}_{A,l}$ is the direction of arrival (DoA), and $\mathbf{\Omega}_{D,l}$ is the direction of departure (DoD) of the l^{th} path. Equation (2.1) can be extended considering the two orthogonal polarization components as

$$\mathbf{H}(\tau, \mathbf{\Omega}_D, \mathbf{\Omega}_A) = \sum_{l=0}^{L-1} \mathbf{\Gamma}_l \delta(\tau - \tau_l) \delta(\mathbf{\Omega}_D - \mathbf{\Omega}_{D,l}) \delta(\mathbf{\Omega}_A - \mathbf{\Omega}_{A,l}), \quad (2.2)$$

where $\mathbf{\Gamma}_l \in \mathbb{C}^{2 \times 2}$ is the polarimetric scattering matrix. Let us consider single port antennas at TX and RX with patterns given by $\mathbf{g}_T(\mathbf{\Omega}_D)$ and $\mathbf{g}_R(\mathbf{\Omega}_A)$, respectively. As further discussed in Appendix A.3, after including the antennas, the angular and polarization information of the MPCs is integrated in the *radio-channel* $\tilde{h}(\tau)$:

$$\begin{aligned} \tilde{h}(\tau) &= \int_{S^2} \int_{S^2} \mathbf{g}_R^T(\mathbf{\Omega}_A) \mathbf{H}(\tau, \mathbf{\Omega}_A, \mathbf{\Omega}_D) \mathbf{g}_T(\mathbf{\Omega}_D) d\mathbf{\Omega}_A d\mathbf{\Omega}_D \\ &= \sum_l \underbrace{\mathbf{g}_R^T(\mathbf{\Omega}_{A,l}) \mathbf{\Gamma}_l \mathbf{g}_T(\mathbf{\Omega}_{D,l})}_{a_l} \delta(\tau - \tau_l). \end{aligned} \quad (2.3)$$

Frequently, the different path-level parameters as angles of arrival and departure, time of arrival, polarization, and Doppler (not considered in this example) of (2.3) are retrieved back using antenna arrays and parameter estimation algorithms, as Estimation of Signal Parameters via Rotational Invariance Techniques (ESPRIT) [32], Space-Alternating Generalized Expectation maximization (SAGE) [33, 34], RiMAX [14], Multiple Signal Classification (MUSIC) [35], etc. This has been widely used at sub-6 GHz, frequency range in which there are multiple antenna arrays available [36, 37]. Unfortunately, there are currently no antenna arrays at mm-wave with the capabilities of applying high resolution parameter estimation (HRPE) algorithms. Mostly, due to the large aperture of the antennas and the large measurement bandwidths [38]. In addition, keeping an inter-element distance of $\frac{\lambda}{2}$ in the manufacture process is also challenging with increasing frequency. To the knowledge of the author, only [39] is currently under development and available with some limitations. Moreover, most of the forehand mentioned algorithms need to be adapted to the large measurement bandwidths at mm-wave, [40].

Still, the angular and time-delay characteristics of the channel can be roughly estimated

from measurements with directive antennas using the channel sounding set-up introduced in Section 2.1. Accurate path-level information is still not possible to be retrieved, but large scale parameters as delay and angular spreads can be estimated, to some extent, with certain accuracy (biased by the measurement system characteristics), being the first ones highly dependent on the bandwidth, and the latter, on the antenna directivity (patterns).

Directive Scans and Angular Resolution

The characterization of the channel using directive scans is based on sampling the channel in different directions using high directive dual-polarized antennas. Let us represent the antenna pattern pointing in the i^{th} RX scanning direction as the shifted version of the antenna pattern $\mathbf{g}_R(\boldsymbol{\Omega}_A)$:

$$\mathbf{g}_R(\boldsymbol{\Omega}_A - i\Delta\boldsymbol{\Omega}_A) = \mathbf{g}_R(\boldsymbol{\Omega}_A) * \delta(\boldsymbol{\Omega}_A - i\Delta\boldsymbol{\Omega}_A), \quad (2.4)$$

where $i\Delta\boldsymbol{\Omega}_A = \{\varphi_i, \vartheta_i\}$ is the azimuth and elevation pointing angle at the RX. Following the same approach at the TX side, the CIR of a single scan in an arbitrary $j\Delta\boldsymbol{\Omega}_D$ and $i\Delta\boldsymbol{\Omega}_A$ directions at the TX and Rx, respectively, can be written as:

$$\begin{aligned} \tilde{h}(\tau, i\Delta\boldsymbol{\Omega}_A, j\Delta\boldsymbol{\Omega}_D) &= \int_{\mathcal{S}^2} \int_{\mathcal{S}^2} \mathbf{g}_R^T(\boldsymbol{\Omega}_A - i\Delta\boldsymbol{\Omega}_A) \cdot \mathbf{H}(\tau, \boldsymbol{\Omega}_A, \boldsymbol{\Omega}_D) \cdot \mathbf{g}_T(\boldsymbol{\Omega}_D - j\Delta\boldsymbol{\Omega}_D) d\boldsymbol{\Omega}_A d\boldsymbol{\Omega}_D \\ &= \sum_l \mathbf{g}_R^T(\boldsymbol{\Omega}_{A_l} - i\Delta\boldsymbol{\Omega}_A) \boldsymbol{\Gamma}_l \mathbf{g}_T(\boldsymbol{\Omega}_{D,l} - j\Delta\boldsymbol{\Omega}_D) \delta(\tau - \tau_l). \end{aligned} \quad (2.5)$$

The process of scanning in multiple directions extends the previous equation into a multidimensional equation in which the angular information is given by the different scans:

$$\begin{aligned} \tilde{h}(\tau, \boldsymbol{\Omega}_A, \boldsymbol{\Omega}_D) &= \sum_i \sum_j \sum_l \overbrace{\mathbf{g}_R^T(\boldsymbol{\Omega}_{A_l} - i\Delta\boldsymbol{\Omega}_A) \cdot \boldsymbol{\Gamma}_l \cdot \mathbf{g}_T(\boldsymbol{\Omega}_{D,l} - j\Delta\boldsymbol{\Omega}_D)}^{a_{i,j,l}} \dots \\ &\dots \delta(\tau - \tau_l) \delta(\boldsymbol{\Omega}_A - i\Delta\boldsymbol{\Omega}_A) \delta(\boldsymbol{\Omega}_D - j\Delta\boldsymbol{\Omega}_D), \end{aligned} \quad (2.6)$$

where $a_{i,j,l} = \mathbf{g}_R^T(\boldsymbol{\Omega}_{A_l} - i\Delta\boldsymbol{\Omega}_A) \cdot \boldsymbol{\Gamma}_l \cdot \mathbf{g}_T(\boldsymbol{\Omega}_{D,l} - j\Delta\boldsymbol{\Omega}_D)$ is the measured channel coefficient with the antennas pointing in the RX i^{th} and TX j^{th} scanning directions. We can see that the angular domain now is recovered, but by discrete samplings of $\boldsymbol{\Omega}_{A/D}$ in $\Delta\boldsymbol{\Omega}$ steps. Each of these samples, contains all the MPCs weighted by the antenna pattern pointing in that direction. The angular resolution can be increased by the directivity of the antenna. However, as discussed in Section 3.7, the scanning intervals must be reduced $\Delta\boldsymbol{\Omega} \rightarrow 0$, which creates a trade-off between measurement time and resolution.

Band Limited Measurements and Delay Resolution

Let us consider a band limited system with an ideal sample-and-hold digitizer with a sampling frequency⁵ $f_s = 1/\Delta\tau = B$, and B the signal bandwidth after sampling. The *digitized channel* $\hat{h}(\tau)$ (discretized radio-channel) can be represented as a linear time-invariant (LTI) finite impulse response (FIR) filter with $k \in \{1, 2, \dots, K\}$ channel taps⁶:

$$\hat{h}(\tau) = \sum_k \left[\underbrace{\sum_l \mathbf{g}_R^T(\boldsymbol{\Omega}_A - \boldsymbol{\Omega}_{A,l}) \cdot \boldsymbol{\Gamma}_l \cdot \mathbf{g}_T(\boldsymbol{\Omega}_D - \boldsymbol{\Omega}_{D,l}) \cdot \frac{1}{\Delta\tau} \text{sinc}\left(\frac{k\Delta\tau - \tau_l}{\Delta\tau}\right)}_{\hat{a}_k} + z(k\Delta\tau) \right] \delta(\tau - k\Delta\tau), \quad (2.7)$$

where $z(k\Delta\tau) \sim \mathcal{N}(0, \sigma_\eta^2)$ is zero-mean additive white Gaussian noise (AWGN), and $\hat{a}_k \in \mathbb{C}$ is the summation of L multipath components weighted by τ_l shifted *sinc* functions falling within the k^{th} channel tap. Depending on the number of multipath components L falling within the k^{th} channel tap, their relative phases, and the filtering effect of the antennas, $\alpha_{i,j,k}$ might experience large variations in the amplitude, generating *small scale fading* as introduced in Appendix B.3. The effects of bandwidth and directivity on fading are theoretically addressed by simulations in Appendix D.2 and empirically analysed in Section 5.3.

Now, (2.7) can be extended considering the directive scan approach in (2.6) as:

$$\begin{aligned} \hat{h}(\tau, \boldsymbol{\Omega}_A, \boldsymbol{\Omega}_D) &= \sum_k \left[\tilde{h}(k\Delta\tau, \boldsymbol{\Omega}_A, \boldsymbol{\Omega}_D) + z(k\Delta\tau, \boldsymbol{\Omega}_A, \boldsymbol{\Omega}_D) \right] \delta(\tau - k\Delta\tau) \\ &= \sum_k \sum_i \sum_j \left[\underbrace{a_{i,j,k} + z_{i,j,k}}_{\hat{a}_{i,j,k}} \right] \delta(\boldsymbol{\Omega}_D - j\Delta\boldsymbol{\Omega}_D) \delta(\boldsymbol{\Omega}_A - i\Delta\boldsymbol{\Omega}_A) \delta(\tau - k\Delta\tau), \end{aligned} \quad (2.8)$$

where $a_{i,j,k} = \sum_l \mathbf{g}_R^T(\boldsymbol{\Omega}_{A,l} - i\Delta\boldsymbol{\Omega}_A) \cdot \boldsymbol{\Gamma}_l \cdot \mathbf{g}_T(\boldsymbol{\Omega}_{D,l} - j\Delta\boldsymbol{\Omega}_D) \frac{1}{\Delta\tau} \text{sinc}\left(\frac{k\Delta\tau - \tau_l}{\Delta\tau}\right) \in \mathbb{C}$ are the samples in the different directions i, j , at the delay k , and the noisy version $\hat{a}_{i,j,k}$ are the coefficients that we actually measure. It is worth to notice that every channel sample is contaminated by noise.

The delay resolution $\Delta\tau = 1/B$ directly depends on the system bandwidth: with a larger bandwidth, the time resolution increases, and more multipath components can be resolved since they are distributed in different channel taps. As shown in Fig. 3.2a, this defines the spatial resolution: ideally, scattering objects located $\Delta r = 2 \cdot c \cdot \Delta\tau$ apart can be differentiated as different peaks in the measured power delay profile (PDP), where c is the propagation speed of light.

⁵Usually, as defined by Nyquist, a sampling process requires $f_s \geq 2B$. However, a sub-sampling method can be applied in correlation based channel sounders [41].

⁶For more details, please refer to Appendix D.2.

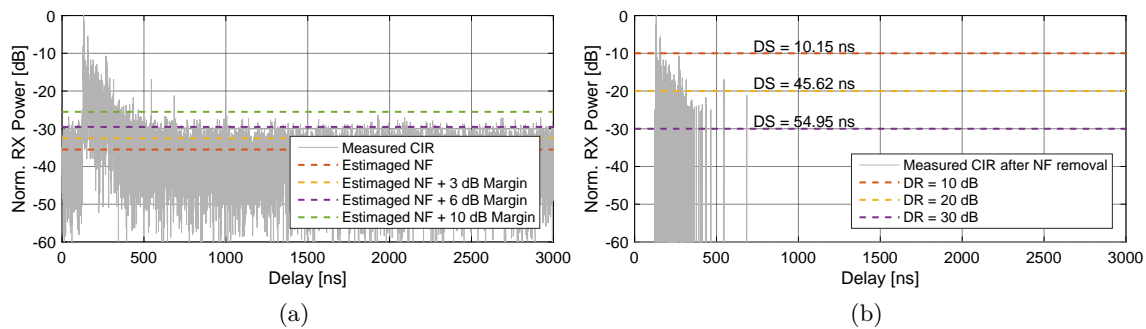


Figure 2.4: (a) Measured CIR and the estimated noise floor (NF) with different margins. (b) Measured CIR after NF removal with different dynamic range limitations and the influence on DS.

2.2.2 Noise Floor Estimation and Removal

Every measured CIR is contaminated by additive noise which causes bias in the estimation of parameters for channel characterization. Figures as PDP, and consequently DS and delay window, are affected by considering noise samples as paths. Therefore, in a pre-processing step, the noise floor is removed from the measured CIR.

Dominating reasons for noise are low noise amplifier (LNA) noise and analog-to-digital converter (ADC) quantization noise. Generally, the effective noise level varies with received power and automatic gain control (AGC) settings. Hence, the measured noise is related to path-loss and fading, changing from snapshot to snapshot when directive antennas are used to scan the environment. Therefore, it is necessary to estimate the noise level for each snapshot, especially when significant variations of received power between snapshots is observed.

In practice, the noise floor level is estimated independently for each measured CIR in the instantaneous delay domain by applying the null hypothesis test. Once the noise level power N_{dB} is estimated, a threshold of ΔN_{dB} is applied and all the samples lower than $N_{\text{dB}} + \Delta N_{\text{dB}}$ are set to zero:

$$\hat{h}(k\Delta\tau, i\Delta\Omega_A, j\Delta\Omega_D) = \begin{cases} \hat{h}(k\Delta\tau, i\Delta\Omega_A, j\Delta\Omega_D) & \text{if } |\hat{h}(k\Delta\tau, i\Delta\Omega_A, j\Delta\Omega_D)|_{\text{dB}}^2 \geq N_{\text{dB}} + \Delta N_{\text{dB}} \\ 0 & \text{if } |\hat{h}(k\Delta\tau, i\Delta\Omega_A, j\Delta\Omega_D)|_{\text{dB}}^2 < N_{\text{dB}} + \Delta N_{\text{dB}} \end{cases} \quad (2.9)$$

Under the assumption of AWGN, the noise content inside the squared absolute value of a measured CIR follows a central χ^2 distribution with $\nu = 2$ degrees of freedom. As discussed in details in [42], adding a threshold reduces the probability of taking noise sample as valid signal. The false alarm probability is calculated as the p-values of the $\chi_{\nu=2}^2$ with a significance level α . The threshold is calculated as $\frac{\alpha}{\nu}$. As shown in Table 2.1, using $\Delta N_{\text{dB}} = 3$ dB reduces the false alarm probability to 0.13. Fig. 2.4a shows an example of the cutting line of different thresholds in a measured CIR at 30 GHz in industry scenario.

Table 2.1: False alarm probability for different threshold values with $\nu = 2$.

α	$\Delta N_{\text{dB}} = 10 \cdot \log_{10} \left(\frac{\alpha}{\nu} \right)$ [dB]	False alarm probability (p-value)
2	0	0.36
4	3.01	0.13
12	6.02	0.002
20	10	0.00005

We can see that without a threshold ($\Delta N_{\text{dB}} = 0$ dB), the chance of leaving noise samples in the CIR after cutting is significantly high (≈ 0.36). Therefore, in this work we adopt a threshold of $\Delta N_{\text{dB}} = 10$ dB, which reduces this probability to ≈ 0 .

2.2.3 Marginal Power Profiles from Directive Scans

The multi-dimensional channel is characterized, in the different dimensions, by the marginal power profiles⁷. Let us neglect the AWGN and define the measured joint power delay/angular profile (PDAP) as

$$\begin{aligned} \text{PDAP}(\tau, \boldsymbol{\Omega}_A, \boldsymbol{\Omega}_D) &= |\hat{h}(\tau, \boldsymbol{\Omega}_A, \boldsymbol{\Omega}_D)|^2 \\ &= \sum_i \sum_j \sum_k |\hat{a}_{i,j,k}|^2 \delta(\tau - k\Delta\tau) \delta(\boldsymbol{\Omega}_A - i\Delta\boldsymbol{\Omega}_A) \delta(\boldsymbol{\Omega}_D - j\Delta\boldsymbol{\Omega}_D). \end{aligned} \quad (2.10)$$

The marginal power profiles in the different dimensions (angular and delay) are calculated by integrating (2.10) in the dimensions of no interest⁸. The PDP can be calculated independently for a single scan in the $i\Delta\boldsymbol{\Omega}_A$ and $j\Delta\boldsymbol{\Omega}_D$ RX and TX directions, respectively, or as the sum over multiple directive scans as a synthesis of a new antenna pattern. For the first case, we denominate it beam-scan PDP and is calculated as:

$$\begin{aligned} \text{PDP}_{\text{BS}}(\tau) &= \int_{\mathcal{S}^2} \int_{\mathcal{S}^2} |\hat{h}(\tau, i\Delta\boldsymbol{\Omega}_A, j\Delta\boldsymbol{\Omega}_D)|^2 d\boldsymbol{\Omega}_A d\boldsymbol{\Omega}_D \\ &= \sum_k |\hat{a}_{i,j,k}|^2 \cos(i\Delta\theta_A) \cos(j\Delta\theta_D) \delta(\tau - k\Delta\tau). \end{aligned} \quad (2.12)$$

A wider pattern can also be synthesized out of different measurements, being the extreme case the synthetic omni-directional with $i\Delta\phi_A$ and $j\Delta\phi_D$ ranging from $-\pi$ to π , and $i\Delta\theta_A$ and $j\Delta\theta_D$ from $-\frac{\pi}{2}$ to $\frac{\pi}{2}$. The PDP is calculated as:

$$\text{PDP}_{\text{SO}}(\tau) = \int_{\mathcal{S}^2} \int_{\mathcal{S}^2} |\hat{h}(\tau, \boldsymbol{\Omega}_A, \boldsymbol{\Omega}_D)|^2 d\boldsymbol{\Omega}_A d\boldsymbol{\Omega}_D$$

⁷This is further developed in Appendix A.2.2.

⁸Keeping in mind the following relation:

$$\int_{\mathcal{S}^2} f(\boldsymbol{\Omega}) d\boldsymbol{\Omega} = \int_{\phi} \int_{\theta} f(\phi, \theta) \cos(\theta) d\phi d\theta. \quad (2.11)$$

$$= \sum_k \underbrace{\sum_{\forall i} \sum_{\forall j} |\hat{a}_{i,j,k}|^2 \cos(i\Delta\theta_A) \cos(j\Delta\theta_D)}_{|\hat{a}_k|^2} \delta(\tau - k\Delta\tau). \quad (2.13)$$

The marginal power angular profiles are calculated by integrating in the delay and the remaining angular dimensions as follows:

$$\text{PAP}_R(\phi_A) = \sum_i \sum_{\forall j} \sum_{\forall k} |\hat{a}_{i,j,k}|^2 \cos(i\Delta\theta_A) \cos(j\Delta\theta_D) \delta(\phi_A - i\Delta\phi_A), \quad (2.14)$$

$$\text{PAP}_T(\phi_D) = \sum_j \sum_{\forall i} \sum_{\forall k} |\hat{a}_{i,j,k}|^2 \cos(i\Delta\theta_A) \cos(j\Delta\theta_D) \delta(\phi_D - j\Delta\phi_D), \quad (2.15)$$

$$\text{PEP}_R(\theta_A) = \sum_i \sum_{\forall j} \sum_{\forall k} |\hat{a}_{i,j,k}|^2 \cos(j\Delta\theta_D) \delta(\theta_A - i\Delta\theta_A), \quad (2.16)$$

$$\text{PEP}_T(\theta_D) = \sum_j \sum_{\forall i} \sum_{\forall k} |\hat{a}_{i,j,k}|^2 \cos(i\Delta\theta_A) \delta(\theta_D - j\Delta\theta_D). \quad (2.17)$$

Finally, the total received power in a certain position can be calculated as the summation over the different dimensions

$$P_{\text{BS/SO}} = \sum_{\forall i} \sum_{\forall j} \sum_{\forall k} |\hat{a}_{i,j,k}|^2 \cos(i\Delta\theta_A) \cos(j\Delta\theta_D). \quad (2.18)$$

The complete procedure is summarized in Fig. 2.5, considering only the RX angular domain for sake of simplicity.

2.2.4 Time and Angular Spreads from Directive Scans

The non-parametric delay and angular spreads are calculated directly from the measurements using the marginal power profiles introduced in the previous sub-section. The RMS-DS can be calculated for the synthetic omni-directional or for a single scan with

$$\text{DS}_{\text{SO/BS}} = \sqrt{\underbrace{\frac{\int_{\tau} \tau^2 \cdot \text{PDP}_{\text{SO/BS}}(\tau) d\tau}{\int_{\tau} \text{PDP}_{\text{SO/BS}}(\tau) d\tau}}_{\overline{\tau^2}} - \left(\underbrace{\frac{\int_{\tau} \tau \text{PDP}_{\text{SO/BS}}(\tau) d\tau}{\int_{\tau} \text{PDP}_{\text{SO/BS}}(\tau) d\tau}}_{\overline{\tau}} \right)^2}. \quad (2.19)$$

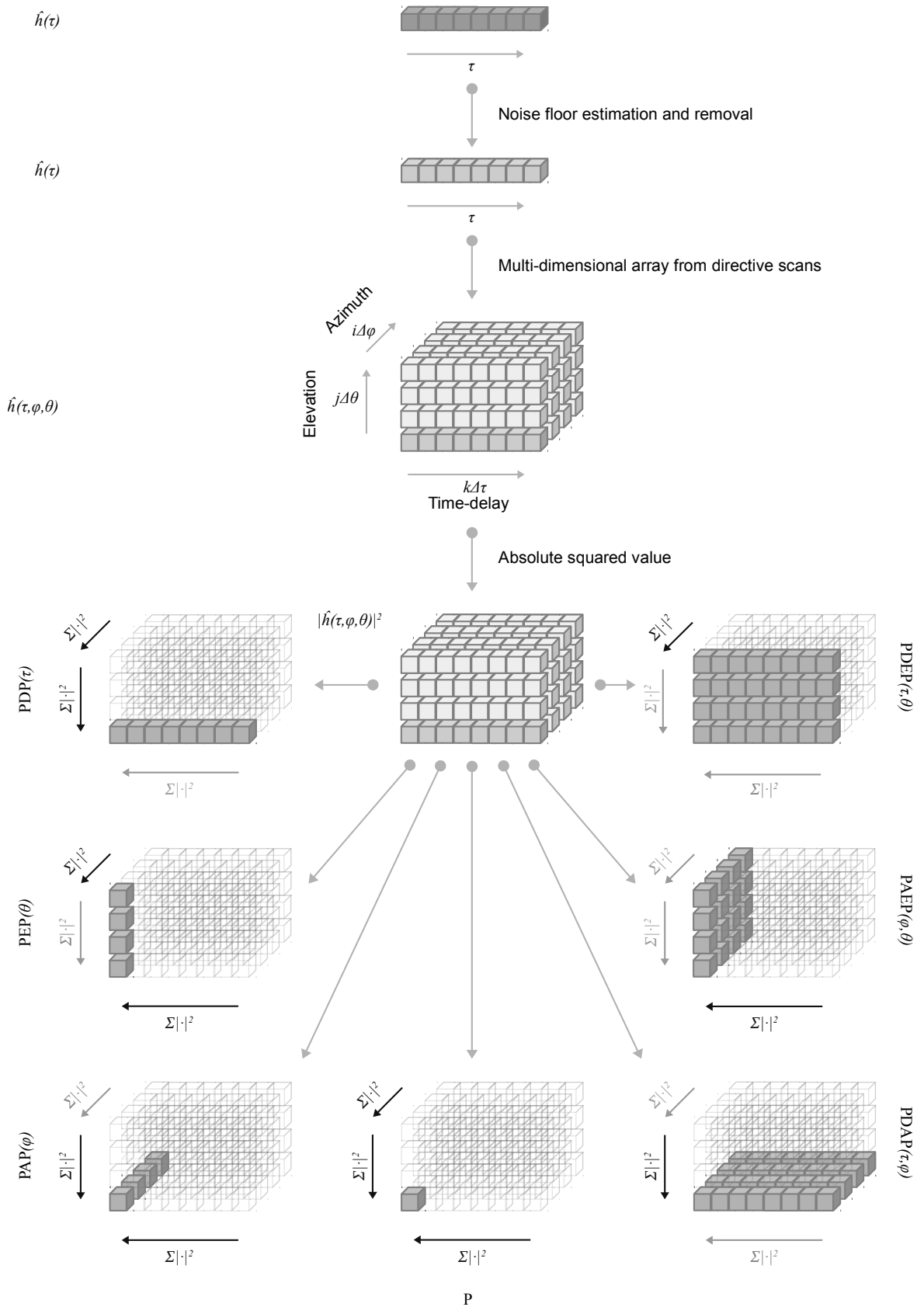


Figure 2.5: Flow chart of the pre-processing and calculation of the marginal power profiles used to determine the LSPs.

Similarly, the azimuth spread (AS) and elevation spread (ES) are calculated using the marginal power angular profiles:

$$\text{ASD} = \sqrt{\frac{\int_{\phi_D} \phi_D^2 \text{PAP}_T(\phi_D)}{\int_{\phi_D} \text{PAP}_T(\phi_D)} - \left(\frac{\int_{\phi_D} \phi_D \text{PAP}_T(\phi_D)}{\int_{\phi_D} \text{PAP}_T(\phi_D)} \right)^2}, \quad (2.20)$$

and

$$\text{ESD} = \sqrt{\frac{\int_{\theta_D} \theta_D^2 \text{PEP}_T(\theta_D)}{\int_{\theta_D} \text{PEP}_T(\theta_D)} - \left(\frac{\int_{\theta_D} \theta_D \text{PEP}_T(\theta_D)}{\int_{\theta_D} \text{PEP}_T(\theta_D)} \right)^2}. \quad (2.21)$$

For the azimuth spread of arrival (ASA) and elevation spread of arrival (ESA), ϕ_D is replaced by ϕ_A , PAP_T by PAP_R , θ_D by θ_A , and PEP_T by PEP_R . Furthermore, when the whole azimuthal circumference is measured, the periodicity must be considered into the calculation of the spreads.

2.2.5 Dynamic Range Limitation for Delay Spread Calculation

Dynamic range (DR) is one of the key parameters of channel sounding. The capability of a channel sounder to distinguish between the maximum and minimum signal strength in a single measurement varies considerably depending on the sounding technique, bandwidth, AGC characteristics, electronics, noise figures, etc.

The DR determines the number of MPCs visible in a single snapshot, therefore, it has a strong influence in parameters as DS. The effect of the measurement DR on the DS is shown in Fig. 2.4b.

Since different channel sounders have a diverse spectrum of DRs, it is a common practice to reduce the dynamic range of the measurements to a trivial number in order to make fair comparisons between measurements carried out with different devices. This is done by setting to 0 all the samples lower than the instantaneous maximum M_{dB} per snapshot minus DR_{dB} :

$$\hat{h}(k\Delta\tau, i\Delta\Omega_A, j\Delta\Omega_D) = \begin{cases} \hat{h}(k\Delta\tau, i\Delta\Omega_A, j\Delta\Omega_D) & \text{if } |\hat{h}(k\Delta\tau, i\Delta\Omega_A, j\Delta\Omega_D)|_{\text{dB}}^2 \geq M_{\text{dB}} - \text{DR}_{\text{dB}} \\ 0 & \text{if } |\hat{h}(k\Delta\tau, i\Delta\Omega_A, j\Delta\Omega_D)|_{\text{dB}}^2 < M_{\text{dB}} - \text{DR}_{\text{dB}} \end{cases} \quad (2.22)$$

where $M_{\text{dB}} = \max_{k\Delta\tau} \{|\hat{h}(k\Delta\tau, i\Delta\Omega_A, j\Delta\Omega_D)|^2\} \forall k$ is the maximum over the delay domain. A DR between $\text{DR}_{\text{dB}} = 20\text{dB}$ and $\text{DR}_{\text{dB}} = 30\text{dB}$ is widely used in the scientific community, which also represents a frequent dynamic range of communication systems commercially available.

2.2.6 Multi-band Path-loss from Measurements

The total RX power P measured per TX-RX distance d is calculated with (2.18)⁹. Let us construct the measured path loss (PL) vector in the frequency band m as the total RX power normalized to the free-space path-loss (FSPL) in the position d_0 :

$$\mathbf{x}_m = \underbrace{10 \cdot \log_{10} \left(\frac{4\pi f_m d_0}{c} \right)^2}_{\text{FSPL at } d_0} + 10 \cdot \log_{10} (P(d_0)) - 10 \cdot \log_{10} (P(\mathbf{d})). \quad (2.23)$$

Multi-band ABG Model

The PL equation in (B.8) can be rewritten on its vectorial form as

$$\mathbf{x} = \underbrace{\alpha_{\text{ABG}} \cdot 10 \cdot \log_{10} \left(\frac{\mathbf{d}}{d_0} \right)}_{\mathbf{a}} + \beta_{\text{ABG}} \cdot \underbrace{\mathbf{1}}_{\mathbf{b}} + \underbrace{\gamma_{\text{ABG}} \cdot 10 \cdot \log_{10}(\mathbf{f})}_{\mathbf{c}}, \quad (2.24)$$

where $\mathbf{x} \in \mathbb{R}^{(N_1+N_2+\dots+N_M) \times 1}$ is the column vector containing the measured PL (relative to the FSPL at the reference distance d_0), being N_m the number of observations in the m^{th} frequency band (out of a total of M frequency bands), $\mathbf{d} \in \mathbb{R}^{(N_1+N_2+\dots+N_M) \times 1}$ is the vector containing the TX-RX distances, $\mathbf{1} \in \mathbb{R}^{(N_1+N_2+\dots+N_M) \times 1}$, and $\mathbf{f} \in \mathbb{R}^{(N_1+N_2+\dots+N_M) \times 1}$ is the vector containing the carrier frequencies:

$$\begin{aligned} \mathbf{x}^T &= \begin{bmatrix} \mathbf{x}_1^T & \mathbf{x}_2^T & \dots & \mathbf{x}_M^T \end{bmatrix} \\ \mathbf{d}^T &= \begin{bmatrix} \mathbf{d}_1^T & \mathbf{d}_2^T & \dots & \mathbf{d}_M^T \end{bmatrix} \\ \mathbf{f}^T &= \begin{bmatrix} f_1 \cdot \mathbf{1}_{1 \times N_1} & f_2 \cdot \mathbf{1}_{1 \times N_2} & \dots & f_M \cdot \mathbf{1}_{1 \times N_M} \end{bmatrix}. \end{aligned} \quad (2.25)$$

In order to perform the least-squares regression, (2.24) is written as the multiplication of a matrix containing the constants and a vector with the parameters to estimate

$$\begin{aligned} \mathbf{x} &= \underbrace{\begin{bmatrix} \mathbf{a} & \mathbf{b} & \mathbf{c} \end{bmatrix}}_{\mathbf{A}} \begin{bmatrix} \alpha_{\text{ABG}} \\ \beta_{\text{ABG}} \\ \gamma_{\text{ABG}} \end{bmatrix}, \\ &= \mathbf{A} \cdot \hat{\mathbf{x}}, \end{aligned} \quad (2.26)$$

and the least-squares solution provides the estimation of the ABG parameters

$$\hat{\mathbf{x}} = \mathbf{A}^+ \cdot \mathbf{x} \begin{cases} \hat{x}_1 = \alpha_{\text{ABG}} \\ \hat{x}_2 = \beta_{\text{ABG}} \\ \hat{x}_3 = \gamma_{\text{ABG}} \end{cases} \quad (2.27)$$

⁹A more precise background on the different models can be found in Appendix B.2.

Multi-band CI Model

On the other hand, the close-in (CI) model equation (B.7) can be rewritten in vectorial notation as

$$\begin{aligned} \mathbf{x} &= \underbrace{\alpha_{\text{CI}} \cdot 10 \cdot \log_{10} \left(\frac{\mathbf{d}}{d_0} \right)}_{\mathbf{a}} + \underbrace{10 \cdot \log_{10} \left(\frac{4\pi \mathbf{f} d_0}{c} \right)^2}_{\mathbf{b}=\text{FSPL}}, \\ &= \alpha_{\text{CI}} \mathbf{a} + \mathbf{b}. \end{aligned} \quad (2.28)$$

The estimated path-loss exponent (PLE) is then calculated using the least-squares solution

$$\alpha_{\hat{\text{CI}}} = \mathbf{a}^+ \cdot (\mathbf{x} - \mathbf{b}). \quad (2.29)$$

The standard deviation of the log-normal shadowing factor X_σ in both models is estimated from the measurements by

$$\hat{\sigma} = \sqrt{\frac{\sum_{i=1}^{N_1+N_2+\dots+N_M} (x_i - \mu_{\mathbf{x}})^2}{N_1 + N_2 + \dots + N_M - 1}}, \quad (2.30)$$

where x_i is the i^{th} measurement and $\mu_{\mathbf{x}} = \text{E}\{\mathbf{x}\}$ is the mean value of the measurement vector.

2.3 Parametric Estimation of Specular and Dense Multi-path Components

The estimation of the specular and diffuse power has been conducted using RIMAX. Relevant information on the the estimation process can be found in [14]. In this work, due to the lack of antenna arrays and the measurement set-up (scanning the angular domain by rotating directive antennas at TX and a dipole at RX), only the delay dimension has been used on the estimation of specular and diffuse MPCs. Furthermore, the estimation has been performed independently per TX angular scan $i\Delta\Omega$, and the antenna patterns were not de-embedded. Therefore, from the specular components is obtained only the path gain (affected by the antenna) in the vertical polarization $\gamma_l^{\theta\theta}(i\Delta\Omega)$ and TDoA $\tau_l(i\Delta\Omega)$. The estimated CIR $\hat{h}_{\text{SC}}(l, i\Delta\Omega)$ containing the specular paths after the estimation is re-constructed as

$$\hat{h}_{\text{SC}}(l, i\Delta\Omega) = \sum_l \gamma_l^{\theta\theta}(i\Delta\Omega) \delta(\tau - \tau_l(i\Delta\Omega)). \quad (2.31)$$

On the other hand, the DMC are also calculated per scanning direction, and therefore the parameters $\beta(i\Delta\Omega)$, $\tau_d(i\Delta\Omega)$, $\alpha_1(i\Delta\Omega)$, and $\alpha_0(i\Delta\Omega)$ also depend on the pointing direction

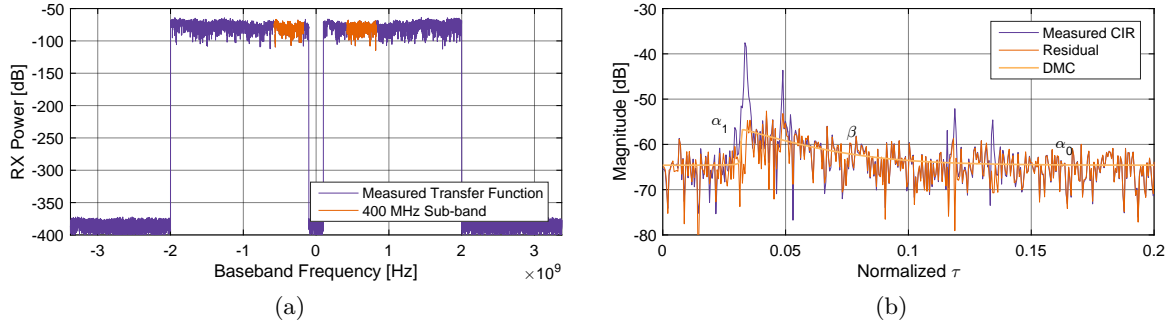


Figure 2.6: (a) Sub-band selection from the complete measured transfer function after back-to-back calibration and windowing. (b) RIMAX estimation process: sub-band limited measured CIR, residual signal after removing the specular components, and remaining DMC.

and pattern of the antennas. The estimated DMC is modelled as

$$\mathbb{E} \left\{ |\hat{h}_{\text{DMC}}(\tau, i\Delta\Omega)|^2 \right\} = \begin{cases} 0, & \text{if } \tau < \tau_d(i\Delta\Omega) \\ \frac{1}{2} \cdot \alpha_1(i\Delta\Omega), & \text{if } \tau = \tau_d(i\Delta\Omega) \\ \alpha_1(i\Delta\Omega) \cdot e^{-\beta(i\Delta\Omega) \cdot (\tau - \tau_d(i\Delta\Omega))}, & \text{if } \tau > \tau_d(i\Delta\Omega). \end{cases} \quad (2.32)$$

It is worth to mention that since all these estimated parameters are highly influenced by the antenna patterns, they cannot be compared to the isotropic characteristics of the channel. However, under the assumption of a similar influence of the antenna characteristics on the specular and DMC power, the calculated power ratios should still be valid. This also applies for the inter-band comparison and the results can provide fruitful insights on this power ratio over frequency.

In order to increase the robustness of the estimation, the measured transfer function of the channel is split into 400 MHz sub-bands and two of them are selected (with the largest SNR) as two independent snapshots of the same CIR. The sub-bands selection is shown in Fig. 2.6a and an example of the RIMAX estimation result is shown in Fig. 2.6b.

The specular to dense multipath power ratio per angular scan $P_{\text{SP2DMC}}(i\Delta\Omega)$ is then calculated as

$$P_{\text{SC2DMC}}(i\Delta\Omega) = \frac{P_{\text{SC}}}{P_{\text{DMC}}} = \frac{\sum_l |\hat{h}_{\text{SC}}(l, i\Delta\Omega)|^2}{\int_{\tau} |\hat{h}_{\text{DMC}}(\tau, i\Delta\Omega)|^2 d\tau}. \quad (2.33)$$

Results and multi-band analysis on the specular to dense multipath power dependency on frequency in industry scenario are presented in Section 4.5.6.

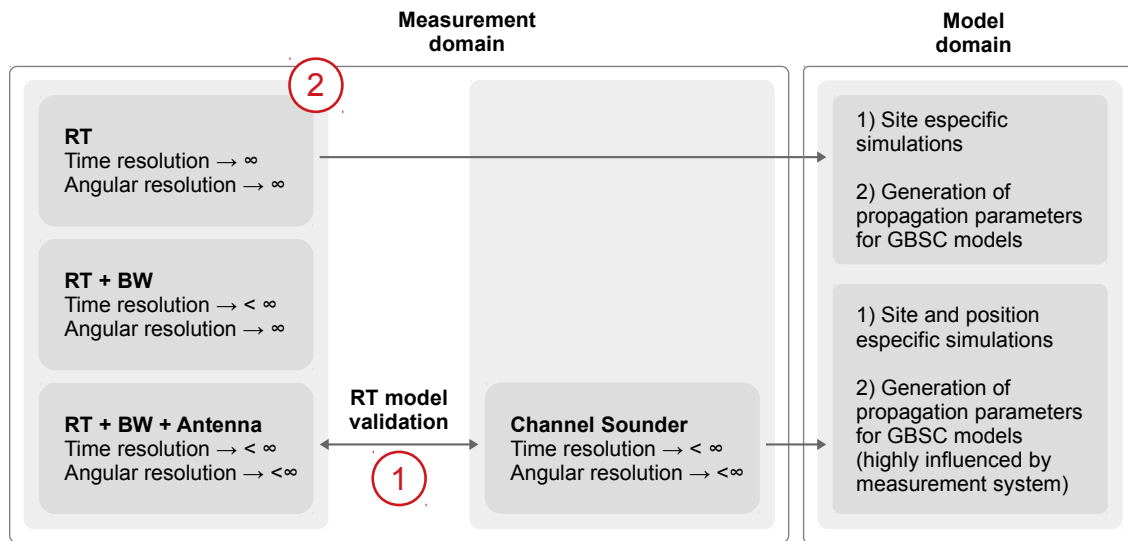


Figure 2.7: Validation of RT from measurements and parametrization of SCMs.

2.4 Future of Channel Sounding and Modelling

The future of wireless communications considers the utilization of higher ranges of frequency bands. With the congestion of the sub-6 GHz bands, the mm-waves are gaining territory and penetrating in different application segments as public cellular networks and V2V, in which years ago, mm-wave communications were considered unfeasible. Nowadays, the sub-and Terahertz ranges are under investigation for high data-rate and short-range applications as inter-rack communications [43], [44]. However, if we compare to the early years of the mm-waves communications, we can fairly predict that applications of these frequency ranges will also be diversified [45].

Therefore, channel sounding and modelling also needs to envision the future trends. However, we will face similar limitations as the ones we currently have at mm-waves: HRPE from measurements due to the challenging production of antenna arrays, which will be even more difficult with increasing carrier frequencies. In addition, the needed gains of the measurement antennas (directivity) also needs to be increased, reducing the scanning steps, and increasing measurement times. Therefore, at the beginning we might need to rely more on simulation tools as RT, either by having very accurate models (maps and materials) for site specific simulations, or to use those models to generate multiple realizations and rich data-sets for statistics to feed stochastic channel models.

The development of high accuracy technologies as 3D laser scanners facilitate the production of digital maps with a formidable level of details. The electromagnetic properties of the constructive materials in the environment can be chosen from data-bases, or adjusted after specifically designed in-situ measurements. In addition, the overall performance of the RT simulations and validation of the model (map and electromagnetic properties of the materials) can be performed by comparing the simulations with measurements, as shown in Fig. 2.7. In a first step, the validation of the RT model is done by comparing measured LSPs (or any other arbitrary channel characteristic) with the RT simulations emulating the

sounding process. After the validation is passed (based on a pre-defined criteria of acceptance), LSPs can be calculated from simulations considering infinite resolution in time-delay and angle. In addition, RT generates richer statistics compared to the usual limited number of measurements in a single scenario, due to the possibility of simulating multiple points in a single scenario.

3 Validation of the Multi-band Measurement and Estimation Methodology

“He rocks on the stage.”

An Italian student about a German Professor.

Overview

This chapter is related to validation of the multi-band channel sounder and measurement methodology addressed in Chapter 2. We characterize the errors introduced by the measurement methodology and equipment with a hybrid measurement/simulation approach. The first ones result from calculating LSPs from the synthesis of patterns from directive scans. The second ones, are generated by the finite resolution of the devices in the different measurement domains. In addition, there are systematic differences between the measured bands introduced by the difference between the antenna patterns and electronic components of the different measurement devices.

From this chapter, my personal contribution is the design of the methodology (and subsequent calculation of the results) to characterize and analyse the error on the estimation of power profiles and LSPs using the aforementioned measurement set-up, and finally, the validation of the multi-band measurement approach.

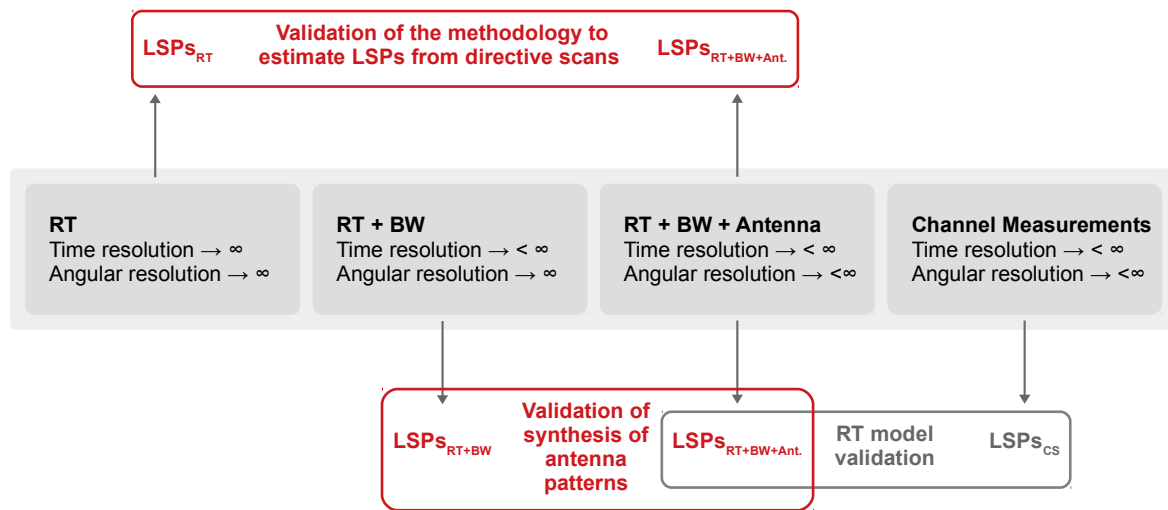


Figure 3.1: RT and measurement comparison considering the influence of resolution.

3.1 Introduction

In this chapter, we analyse the influence of

- bandwidth,
- directivity of the measurement antennas,
- scanning steps in the angular domain,
- synthesis of patterns from directional measurements, and
- utilization of different hardware to measure in the different bands

on the estimation of marginal power profiles and LSPs. This influence is quantized in a simulative analysis using RT as a reference channel and emulating the sounding process by introducing the channel sounder response in the simulations and comparing the results. As shown in Fig. 3.1, we compare LSPs calculated using pure path-level information from RT (with infinite bandwidth and angular resolution, similar to results obtained from HRPE) with LSPs estimated using limited bandwidth with ideal isotropic antennas, and with limited bandwidth and synthetic patterns from angular scans. The latter emulates the channel sounding process, and allow us to introduce the different measurement antenna patterns and evaluate the measurement errors.

Firstly, we characterize the errors on the estimation of LSPs using the channel sounder and measurement set-up introduced in Section 2.1, based on the methodology of using directive antennas to synthesize omni-directional patterns. The influence of bandwidth and angular steps are also analysed. Secondly, we characterize the errors between the different bands, with the objective of validating the simultaneous multi-band channel sounder set-up used along this thesis.

3.2 Characterization of Errors on the Estimation of Multi-band Large Scale Parameters from Directive Scans

This error characterization provides an insight into the quality of the marginal power profiles and LSPs directly estimated from measurements with the set-up introduced in Section 2.1, without utilizing HRPE. We study the errors introduced by

- limited resolution in time-delay and angle (related to measurement bandwidth and directivity of the measurement antenna): it produces differences between the marginal power profiles and spreads calculated directly from the measured CIR using this sounding methodology, and the ones calculated from CIRs generated with path-level information estimated with HRPE from measurements or RT simulations,
- measurement set-up and limited scans (related to the measurement set-up and utilization of directive scans in the angular domain): in order to save measurement time, and because of availability of antennas, low directive antennas are used to scan, usually, with scanning steps equal to the half-power beam-width (HPBW) of the antenna. In addition, only a limited number of elevation cuts from the 3D sphere are usually available. This generates a deviation to the isotropic characteristic of the channel,
- inter-band errors (originated by the differences between the antenna patterns, electronics, and calibration of the measurement systems in the different bands): while the antennas have been carefully selected to have very similar patterns in the different bands, there are slight variations on the patterns within the measurement bandwidths. This creates differences between the results obtained in the different bands.

Next, we will characterize the different errors using the following definitions. Let us define the percent *relative error* as the difference between the measured quantity X and the true value T (reference). In this case, the LSP considering a certain bandwidth and realistic antennas and the LSP calculated from RT using infinite bandwidth and isotropic antennas,

$$\text{relative error \%} = \left| \frac{X - T}{T} \right| \cdot 100. \quad (3.1)$$

In addition, let us also define the percent *difference error* as the difference between two measured quantities X_1 and X_2 . Note that the difference error doesn't hold a reference. In this case, the difference error is calculated between the LSPs estimated either using different scanning steps during measurements, or LSPs calculated in different bands,

$$\text{difference error \%} = \left| \frac{X_1 - X_2}{(X_1 + X_2)/2} \right| \cdot 100. \quad (3.2)$$

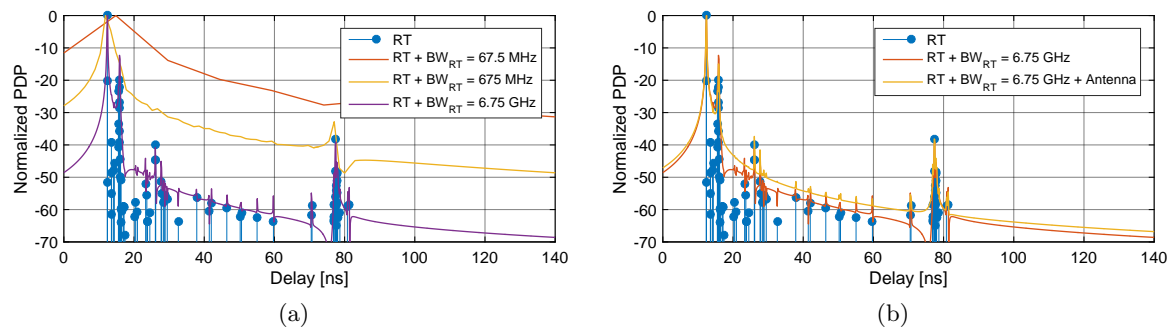


Figure 3.2: (a) Ideal PDP from RT with infinite bandwidth and isotropic radiators and the influence of the measurement system bandwidth. (b) Comparison of PDP from RT with ideal isotropic antennas and the reconstruction using directive scans with 30° HPBW antennas at 30 GHz.

3.3 Error Quantization by Simulative Analysis using Ray-Tracing

3.3.1 Emulated Channel Sounder Equation Model

RT provides at each simulated position path-level information of the polarimetric scattering matrix Γ_l , TDoA τ_l , angles of arrival ($\phi_{A,l}, \theta_{A,l}$) and of departure ($\phi_{D,l}, \theta_{D,l}$). For sake of simplicity, let us consider the CIR on the vertical polarization

$$h_{\text{RT}}(\tau) = \sum_l \gamma_l^{\theta\theta} \cdot \delta(\tau - \tau_l). \quad (3.3)$$

The previous equation considers infinite bandwidth and isotropic radiators. However, if we want a fair comparison with band-limited measurements, system bandwidth needs to be included in (3.3). This limits the identification of MPCs in the time-delay domain and introduces small scale fading as shown in Fig. 3.2a and discussed in Section 2.2.1. Let's assume a system with a flat transfer function, bandwidth BW , and isotropic antennas. The CIR can be calculated as the inverse Fourier transform of the transfer function $\hat{H}_{\text{RT}+BW}(f_k)$, calculated from the RT CIR by

$$\hat{H}_{\text{RT}+BW}(f_k) = \sum_{l=1}^L \gamma_l^{\theta\theta} e^{-j2\pi f_k \tau_l} \bullet \longrightarrow \hat{h}_{\text{RT}+BW}(\tau), \quad (3.4)$$

where f_k are the sampled frequency points. Fig. 3.2a shows the PDP $|h_{\text{RT}}(\tau)|^2$ from the RT considering infinite bandwidth and isotropic antennas, and the PDP $|\hat{h}_{\text{RT}+BW}(\tau)|^2$ considering the influence of different bandwidths, but still isotropic antennas. The effect of the system bandwidth on the delay resolution can be observed in the widening of the impulses and the impossibility to resolve many closely located MPCs. This shows the limitations of peak-detector algorithms on the identification of MPCs, since many MPCs are concentrated in a single peak. Moreover, the amount of diffuse power is clearly dependent on the measurement bandwidth.

Let us now consider the CIR obtained with the emulated channel sounding process using directive scans in the TX direction $(m\Delta\phi_D, n\Delta\theta_D)$ and RX direction $(i\Delta\phi_A, j\Delta\theta_A)$. This is introducing the antennas into (3.4),

$$\begin{aligned} \hat{H}_{\text{RT+BW+Ant}}(f_k, i\Delta\phi_A, j\Delta\theta_A, m\Delta\phi_D, n\Delta\theta_D) &= \dots \\ \sum_{l=1}^L \hat{\mathbf{g}}_R^T(\phi_{A,l} - i\Delta\phi_A, \theta_{A,l} - j\Delta\theta_A) \cdot \mathbf{\Gamma}_l \cdot \hat{\mathbf{g}}_T(\phi_{D,l} - m\Delta\phi_D, \theta_{D,l} - n\Delta\theta_D) \cdot e^{-j2\pi f_k \tau_l}, \\ &= \sum_{l=1}^L \hat{\gamma}_{l,i,j,m,n} \cdot e^{-j2\pi f_k \tau_l} \bullet \circ \hat{h}_{\text{RT+BW+Ant}}(\tau, i\Delta\phi_A, j\Delta\theta_A, m\Delta\phi_D, n\Delta\theta_D), \end{aligned} \quad (3.5)$$

where $\hat{\mathbf{g}}_{R/T}(\cdot) \in \mathbb{R}^{2 \times 1}$ is the measured antenna pattern used during the sounding process. It worth to mention that the antennas are assumed to be frequency independent, which is not realistic, but an approximation. The synthetic omni-directional PDP $|h_{\text{RT+BW+Ant}}(\tau)|^2$ is calculated with (2.13). Fig. 3.2b shows the difference between the PDP assuming infinite bandwidth and isotropic radiators $|h_{\text{RT}}(\tau)|^2$, considering system bandwidth and isotropic antennas $|h_{\text{RT+BW}}(\tau)|^2$, and the emulation of the sounding process with scans in the angular domain considering finite bandwidth and synthetic patterns $|h_{\text{RT+BW+Ant}}(\tau)|^2$.

3.3.2 Influence of Bandwidth and Directivity on the Estimation of Large Scale Parameters from Directive Scans

The influence of bandwidth on the estimation of the different LSPs can be observed in Fig. 3.3. As shown in Fig. 3.2a, with larger bandwidths, more specular MPCs are resolved in time-delay and the diffuse power product of the low time-delay resolution decreases. Therefore, figures as DS estimated directly from the measurements approximate more to the reference DS calculated from RT considering infinite bandwidth and ideal isotropic antennas. In this particular scenario, Fig 3.3a shows a good match on the statistics of the emulated measured DS and the reference DS from RT.

On the other hand, the influence of the resolution in the angular domain (limited to 30° due to the HPBW of the antennas) is shown in Fig 3.3b. The ASs calculated from the reference RT CIR diverge considerably from the ones estimated using the emulated channel sounding set-up. Besides, the minimum ASs that can be estimated is tied to the directivity of the antenna.

3.4 Characterization of Errors from Limited Resolution in the Measurement Equipment

The distribution of the relative error between the LSPs calculated emulating the sounding process with a $BW = 6.75$ GHz in the different bands and the reference RT is shown in Fig. 3.4a. A mean relative error of 17.6 % and 23 % can be observed on the DS at 30 GHz and 60 GHz, respectively. On the other hand, the low angular resolution given by the

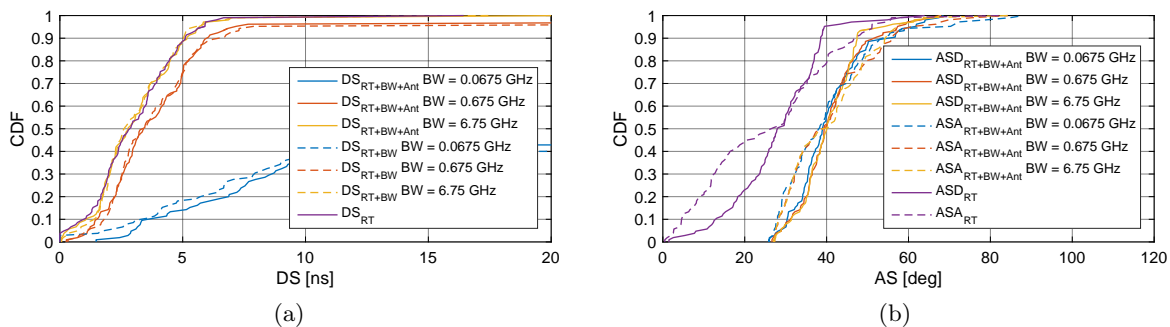


Figure 3.3: (a) Empirical cumulative distribution of the DS estimated using different bandwidths and antennas (isotropic and synthetic patterns from directive scans) compared to DS estimated from reference RT CIR at 30 GHz. (b) Empirical cumulative distribution of ASs estimated using different bandwidths compared to reference RT CIR at 30 GHz.

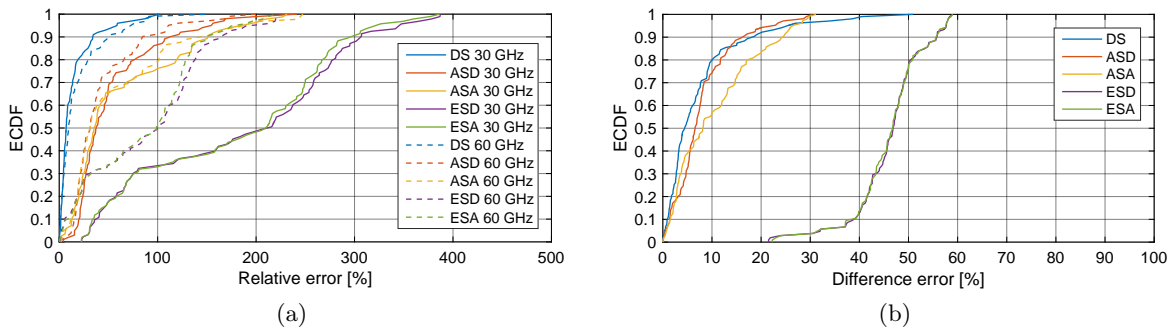


Figure 3.4: (a) Empirical cumulative distribution of the relative error between the LSPs in the different bands with the reference RT. (b) Empirical cumulative distribution of the difference error between the emulated sounding process at 30 GHz and 60 GHz.

directivity of the antennas introduces larger relative errors in the angular spreads.

While the relative error on the DS and ASs are similar in the different bands, the ESs showed significant differences. This is due to the differences on the antenna patterns at 30 GHz and 60 GHz. Since the directivity of the measurement antenna at 60 GHz is slightly higher than the directivity of the measurement antenna at 30 GHz, the relative error in the angular spreads is smaller at 60 GHz.

3.5 Characterization of the Errors in the Estimation of the Multi-band Large Scale Parameters

Ideally, if the channel sounder doesn't introduce a systematic error in the different bands, the LSPs calculated from the same CIR should be identical along the measured bands. However,

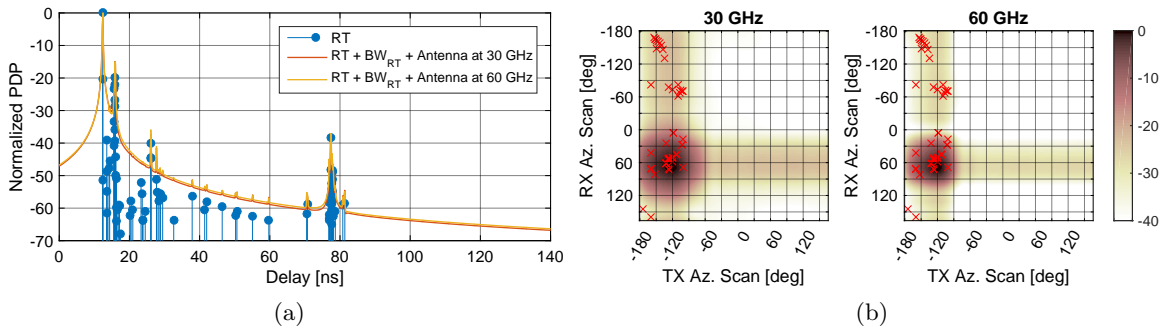


Figure 3.5: (a) Comparison of the synthetic omni-directional PDP from the emulated sounding process at 30 GHz and 60 GHz with the reference RT PDP. (b) Power bi-azimuthal profile in the different bands with the reference RT PDP (in crosses).

Table 3.1: Relative and difference error on the estimation of multi-band LSPs from directive scans.

LSP	Relative error at 30 GHz [%]		Relative error at 60 GHz [%]		Difference error [%]	
	Mean	Std.	Mean	Std.	Mean	Std.
DS	14.75	19.83	19.31	25.52	7.62	8.99
ASD	54.26	44.17	43.79	37.15	8.05	6.41
ASA	62.51	58.45	58.19	58.67	10.50	8.52
ESD	183.62	107.95	89.60	62.11	46.21	7.13
ESA	178.82	103.10	85.59	57.70	46.12	7.11
P	5.41	1.81	1.44	0.63	4.20	1.49

variations can be expected due to the differences on the antenna patterns. The reference RT CIR and the synthetic omni-directional PDP obtained from the emulation of the sounding process at different frequencies are displayed in Fig. 3.5a. On the other hand, the power bi-azimuth profile in the different bands is displayed in Fig. 3.5b.

These differences are not related to propagation characteristics, and only depend on the measurement equipment and set-up. The mismatch between the marginal power profiles produce also a divergence on the LSPs. The inter-band *difference error* between the LSPs calculated emulating the sounding process at 30 GHz and at 60 GHz are displayed in Fig. 3.4b. We can observe that in this reference scenario, the difference error in DS and ASD is less than 20 % in the 90 % of the measurements. In the case of the ASA, the difference error grows up to less than 25 % in the 90 % of the cases. On the other side, the ESs show a larger difference error of up 55 % in the 90 % of the cases. This is expected due to the difference on the ES shown in Fig. 3.3b. The mean and standard deviation of the relative and difference error in the LSPs are summarized in Table 3.1.

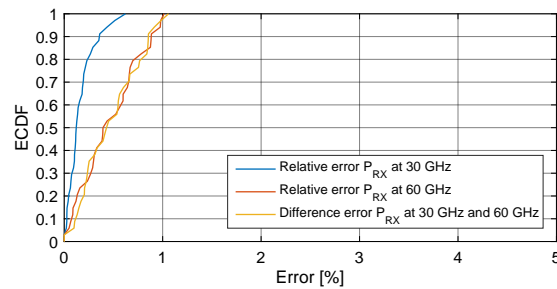


Figure 3.6: Empirical cumulative distribution of the relative error between the estimated total received power with the emulated sounding process and the reference RT, and difference error between the estimated total received power in the different bands.

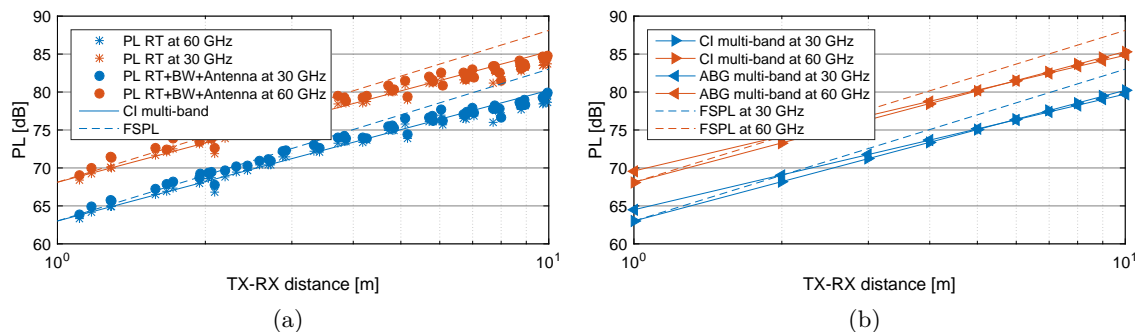


Figure 3.7: (a) Synthetic omni-directional multi-band PL using : RT and emulation of measurements. (b) Relative and difference error between RT and emulated measurements.

3.6 Characterization of the Errors in the Estimation of Total Received Power and Multi-band Path-loss

The relative and difference errors on the total received power calculated using the emulation of the sounding process in the different bands (after the compensation described in Section 3.7.1) are shown in Fig. 3.6. We can observe a larger relative error at 60 GHz due to the higher Ripple of the synthesis of omni-directional patterns from Section 3.7.1. On the other hand, the difference error is less than approx. 1 % in the 90 % of the measurements, which is within acceptable margins.

The estimated path-loss using the emulated channel sounding process and reference RT is shown in Fig. 3.7a. We can observe a higher path-loss estimated from the emulated measurements, which is mostly due to the lack of scans in the elevation domain.

3.7 Influence of the Scanning Step on the Estimation of Large Scale Parameters from Directive Scans

3.7.1 Synthesis of Antenna Patterns using Directive Measurements

In the set-up utilized along this thesis, the angular characteristic of the propagation channel is mostly derived by scanning the environment with high directive antennas pointing in the different directions. In Section 2.2.3, omni-directional patterns, and LSPs as DS has been synthesized by combining adjacent scans in the power domain [27, 46].

For sake of simplicity, let's neglect polarization in the following analysis. We define the ideal omni-directional (isotropic) PDP as

$$\begin{aligned}
 \text{PDP}_{\text{omni}}(\tau) &= \int_{\mathcal{S}^2} \int_{\mathcal{S}^2} |h(\tau, \boldsymbol{\Omega}_A, \boldsymbol{\Omega}_D)|^2 d\boldsymbol{\Omega}_A d\boldsymbol{\Omega}_D \\
 &= \int_{\mathcal{S}^2} \int_{\mathcal{S}^2} \sum_l |\gamma_l|^2 \delta(\tau - \tau_l) \delta(\boldsymbol{\Omega}_A - \boldsymbol{\Omega}_{A,l}) \delta(\boldsymbol{\Omega}_D - \boldsymbol{\Omega}_{D,l}) d\boldsymbol{\Omega}_A d\boldsymbol{\Omega}_D \\
 &= \sum_l |\gamma_l|^2 \delta(\tau - \tau_l) \int_{\mathcal{S}^2} \int_{\mathcal{S}^2} \delta(\boldsymbol{\Omega}_A - \boldsymbol{\Omega}_{A,l}) \delta(\boldsymbol{\Omega}_D - \boldsymbol{\Omega}_{D,l}) d\boldsymbol{\Omega}_A d\boldsymbol{\Omega}_D \\
 &= \sum_l |\gamma_l|^2 \delta(\tau - \tau_l). \tag{3.6}
 \end{aligned}$$

Let's now assume we have a PDP measured with a directional antenna in the TX and RX direction $j\Delta\boldsymbol{\Omega}_D$ and $i\Delta\boldsymbol{\Omega}_A$, respectively, with $\{i, j\} \in \mathbb{N}\{0, M-1\}$ and $\Delta\boldsymbol{\Omega}_{A/D} = \frac{2\pi}{M}$, from (2.10):

$$\begin{aligned}
 \text{PDP}_{\text{SO}}(\tau) &= \int_{\mathcal{S}^2} \int_{\mathcal{S}^2} \text{PDAP}(\tau, \boldsymbol{\Omega}_A, \boldsymbol{\Omega}_D) d\boldsymbol{\Omega}_A d\boldsymbol{\Omega}_D \\
 &= \sum_l |\gamma_l|^2 \sum_i \sum_j \underbrace{|g_R(\boldsymbol{\Omega}_{A,l} - i\Delta\boldsymbol{\Omega}_A) g_T(\boldsymbol{\Omega}_{D,l} - j\Delta\boldsymbol{\Omega}_D)|^2}_{\kappa(\boldsymbol{\Omega}_{A,l}, \boldsymbol{\Omega}_{D,l})} \delta(\tau - \tau_l) \\
 &= \sum_l |\gamma_l|^2 \kappa(\boldsymbol{\Omega}_{A,l}, \boldsymbol{\Omega}_{D,l}) \delta(\tau - \tau_l). \tag{3.7}
 \end{aligned}$$

From (3.7) we can see that the energy $|\gamma_l|^2$ of each MPC is scaled by the sum of the rotated antenna patterns at TX and RX $\kappa(\boldsymbol{\Omega}_{A,l}, \boldsymbol{\Omega}_{D,l})$. The difference (error) between the omni-directional and the measured synthetic omni-directional propagation channel can be calculated as

$$\begin{aligned}
 \epsilon(\tau) &= \text{PDP}_{\text{omni}}(\tau) - \text{PDP}_{\text{SO}}(\tau) \\
 &= \sum_l |\gamma_l|^2 \delta(\tau - \tau_l) \left(1 - \kappa(\boldsymbol{\Omega}_{A,l}, \boldsymbol{\Omega}_{D,l})\right) \tag{3.8}
 \end{aligned}$$

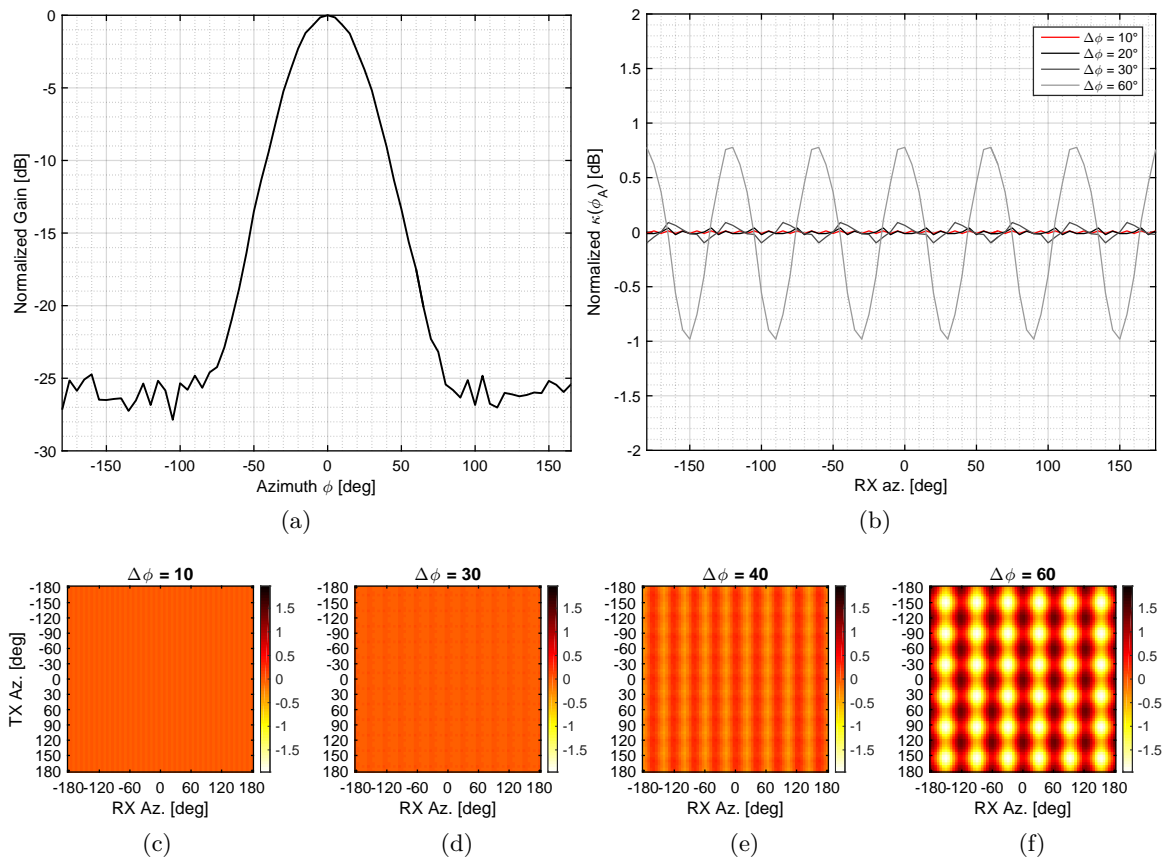


Figure 3.8: (a) Elevation cut of the measured horn antenna pattern (E-plane) with 30° HPBW at 33.75 GHz. (b) Normalized $\kappa(\phi_A)$ for different scan steps $\Delta\phi_A$ values. (c-f) $\kappa(\phi_A, \phi_D)$ in dB using a horn antenna with 30° HPBW at 30 GHz for different scanning steps $\Delta\phi_A = \Delta\phi_D$.

If the error is constant over the different angles, then $\kappa(\Omega_A, \Omega_D) = C, \forall\{\Omega_A, \Omega_D\}$. This results in a constant difference on power for each MPC within the PDP, and this difference on path gain can be easily compensated in a post-processing step by scaling the synthetic omni-directional PDP by $\frac{1}{C}$. On the other hand, if the error term varies over the angles of arrival and departure, each MPC in (3.7) is scaled with a different gain.

The term $\kappa(\Omega_A, \Omega_D)$ depends on the scanning step size as shown in Fig 3.8b. For example, a Ripple of ≈ 0.2 dB is observed with a scanning step chosen as the HPBW of the antenna, being this value negligible. The combination of the TX and RX synthesized patterns and their influence on the different angles can be seen in Fig 3.8c-3.8f. A large variation on the measurement gain between closely located paths in the angular domain can be observed with scanning steps larger than the HPBW of the antenna in Fig. 3.8f. The effect on the synthesised omni-directional PDP is further displayed in Fig. 3.2b.

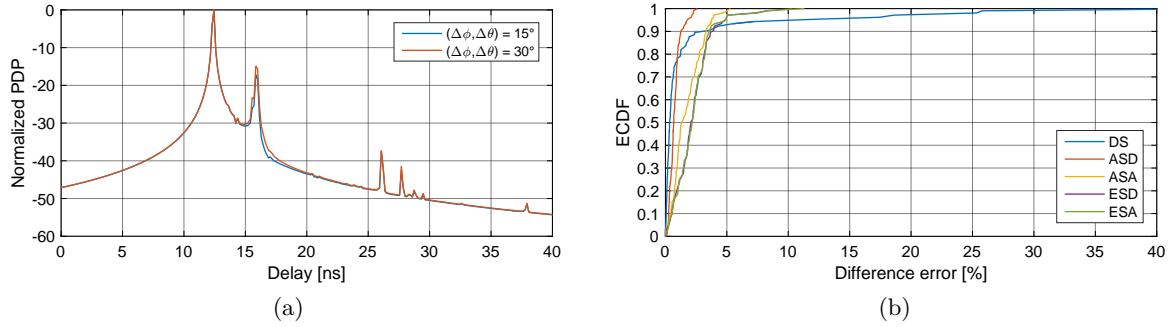


Figure 3.9: (a) Synthetic omnidirectional PDP using $\Delta\Omega = 15^\circ$ and $\Delta\Omega = 30^\circ$ scanning steps at 30 GHz with 30° HPBW antenna. (b) Difference error in the LSPs at 30 GHz using the different scanning steps in (a).

3.7.2 Influence on the Marginal Power Profiles and Large Scale Parameters

The synthetic omnidirectional PDP $|h_{\text{RT}+\text{BW}+\text{Ant}}(\tau)|^2$ using different scanning steps is displayed in Fig. 3.9a. As predicted beforehand, there is a small difference of power in the different delay samples.

The distribution of the relative errors of the different LSPs using different scanning steps can be seen in Fig. 3.9b. We can see that in the 90% of the cases, the relative error of all the LSPs is smaller than 4%. Therefore, considering the trade off between measurement time (larger angular scanning steps) and *the difference error*, utilizing steps equal to the HPBW results in an acceptable performance.

3.8 Conclusions

In this chapter we have characterized the errors on the calculation of the marginal power profiles and LSPs from directive measurements with limited resolution in the angular and time-delay domain. We have validated the utilization of HPBW as scanning steps since this is the most convenient value considering measurement time and accuracy. Then, we have shown that the LSPs calculated directly from the measurements with this set-up (RT+BW+Antennas) approximates the LSPs obtained from the reference RT simulations (infinite bandwidth and angular resolution).

Finally, the comparison between the different bands shows that while there is a clear influence of the measurements systems on the estimation of the LSPs, more precisely from the antennas, the mean percentage errors can be considered negligible in DS, ASs, and power, validating the inter-band comparisons carried out during this work.

4 Characterization of Propagation from Measurements and Simulations

“Everybody believes in measurements, but the one who made them. Nobody believes in simulations, but the one who made them.”

A Danish Professor.

Overview

This chapter contains the main empirical contribution of the present work. By exhaustive measurement campaigns in multiple scenarios, we have tried to characterize propagations at mm-wave, sub-THz, and in most of the cases, with a direct comparison to the sub-6 GHz band.

These chapter follows a progression on the complexity of the measurements and scenarios. In the first sections, we demonstrate the theoretical assumptions introduced in Chapter A regarding specular and diffuse scattering, and the influence on polarization with measurements in the anechoic chamber and isolated scatterers. Besides, we contrast the accuracy of different models of human shadowing with measurements. These results are used later to justify the need of mechanisms to counteract blockage loss in high frequency communication systems.

Later, we present multi-band measurements in a rich number of scenarios and a meticulous analysis of the results with the objective of characterizing propagation. Per-scenario, we first characterize the influence of the environment on the channel. Then, we investigate the statistics of the multi-band LSPs. Finally, we identify common fundamental modelling aspects for mm-wave, sub-THz, and correlated multi-band channel models, considering the key system requirements for high frequency communications. These aspects are contrasted with the current modelling approach introduced in Chapter C, and summarized with implementations receipts in Chapter 6.

The list of the antennas used during the different measurements can be found in Appendix D.8.

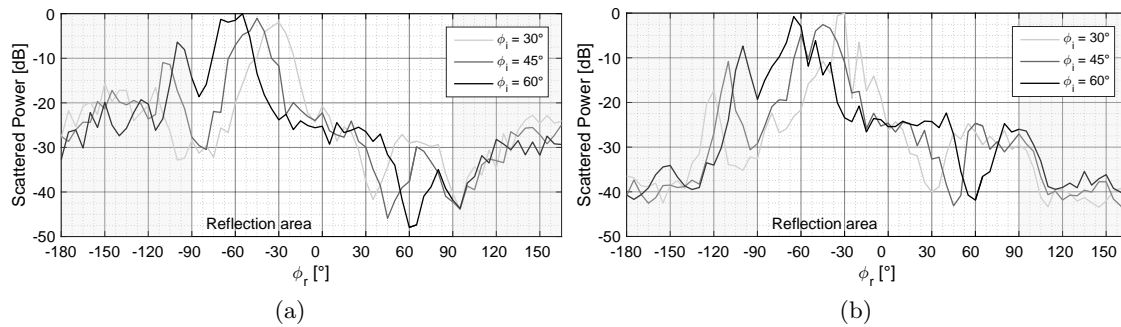


Figure 4.1: Normalized scattering pattern for different incident angles (a) brick wall, and (b) flat screen monitor.

4.1 Item Level Characterization at 70 GHz in Anechoic Chamber

4.1.1 Specular and Diffuse Scattering

The scattering properties of canonical objects that can easily be found in indoor environments have been measured at 70 GHz with the objective of characterizing the propagation mechanisms. The measurements were carried out in an anechoic chamber with 15° HPBW antennas to isolate the scattering process of the objects under test.

These results have been used to parametrize deterministic tools as RT in [47], and also to collect a series of scattering footprints of different objects to be used as cluster models in hybrid deterministic-stochastic models, in which the location of the clusters is deterministic, but their properties are drawn from stochastic processes obtained from measurements.

Two different scattering patterns can be observed: specular and diffuse. In the first case, the specular component is dominant (strongest scattering angle ϕ_r is equal to the incident angle ϕ_i) and there is a continuous smooth decay on the scattered power for $\phi_r \neq \phi_i$. In the second case, the specular component doesn't necessarily need to be the strongest, but the major difference is the non-continuous decay, showing strong components also in different directions. Example of a specular pattern is the reflection in a brick wall, displayed in Fig. 4.1a. Also, as determined by the Fresnel's law, the reflection is stronger with increasing incident angle. On the other hand, as shown in Fig. 4.1b, the flat screen monitor has a more diffuse and irregular scattering pattern, which is also different for each incident angle. Most probably, the reason is the presence of multiple conductive and metallic components inside.

4.1.2 Polarimetric Analysis of the Scattering Process

The polarimetric decomposition of the scattering pattern of the brick wall sample and the flat screen monitor can be observed in Fig. 4.2. As predicted by Fresnel's law, the VV component (TE component, perpendicular to the plane containing the rays) is reflected stronger than the HH (TM component), being the difference larger for increasing incident angles. The

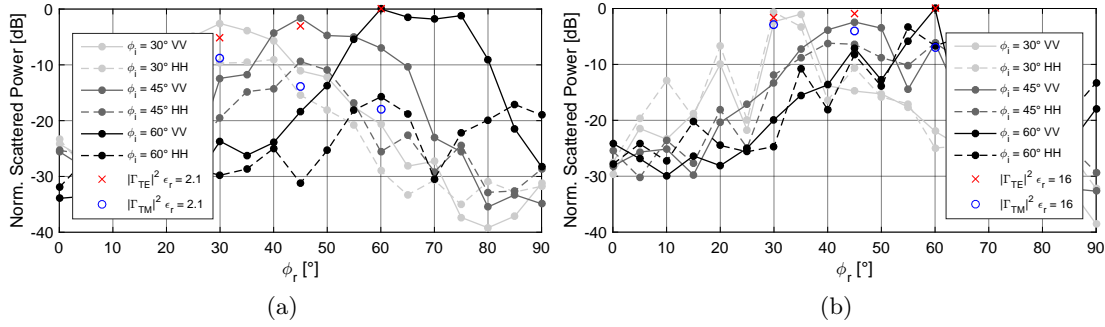


Figure 4.2: Polarimetric decomposition of the scattering pattern for (a) reflection in a wall, and (b) in the flat screen monitor.

theoretical reflection coefficients of the materials (represented by their relative permittivity ϵ_r) is plotted for the specular angles in crosses.

These results show the polarimetric selectivity of the reflections. If we consider indoor scenarios, in which the strongest MPC are specular components from reflections in perpendicular structures as walls, the influence of the polarimetric filtering phenomena of scattering becomes more relevant, since depending on the incident angle, we can have a large power unbalance between the co-polarized channels. Further measurements in more complex scenarios as entrance hall can be found in Section 4.3.4, and conference room in Section 4.3.5. On the other hand, due to the change on the reference plane, the opposite happens with ground reflections, as shown in Section 6.3.1.

Modelling aspects in SCMs considering this selectivity effect on polarization after reflection are addressed in Chapter 7.

4.1.3 Obstruction Loss

The obstruction loss of the different items has been already presented in [17] and is summarized in Table 4.1. The measured large obstruction loss of the brick wall (25.3 dB) limits the propagation through walls, restricting this range of mm-wave communications mostly to intra-room applications in indoor scenarios, and limiting the interference from outdoor to indoor deployments. Outdoor to indoor measurements at mm-wave showing penetration through windows are presented in [18].

Moreover, a single object as a monitor can generate deep obstruction fading, with up to 34 dB at 70 GHz. This makes necessary the utilization of MPC to reach those spots. Especially, considering that one of the target applications in this range of mm-wave is wireless office. Moreover, since the other furniture also exhibit a large loss, we can expect regions with large shadowing losses in indoor environments.

Table 4.1: Scattering parameters and obstruction loss of different tested objects at 70 GHz.

Object	W × H × D [cm]	Obstruction loss [dB]	Azimuth Spread ^a [deg]
Brick wall	50 × 50 × 9	25.3	28.10
Flat screen monitor	45 × 36.8 × 5.8	34.0	19.86
Bookshelf	43.5 × 32 × 30	30.0	72.40
Speaker	24 × 42 × 21.5	18.2	61.28
Plant pot	27.3 Ø × 26	16.0	52.95
Wooden panel	56.5 × 30 × 1.3	2.7	-
Wooden cabinet	56.5 × 30 × 38.1	35.3	-

^aCalculated from the scattering pattern.

4.2 Human Shadowing Loss

Losses by human shadowing can be modelled using either a stochastic or a deterministic approach. The former is based on the statistics of measured signal level attenuation, and the latter on the diffraction of plane waves around different geometric objects emulating human figures.

Following the stochastic approach, several measurements at mm-wave in dynamic scenarios have been introduced in [7], [48], and [49], between others. The time variant human shadowing statistics at 60 GHz inside an Airbus 340 have been studied using different antenna types in [7]. [48] presents short-range measurements also at 60 GHz, showing that the signal level attenuation follows a Gaussian distribution. In [49], 73.5 GHz measurements in pedestrian crowd scenarios have been used to derive a model based on Markov's chain, which is also considered under the stochastic modelling approach in the 3GPP TR 38.901 [4].

On the other hand, deterministic models based on the knife-edge diffraction principle can be separated into two subcategories, depending on the geometric figure used to emulate the human being: cylindrical and absorbing screen models. A good introduction to the mathematics behind these models can be found in [50]. The double knife-edge diffraction (DKED) model predicts the obstruction loss based on the Huygens' principle: the diffracted front waves interfere constructively and destructively behind the blocker. The blocker is considered as a vertically infinite screen with an infinitesimal depth, as shown in Fig.4.3. The input parameters are the size of the blocker, its distance to the transceivers, and the carrier frequency. DKED can be extended to the quadruple knife-edge diffraction (QKED) by considering a finite height of the screen. This modelling approach is adopted in the Mobile and wireless communications Enablers for the Twenty-twenty Information Society (METIS) project, and an extension in the Millimetre-Wave Based Mobile Radio Access Network for Fifth Generation Integrated Communications (mmMAGIC) project [51].

The losses using the DKED and QKED models (as it is considered within the METIS project) are calculated as

$$L_{\text{dB}}^{\text{DKED}} = -20 \log_{10} (1 - (1 - F_{w_1} - F_{w_2})), \quad (4.1)$$

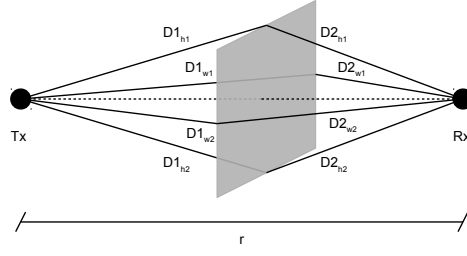


Figure 4.3: DKED and QKED model using an absorbing screen.

and

$$L_{\text{dB}}^{\text{QKED}} = -20 \log_{10} (1 - (1 - F_{h_1} - F_{h_2})(1 - F_{w_1} - F_{w_2})), \quad (4.2)$$

respectively, where

$$F_{w_1/w_2/h_1/h_2} = \frac{1}{2} - \frac{\tan^{-1} \left(\pm \frac{\pi}{2} \sqrt{\frac{\pi}{\lambda} (D2_{w_1/w_2/h_1/h_2} + D1_{w_1/w_2/h_1/h_2} - r)} \right)}{\pi}, \quad (4.3)$$

being $D1$ and $D2$ the length of the rays from the TX to the blocker and from the blocker to the RX, respectively, and r the radial distance between TX and RX, as shown in Fig. 4.3.

However, the previous equations consider isotropic radiators, e.g., the direct and diffracted rays have the same strength. In more realistic scenarios, considering application systems with beam-forming or directive antennas, the directivity of the pattern plays a major role, since the direct component is stronger than the diffracted. In this case, the diffracted field is weighted by the antenna gain $G(\boldsymbol{\Omega}_{w_1/w_2/h_1/h_2})$ in the direction of the diffracted components, and then used in (4.1) and (4.2):

$$\hat{F}_{w_1/w_2/h_1/h_2} = \sqrt{G_T(\boldsymbol{\Omega}_{w_1/w_2/h_1/h_2})} \sqrt{G_R(\boldsymbol{\Omega}_{w_1/w_2/h_1/h_2})} F_{w_1/w_2/h_1/h_2}. \quad (4.4)$$

We have measured human shadowing at 70 GHz in a controlled environment (large hall) to characterize the obstruction loss suffered when a person crosses the link and to validate the DKED and QKED models. The results displayed in Fig. 4.4 show a good match of the measurements with the DKED model when the blocker is closer to the transceivers, but an overestimation of the losses at larger distances. On the other hand, the QKED compensates the losses by the extra field from the top and bottom of the screen, matching better to the measurements when the obstructor is further from the transceivers. However, for shorter distances, the shadowing loss has been underestimated by the model. The reason is that the model considers isotropic characteristics on the transceiver antennas, but the measurements were performed using directive antennas. The main beam is completely covered when the person is close to the transceivers, making not possible any diffraction. The extensions considering the directivity of the antennas have shown a better match in both cases in which the blocker is close and far from the transceivers. Similar measurements at 73.5 GHz in a laboratory and the effects of considering or neglecting directivity can also be found in [52]. A complete comparison between measurements and different models at several frequencies, covering also the mm-wave bands, can be found as well in [53] and [54].

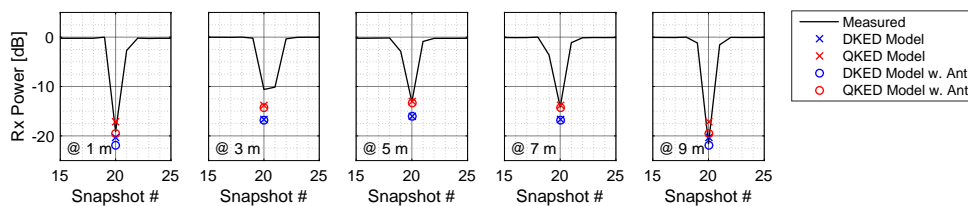


Figure 4.4: Measured and modelled human blockage at 70 GHz for a person crossing the link at different distances from the TX to the RX.

4.3 Indoor Propagation Analysis and Characterization

4.3.1 Introduction

Propagation in indoor scenarios is usually dominated by the presence of a large set of MPCs product, between others, of scattering from walls, ground, and ceiling in a simplified description of the environment, and of furniture, if more complex details are considered. The distance of the communication units to these scatterers is frequently reduced compared to outdoor scenarios, depending mostly on the size of the room. Clusters tend to be compacted in space (angle and delay), making that low resolution communication systems suffer of severe fading. The impossibility of resolving scatterers in space and time also motivates a random description of the channel based on the superimposition of a rich number of unresolvable MPCs.

In contrast to what was expected at the beginning, multiple measurements have shown a rich multipath channel at mm-waves in indoor scenarios [55, 56]. Path-loss results and time dispersion characteristics at 28 GHz and 73 GHz are presented in [57], showing a larger PLE at 73 GHz than at 28 GHz and shorter DSs when using directive antennas. Measurements at 60 GHz and 70 GHz in [58] show similarities between these bands. In addition, measurements and clustering of MPCs at 60 GHz are reported in [59]. Penetration losses of different materials in indoor back-haul scenarios at 72 GHz are presented in [60], showing a range of losses between 5.3 dB (for cubicle wall) and 36.8 dB (concrete wall and multiple partitions), similar to our findings in Section 4.1.3.

Moreover, measurements at sub-THz in the range from 126 GHz to 150 GHz in three different indoor scenarios have been introduced in [61]. The reported results show that the DS increases with TX-RX distance and a linear model is proposed. However, as it is shown in this section, multiple measurements at different frequencies in indoor and outdoor scenarios contradict this model, since with increasing TX-RX distance, the DS increases up to a maximum, and then it decreases due to the relative power and propagation distance of the LOS component to back reflections, [62] and [63]. In addition, these measurements report that the LOS component is carrying most of the energy, minimizing the contribution of scattered components. On the other hand, indoor measurements at 300 GHz in [64] have shown the presence of multiple specular reflections.

Related to multi-band measurements, several works can be found in the literature comparing

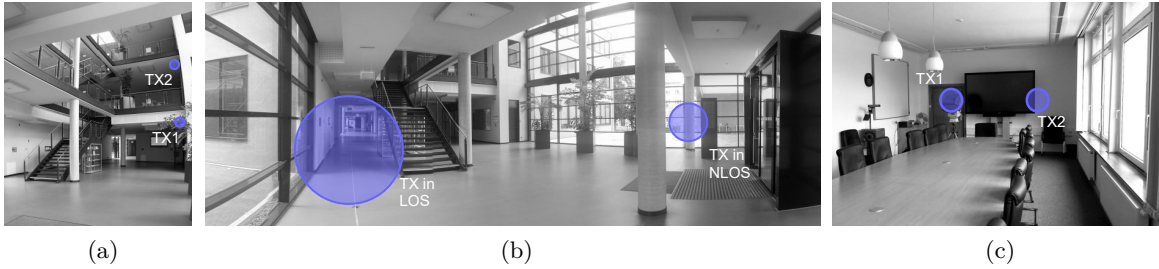


Figure 4.5: Location of the TX in indoor scenarios: (a) multi-store entrance hall, (b) large corridor, and (c) conference room.

LSPs at different bands. Path-loss, DS, and ASA at 28 GHz and 140 GHz are compared in a shopping mall scenario in [65]. Within the results reported in mmMAGIC project, no clear dependency of DS was found in [66]. In [67], power angular profiles and spreads from sub-6 GHz to 60 GHz are compared showing similarities. Valuable multi-band measurement at 10 GHz, 60 GHz, and 300 GHz in a small office are introduced in [68], in which a large number of common scatterers with similar power are identified.

Therefore, in this section we study different aspects of propagation in indoor scenarios and their dependency on the carrier frequency by intensive measurement campaigns covering the spectrum from sub-6 GHz to 190 GHz. In addition, RT simulations with accurate 3D models from laser scans of the measured environments have been conducted to support the interpretation of results and to generate a rich data-set for meaningful statistics. Considering the main characteristics of communication systems at mm-wave and terahertz, high resolution in the angular and time domain (given by high directivity and large bandwidth), we focus the analysis on key aspects for channel modelling as spatial consistency and the need of including deterministic components in stochastic models for beam-tracking and beam-forming analysis. In addition, we show that since few number of MPCs are isolated with high resolution systems, polarization becomes more relevant and deterministic as its behaviour can be predicted depending on the geometry of the scatterer. Finally, we analyse the inter-band dependency of LSPs and derive statistics for stochastic models parametrization.

4.3.2 Scenarios and Set-up

We have conducted multiple measurements campaigns in different indoor environments with different sizes and targeting several applications, all summarized in Fig. 4.5 and Table 4.2.

The first one, I1, is a multi-band multi-store entrance hall access point (AP) to user equipment (UE) application scenario at 30 GHz and 60 GHz, in which there were two APs (TX), one located in the same floor (ground floor) as the UEs (RX) and another one in the floor above (first floor). The second scenario I2, is a large corridor in the same building as I1, but in this case, the measurements were simultaneously at 6.75 GHz, 30 GHz, and 60 GHz, with the TX and RX at the same height. Finally, the third scenario is a small conference room with multiple TX and RX positions at the same height. The measurements were performed with a higher resolution in the angular domain and at 190 GHz. Details on the channel

Table 4.2: Indoor measurement campaigns.

Campaign	Scenario	Frequency	Application	Visibility	Description
I1	Multi-store entrance hall	30 GHz and 60 GHz	base station (BS) to UE	LOS, obstructed-line of sight (OLOS), and NLOS	TX in multiple floors, RX in ground floor
I2	Large corridor	6.75 GHz, 30 GHz, and 60 GHz	TX and RX at the same height	LOS, OLOS, and NLOS	RX in multiple positions along the corridor
I3	Conference room	190 GHz	TX and RX at the same height	LOS	Multiple TX and RX positions in the room

Table 4.3: Measurement set-up.

Campaign	Band	BW	TX Azimuth	TX Elevation	RX Azimuth	RX Elevation
I1	30 GHz 60 GHz	2.16 GHz	$-90^\circ:30^\circ:90^\circ$	$-30^\circ:30^\circ:30^\circ$	$-150^\circ:30^\circ:180^\circ$	$-30^\circ:30^\circ:30^\circ$
I2	6.75 GHz 30 GHz 60 GHz	6.75 GHz	0°	0°	$-150^\circ:30^\circ:180^\circ$	$-30^\circ:30^\circ:30^\circ$
I3	190 GHz	7.5 GHz	$-165^\circ:15^\circ:180^\circ$	$-45^\circ:15^\circ:45^\circ$	$-165^\circ:15^\circ:180^\circ$	$-45^\circ:15^\circ:45^\circ$

sounder (CS) configuration and set-ups are summarized in Table 4.3.

4.3.3 Multi-Store Entrance Hall Scenario at 30 GHz and 60 GHz

The measurements were conducted in the entrance hall of the Zusebau at the TU Ilmenau. The RX was located at 1.4 m height in the ground floor in 9 different positions along a line, as shown in Fig. 4.6. On the other hand, the TX was located in the ground floor (TX1) and in the first floor (TX2), in both cases, as an AP at 2.8 m height from the ground. In total, $2 \cdot 9 = 18$ links were measured, but due to different artefacts only 14 links are available for analysis. Depending on the position, the RX was set in different visibility conditions: LOS, OLOS (obstructed by the stairs), and NLOS.

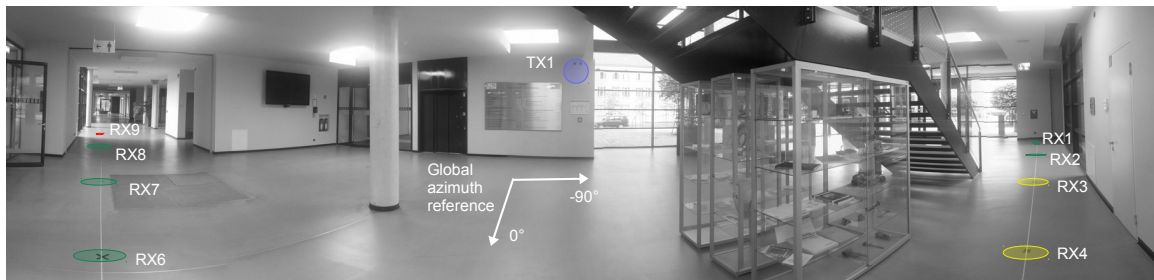


Figure 4.6: View from RX5 towards TX1 (AP in ground floor) in entrance hall scenario.

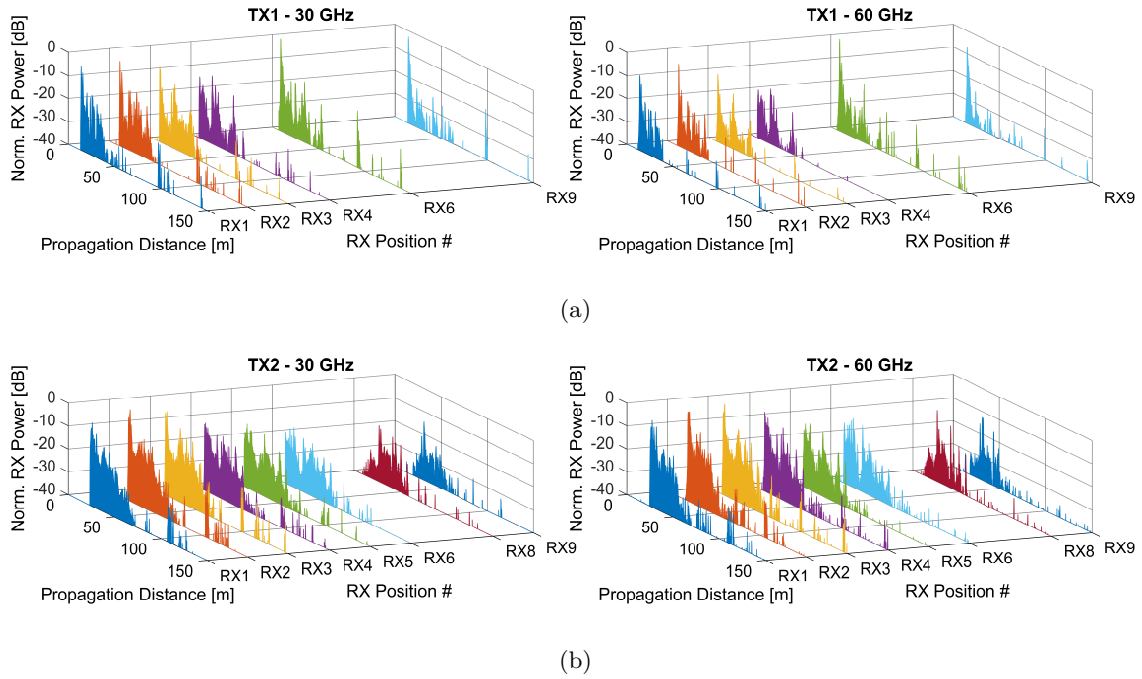


Figure 4.7: Per-position synthetic omni-directional PDP at 30 GHz and 60 GHz with (a) TX1 and (b) TX2.

Environment and Propagation Characterization

The synthetic omni-directional PDP in the different RX positions is displayed in Fig. 4.7 and shows the dynamic of the channel in which the UE goes from LOS, to OLOS (by the stairs), to LOS again, and finally to NLOS with the TX1, and from OLOS to NLOS with the TX2. A comparison of the different bands shows similarities on the shape of the PDP, and therefore, a similar number and influence of scatterers.

Analysis of Large Scale Parameters

The per-link LSPs in the different bands are displayed in Fig. 4.8. The per-position RX power analysis provides insights on the dynamic of the isotropic channel during the displacement of the UE. The per-band normalized synthetic omni-directional RX power shows a difference of approx. 20 dB between the best and worst TX-RX link, TX1-RX6 and TX2-RX9, respectively. Since the difference of power between TX1 and TX2 from RX1 to RX4 is small, TX diversity could be beneficial for stream diversity, to increase RX power, or avoid human shadowing.

The per-position DS shows a high correlation between the different bands. As expected, due to the visibility conditions, the DS is larger in the TX2 links (with OLOS and NLOS) than in TX1. In addition, DS is slightly smaller at 60 GHz than at 30 GHz. ASs show also a high correlation between bands and shorter values in most of the cases at 60 GHz.

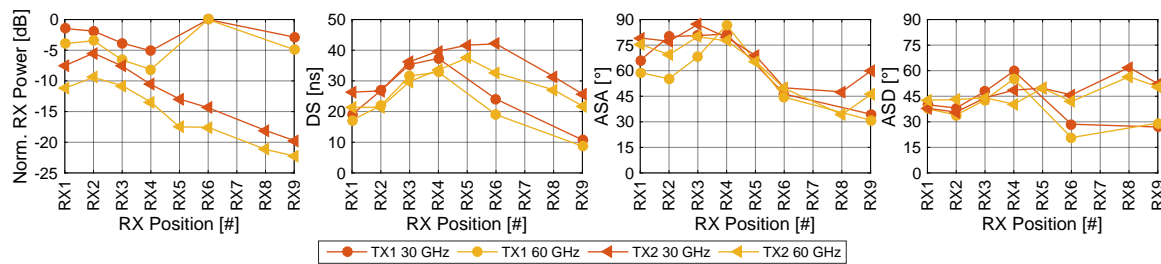


Figure 4.8: LSPs at 30 GHz and 60 GHz with TX1 and TX2.

Table 4.4: Multi-band large scale parameters from measurements in entrance hall scenario^a.

Visibility	Band	DS		ASA		ASD		ESA		ESD	
		Mean	Std.	Mean	Std.	Mean	Std.	Mean	Std.	Mean	Std.
LOS	30 GHz	20.18	7.06	56.74	20.29	33.42	6.59	20.28	0.84	19.41	0.81
	60 GHz	16.71	5.68	47.38	12.54	30.39	7.32	15.44	1.15	15.64	2.73
OLOS	30 GHz	32.40	5.40	81.14	3.72	45.06	9.55	22.47	0.83	20.14	0.82
	60 GHz	27.40	5.60	75.97	7.68	45.57	5.40	21.87	2.65	19.75	2.83
NLOS	30 GHz	36.12	7.23	61.16	13.32	51.68	6.19	21.26	0.50	20.82	1.03
	60 GHz	30.51	6.12	54.57	17.02	47.81	6.64	19.08	0.81	19.72	1.01

^aFrom measurements with 30° HPBW scans at TX and RX and 2.16 GHz bandwidth.

The mean and standard deviation of the LSPs are summarized in Table 4.4.

4.3.4 Large Corridor Scenario at 6.75 GHz, 30 GHz, and 60 GHz

In this scenario, the dominant materials in the environment are glass (large windows covering walls and doors), concrete (walls and columns), and metal frames in windows and stairs. The different TX and RX positions are shown in Fig. 4.9. The TX was located at 1.5 m height in two different positions: the first one for the LOS and OLOS measurements shown in Fig. 4.9a, and a second one for the NLOS shown in Fig. 4.9b. The RX was also at 1.5 m height following the same path in the two sets of measurements, with 2 m steps between positions in the LOS case, and 1 m in the NLOS. There is a transition from LOS to OLOS when the RX is located behind the stairs shown in Fig. 4.9d (marked as Scatterer C).

Environment and Propagation Characterization

The per-position normalized synthetic omni-directional PDP in the different RX positions in the campaign are shown in Fig. 4.10. Multiple dominant common scatterers have been identified in the measurements in the different bands and visibility conditions. They were identified using the propagation distance and the pointing direction of the angular scans and contrasted with RT simulations with a model of the building: scatterer B was identified as the reflection from the back side (metal frames, wall and door made out of glass visible in

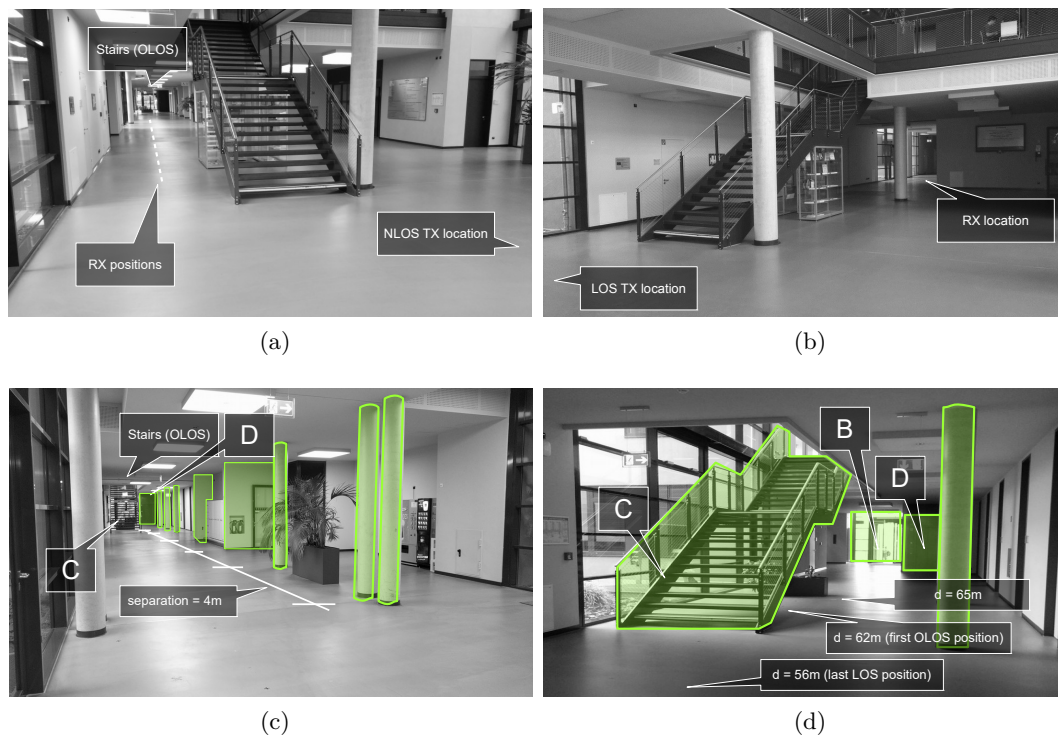


Figure 4.9: View from the TX in the corridor scenario in (a) LOS, and (b) NLOS. (c) Columns and regular structures and (b) stairs at the end of the corridor.

Fig. 4.9). This component becomes stronger when the RX is approaching to the end of the building. The scatterer C are the MPCs from the stairs that later obstruct the LOS. The metal door from an elevator located behind the stairs was identified as scatterer D. The regularly spaced scatterers arriving from the opposite direction of the LOS component are a set of columns and walls set 4 m apart from each other, shown in detail in Fig. 4.9c. Finally, scatterer E is a double reflection from the back and front. Similar results can be observed in the NLOS case, in which the channel consists of a strong diffracted component and multiple reflections. The scatterers parallel to the main component are reflections from the side walls.

From a visual inspection, we can see that there is less DMC power with increasing frequency: while the main scatterers are present in all the measured bands, the amount of MPCs within the time-delay clusters and their relative power changes depending on the band (region A in Fig. 4.10).

The most relevant scatterers can be tracked during the displacement of the RX, showing the influence of the environment geometry on the channel during the displacement of the RX. Therefore, spatial consistency in channel models becomes relevant to test beam-tracking and beam-forming applications.

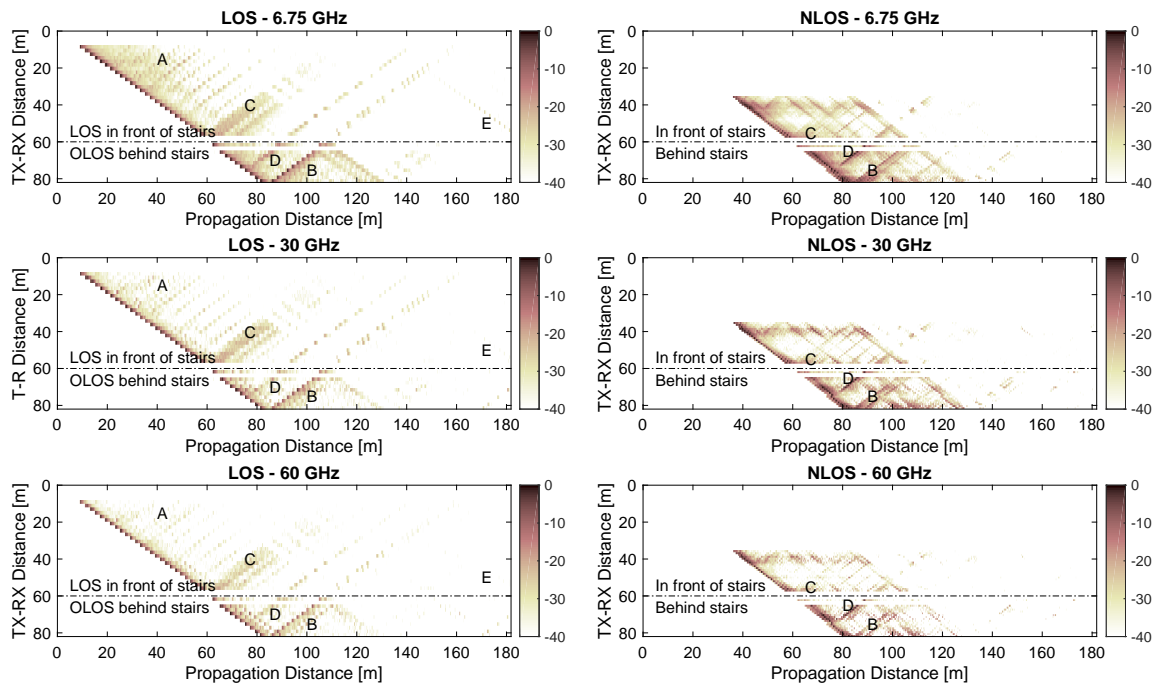


Figure 4.10: Per-position multi-band synthetic omni-directional PDP in corridor scenario at 6.75 GHz, 30 GHz, and 60 GHz in LOS and NLOS.

Analysis of Large Scale Parameters

The measured DSs in the different bands are shown in Fig. 4.11a for LOS and OLOS, and in Fig. 4.11b for NLOS. The geometry of the scenario introduces a clear influence on the DS values.

In LOS, the DS increases with TX-RX distance due to the back reflections: the relative difference of power between the LOS component and the back reflection decreases and the DS increases. After a certain distance, the DS is more influenced by the relative distance between the LOS component and the back reflection than by their relative power. Therefore, the DS decreases with increasing TX-RX distance. In OLOS, the LOS component is attenuated and the back reflections from the scatterer B and D from Fig. 4.10 dominate the spread. Hence, the DS decreases with the RX approaching to the end of the building. Differently, in NLOS, the DS varies considerably depending on the location of the RX. From the Fig. 4.10, it can be observed that there are regions with multiple reflections from the side walls (reflections parallel to the diffracted component) increasing the DS (and as shown later, ASAs) and regions with no other components than the defracted ones, with shorter DSs and ASA. While there is no clear relation between the DS value and the carrier frequency under the different visibilities, a correlation between the different bands can be observed in Fig. 4.11a and Fig. 4.11b.

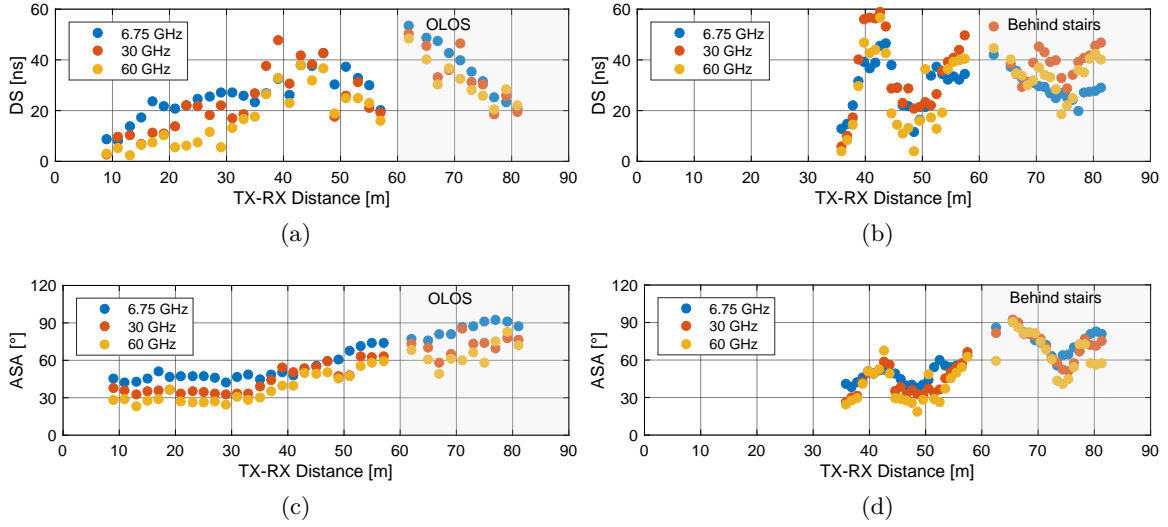


Figure 4.11: Multi-band LSPs from measurements in large corridor scenario: DS in (a) LOS and (b) NLOS, and ASA in (c) LOS and (d) NLOS.

Table 4.5: Multi-band large scale parameters from measurements in corridor scenario.

		LOS						NLOS					
		DS		ASA		ESA		DS		ASA		ESA	
	Band	Mean	Std.	Mean	Std.	Mean	Std.	Mean	Std.	Mean	Std.	Mean	Std.
Measured ^a	6.75 GHz	33.03	10.67	63.07	16.72	19.63	1.22	32.15	8.76	61.39	15.13	18.74	0.98
	30 GHz	53.61	6.43	53.57	15.66	18.46	1.40	53.26	5.45	57.04	18.09	18.16	1.27
	60 GHz	56.10	6.32	46.59	15.99	15.31	1.58	49.40	7.67	52.39	19.13	12.93	1.84
RT ^b	6.75 GHz	42.31	22.02	53.19	22.53	5.17	3.39	10.82	7.77	27.85	15.72	3.75	2.82
	30 GHz	45.90	23.11	52.54	21.38	5.24	3.50	9.89	8.71	24.35	16.88	3.68	2.89
	60 GHz	46.56	22.80	51.68	20.99	5.28	3.54	9.64	9.13	23.09	17.12	3.62	2.91

^aWith single 30° HPBW sector at TX and synthetic omni-directional from 30° HPBW scans at RX, and 6.75 GHz bandwidth.

^bFrom path-level parameters.

The influence of the reflections from the back on the ASAs in LOS can be observed in Fig. 4.11c: the ASA increases with TX-RX distance since the back reflection arriving 180° from the LOS component becomes stronger while the LOS component decreases. On the other hand, the flashing scatterers visible in NLOS in Fig. 4.10 increase the DSs and ASAs when they are present. Therefore, DS and ASA exhibit a correlated oscillating shape in Fig. 4.11b and Fig. 4.11d.

The statistics of the LSPs are summarized in Table 4.5, in which the LOS and OLOS records were combined.

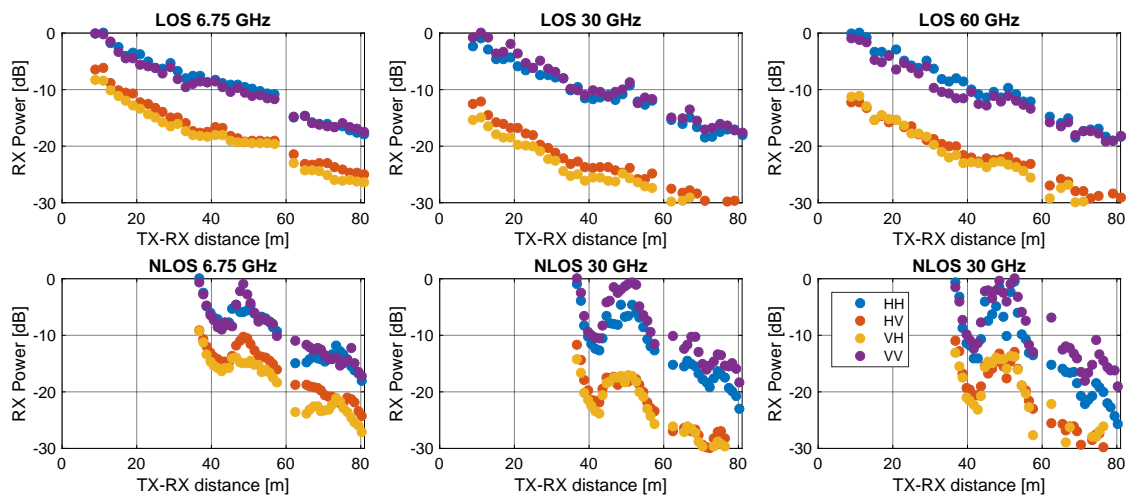


Figure 4.12: Multi-band per-position polarimetric synthetic omni-directional RX power in LOS (combined with OLOS records) and NLOS in large corridor scenario.

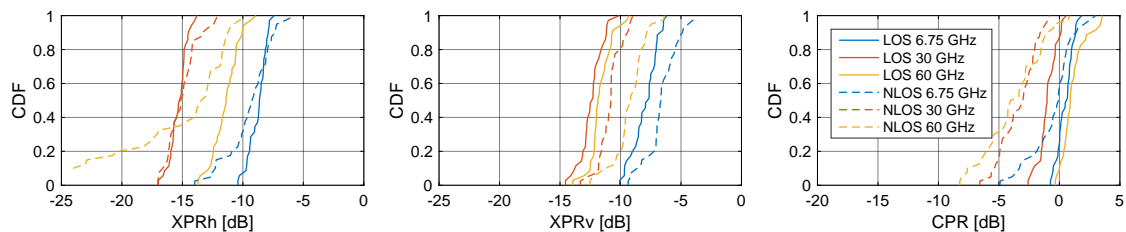


Figure 4.13: CDF of the per-position isotropic polarimetric power ratios (PPRs) in LOS (combined with OLOS records) and NLOS in large corridor scenario.

Polarimetric Power Ratios

The per-position synthetic omni-directional RX power decomposed on its polarimetric components is displayed in Fig. 4.12. It can be observed that in LOS and OLOS, the isotropic channel is dominated by the LOS component, and therefore the TX φ - RX ϕ and TX ϑ - RX θ channels carry similar power levels. However, since the ground and ceiling reflections are stronger in the TX φ - RX ϕ combination than in the TX ϑ - RX θ , this channel carries more power in the TX and RX horizontal polarization. Therefore, the mean co-polarization ratio (CPR) is larger than 0 dB, as shown in the cumulative distribution function (CDF) in Fig. 4.13.

On the other hand, in NLOS, the signal reaches the RX mostly by reflections from walls, columns, and window frames. All these structures are vertical planes producing stronger reflections in the vertical polarimetric channel TX ϑ - RX θ than in the horizontal TX φ - RX ϕ . In addition, single bounce ground and ceiling reflections are not present any more. As a consequence, the mean CPR is noticeably reduced. There is a clear dependency of CPR on frequency: as the channel becomes more specular with increasing frequency, the polarization becomes also more deterministic since there are less DMC product of diffuse scattering. Therefore, the synthetic omni-directional (isotropic) CPR is smaller at mm-waves.

Table 4.6: Multi-band PPRs from measurements in large corridor scenario^a.

Band	LOS						NLOS					
	XPRh		XPRv		CPR		XPRh		XPRv		CPR	
	Mean	Std.	Mean	Std.	Mean	Std.	Mean	Std.	Mean	Std.	Mean	Std.
6.75 GHz	-8.75	0.73	-7.94	1.04	0.48	0.65	-9.40	1.81	-6.55	1.31	-0.49	1.72
30 GHz	-15.31	0.72	-12.41	0.95	-0.93	0.75	-15.05	1.24	-10.89	0.95	-3.32	1.45
60 GHz	-11.46	1.10	-11.64	0.93	1.23	1.00	-14.54	3.73	-9.24	1.34	-3.70	2.37

^aCalculated from synthetic omni-directional patterns.

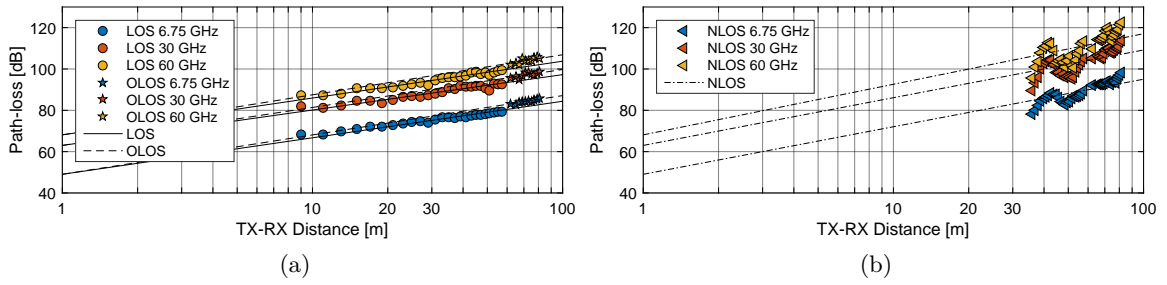


Figure 4.14: Multi-band path-loss from measurements in corridor scenario in (a) LOS and OLOS, and (b) NLOS.

The statistics of the measured and simulated PPRs are summarized in Table 4.6.

Empirical Multi-band Path-loss

The measured PL and the fit to the empirical CI PL model is shown in Fig. 4.14a for LOS and OLOS and in Fig. 4.14b for NLOS. The model parameters are summarized in Table 4.7. The results show a small PLE for LOS, close to 1.7 for the different bands. This value is similar to other indoor results presented in [69]. On the other hand, in the NLOS, the PLE scales up to 2.31 at 6.75 GHz and 2.44 at 60 GHz. These values are also similar to the ones presented in [69]. Furthermore, there is a relation of increasing shadowing σ_X with frequency.

Ray-Tracing Comparison

The measured and RT simulated¹ per-position normalized PDPs at 60 GHz in LOS and NLOS are displayed in Fig. 4.15. The main scatterers identified in the measurements can be observed also in the simulations. Between the major differences, we can mention scatterer C and E, which are highly attenuated in the measurements. This is because these scatterers are located in the region shadowed by the CS. Therefore, figures as DSs and ASAs, shown in Fig. 4.16, are shorter in LOS in the measurements than in the simulations, since the late

¹The parameters of the simulations can be found in Appendix D.5.

Table 4.7: Multi-band path-loss parameters from measurements in large corridor scenario^a.

Band	LOS		OLOS		NLOS	
	n	σ_X	n	σ_X	n	σ_X
6.75 GHz	1.77	3.40	1.90	0.95	2.30	4.89
30 GHz	1.72	3.70	1.84	1.21	2.31	5.94
60 GHz	1.78	3.87	1.93	1.31	2.44	6.72
Multi-band	1.76	3.64	1.89	1.37	2.35	5.96

^aWith a single sector of 30° HPBW at TX and synthetic omni-directional characteristics from 30° HPBW scans at RX.

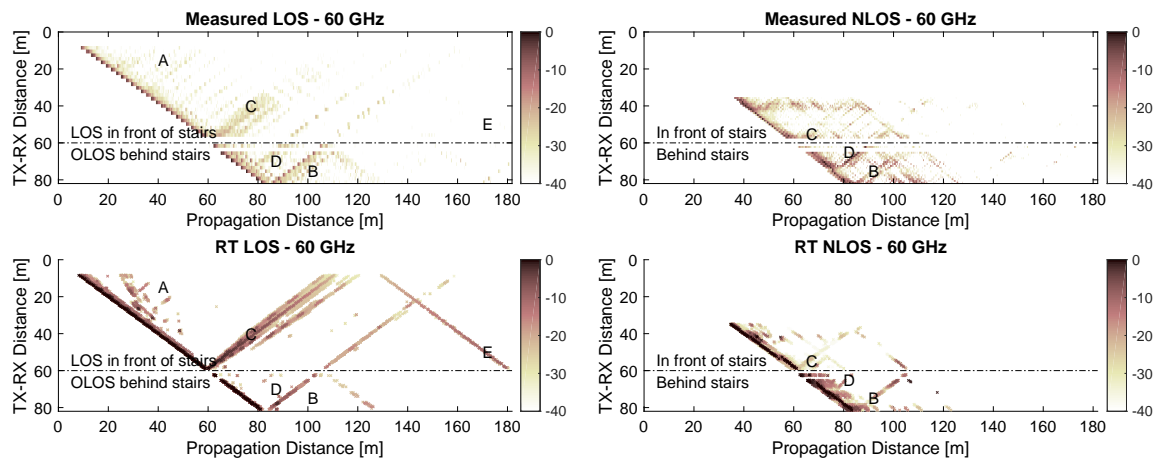


Figure 4.15: Per-position normalized measured and simulated PDP at 60 GHz in LOS and NLOS in the large corridor scenario.

(originating an increase on DS) reflections from the back (originating an increase on the ASA) are shadowed. The influence of the CS shadowing multiple clusters is also frequency dependent. Similar results can be observed in the conference room scenario in Section 4.3.5. Further studies on its subject and how to infer the effects and compensate its lost have to be conducted.

On the other hand, in NLOS, the main scatterers also coincide with the simulations. However, since only 100 paths and up to fifth order reflections were simulated in the RT, several paths that were present in the measurements are not visible in the simulations. Therefore, figures as DS and ASA are larger in the measurements than in the simulations.

The estimated LSPs from measurements and RT simulations show differences on the absolute values due to the limited bandwidth and angular resolution in the measurements, as discussed in Section 3.1, and because of the shadowing effects of the CS. However, similar trends can be observed between the measurements and simulations. This is because the location of the main scatterers coincide with the simulations, and those scatterers are the ones that dominate the LSPs.

The statistics of the LSPs from the RT simulations are summarized in Table 4.5.

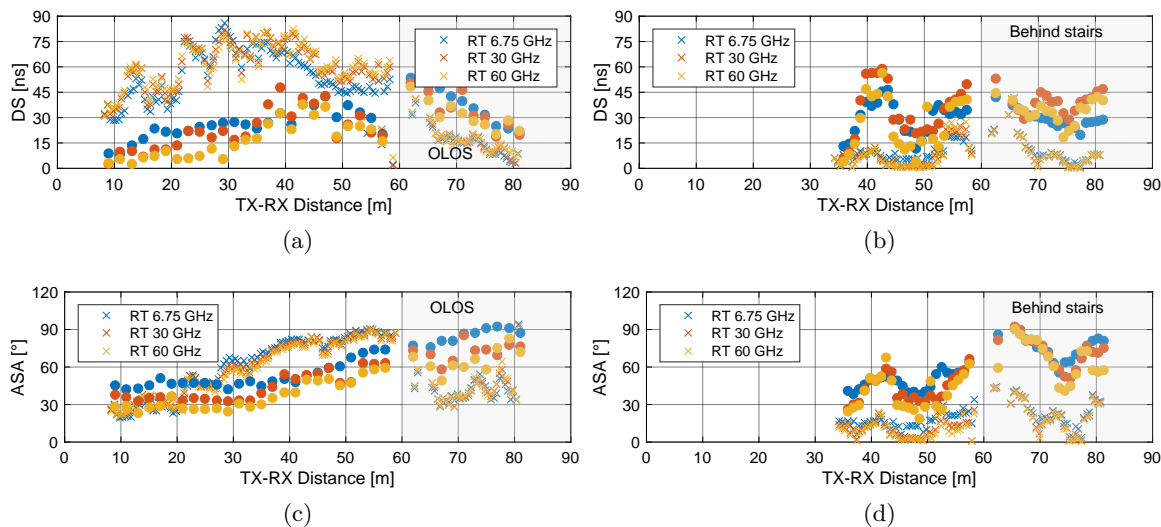


Figure 4.16: Simulated (crosses) and measured (round bullets) LSPs in the corridor scenario: DS in (a) LOS and (b) NLOS, and ASA in (c) LOS and (d) NLOS.

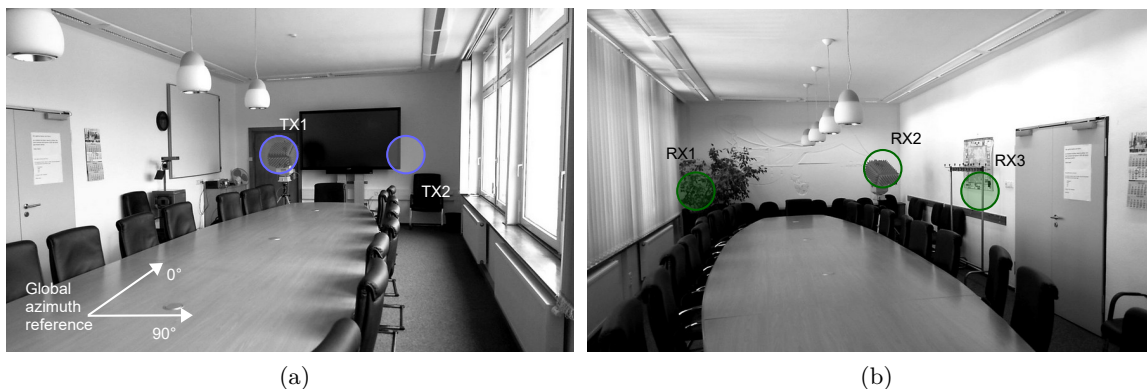


Figure 4.17: (a) View from RX1 towards the TX1 and TX2 positions and (b) view from TX2 towards the RX positions in the conference room scenario.

4.3.5 Conference Room at 190 GHz

Typical furniture as a big table, chairs, blackboards, large flat screen, and light bulbs, can be found in this scenario, as shown in Fig. 4.17. In total, there are 6 measurement links: a combination of 2 TX and 3 RX positions, both the TX and RX are at approx. 1.3 m height.

Environment and Propagation Characterization

Different scatterers have been identified using the pictures from the scanning directions, the path propagation distance from the directive PDPs, and the RT simulations.

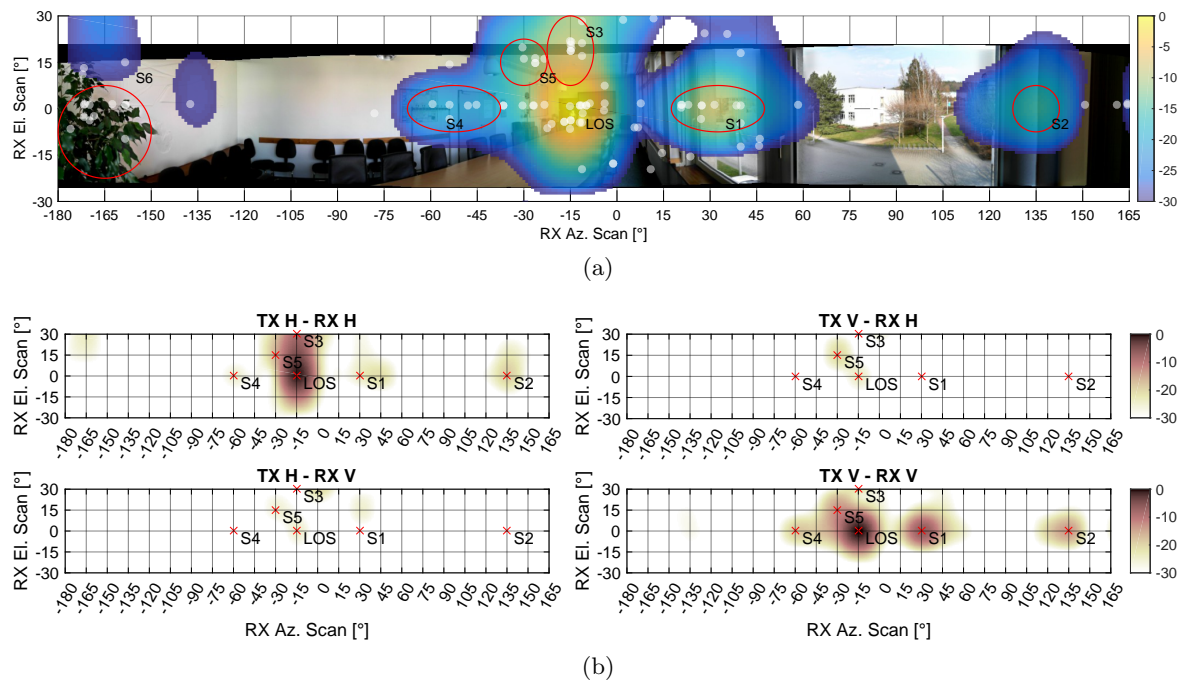


Figure 4.18: (a) Superimposed RT simulations (white bullets) over the measured PAEP in the link TX1-RX1 in conference room scenario and (b) the polarimetric decomposition of the measured PAEP.

The superposition of the measured power azimuth/elevation profile (PAEP), the RT simulation², and the 360° picture taken by the CS in the link TX1-RX1 is displayed in Fig. 4.18a. A rich multi-path channel can be observed in this scenario, where most of the paths are scattered from the direction of the walls, ceiling, and table (since the floor is hidden by it). Together with the LOS component, we can observe reflections from the window frames (S1 and S2), fluorescent light covers (S5), ceiling (S3), table, lateral (S4) and back walls, showing a good match between the DoA from the RT simulations and the measurements. However, there are two clusters that do not coincide: S2 is present in the measurements but not in the RT simulations, and the opposite happens with S6. Similarly to what was observed in the large corridor scenario, the influence of the CS during the measurements can be seen in the scatterer S6: the CS was shadowing all the reflections arriving from behind the RX.

The polarimetric decomposition of the PAEP displayed in Fig. 4.18a is presented in Fig. 4.18b. Scatterers as S1 and S2 (scattering in windows and frames), and S4 (scattering in side walls) are predominant in TX ϑ - RX θ since they are reflections in vertical structures. The opposite happens in the reflections in the ceiling S3, in which the dominant component is TX φ - RX ϕ . In addition, reflections in the fluorescent light covers S5 present a high cross-polarization leakage from TX φ to RX θ . This selectivity of the scatterers to polarization shows the need of implementing dual-polarized systems since it increases the number of “visible” scatterers which can be used for spatial diversity and to avoid human shadowing. On the other side, the polarization selectivity of the scatterers decrease polarization diversity within a single beam, since one of the two orthogonal polarimetric channel is severely attenuated.

²The parameters of the simulations can be found in Appendix D.5.

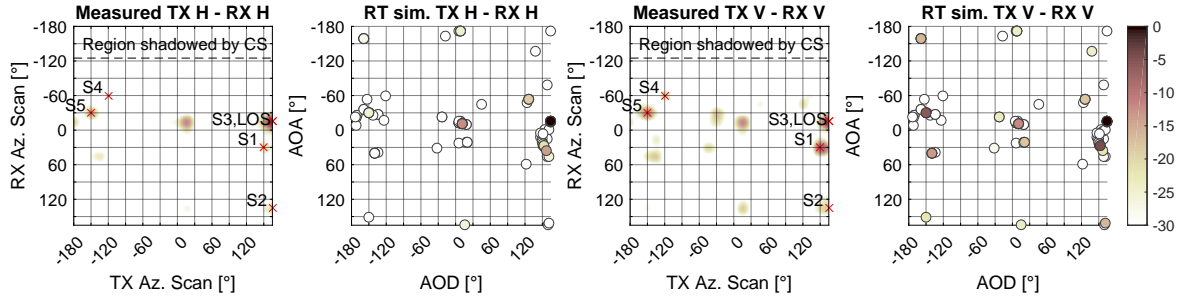


Figure 4.19: Measured and simulated co-polarized PAAP in conference room scenario.

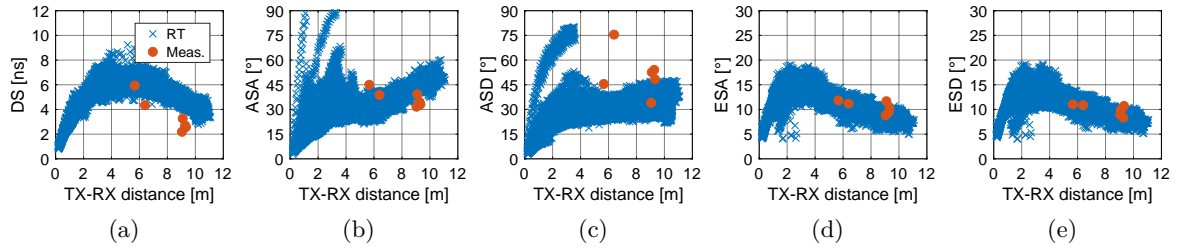


Figure 4.20: Measured and simulated LSPs at 190 GHz in the conference room scenario.

The power bi-azimuth profile (PAAP) decomposed on its co-polarized channels TX φ - RX ϕ and TX ϑ - RX θ is displayed with the labelled scatterers for the link TX1-RX1 in Fig. 4.19. There is a good match between the measurements and simulations on the location of the scatterers in the angular domain and the estimated power for the different polarizations. The scatterers are distributed in a wide range in the angular domain at the RX. This can be exploited to counteract human shadowing by utilizing multiple-beams. On the other hand, the scatterers are concentrated in a short range of angles at the TX side, which encourages further investigations on TX (AP) diversity to compensate human shadowing losses.

Analysis of Large Scale Parameters

The DSs in the different positions are shown in Fig. 4.20a. Due to the TX positions, the DS in the measurements and RT simulations is larger in the middle of the room and decreases when the RX is approaching the walls (short or large TX-RX distances). The same behaviour has been observed in all the other measured scenarios in which the RX was between the TX and a limiting wall/building as the corridor and street canyon scenarios. The linear model introduced in [61] is not able to mimic this behaviour.

The ASA and azimuth spread of departure (ASD) are shown in Fig. 4.20b and Fig. 4.20c, respectively. The measured ASD was larger than the ASA due to the MPCs that were blocked by the CS during the measurements. The measured ESA was very similar to the elevation spread of departure (ESD) and to the RT simulations, displayed in Fig. 4.20d and Fig. 4.20e, respectively. It is worth to notice, that even with a reduced measurement resolution in comparison to RT, LSPs are similar and they follow the same trend than the simulations over TX-RX distance.

Table 4.8: Large scale parameters from measurements and RT simulations in conference room scenario at 190 GHz.

Source	Band	DS		ASA		ASD		ESA		ESD	
		Mean	Std.	Mean	Std.	Mean	Std.	Mean	Std.	Mean	Std.
Measurements ^a	190 GHz	3.51	1.41	37.04	4.87	51.65	13.63	10.55	1.27	9.96	1.10
RT ^b	190 GHz	5.16	1.38	32.41	11.68	28.86	11.25	11.81	2.83	11.70	2.89

^aFrom synthetic omni-directional patterns with 15° HPBW scans at TX and RX and 7.5 GHz bandwidth.

^bFrom path-level parameters.

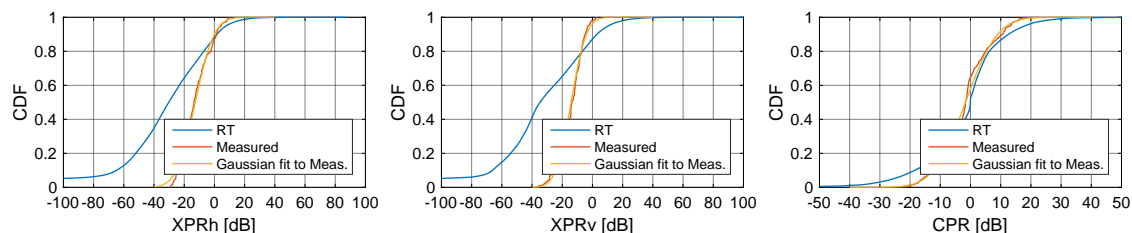


Figure 4.21: CDF of the PPRs in conference room scenario at 190 GHz.

The statistics of the measured and RT simulated LSPs are summarized in Table 4.8.

Polarimetric Power Ratios

The small size of the room and the narrow beam-widths utilized during the measurements allow a quasi-cluster level isolation per measurement beam. Therefore, the analysis of the PPRs has been performed based on the 100 strongest measured beams per link. The CDF of the PPRs from measurements and RT are displayed in Fig. 4.21, and the statistics summarized in Table 4.9. Differently to the large corridor scenario, the mean measured and RT simulated CPR in LOS is smaller than 0 dB, showing that the environment has a preference to the TX ϑ - RX θ combination of polarization.

It is worth to notice, that the measurement of PPRs are highly influenced by the antenna patterns and cross-polarization isolation (XPI) of the antennas, since the XPI usually is not constant over the angular pattern. In addition, a minimum cross-polarization ratio (XPR) of only ≈ -25 dB can be measured due to the XPI of these antennas (in the same order of magnitude).

Empirical Path-loss

Since the amount of measurement points in the room was reduced, the measured empirical path-loss was contrasted with RT simulations. The measured synthetic omni-directional and RT simulated isotropical path-loss is displayed in Fig. 4.20. The estimated PLE for the CI model is slightly smaller than 2, both in the measurements and simulations. This coincides

Table 4.9: PPRs and path-loss parameters from measurements in conference room scenario at 190 GHz.

Source	Band	XPRh		XPRv		CPR		Path-loss ^a	
		Mean	Std.	Mean	Std.	Mean	Std.	n	σ_X
Measurements ^b	190 GHz	-12.68	9.90	-14.13	7.95	-1.66	8.33	1.99	2.36
RT ^c	190 GHz	-35.45	39.66	-36.71	40.26	-1.73	13.02	1.97	1.44

^aFrom synthetic-omni directional TX and RX characteristics using 15° HPBW antennas.

^bConsidering the 100 strongest beams per-position with 15° HPBW scanning antennas.

^cFrom path-level parameters.

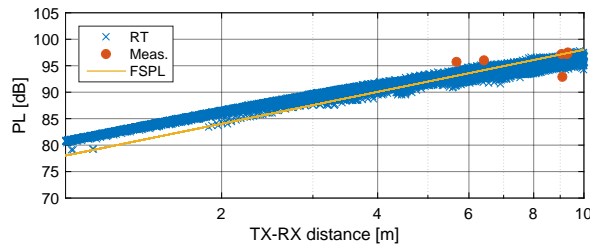


Figure 4.22: Measured and simulated path-loss in the conference room scenario at 190 GHz.

with the results reported at 150 GHz in [61] and at 300 GHz in [64]. On the other hand, the shadowing factor is larger in the measurements than in the RT simulations, possible due to the small number of samples. The parameters are summarized in Table 4.9.

4.4 Outdoor Propagation Analysis and Characterization

4.4.1 Introduction

Valuable multi-band measurements in different environments and scenarios can be found in the literature. Path-loss and DS in outdoor measurements covering the spectrum from 0.8 GHz to 73 GHz in a residential area in England can be found in [70]. In addition, measurements at 73 GHz and modelling aspects in rural areas are introduced in [49]. While path-loss in macro-cell environments in different cities in Japan is analysed in [71], [72] presents a similar work at 38 GHz in Austin, USA. Street canyon measurements at mm-waves in New York can be found in [10] and [73], and a comparison with measurements in Korea is presented in [74]. Similarly, multi-band measurements at 10 GHz and 60 GHz in street canyon scenario in Germany can be found in [75].

However, many of these multi-band measurements have been conducted using channel sounders having different bandwidths and antenna set-ups with different characteristics in each measured band, making a fair comparison of pure propagation aspects not possible. In that regard, in this section we introduce the measurement campaigns and results of multi-band measurements using the same channel sounder in two different locations: in Ilmenau (Germany) and

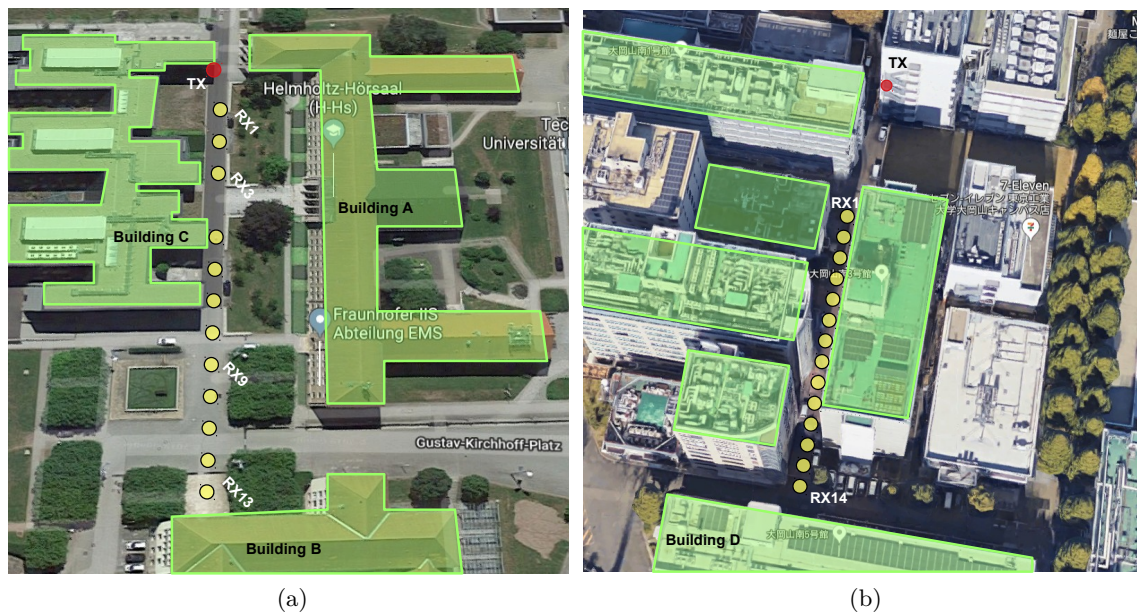


Figure 4.23: TX and RX positions in (a) Ilmenau, and (b) Tokyo.

in Tokyo (Japan). Since the measurement system was the same (antennas and bandwidth), significant results can be extracted by comparing the influence of the architecture of the different scenarios.

4.4.2 Scenarios and Measurement Set-up

As it is shown in Fig. 4.23, the Ilmenau scenario consists of a wide street with multiple buildings with irregular shapes (also quite typical in big cities in Germany), the Tokyo scenario is characterized by a narrower street with higher buildings with a more regular shape. In both cases, there was a building at the end of the street (Building B in Ilmenau and Building D in Tokyo), which introduced a high influence on the measurements.

In Ilmenau, the measurements were conducted in the campus of the TU Ilmenau. The TX was located in the fire scape staircase of the tallest building emulating a base station at approximately 17 m, as shown in Fig. 4.24a. On the other side, the RXs were located at 1.6 m height in 13 different positions over the street separated 10 m away from each other, with clear LOS, as shown in Fig. 4.23a. Unfortunately, the position RX4 was corrupted and is not considered in the analysis.

On the other hand, in Tokyo the measurements took place in the campus of the Tokyo University of Technology. The TX was located at approximately 17.5 m height in the staircase pointing in the direction of the street canyon, as shown in Fig. 4.24b. The RX was placed in 14 different positions separated every 5 m at a height of 1.6 m.

The configuration of the CS in the measurements is summarized in Table 4.10.

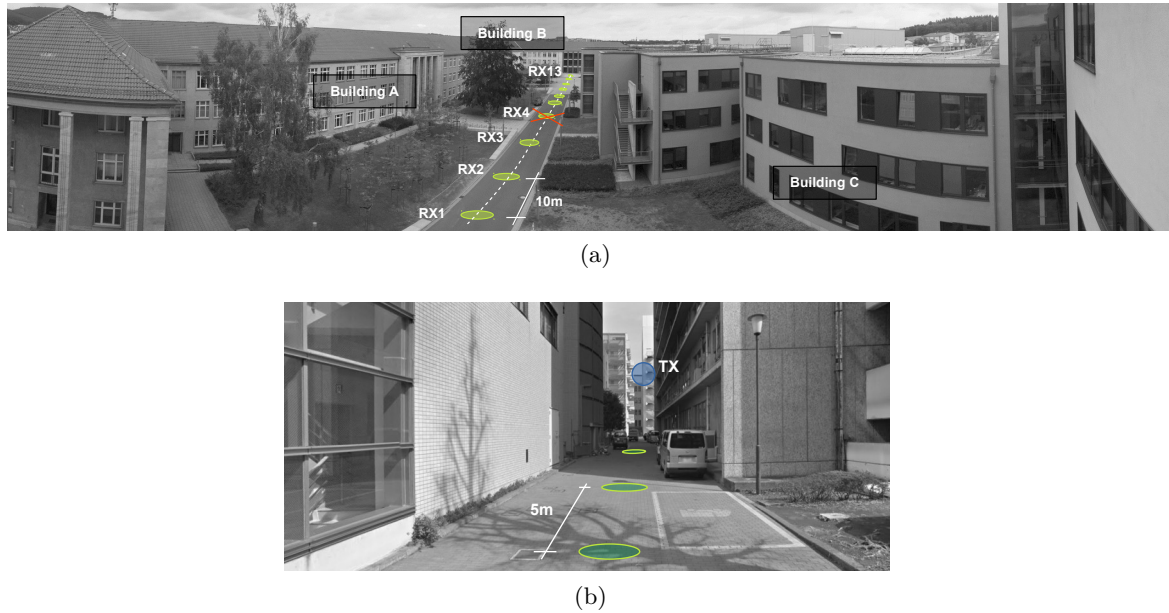


Figure 4.24: (a) View from the TX into the street canyon in the Ilmenau scenario and (b) view from position RX13 towards the TX in the Tokyo scenario.

Table 4.10: Measurement set-ups in street canyon scenarios.

Campaign	Band	BW	TX Azimuth	TX Elevation	RX Azimuth	RX Elevation
Ilmenau	6.75 GHz	6.75 GHz	$-90^{\circ}:30^{\circ}:90^{\circ}$	$-45^{\circ}:30^{\circ}:-15^{\circ}$	$-150^{\circ}:30^{\circ}:180^{\circ}$	$-30^{\circ}:30^{\circ}:30^{\circ}$
	30 GHz					
Tokyo	60 GHz	6.75 GHz	$-90^{\circ}:30^{\circ}:90^{\circ}$	$-60^{\circ}:30^{\circ}:0^{\circ}$	$-150^{\circ}:30^{\circ}:180^{\circ}$	$-30^{\circ}:30^{\circ}:30^{\circ}$
	30 GHz					
	60 GHz					

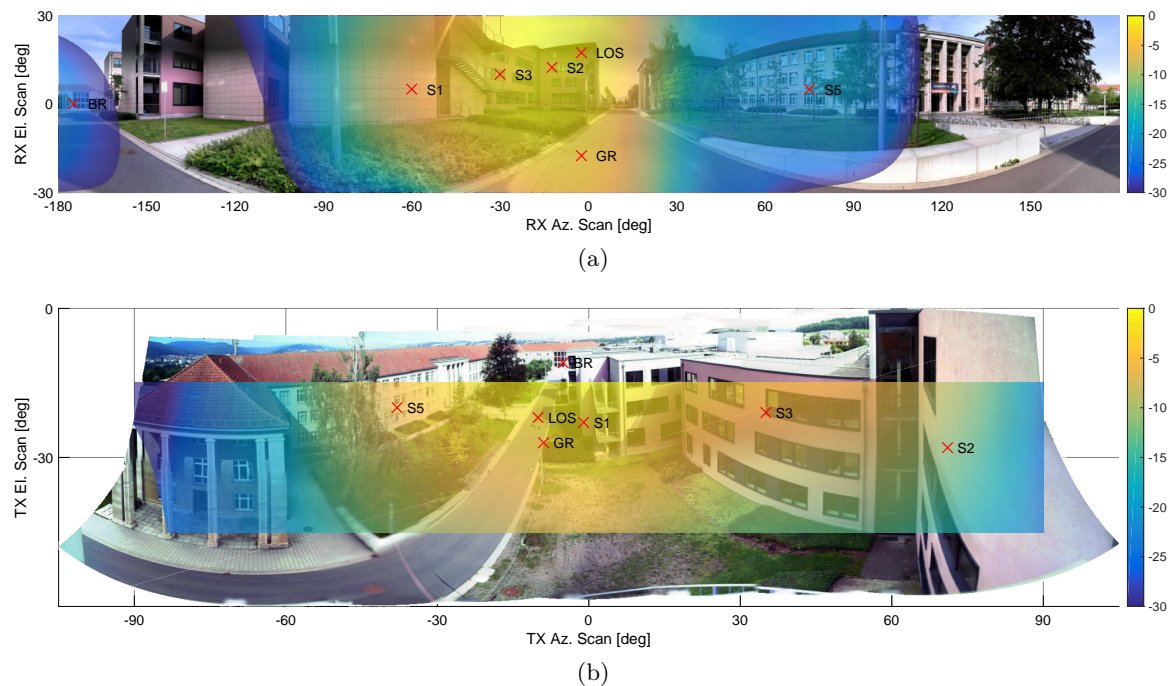


Figure 4.25: Measured PAEP at 60 GHz in RX3 in Ilmenau at (a) RX, and (b) TX.

4.4.3 Environment Characterization from Measurements

Different scatterers were identified using the scanning direction, time-delay of the observed peaks in the PDP, and pictures taken by the channel sounder. As an example, the PAEP at 60 GHz in the position RX3 in Ilmenau is overlaid in the panorama picture in Fig. 4.25. The main scatterers are indicated in the angular domain and later labelled in the time-delay domain in the multi-band synthetic omni-directional PDP in Fig. 4.26a. Apart from scatterers as S2, the majority and most relevant components are present with similar power at sub-6 GHz and in the mm-wave bands. Remarkable is scatterer S3, which is a reflection on the Building C in Fig. 4.24a and appears approx. 3 dB lower than the LOS. Moreover, the back reflection in the Building B is also observable in the Fig. 4.25. This scattering process influences the behaviour of the LSPs in the different positions.

Similarly, Fig. 4.26b shows the multi-band synthetic omni-directional PDP in the position RX3 in Tokyo. The ground reflection (GR) is also resolved in the time-delay domain, but compared to the Ilmenau scenario, the relative power of GR to the LOS component is lower, mostly influenced by the incident angles and material properties of the ground. Further discussions on modelling aspects in GR can be found in Section 6.3.1.

In addition, the influence of the street width is noticeable in the spread of the signal in delay in the detailed Fig. 4.26: within a narrow street, side reflections arrive closer to the LOS component (Tokyo), and with a wider street, the side reflections arrive later in the PDP (Ilmenau).

The evolution of the channel in the different positions is presented in Fig. 4.27. Since it is a

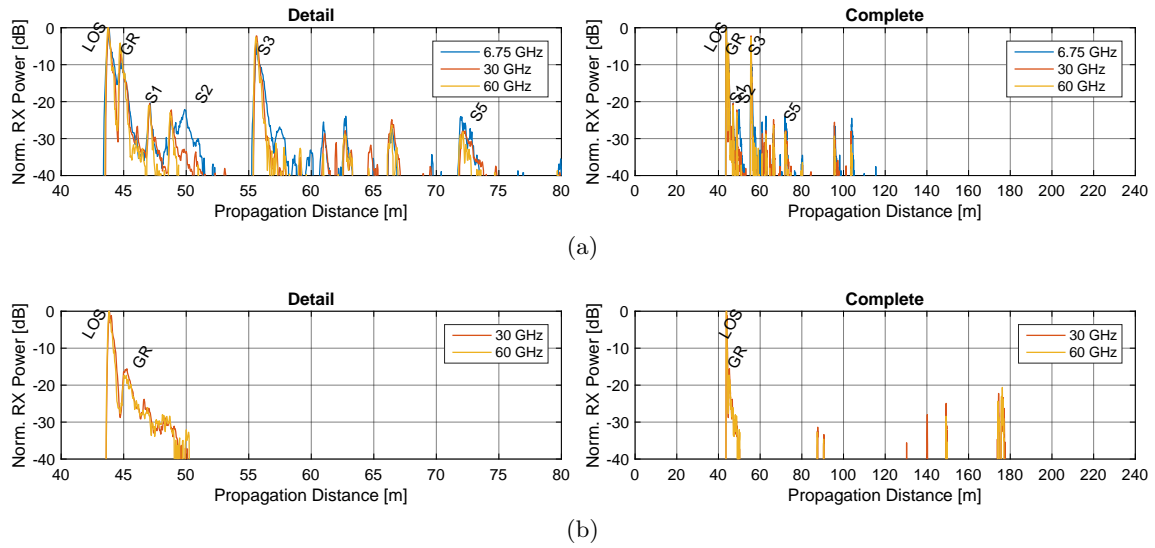


Figure 4.26: Detailed and complete multi-band synthetic omni-directional PDP in the position RX3 in (a) Ilmenau and (b) Tokyo.

LOS scenario, a relative constant channel can be observed. Only time to time some scatterers appear and disappear depending on the incident angles to the side buildings. Scatterers can be traced in the time-delay domain. Specially, reflections from the side and back buildings. It is worth to observe the amount of scatterers within the considered dynamic range. Due to the geometry of the scenario, and the TX and RX location, the back reflections are visible within the 30 dB dynamic range only in some positions in Ilmenau. On the other hand, it is visible in all the positions in Tokyo since the back building is located closer to the TX. A more specular process can be observed in the back reflection in Ilmenau, in which the RX power increases when the RX is approaching to it. On the other hand, in Tokyo it looks more like a diffuse scattering process, since there is no constant increment of RX power when the RX is approaching to it. This coincides with the irregular facade of the Building D.

4.4.4 Analysis of Large Scale Parameters

The multi-band per-position DS in the Ilmenau and Tokyo scenarios are shown in Fig. 4.28a and 4.28d, respectively. In average, the DS is shorter in Ilmenau than in Tokyo. There is an increase with a consequent decrease of the DS over TX-RX distance in both scenarios. This is caused by the reflection from Building B in Ilmenau and Building D in Tokyo. In the initial RX positions (short TX-RX distance), these reflections are not within the 30 dB dynamic range considered for the calculation of the DS. However, when the RX is moving closer to the building at the end of the street, the LOS component decreases due to the increased TX-RX distance, and the reflection becomes stronger due to the decrease on RX-back building distance. The maximum is reached in the position RX9 and RX10 in Ilmenau, and RX11 in Tokyo. After these positions, the difference of power between the LOS and reflected path becomes even smaller, but also the time difference between them, resulting on a subsequent decrease on DS. A shorter DS is observed in the first positions in Ilmenau since the back reflection from Building B is not within the dynamic range in the calculation of the DS.

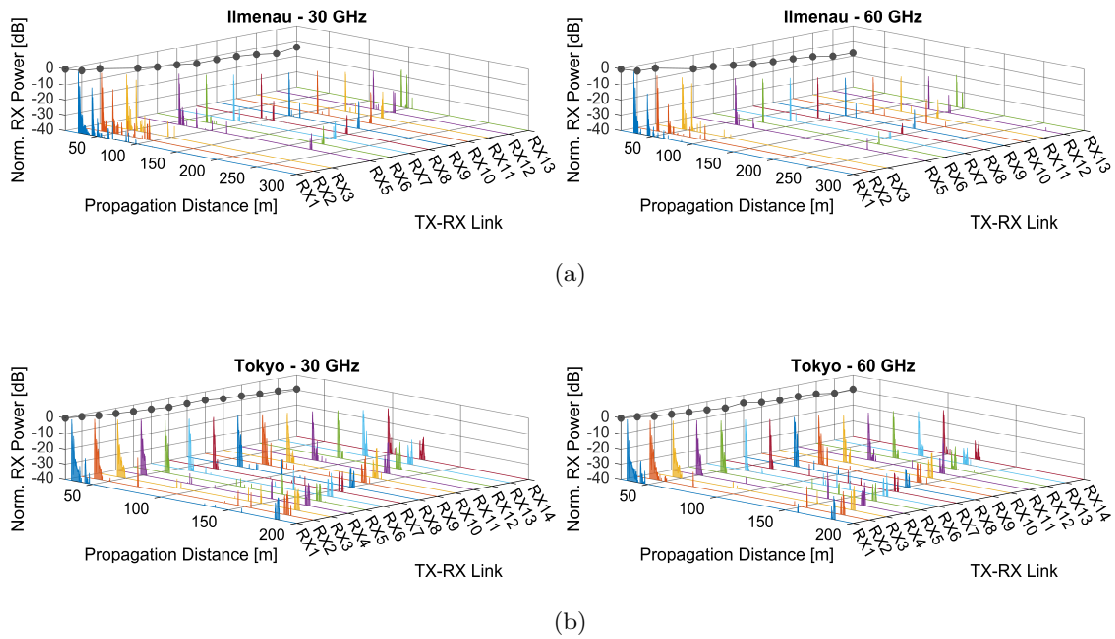


Figure 4.27: Synthetic omni-directional PDPs at mm-waves in (a) Ilmenau and (b) Tokyo.

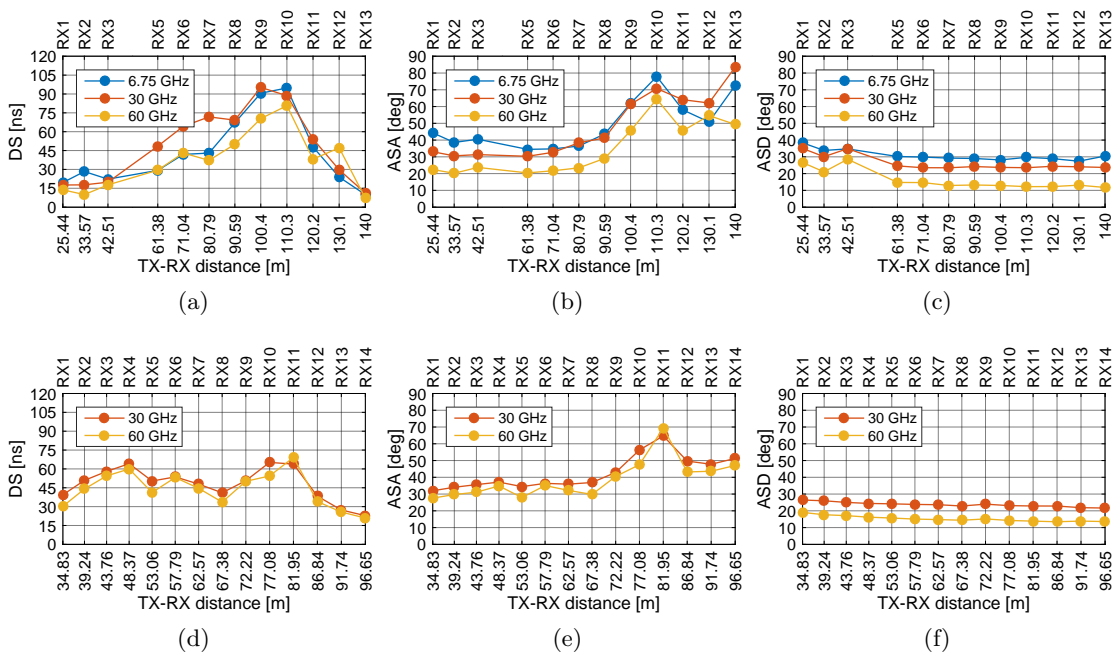


Figure 4.28: Multi-band large scale parameters from measurements in Ilmenau: (a) DS, (b) ASA, and (c) ASD, and in Tokyo: (d) DS, (e) ASA, and (f) ASD.

Table 4.11: Multi-band LSPs from measurements in street canyon scenarios^a.

Scenario	Band	DS		ASA		ASD		ESA		ESD	
		Mean	Std.	Mean	Std.	Mean	Std.	Mean	Std.	Mean	Std.
Ilmenau	6.75 GHz	40.91	27.72	47.19	16.52	32.98	8.33	20.31	1.43	12.48	1.40
	30 GHz	49.56	28.24	48.78	18.12	28.85	10.27	18.86	1.06	11.74	2.39
	60 GHz	38.62	22.95	37.58	17.69	19.38	12.89	16.99	3.02	8.39	3.71
Tokyo	30 GHz	48.11	13.12	42.50	9.90	23.76	1.39	18.94	1.47	18.42	0.51
	60 GHz	43.98	13.85	38.53	11.32	15.30	1.68	19.16	1.93	15.75	1.24

^aWith 30° HPBW scans at TX and RX, and 6.75 GHz bandwidth (BW).

The per-position and per-band ASs in Ilmenau and Tokyo are shown in Fig. 4.28. Similarly to what happens with the DS in Fig. 4.28a, the ASA is also affected by the reflections from the buildings at the end of the street. A slightly larger ASA can be observed in Ilmenau in the position RX1 when compared to Tokyo. This is due to the short TX-RX distances and larger street width (wide area between Building A and C in Fig. 4.24a): reflections from these buildings arrive from angles widely separated from the LOS. According the RX moves away from the TX, the reflections from the side buildings turn to arrive from angles closer to the LOS, and therefore the ASA slightly decreases up to the position RX6, in which the back reflection from the Building B starts to become more relevant. Since this reflection arrives almost 180° away from the LOS, the ASA values start to increase while the RX positions approach the Building B.

Exactly the same trend in the ASA due to the reflection in the Building D at the end of the street can be observed in Tokyo. On the other hand, as expected, the ASD decreases with increasing TX-RX distance. In the RX positions closer to the TX, the TX reaches the RX with first order reflections from broad angles to the LOS, and conforming the RX moves away, the reflections angles start to get closer to the LOS.

The similar trend on the values along the RX displacement shows the similarities of the channel in the different bands. While the ASA is quite similar in both scenarios, the ASD is smaller in Tokyo, since the street is narrower.

The mean and standard deviation of the multi-band LSPs are summarized in Table 4.11.

4.4.5 Multi-band Empirical Path-loss

The measured path-loss from the synthetic omni-directional channel in the Ilmenau and Tokyo street canyon scenarios and its fit to the ABG model (named as TUIL model, using the combined data-set) is displayed in Fig. 4.29. The parameters for the multi-band empirical path-loss obtained from the measurements in Ilmenau and Tokyo, independent and combined data-sets, are shown in Table 4.12.

In the Ilmenau scenario, the estimated multi-band PLE $\alpha = 2.19$, reference path-loss $\beta =$

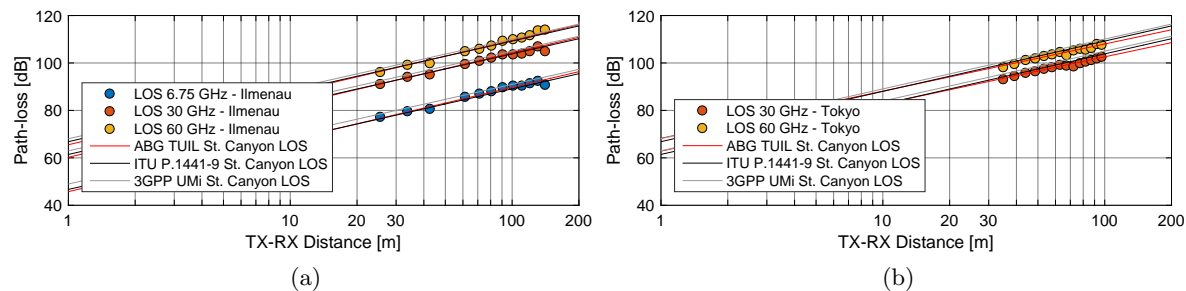


Figure 4.29: Multi-band path-loss from measurements and models in street canyon scenario in (a) Ilmenau, and (b) Tokyo.

Table 4.12: Path-loss parameters from measurements in street canyon scenarios: comparison to 3GPP and ITU-R street canyon models.

Model and measurements	α	β	γ	σ
ITU-R P.1441-9 Street Canyon	2.12	29.2	2.11	5.06
3GPP UMi Street Canyon	2.1	32.4	2	4
Ilmenau (measured)	2.19	28.79	2.05	5.68
Tokyo (measured)	1.95	31.93	2.09	3.73

28.79, and $\gamma = 2.05$ are within the range of the ones found in the literature [70], [71], and [69]. Hence, a good match between our measurements and the 3GPP and ITU-R models can be observed. On the other hand, the PLE in Tokyo was estimated to $\alpha = 1.95$, which is slightly below 2. This can be caused by a stronger canyon effect due to the smaller street width (≈ 7.5 m) in comparison to Ilmenau (in average, ≈ 32 m).

The influence of the regularity of the buildings facades can also be seen in the standard deviation of the shadow fading, being higher in Ilmenau.

4.5 Industry Scenario Propagation Analysis and Characterization

4.5.1 Introduction

Industry 4.0 is envisioned as a revolutionary process in which machines are augmented with wireless connectivity and multiple sensors [76]. While the bandwidth requirements for such applications can be fulfilled with the large blocks of spectrum available at mm-waves, propagation characteristics in those frequencies are still under investigation. Particularly, in industry scenarios, in which the large amount of machines and metallic items might introduce significant differences on propagation between bands and compared to other indoor scenarios.

Multiple measurements covering the sub-6 GHz spectrum can be found in the literature

[77, 78, 79]. Apart from the analysis of propagation, [79] presents model parameters for Quasi Deterministic Radio Channel Generator (QuaDRiGa). Since mm-wave measurements in these scenarios are rare to find in the literature, several works have been utilizing ray-tracing to characterize propagations: the analysis of propagation properties at 28 GHz and 60 GHz in two different scenarios in industrial settings presented in [80] shows differences with the current modelling approach for indoor scenarios at sub-6 GHz. The LOS probability is heavily affected and influenced by the density of machines. Furthermore, the amount of scattered paths is also increased due to the number of metallic scatterers in the environment.

Furthermore, the relative size of reflectors to wavelength might turn diffuse into specular scatterers. Since specular reflections only reach the RX if the incident and reflected angles are appropriate, the probability that a scattered path reaches the RX is higher compared to a specular path, [14]. Therefore, there is an expectation of having a larger amount of DMC power at lower frequencies (where scatterers are less specular). While recent publications have shown that ray-tracing simulations match better to mm-wave measurements in outdoor scenarios when diffuse scattering is considered [81], multiple measurements have shown and described a more specular-like characteristic of the mm-wave channel [65]. From the multi-band measurements in different scenarios as V2V [82], street canyon [83], and large indoor halls [84], we have observed that while the peaks (assumption of specular paths) of the PDP look similar in the different bands, the DMCs seems to be reduced with increasing frequency. However, a systematic and quantitative analysis has not been yet conducted.

Applications as localization in industrial environments can also be benefited from the utilization of broadband signals. However, whether the first significant MPC arrived under NLOS is specular or not, its frequency dependency, and how to model it, is still also under discussions.

Therefore, we introduce simultaneous multi-band measurements in industry scenarios with the aim of characterizing propagation at mm-waves and to compare with the well-known sub-6 GHz channel. A systematic analysis of specular to DMC power ratio and LSPs is presented in the different bands, sub-scenarios, and visibility conditions.

4.5.2 Scenarios and Measurement Set-up

The measurement campaign was conducted in the machine hall of the Newtonbau in the TU Ilmenau. It consists of a big hall with a tall ceiling and multiple open cubicles with several machines and devices, as seen in Fig. 4.30. A single TX station was used with two RX stations measuring LOS and NLOS in parallel. Two different sub-scenarios were studied, TX below and TX above clutter level. In the first case, the TX was at approx. 2 m height and the RX antennas were at 1.36 m height at 6.75 GHz and 30 GHz, and at 0.42 m at 60 GHz. On the other hand, in the TX above clutter level sub-scenario, the TX was in the same position but at approx. 4 m height. The RX antennas were at the same heights as in the TX below clutter level case.

At the TX side, 30° HPBW were used to scan the azimuth from -60° to 60° and the elevation from -30° to 0° with 30° scanning steps. On the other hand, dipoles were used at the RX side. A single wideband dipole (covering from approx. 0.5 GHz to 45 GHz) controlled by a

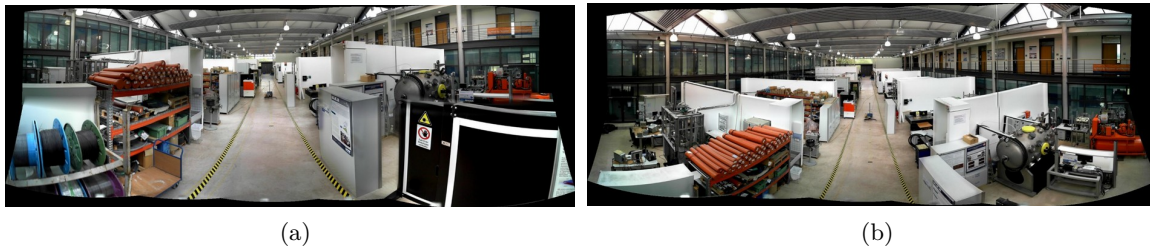


Figure 4.30: CS view from the TX in sub-scenario (a) below, and (b) above clutter level.

Table 4.13: Industry scenario measurement set-up.

Sub-Scenario	Frequency	TX Height	RX Height	TX Az.	TX El.	RX Az.	RX El.
TX below clutter level	6.75 GHz	2.45 m	1.36 m				
	30 GHz	2.15 m		$-60^\circ:30^\circ:60^\circ$	$-30^\circ:30^\circ:0^\circ$	Omni	Omni
	60 GHz	2.23 m	0.42 m				
TX above clutter level	6.75 GHz	4.21 m	1.36 m				
	30 GHz	4.06 m		$-60^\circ:30^\circ:60^\circ$	$-30^\circ:30^\circ:0^\circ$	Omni	Omni
	60 GHz	3.99 m	0.42 m				

switch was used at 6.75 GHz and 30 GHz. Therefore, these two bands can be fairly compared. A different antenna was used at 60 GHz, which was located below, in front of the CS. It is worth to notice, that the CS itself blocked all the scattering from the back of the environment. The different location of the 60 GHz antenna makes a direct comparison with the other bands not possible. However, this channel emulates the case of trolleys or machines with antennas located at a very low height. More details on the antennas positions in the different sub-scenarios are summarized in Table 4.13.

The RX stations were located, both in LOS and NLOS, in a raster of 2 m separation, as shown in Fig. 4.31. The nomenclature is as follows: RXLx corresponds to the position “x” in LOS, and RXNx to the position “x” in NLOS.

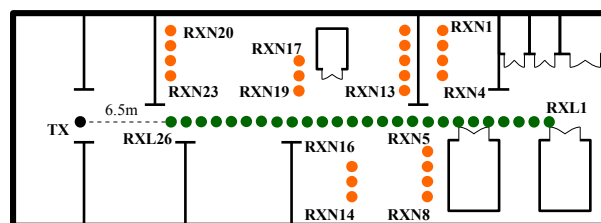


Figure 4.31: TX and RX positions in industry scenario: RXL in LOS, and RXN in NLOS.

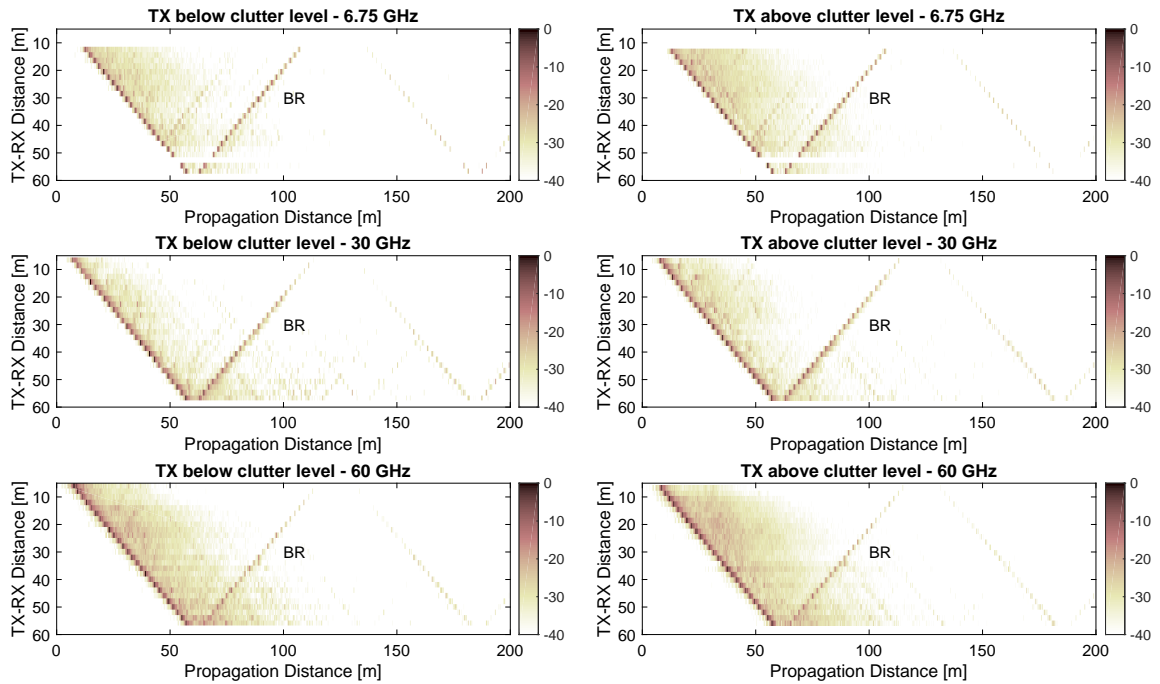


Figure 4.32: Per-position multi-band normalized PDPs in LOS.

4.5.3 Environment Characterization

The per-position normalized PDPs in LOS with TX below and above clutter level are shown in Fig. 4.32. Besides the LOS component, a strong back reflection from the end of the hall and other specular back reflections from the machines and furniture on the corridor can be observed. In addition, there are high order reflections between the beginning and end of the hall within the displayed 40 dB dynamic range.

The strongest peaks (assumed to be specular reflections) are similar between the 6.75 GHz and 30 GHz. The scatterer BR is the back reflection from the end of the machine hall. At 60 GHz, this back reflection appears more attenuated since due to the location of the antenna, the CS obstruct all the scattering from the back side.

A direct comparison in Fig. 4.32 shows more DMCs at 6.75 GHz than at 30 GHz, visible as a longer tail within the same dynamic range. On the other hand, more DMC power is observed at 60 GHz. However, it is not comparable to the other bands because of the different (low, at floor level) location of the RX antenna. A comparison between sub-scenarios, independently from the frequency band, shows similar specular components, but richer DMC process in the TX above clutter level case. Probably, because with the TX above clutter level, the TX can reach the RX from multiple scatterers that are blocked when the TX is below clutter level.

The per-position per-band normalized marginal power azimuth profile (PAP) at TX with TX below and above clutter level in LOS and NLOS is shown in Fig. 4.33a and Fig. 4.33b, respectively. During LOS, as expected, the maximum is obtained in the beam pointing towards the corridor. However, a comparison between the 6.75 GHz and the 30 GHz bands

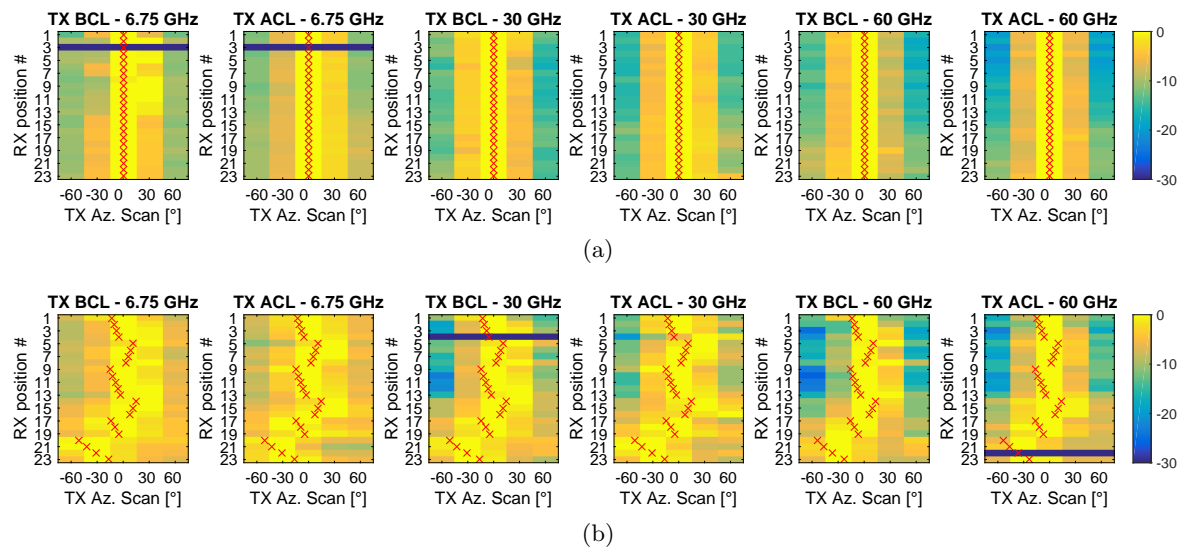


Figure 4.33: Measured multi-band PAP at TX and LOS radial direction (in crosses) in industry scenario with TX below and TX above clutter level in (a) LOS, and (b) NLOS.

shows a smaller difference between the LOS and the other beams at lower frequency. This might be attributed to more diffuse scattering at lower frequencies since the TX reaches with more power the RX from a wider range of directions than at mm-waves.

A comparison between the sub-scenarios shows that with TX below clutter level, the PAP is less regular than with the TX above clutter level. This is because in the second case there is less shadowing and the power is more uniformly distributed in the environment. Therefore, ASDs are slightly larger in the TX above clutter level sub-scenario, as shown in Fig. 4.34e and Fig. 4.34f.

On the other hand, in NLOS, the maximum power is obtained when the TX beam is pointing in the direction of the corridor (0° TX Az. scan) and in the virtual LOS direction to the RX. This suggests that the signal comes from diffracted paths and scattered components in the vicinity of the outlet to the main corridor.

4.5.4 Analysis of Large Scale Parameters

It is worth to remember that in these measurements, only a direct comparison between the 6.75 GHz and 30 GHz can be done since the antennas were co-located. Interestingly, even if the 60 GHz antenna was located in a different position, and blocked by the CS, the LSPs still have a similar trend as the lower frequencies.

The influence of the specular reflections on the back of the building can be observed in the DS, displayed in Fig. 4.34a and Fig. 4.34b. With shorter TX-RX distances, the DS is dominated by local scattering at the RX. When the TX-RX separation increases, the influence of the back reflection is stronger and the DS increases. Finally, the delay difference between the LOS

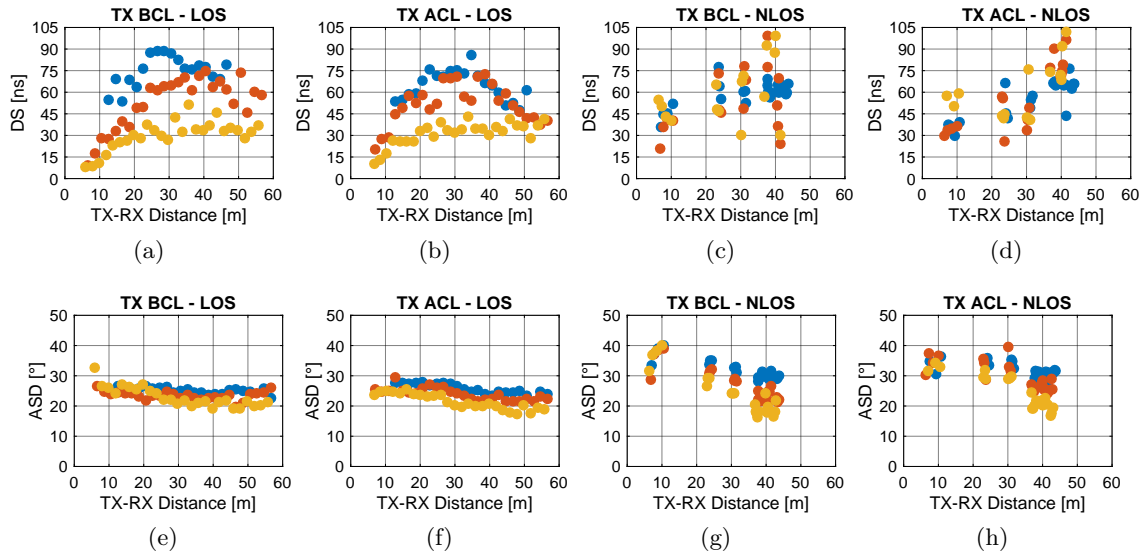


Figure 4.34: Multi-band large scale parameters from measurements in industry scenario: 6.75 GHz in blue, 30 GHz in red, and 60 GHz in yellow.

and back reflection and their respective relative difference of power decreases with increasing TX-RX distance and therefore, the DS starts to decrease. A similar behaviour has been detected in the indoor large corridor scenario in Fig. 4.11a, the conference room scenario in Fig. 4.20a, and in the street canyon scenario in Fig. 4.28a. On the other hand, there is a clear trend on increase and dispersion of DS values with increasing TX-RX distance in NLOS.

Both in LOS and NLOS, the ASD decreases with increasing TX-RX distance. However, the decreasing rate is sharper in NLOS. The ASD is relatively constant over distance in LOS since the RX is aligned with the TX, and most of the signal power reaches the RX from the same TX beam (also the back reflections). On the other hand, a larger variation is observed in the NLOS case, in which shorter spreads are obtained at larger TX-RX distances, which means that the power is concentrated in a few or single beams. Even if the ASDs values might differ from band to band, they follow the same trend.

Table 4.14: Multi-band LSPs from measurements in industry scenarios^a.

Scenario	Band	LOS		NLOS		LOS		NLOS	
		Mean	Std.	Mean	Std.	Mean	Std.	Mean	Std.
TX below clutter level	6.75 GHz	87.32	32.69	25.11	1	59.02	8.81	31.97	3.38
	30 GHz	57.22	13.32	23.27	1.34	68.79	41.3	28.17	5.61
	60 GHz	32.78	7.47	22.25	2.52	74.35	33.15	24.7	7.41
TX above clutter level	6.75 GHz	69.94	19.92	25.83	1.57	56.4	13.1	32.17	2.46
	30 GHz	55.05	10.7	23.82	2.11	68.27	36.28	30.05	4.57
	60 GHz	33.55	5.14	21.08	2.51	77.83	32.84	25.71	5.24

^aWith 30° HPBW scans at TX and dipole at RX.

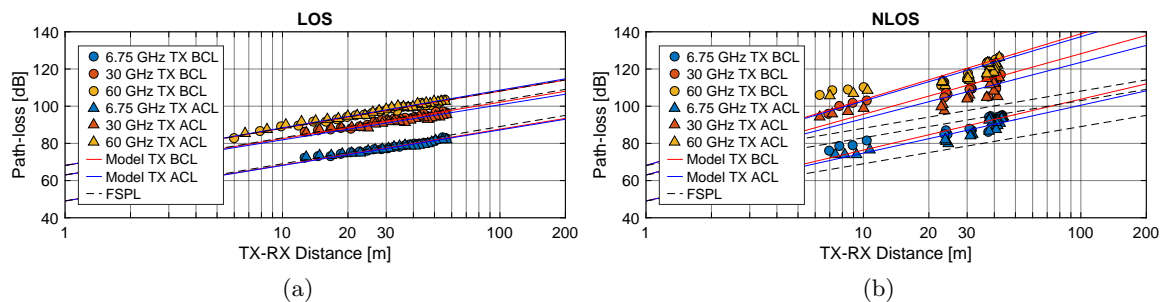


Figure 4.35: Multi-band path-loss from measurements in industry scenarios in (a) LOS and (b) NLOS.

The mean and standard deviation of the DS and ASD are summarized in Table 4.14.

4.5.5 Multi-band Empirical Path-loss

The path-loss results for the different sub-scenarios and visibility conditions are shown in Fig. 4.35 and the estimated coefficients summarized in Table 4.15. The PLE was larger when the TX was located below clutter level, both in LOS (slightly) and NLOS (significantly). In addition, while the PLE in LOS is similar in the sub-6 GHz and 30 GHz bands, it is remarkable larger at 30 GHz in NLOS. Also, the standard deviation of the shadowing factor in NLOS is considerably larger at 30 GHz compared to the sub-6 GHz.

Since the 60 GHz band was measured with the antennas in a different position, a fair comparison with the other bands is not possible. However, the same trend of having a lower PLE but a larger shadowing factor with TX above clutter level in NLOS is observed.

Since the CI model is anchored to the reference FSPL at 1 m, this model produces an over-estimation of path-loss at larger TX-RX distances and an under estimation at shorter TX-RX distances. Consequently, the floating-intercept (FI) model, in which there is no anchor to a reference, might be more accurate to address NLOS. This can be observed in Fig. 4.35 at 60 GHz, in which the measured PL is smaller as the estimated at larger TX-RX distances in NLOS.

4.5.6 Specular to Dense Multipath Components Power Ratio

The specular and dense power per TX scanning direction $P_{SC}(\tau, \phi, \theta)$ and $P_{DMC}(\tau, \phi, \theta)$, respectively, is calculated from the measurements with (2.33) as indicated in Section 2.3. The mean and normalized standard deviation over the different scanning directions in the different measured positions is displayed in Fig. 4.36. In average, the specular power in LOS is larger at 30 GHz than at 6.75 GHz, both with TX below and above clutter level (see Fig. 4.36a and Fig. 4.36c). The opposite happens in NLOS, where the specular power is larger at 6.75 GHz.

Table 4.15: Multi-band path-loss parameters from measurements in industry scenarios^a.

Band	TX below clutter level				TX above clutter level			
	LOS		NLOS		LOS		NLOS	
	PLE	σ	PLE	σ	PLE	σ	PLE	σ
6.75 GHz	1.93	0.75	2.73	2.07	1.91	0.91	2.57	2.91
30 GHz	1.96	1.00	3.34	5.35	1.90	1.36	3.2	7.72
Multi-band (6.75 and 30 GHz)	1.95	0.92	3.03	6.06	1.90	1.16	2.88	7.33
60 GHz	2.00	0.58	3.65	6.95	2.02	0.61	3.54	7.36

^aWith 30° HPBW scans at TX and dipole at RX.

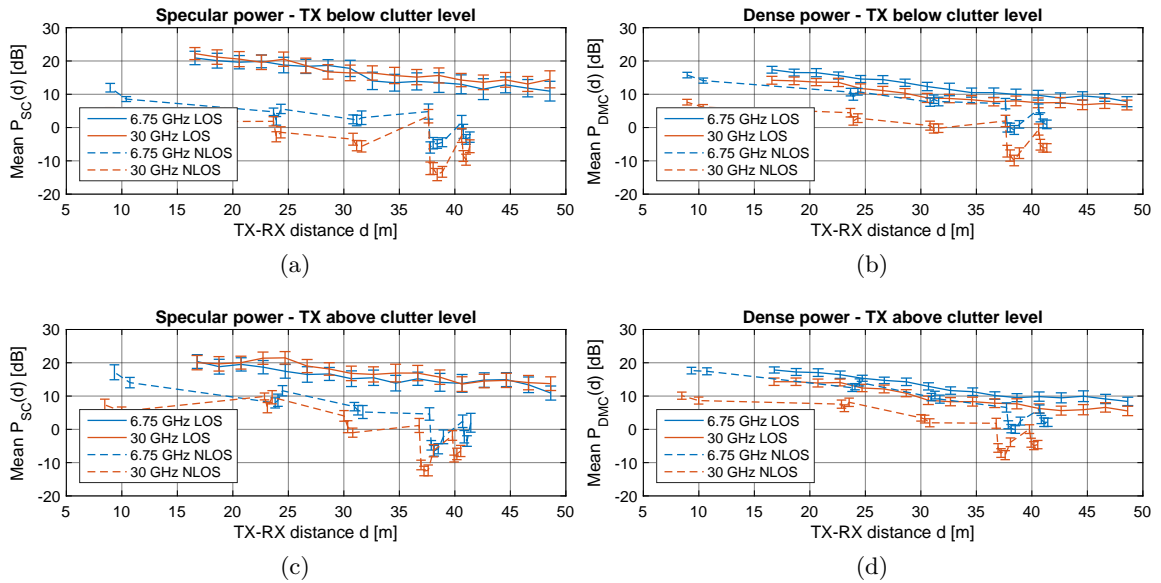


Figure 4.36: Multi-band mean and standard deviation of specular power and dense power in LOS and NLOS with TX below and above clutter level.

Table 4.16: Multi-band specular to dense power ratio from measurements in industry scenarios^a.

		LOS				NLOS			
		6.75 GHz		30 GHz		6.75 GHz		30 GHz	
Sub-scenario		Mean	Std.	Mean	Std.	Mean	Std.	Mean	Std.
SP	TX below clutter level	15.83	8.15	16.97	7.25	1.13	6.92	-5.02	7.75
	TX above clutter level	15.86	7.12	17.24	6.9	3.6	8.77	-1.33	8.89
DMC	TX below clutter level	12.24	4.98	9.78	4.82	6.04	6.28	-1.52	6.79
	TX above clutter level	12.66	4.79	9.58	5.01	7.5	6.78	0.79	6.92
SP2DMC	TX below clutter level	3.59	4.37	7.19	3.54	-4.91	2.34	-3.49	2.62
	TX above clutter level	3.21	4.08	7.67	3.49	-3.89	3.25	-2.12	3.18

^aEstimated with RIMAX from measurements with 30° HPBW scans at TX and a dipole at RX.

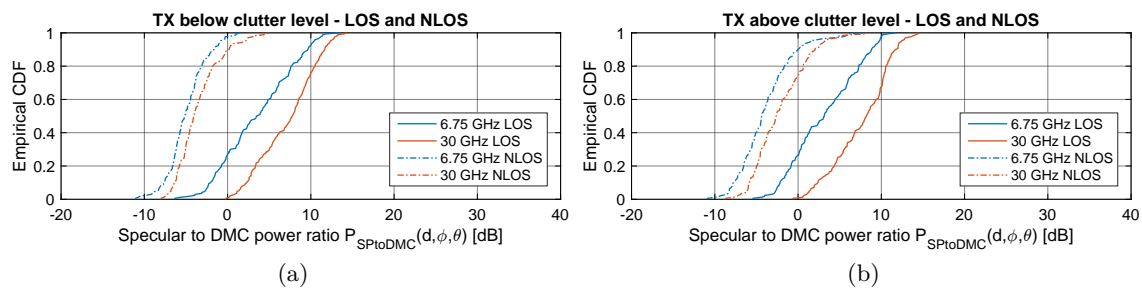


Figure 4.37: Multi-band specular to DMC power ratio in LOS and NLOS with (a) TX below and (b) TX above clutter level.

On the other hand, Fig. 4.36b and Fig. 4.36d show the dense power. As expected, in average the DMC is larger at 6.75 GHz than at 30 GHz, both in LOS and NLOS, and with TX below and above clutter level. However, the difference between bands is larger in NLOS. The mean and standard deviation of the specular, DMC power, and specular to DMC ratio per band, sub-scenario, and visibility showing the clear trend mentioned before are presented in Table 4.16.

The CDF of $P_{\text{SP2DMC}}(\phi, \theta)$ in the different sub-scenarios and visibilities are displayed in Fig. 4.37. As expected, the ratio is larger at mm-waves (meaning less DMC power), both in LOS and NLOS. However, in LOS the difference between the ratios in the different bands is larger. This is because the specular power at mm-waves is also reduced in NLOS due to obstruction losses. In addition, the ratio in NLOS is larger in both bands with TX above clutter level. This is because more specular reflections are attenuated with TX below clutter level than with the TX above clutter level.

4.6 V2V Propagation Analysis and Characterization

4.6.1 Introduction

While there is already an extension of the IEEE 802.11 protocol for Wireless Access in Vehicular Environment (WAVE) at sub-6 GHz, the IEEE 802.11p standard, it is still not well established and has few adoptions in the automotive industry. This is contradictory considering the incredible wide spectrum of applications for wireless communications in vehicular context: from autonomous and/or automatic driving, passing by safety applications, to the delivery of multimedia content for entertainment. Also, considering the boom of IoT, it is predicted the concurrence of millions of sensors distributed around roads and cities, which can be used, between others, to assist driving by providing real-time traffic information from cloud computing, weather conditions, data for cruise control, blind spot detection, and so on. Furthermore, we can also consider vehicles as moving sensors with the capability of collecting and distributing information. Nowadays, vehicles are provided of global positioning system (GPS), radars (mostly operating at mm-waves), video cameras, temperature sensors, etc. In addition, there is a current boom in the research on machine learning algorithms for applications that can use all this collected data to enhance the driving and travelling experience. However, these vehicular-to-infrastructure (V2I, or V2X) applications need the distribution of large volumes of data by means of high data-rate wideband communications.

Thus, mm-wave frequencies appear as a solution to provide the instantaneous high data-rate communications to expand the range of applications in V2V and V2X platforms.

However, there are multiple challenges when we come to the point of vehicular communications:

- high mobility: the need of directive radio-channels to compensate isotropic path-loss requires fast adaptive beam-forming techniques,
- large blockage loss: blockage losses by vehicles (NLOS_v) increase with frequency, and the size of vehicles also increases the blockage loss and range. Therefore, alternative paths have to be found to avoid cuts on communications,
- sparse or rich multi-path channel? do we have the same opportunities as in the sub-6 GHz channel?

At this point, there is one trend of splitting low latency and low data-rate crucial communications in reliable sub-6 GHz links, and high data-rate less critical data into the mm-waves, [85]. While the sub-6 GHz have been extensively measured and investigated from the legacy standards, mm-waves propagations in vehicular environments are still under characterization: what do we see? How different is compared to sub-6 GHz?

Therefore, in order to understand a little bit more propagations in vehicular environments, we have conducted several measurement campaigns simultaneously at different frequencies in V2V scenarios. Due to the limitations introduced by the set-up, all the measurements have

Table 4.17: Multi-band V2V measurement campaigns.

Campaign	Scenario	Frequency	Description
V1	Blockage by overtaking		Fix TX-RX distance, antennas at rooftop level, passenger vehicle as blocker moving between the TX and RX
V2	Blockage by overtaking	6.75 GHz, 30 GHz, and	Fix TX-RX distance, antennas at rooftop level, pick-up truck vehicle as blocker moving between the TX and RX
V3	Multiple vehicles blockage	60 GHz	Fix TX-RX distance, antennas at rooftop level, different number of passenger vehicles between TX and RX
V4	Corner scenario		Different TX-RX distance in a corner scenario, antennas at rooftop level
V5	Path-loss and blockage		Different TX-RX distance in a straight line, in LOS and NLOS conditions, antennas at rooftop level

been conducted in static environments. The mobility has been emulated by sampling the channel in different positions. In all the scenarios, 30° HPBW antennas were used to scan the environment, and otherwise indicated, only the azimuth plane at 0° elevation was scanned. The different measurement campaigns and the scenarios are summarized in Table 4.17.

4.6.2 Corner scenario

As shown in Fig. 4.38, in this scenario the TX was fixed and the RX was located in different positions emulating a situation in which two vehicles are communicating to each other and suddenly the RX turns into a corner, going from LOS, to OLOS (by vegetation), and finally to NLOS (by Building A). There are five different RX positions, but Position 1 was measured twice: Position 1a without parked vehicles in the scenario (blue bullets in Fig. 4.38), and Position 1b with the parked vehicles in the surrounding area.

Environment Characterization

From the measurements we have identified several scatterers in the environment using the scanning directions of the antennas, the propagation distance, the pictures taken by the channel sounder, and the assistance of Google maps with in-situ distance measurements. Some of these common scatterers are: a far reflection from Building D (190 m propagation distance, Path P2 in Fig. 4.38) is observed in the time and angular domain in Fig. 4.39 and Fig. 4.40. Even if this is a weak reflection (approx. 30 dB lower than the LOS component), it is present in the different bands from LOS in Position 1 to NLOS in Position 3.

The surrounding buildings have also been identified in the angular and time domain: Building A generates Path P1a (visible in the PDP in Fig. 4.39), and Building B (Path P3) as the strong reflection together with the diffracted LOS in the remaining NLOS positions, visible in the PDP in Fig. 4.39. The 30 dB per-position dynamic range is also displayed. It can be observed that while the channel is similar in the different bands, the number of MPCs within this range is different, generating a divergence between the multi-band DSs as shown

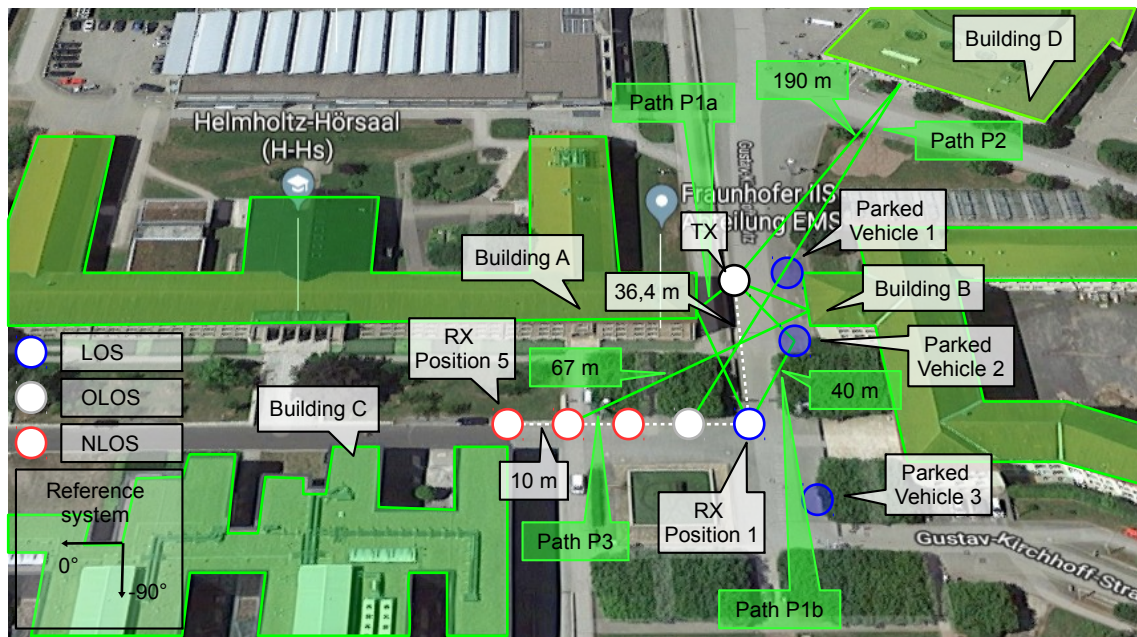


Figure 4.38: Corner scenario with different visibility conditions and parked vehicles in the environment.

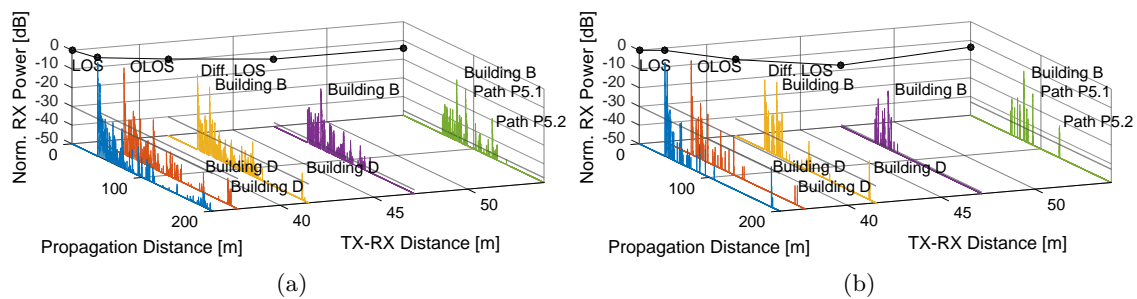


Figure 4.39: PDP in the different RX positions at (a) 6.75 GHz and (b) 60 GHz.

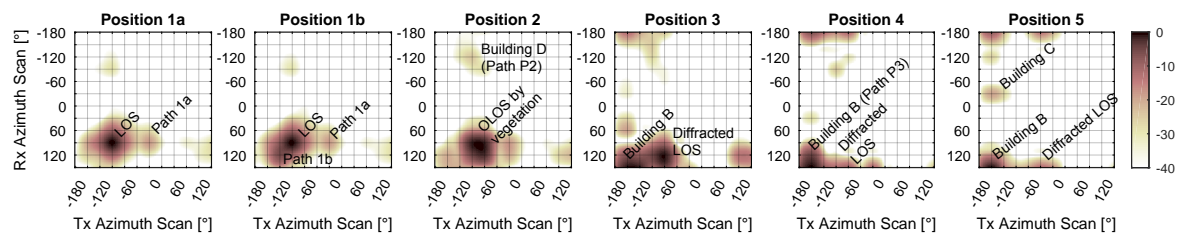


Figure 4.40: Power bi-azimuth profile in the corner scenario at 60 GHz.

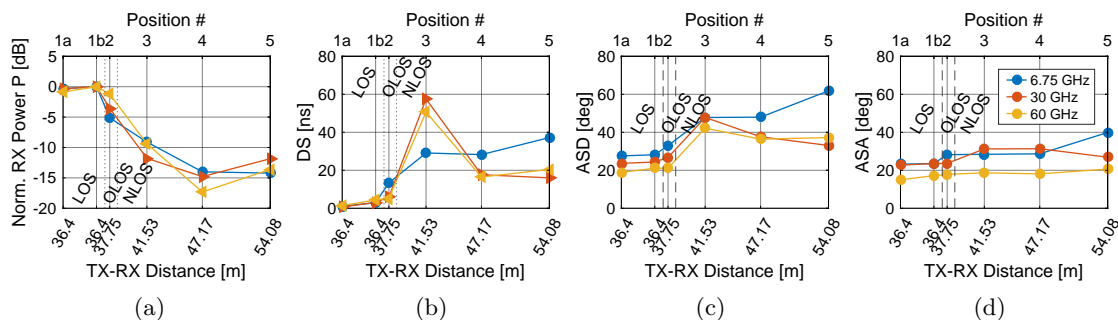


Figure 4.41: Multi-band LSPs from measurements in corner scenario: (a) synthetic omnidirectional RX power, (b) synthetic-omni directional DS, (c) ASD, and (d) ASA.

in Fig. 4.41b. While the DS is highly correlated at mm-waves, the 6.75 GHz band exhibits divergent values in the positions that are not LOS. Example is the Position 5, in which a late strong reflection at with approx. 120 m is within the dynamic range at 6.75 GHz, but not at 60 GHz. The opposite happens in Position 3, in which the Path 3 is visible within the dynamic range only at the mm-waves, but not at 6.75 GHz.

Analysis of Large Scale Parameters

The evolution of the RX power during the transition from LOS to NLOS in the corner scenario can be observed in Fig. 4.41a. The synthetic omnidirectional power is normalized to the Position 1b, including all the parked vehicles in the environment. Therefore, there is a slight increment in the power from Position 1a to Position 1b, being this increment higher at the 60 GHz band. The dynamics of the RX power are similar in the different bands, with a maximal accumulative loss (path-loss plus blockage by building loss) of 17.32 dB at 60 GHz and approx. 14 dB at 6.75 GHz and 30 GHz. These values are similar to the ones measured under vehicle blockage in [86].

Fig. 4.41c shows that there is no clear relation between the DS and the carrier frequency. However, there is a higher correlation within the mm-wave bands. We can observe an increment on the DS from the Position 1a to Position 1b due to the strong reflection on the Parked Vehicle 2 observed in Fig. 4.55. Position 3 shows a larger DS at mm-waves because of the late reflection in Building D, which falls within the dynamic range at mm-waves, but not at sub-6 GHz, visible in Fig. 4.39. On the other hand, the DS is larger at sub-6 GHz in the Position 5 because the Path P5.1 (double reflection in Building A and Building B) is stronger at sub-6 GHz. In addition, Path P5.2, double reflection Building B and C visible in Fig. 4.38, is within the dynamic range only at sub-6 GHz.

The ASD and ASA for the different positions is displayed in Fig. 4.41c and Fig. 4.41d, respectively. The ASD is very similar between Position 1a and Position 1b, since the reflection from the Parked Vehicle 2 falls within the LOS scanning step. However, we can observe that the ASD increases when the RX goes to NLOS. This is mostly because the strongest scatterers are the diffracted LOS and the reflections from Building B, which are separated around 120°

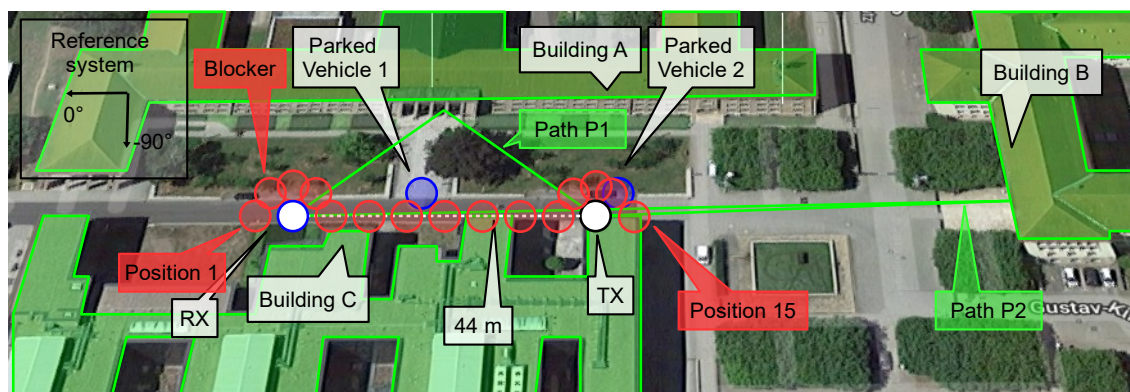


Figure 4.42: Overtaking scenario in an urban environment.

in the angular domain. On the other hand, at the RX, the ASA is quite constant because most of the paths come from the azimuth direction 150° (reflections from Building B and diffracted LOS).

4.6.3 Overtaking in Urban Scenario

This scenario emulates two vehicles communicating to each other at a fixed distance of 44 m when a third vehicle (blocker) starts an overtaking action to both of them, as shown in Fig. 4.42. It is worth to mention, that in this emulation, only the blocker is time dependent, however, in reality also the environment is time dependent.

Following a similar approach that in the corner scenario, we have measured the environment as Position 0a, 0b, and 0c, in which there were no parked vehicles and then we added sequentially the surrounding Parked Vehicle 1 and 2. The measurements were repeated with the same TX and RX positions using two different blocker vehicles: a passenger vehicle and a pick-up truck.

Environment Characterization

The multi-band PDP with some scatterers identified in the time domain is shown in Fig. 4.43, in which a rich multipath environment can be seen in the different bands. Most of the relevant scatterers are present in the 6.75 GHz and mm-waves bands. Furthermore, a far and late reflection in the Building B (named as Path P2 in Fig. 4.42) is also observed in the different bands. The strongest component apart from the LOS is a cluster from Building A, indicated as Path P1 in Fig. 4.42. The influence of the blocker in the rise and fall of these clusters is analysed in the following sub-section.

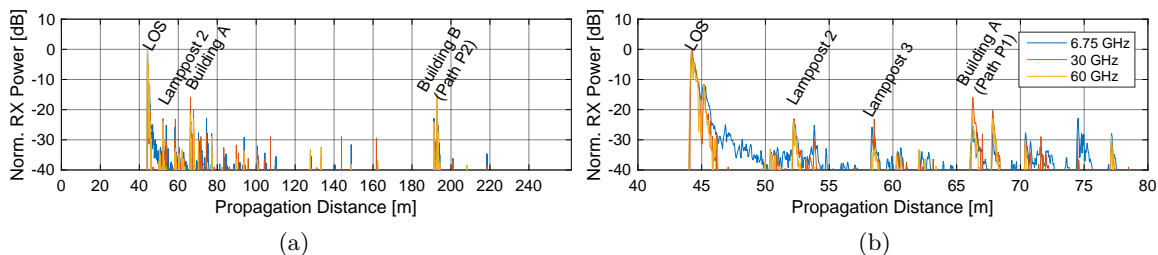


Figure 4.43: Measured multi-band PDP in the overtaking scenario for Position 1c (a) complete, and (b) detail.

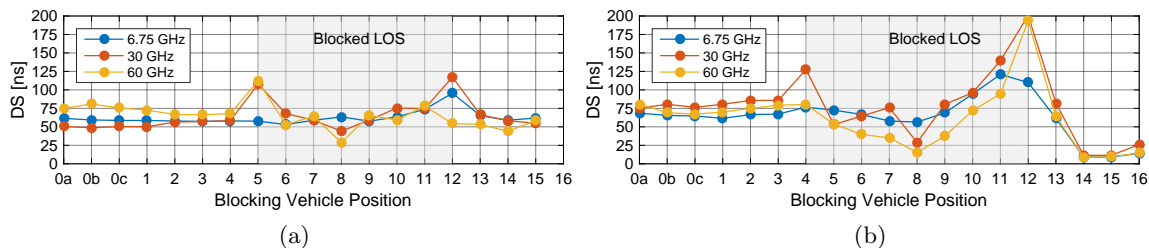


Figure 4.44: Multi-band DS from measurements in overtaking scenario with blocker being (a) passenger car, and (b) pick-up truck.

Analysis of Large Scale Parameters

The variation of the LSPs during the different positions of the blocking vehicles (passenger and pick-up truck) are shown in Fig. 4.44, Fig. 4.45, and Fig. 4.46. The influence of the blocker size shows that with the pick-up truck the DS and angular spreads are larger than with the passenger vehicle.

It is worth to notice, that under blockage, when the blocker is in the middle between the TX and RX, the DS is shorter than in LOS. This is because the blocker interrupts the late reflections from the Building B, which are present in LOS. In addition, most of the transmission is by diffraction over the blocker. Therefore, as observed in Fig. 4.47, the obstructed LOS component is stronger in comparison to all the other positions of the blocker.

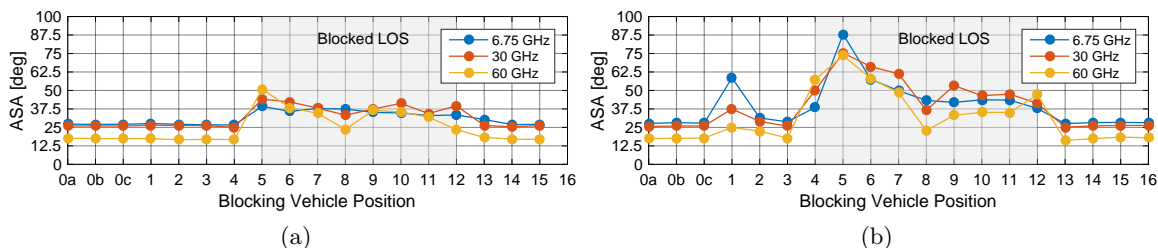


Figure 4.45: Multi-band ASA from measurements in overtaking scenario with blocker being (a) passenger car, and (b) pick-up truck.

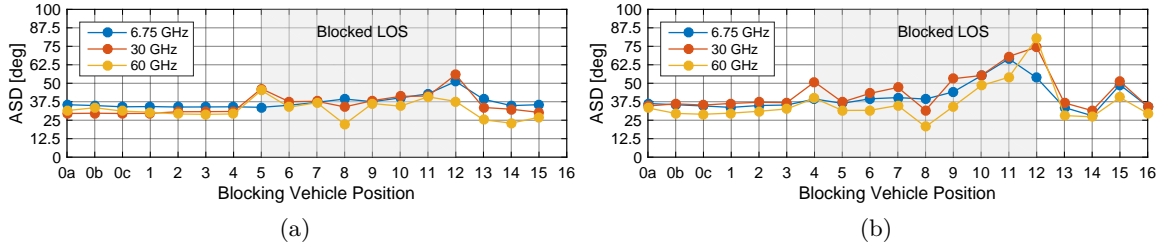


Figure 4.46: Multi-band ASD from measurements in overtaking scenario with blocker being (a) passenger car, and (b) pick-up truck.

Table 4.18: Multi-band large scale parameters in V2V overtaking scenario^a.

Band	NLOSv Passenger Vehicle						NLOSv Pick-up Truck					
	DS		ASA		ASD		DS		ASA		ASD	
	Mean	Std.	Mean	Std.	Mean	Std.	Mean	Std.	Mean	Std.	Mean	Std.
6.75 GHz	65.46	13.62	35.84	2.17	39.62	5.48	80.51	22.88	49.35	15.70	46.04	10.13
30 GHz	75.68	24.98	38.79	3.76	41.52	6.81	96.33	52.26	53.12	12.40	51.24	13.70
60 GHz	64.40	23.85	34.36	8.72	35.93	6.62	69.06	52.91	45.69	15.72	41.78	17.51

^aWith 30° HPBW scans at TX and RX.

The mean and standard deviation of the LSPs are summarized in Table 4.18.

Blockage Loss

The dynamics of the shadowing of the different clusters at 60 GHz during the overtaking action can be observed in Fig. 4.47 for the passenger vehicle and pick-up truck. Due to the size of the blocker, the LOS shadowing starts in Position 5 with the passenger vehicle, and in Position 4 with the pick-up truck. In addition, scatterers as Building A are shadowed during a longer period of time with the larger blocker. Moreover, the influence of the Parked Vehicle 1 is also observed in the Position 1b.

The pick-up truck also obstructs completely the back reflection from Building B. Therefore, the DS on the blocker position 14 to 16 is shorter compared to the passenger vehicle, as seen in Fig. 4.44.

The blockage loss in the overtaking scenario is shown in Fig. 4.48. All the curves are normalized to the Position 1c (environment with parked vehicles but without blocking vehicle). A larger loss is observed when the blocker is closer to the RX or to the TX. The blockage loss increases with frequency. However, when the blocker is in the middle, with the same TX and RX distance to the blocker, the losses are similar in the different bands.

The loss depends on the size of the blocker. With the passenger vehicle as a blocker, a maximum loss of approx. 11 dB is measured at 60 GHz, 9 dB at 30 GHz, and 7 dB at 6.75 GHz. On

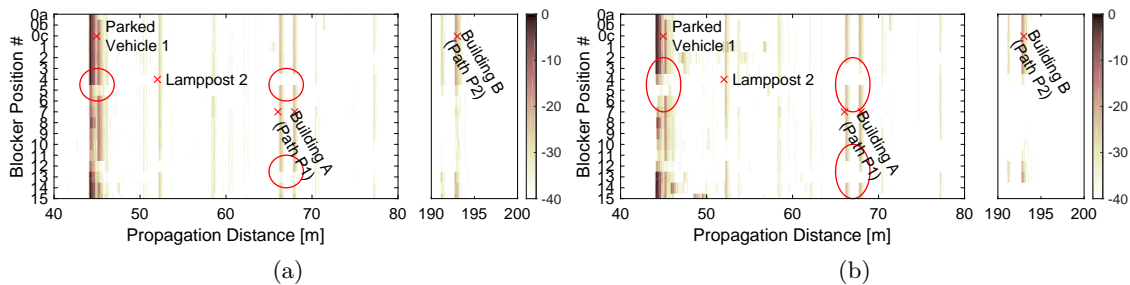


Figure 4.47: PDP during the different blocker positions at 60 GHz with (a) passenger vehicle, and (b) pick-up truck.

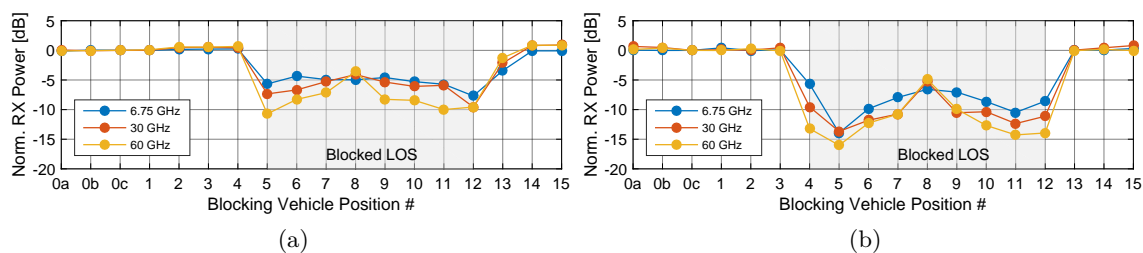


Figure 4.48: Multi-band synthetic omni-directional blockage loss with (a) passenger vehicle, and (b) pick-up truck.

the other hand, with the pick-up truck, these losses increase to 16 dB at 60 GHz and 14 dB at 30 GHz and 6.75 GHz. It is worth to remark that this is the isotropical loss. Communication systems at mm-waves will rely on high gain antennas with a reduced beam-width, therefore, losses are expected to be higher within a single beam, as reported in [82].

4.6.4 Approach Under Blockage in Urban Scenario

In this scenario, the TX was located in a fixed position over the pavement emulating a vehicle, and 9 different RX positions separated 5 m were measured emulating another vehicle approaching to it. The measurements were repeated with a blocking vehicle (pick-up truck) between the TX and RX. In addition, static vehicles were also located in the environment to

Table 4.19: Multi-band blockage loss in V2V overtaking scenario^a.

Band	NLOSv Passenger Vehicle		NLOSv Pick-up Truck	
	Mean	Std.	Mean	Std.
6.75 GHz	4.77	2.12	7.87	3.63
30 GHz	5.54	2.71	9.50	4.13
60 GHz	7.26	3.61	10.81	4.84

^aFrom synthetic omni-directional characteristics with 30° HPBW scans at TX and RX.

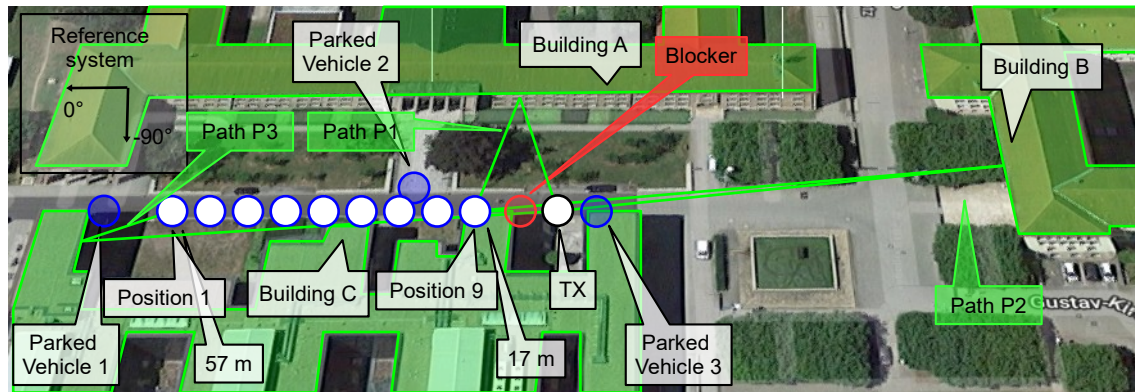


Figure 4.49: Approach under blockage in V2V scenario.

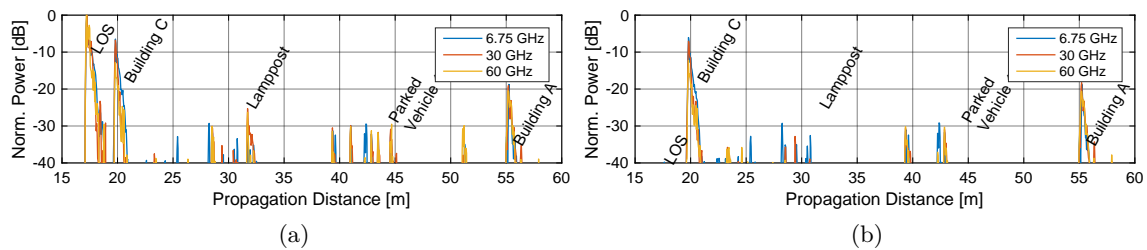


Figure 4.50: Measured multi-band PDP in the approach scenario at Position 9 (a) without blocker, and (b) with blocker.

study the influence of other cars on the street. The schematic of the campaign is shown in Fig. 4.49.

Environment Characterization

A detail of the measured multi-band PDP in the Position 9 with and without blockage is shown in Fig. 4.50. Multiple scatterers can be identified in the different bands. The strongest, apart from the LOS, are Building C and Building A (indicated as Path P1 in Fig. 4.49), which remain unblocked in Fig. 4.50b.

The per-position normalized multi-band PDP without and with blockage are displayed in Fig. 4.51. In the LOS case, the strong LOS component makes that few scatterers are observed within the 40 dB dynamic range. On the other hand, under blockage, more scatterers appear within the same dynamic range. Some of these scatterers are the side reflections in Building C and Building A (Path P1). Also, a back reflection in Building C is also observed as Path P3. The late reflection in Building B is also observed within the dynamic range. However, this is obstructed by the blocker when the RX is closer to the TX in NLOS_v. Therefore, the DS tends to increase with TX-RX distance, as later observed in Fig. 4.53a and Fig. 4.53d.

The location of the scatterers in the angular domain in different RX positions in LOS and NLOS_v can be observed in the power bi-azimuth profile in Fig. 4.52. While the power-bi-

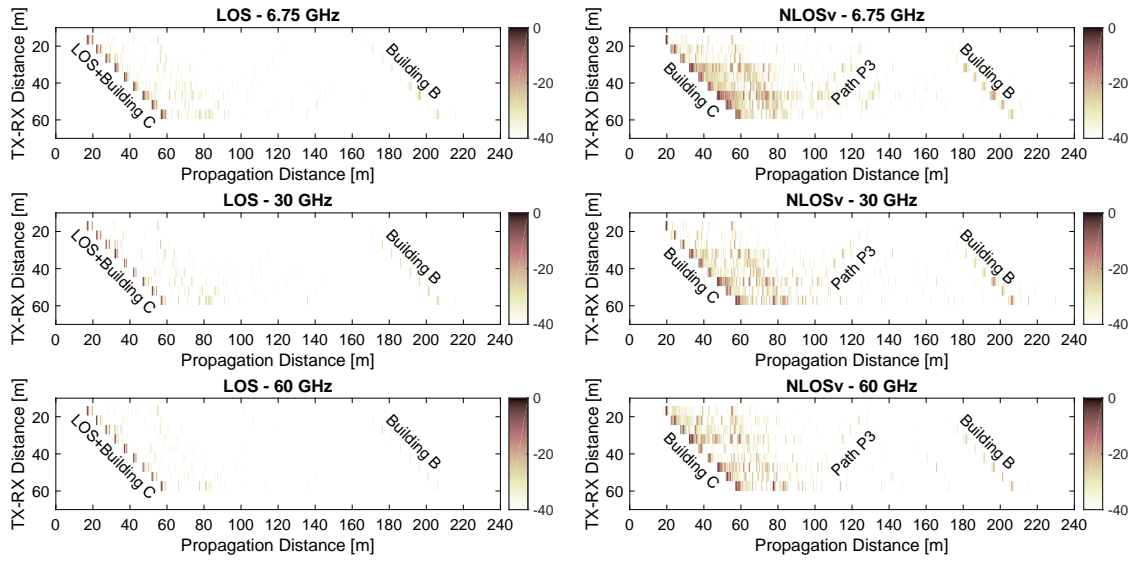


Figure 4.51: Per-position normalized multi-band PDP in the approach scenario in LOS and NLOSv.

azimuth profile is relative static over the different RX positions in LOS, a high dynamics can be observed in NLOSv. This is also observed in the angular spreads in Fig. 4.53.

Analysis of Large Scale Parameters

The multi-band DS estimated from measurements in LOS and NLOSv are displayed in Fig. 4.53a and Fig. 4.53d, respectively. Larger values can be observed in NLOSv compared to LOS. There is a trend of increasing spreads with increasing TX-RX distance.

The ASA and ASD in LOS and NLOSv are presented in Fig. 4.53. No large variations of ASA and ASD over TX-RX distance were observed in LOS. There is a slight increment of ASA with increasing TX-RX distance. This is due to the Path P3, which becomes stronger while the RX moves away from the TX. On the other hand, except in some positions at 6.75 GHz, the ASD is relatively constant over distance.

The angular spreads increase considerably under NLOSv. This is the result of the severe attenuation of the LOS cluster in the different positions, which makes that the MPCs become the dominant contributors of the energy at the RX. The ASA decreases with increasing TX-RX separation, since the main scatterers are the side buildings. Hence, the incident angles also decrease with larger TX-RX distance. On the other hand, it can be observed a trend of increasing ASD with TX-RX distance in NLOSv. This is due to the scattering from Building B (opposite to the blocked LOS), which is more attenuated due to the blocker when the RX is closer to the TX.

The mean and standard deviation of the different LSPs under LOS and NLOSv in this scenario are summarized in Table 4.20.

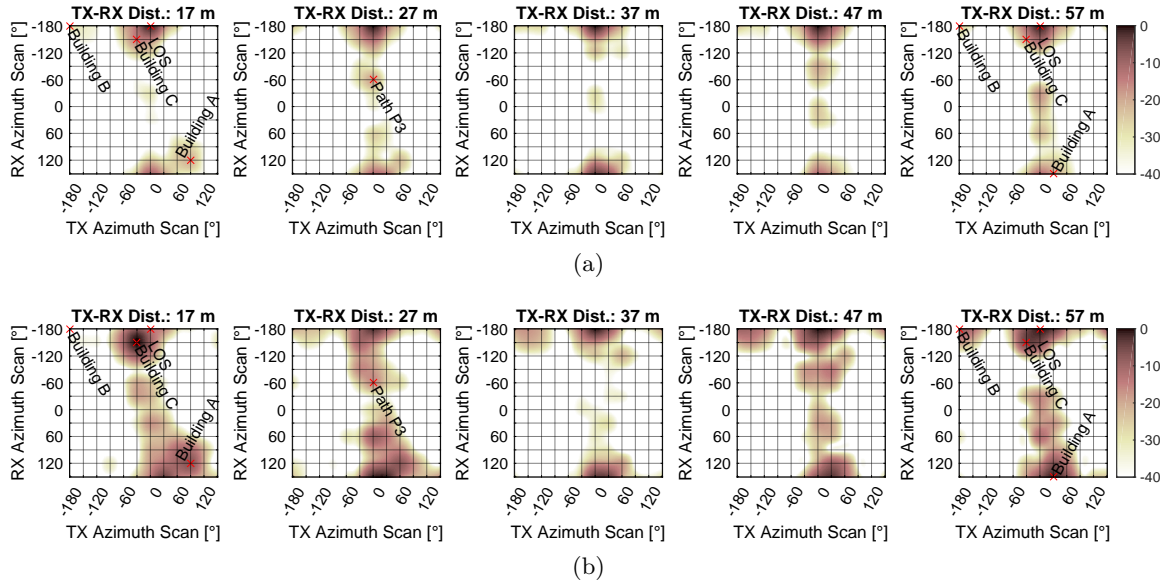


Figure 4.52: Measured power bi-azimuthal profile at 60 GHz in the approach scenario (a) without blocker, and (b) with blocker.

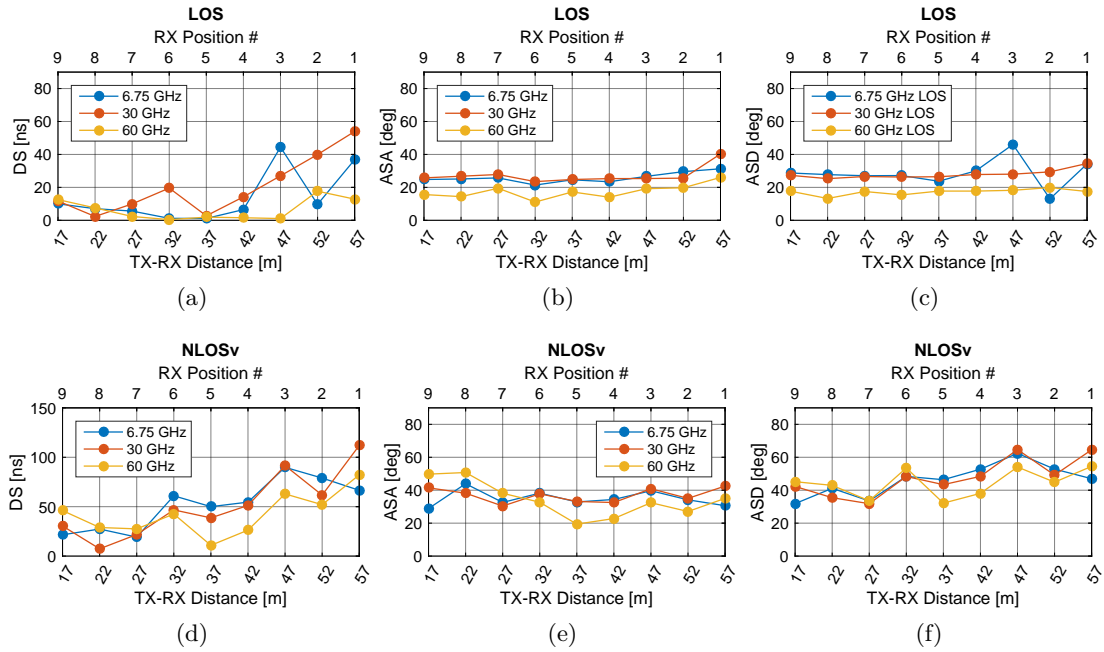


Figure 4.53: Multi-band large scale parameters from measurements in approach scenario: (a) DS, (b) ASA, and (c) ASD without blocker, and (d) DS, (e) ASA, and (f) ASD with blocker in NLOSv.

Table 4.20: Multi-band large scale parameters in V2V approach scenario^a.

Band	LOS						NLOSv					
	DS		ASA		ASD		DS		ASA		ASD	
	Mean	Std.	Mean	Std.	Mean	Std.	Mean	Std.	Mean	Std.	Mean	Std.
6.75 GHz	26.55	27.27	27.06	3.51	31.22	8.83	52.12	25.18	35.03	4.75	46.24	9.66
30 GHz	52.60	60.55	30.20	6.86	35.09	13.12	51.28	33.20	36.88	4.32	47.56	11.32
60 GHz	15.90	18.16	20.07	6.07	18.97	3.65	42.15	21.69	34.23	10.83	44.32	8.58

^aFrom synthetic omni-directional characteristics with 30° HPBW scans at TX and RX.

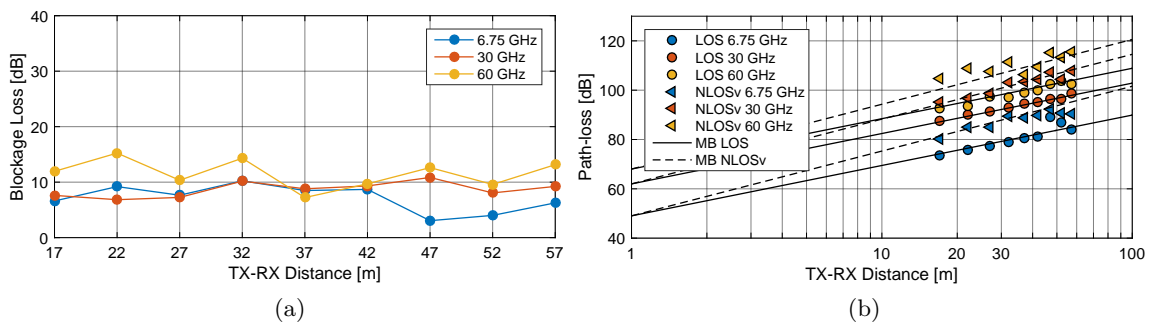


Figure 4.54: Multi-band (a) blockage loss and (b) path-loss from measurements.

Empirical Multi-band Path-loss and Blockage Loss

The blockage loss displayed in Fig. 4.54a is calculated as the difference on isotropical power between the measurement in LOS and NLOSv. A relative constant loss for the different TX-RX distances is observed in the different bands. However, when the RX is closer to the blocker (RX closer to TX), the loss is larger at 60 GHz.

The mean and standard deviation of the blockage loss are summarized in Table 4.21. In average, the blockage loss increases with frequency. A mean value of approx. 11 dB is estimated at 60 GHz, which is similar to the overtaking scenario with pick-up truck, presented in Table 4.19.

The empirical per-band and multi-band path-loss is displayed in Fig. 4.54b, and the parameters for the CI model summarized in Table 4.21. The PLE in LOS in the different bands was ≈ 2 and larger than 2.5 in NLOSv.

4.6.5 Vehicles in the Environment

The influence of the vehicles in the environment has been analysed based on the different measurement campaigns. In the corner scenario, if we compare the PDPs and angular profiles of the Position 1a and Position 1b (without and with parked vehicles in the environment),

Table 4.21: Multi-band path-loss parameters and blockage loss from measurements in V2V approach scenario^a.

Band	LOS		NLOSv		Blockage Loss	
	n	σ_X	n	σ_X	Mean	Std.
6.75 GHz	2.07	2.27	2.52	1.58	7.13	2.39
30 GHz	2.06	0.41	2.62	1.19	8.68	1.35
60 GHz	2.00	0.87	2.74	2.73	11.56	2.56
Multi-band	2.04	1.52	2.63	2.36	N/A	N/A

^aFrom synthetic omni-directional characteristics with 30° HPBW scans at TX and RX.

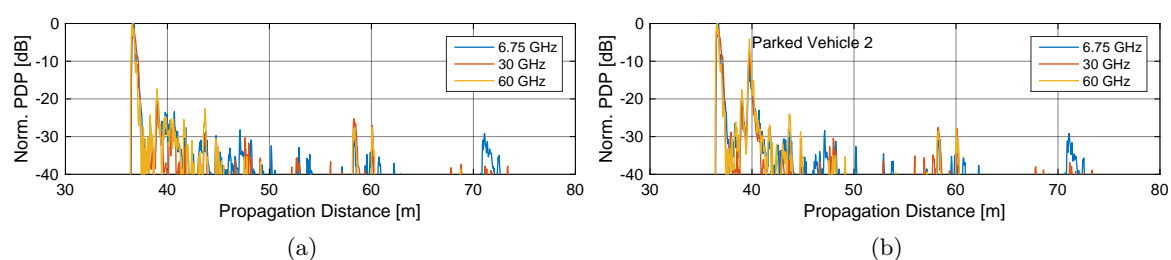


Figure 4.55: Multi-band measured PDP in the corner scenario in (a) Position 1a (without parked cars) and (b) Position 1b (with parked car).

we can clearly identify “Parked Vehicle 2” from Fig. 4.38 in the power profiles in the different frequencies. In this particular case, as seen in Fig. 4.55, the reflection seems to be specular, and therefore, relatively strong compared to the LOS (approx. -3 dB). A similar analysis has been conducted in the overtaking in urban scenario, in which the “Parked Vehicle 1” was observed with approximately -11 dB power compared to the LOS.

In other scenarios, the reflections on surrounding vehicles were not significantly strong, mostly due to the impinging and reflected angles and the scattering properties of the vehicles.

4.7 Conclusions

In this chapter, we have presented several measurement campaigns and results in different frequency bands. We have separated the results covering multiple verticals of 5G. The main objective was to identify common propagation aspects to be addressed in SCMs targeting correlated multi-band channels and high resolution communications systems.

In the item level characterization section, we have focused on polarization and the nature of specular or diffuse scattering. The objective was to study the scattering properties of different objects that could be isolated from the environment by the utilization of narrow beam systems. We have observed that, as predicted by Fresnel, the specular reflected power depends on the polarization and incident angle of the impinging wave. Therefore, clusters

exhibit a polarimetric selective behaviour and more accurate modelling concepts need to be implemented in SCM to avoid overestimation on polarization and spatial diversity.

Indoor measurements have shown a large influence of the environment on the spreading profiles and parameters. The polarimetric power of the clusters depends on the orientation of the scatterers. Therefore, spatial diversity is linked to the polarization. The main scatterers are traceable during the displacement of the RX, showing the importance of spatial consistency for simulation of mobility and localization.

Outdoor measurements in a street canyon scenario in different locations have also shown a clear influence of the architecture and dimensions of the environment on the spreads and power profiles. Ground reflections were also identified as significant contributing components in the link budget.

In vehicular scenarios, we have observed that the vehicles in the environment generate two different effects: they act as blockers of scatterers and they also generate scattering. Obstruction losses in different scenarios have shown a dependence of the loss on the size of the blocker and frequency. Specially, when the TX or RX are closer to the blocker. Different scenarios have shown that the LSPs also are affected differently depending on the blocker size.

In all the scenarios, the LSPs exhibited a high correlation over frequency. This correlation is further studied in Section 6.4.1.

Part II

Influence of System Aspects and Multi-band Channel Modelling Components

5 Influence of System Aspects on Performance and Modelling

“It is better to burn out than to fade away.”

A Canadian musician.

Overview

In this chapter we investigate empirically the influence of mm-wave and sub-THz system aspects in the performance of communication systems. The effect of directivity in DS is shown by analysing the measurements in complex scenarios introduced in Chapter 4. The DS obtained with directive antennas is compared to the results obtained under the assumption of isotropic antennas (omni-directional patterns synthesised from directive scans), showing a clear trend of a reduction on DS with increasing directivity. On the other hand, the theoretical studies of fading introduced in Appendix B is empirically contrasted with a particular measurement set-up. The effect of directivity and bandwidth in the distribution of the amplitude and power shows a clear trend of less stochastic behaviour of the channel when the resolution of the communication system is increased. In addition, the effect of isolating MPCs with directivity are analysed in the Doppler domain, showing that with increasing directivity the Doppler frequency tends to introduce a shift rather than a spread in the signal.

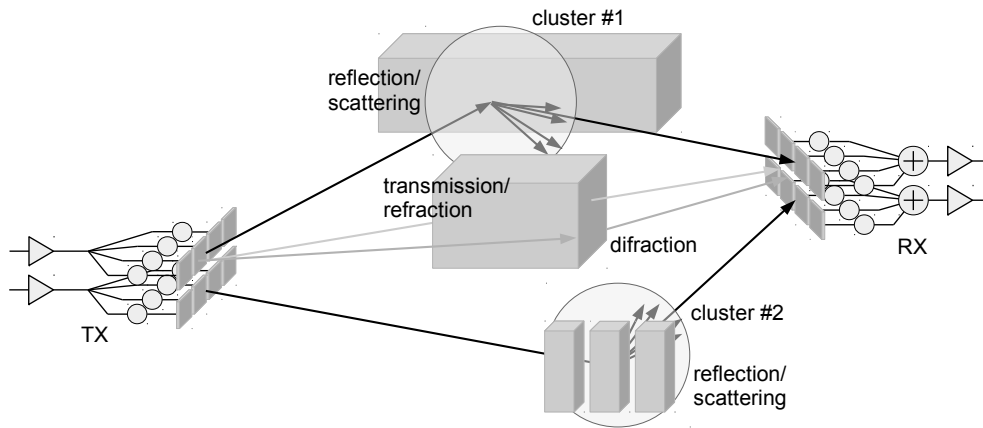


Figure 5.1: Hybrid beam-former with two beams pointing at two clusters. Depending on the directivity, the number of relevant MPC within the cluster.

5.1 Introduction

As previously discussed in the introduction, the major differences between sub-6 GHz and mm-wave communication systems are the directivity and bandwidth. At sub-6 GHz frequencies, low directive antennas are directly connected to the digital interfaces making that each of them samples a quasi omni-directional channel, allowing the digitization of a radio channel which is closer to the isotropical propagation channel (see Fig. 1.3). Therefore, each digital interface observes the interaction of all the MPCs in the propagation channel.

In the traditional narrowband stochastic channel modelling approach for systems with lower directivity, multiple paths arrive with uniformly distributed strength and azimuth of arrival (AoA) in rich scattering environments in NLOS. In addition, with a smaller bandwidth these paths are combined constructively or destructively depending on their relative phases, leading to small-scale fading. Therefore, the absolute value of the RX signal tends to follow a Rayleigh distribution as described in Chapter B. On the other hand, with one dominant strong path in LOS scenarios, the distribution of the absolute value of the amplitude tends to follow a Rician distribution, in which the ratio of deterministic (or constant value) to random (or variable) components is determined by the so called Rician K -factor.

A similar approach is addressed in broadband SCMs as WINNER II [12], COST 2100 [13], and METIS [87]. These models target systems with angular and time-delay resolution provided by antenna arrays and broader bandwidths, respectively. However, the time-delay resolution is still low. Consequently, the scatterers are modelled as zero DS clusters: the sum of an arbitrary number of unresolvable paths with random phases in the time-delay domain. This summation leads to the per-cluster small-scale fading. These models fit very well the propagation and system characteristics at sub-6 GHz: rich scattering environment with multiple reflections, low directivity, and short bandwidths.

On the other hand, as shown in Fig. 5.1, the utilization of beam-forming to counteract path-loss filters out multiple clusters. Therefore, the digital interface at mm-wave observes a spatial pre-filtered channel, what is also widely denominated as a sparse channel. This affects the

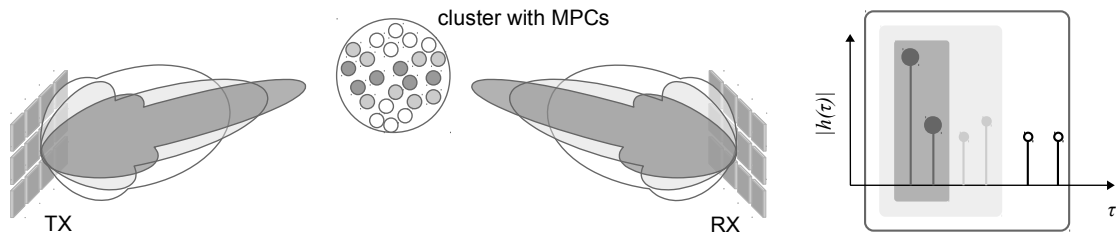


Figure 5.2: Influence of directivity on the intra-cluster number of receiving paths.

large-scale and small-scale parameters. The former ones by removing the influence of multiple scatterers in the link budget, in the DS, and in the Doppler spread. The latter ones, by changing the distribution of the envelope and increasing the influence of deterministic paths. As shown in Fig. 5.2, the MPCs arriving from the beam pointing direction are stronger than the other ones. Furthermore, with larger bandwidths, these paths are resolved in the time-delay domain and they are not randomly combined any more in different positions, reducing the small-scale fading and creating the same conditions for a Rician distribution in the signal amplitude, even in NLOS scenarios. Experimental results using larger bandwidths (800 MHz null-to-null) and directive antennas in outdoor measurements at 28 GHz have shown that the distribution of the signal envelope fits better to a Rician rather than to a Rayleigh distribution, [88]. Similarly, [89] shows that that fit is even better to the two-wave with diffuse power (TWDP) distribution. We have presented similar investigations in indoor scenarios in [90], in which the influence of bandwidth on the Rician K -factor and fade depth is analysed for different scatterers at 30 GHz, showing also a significant deterministic fading behaviour of the channel. Moreover, we have also presented in [91] results on the effects of the directivity and bandwidth on small-scale fading at 60 GHz, separating the analysis on the influence at tap channel level and on the complete channel. Using the same data-set, we continue and extend the analysis in Section 5.3.

In the following Sections, we analyse the influence of directivity and bandwidth in the large and small-scale characteristics of the channel. We start analysing the difference on the DS when isotropic or directive antennas are used. For this, we utilize the results from the previous chapter, and re-calculate DS by selecting the scanning direction that delivers the maximal energy between the TX and RX. On the other hand, small-scale fading needs sampling the channel in at least $\frac{\lambda}{2}$ intervals. Therefore, we introduce a special set-up to evaluate the influence of the system aspects on the fading in the different domains.

5.2 Influence of mm-Wave System Aspects on Delay Spread

The effect of directivity on DS is analysed by the ratio of DS with wide patterns (isotropic in the extreme case, SO) to DS with directive antennas (beam-steering, BS) per i^{th} measured position:

$$R_{\text{DS},i} = \frac{\text{DS}_{\text{SO},i}}{\text{DS}_{\text{BS},i}}. \quad (5.1)$$

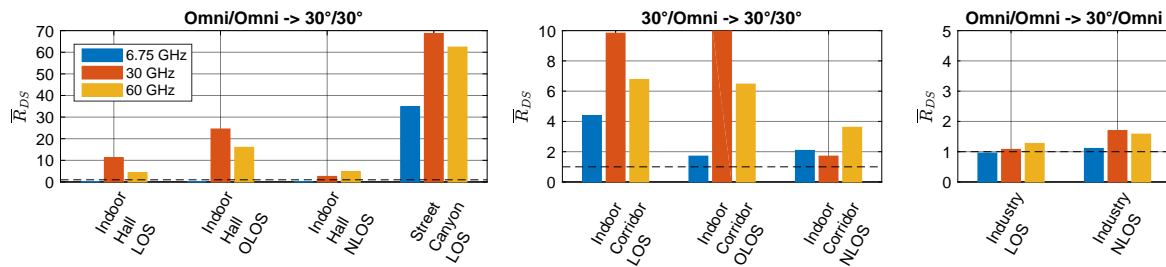


Figure 5.3: Influence of directivity on DS in the measured scenarios and visibilities.

Since this ratio is per-link, and we have measured multiple links per-scenario, we utilize the mean $\bar{R}_{DS} = \frac{1}{N} \sum_{i=1}^N R_{DS,i}(d)$. The results for the different TX and RX directivities, and separated in the different scenarios and visibility conditions, are shown in Fig. 5.3. This ratio is always larger than one, meaning that the DS with isotropic antennas is, in average, larger than with directive antennas. The larger ratio is obtained from TX and RX isotropic conditions to TX and RX beam-steering conditions (first plot in Fig. 5.3), when the change on the directivity is maximal. Furthermore, the ratio is smaller when the directivity is applied at the TX than when it is applied at the RX (second and third plot in Fig. 5.3). In this case, this is due to the back reflections in the environment that are not filtered out by the RX.

5.3 Influence of mm-Wave System Aspects on Small-Scale Parameters

Small-scale fading occurs in the magnitude of wavelengths. Therefore, we have conducted a very precise measurement set-up at 60 GHz in which the TX was located in a fix position, with a high directive antenna with 15° HPBW pointing to a plaster wall. On the other side of the link, the RX was located in an automatic positioner and displaced over $\lambda/2$ steps, as shown in Fig. 5.4. The displacement was in the opposite direction of the specular reflection in the wall. The alignment of the antennas was checked with laser pointers in order to keep the main beam towards the direction of the specular reflection in the wall during the displacement.

Different antennas with directivities from omni to 15° were used at the RX. While the null-to-null measurement bandwidth after calibration was 5.1 GHz, the effect of different bandwidths were later analysed by reducing it in a post-processing step. Finally, as a reference, the measurements were repeated with omni antennas at the TX and RX generating a LOS component. Details on the set-up are summarized in Table 5.1.

This set-up emulates, firstly, movement of the RX in the measurable Doppler range, and secondly, the behaviour of a communication system utilizing high directive radio-interfaces, which can be the result of beam-forming. The objective is to study the effects of high resolution (bandwidth and directivity) in the different domains (frequency and time).

In addition, we have conducted simulations of the main reflection in the wall and the LOS component using deterministic equations in Matlab. They are used as a reference to interpret



Figure 5.4: Measurement set-up for cluster-level fading investigations at 60 GHz.

Table 5.1: Directivities in cluster-level fading investigations at 60 GHz.

TX Directivity	TX Directivity	Visibility
Omni V	Omni V	LOS
HPBW 15°	Omni V	NLOS
HPBW 15°	HPBW 30°	NLOS
HPBW 15°	HPBW 15°	NLOS

the results in the spatial and delay domain. Due to the complexity of the scenario, only the specular reflections in the wall and the LOS were determined and the analysis has been done separately for the LOS components and reflections.

5.3.1 Signal Model

Under the assumption of constant displacement velocity v of the RX, there is a linear relation between the measurement time t and position on the track $x = \{0, \frac{\lambda}{2}, \dots, m\frac{\lambda}{2}, \dots, (T-1)\frac{\lambda}{2}\}$ given by $v = \frac{x}{t}$, where T is the total amount of snapshots. Therefore, from now on we refer indistinctly to the time domain or position on the track. Let us analyse the sampled time variant radio-channel impulse response at the m^{th} time instant as the summation of k samples

$$\hat{h}(t, \tau) = \sum_m \sum_k \sum_l \underbrace{\mathbf{g}_R^T(\Omega_{A_l}) \mathbf{\Gamma}_l \mathbf{g}_T(\Omega_{D,l})}_{a_l} e^{-j2\pi\nu_l m \Delta t} \delta(\tau - k\Delta\tau - \tau_l) \delta(t - m\Delta t) \quad (5.2)$$

where $a_l \in \mathbb{C}$ is the l^{th} antenna weighted path, $\mathbf{g}_R(\cdot)$ and $\mathbf{g}_T(\cdot)$ are the 3D antenna (emulated beam-forming) patterns at RX and TX, respectively, and $\mathbf{\Gamma}_l \in \mathbb{C}^{2 \times 2}$ is the polarimetric path amplitude matrix described in (A.24) (see Appendix A.2.1 for more details). The amplitude of the k^{th} tap in the m^{th} position is the sum of L_k paths arriving within the time-delay range $\{(k-1)\Delta\tau, k\Delta\tau\}$. Depending on their relative phases, they may combine constructively or destructively, as shown in Fig. B.2. These variations on the channel tap introduce small-scale fading.

The number of paths L_k within each k^{th} tap depends on the angular resolution and bandwidth given by $\Delta\tau = 1/\text{BW}$. With high directive beam-forming, several paths are filtered out and $L_k \downarrow$. It is also intuitively to see that when $\text{BW} \uparrow \rightarrow \Delta\tau \downarrow$, and vice versa. A direct consequence is that by increasing the bandwidth of the system ($\text{BW} \uparrow$), we are increasing the delay domain resolution of the system ($\Delta\tau \downarrow$), and the number of path interacting in a single resolvable delay bin reduces, $L_k \rightarrow 1$ (or 0 if there are no paths on the k^{th} bin).

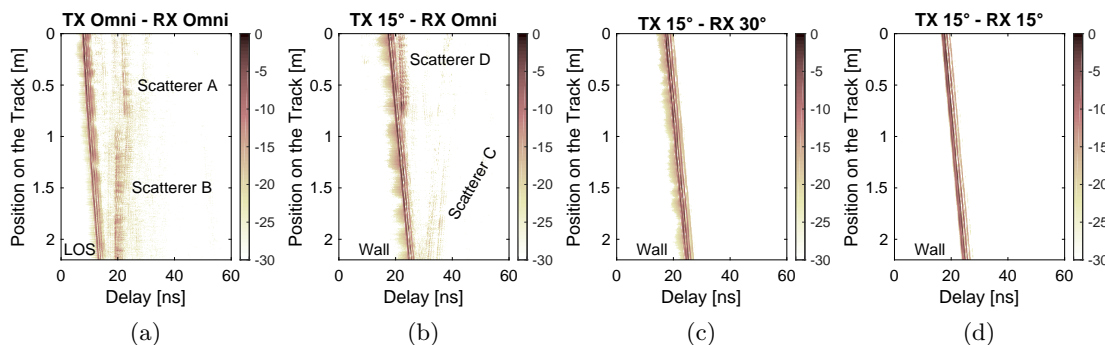


Figure 5.5: Normalized power (in dB) of the time variant impulse response of the channel during displacement with 2 GHz bandwidth for (a) TX and RX omni, (b) TX 15° and RX omni, (c) TX 15° and RX 30°, and (d) TX 15° and RX 15°.

5.3.2 Influence of Directivity in the Time Variant Channel Impulse Response

The evolution of the channel along the track is observed in the RX power $|\hat{h}(t, \tau)|^2$ (squared absolute value of the measured time variant CIR) over the different positions. The results with a bandwidth of 2 GHz and with different directivities at TX and RX are shown in Fig. 5.5. A range of 60 ns is displayed to facilitate the identification of the main scatterers in the time-delay domain. From lower to higher directivity, Fig. 5.5 shows the influence on the amount of scatterers that the RX observes in the different positions along the track. The LOS, scatterer A, and scatterer B have been marked in Fig. 5.5a. While LOS and scatterer A move away during time, scatterer B moves in the opposite direction. Therefore, as shown in Fig. 5.9, the former originates a negative Doppler shift and the latter a positive one. In addition, the incident angle of the LOS changes over time, which is also visible in the Doppler signature.

By applying directive antennas at the TX, we can observe that the LOS component and most of the scattering is filtered out in Fig. 5.5b. The only remaining components are the reflection on the wall and scatterer C and D. Finally, by applying directivity at the RX side as well, we can observe that all the MPCs are filtered out in Fig. 5.5c and Fig. 5.5d, remaining only the reflections in the wall. This reflection consists of three different peaks separated approximately 23 cm from each other, probably, from the different layers of the plaster wall. A 2 GHz bandwidth offers a the delay resolution of $\frac{c}{2\text{GHz}} \approx 15\text{cm}$. Therefore, these multiple reflections are isolated and resolved in different taps in the time domain. However, after reducing the bandwidth, these MPCs start combining depending on their relative phases and amplitudes at each position, originating large variations of power from position to position, as seen in Fig. 5.7a.

On the other hand, as (A.14) describes, all these MPCs are combined in the frequency domain at each frequency component with a different phase. Depending on the number of MPCs, a flat or frequency selective channel can be obtained. The time variant frequency response (Fourier transform of Fig. 5.5 in the delay domain) is displayed in Fig. 5.6. The relation between the spread in the delay domain, the number of MPCs, and the selectivity in the frequency domain can be seen by comparing Fig. 5.6d (few MPCs from the reflection in the

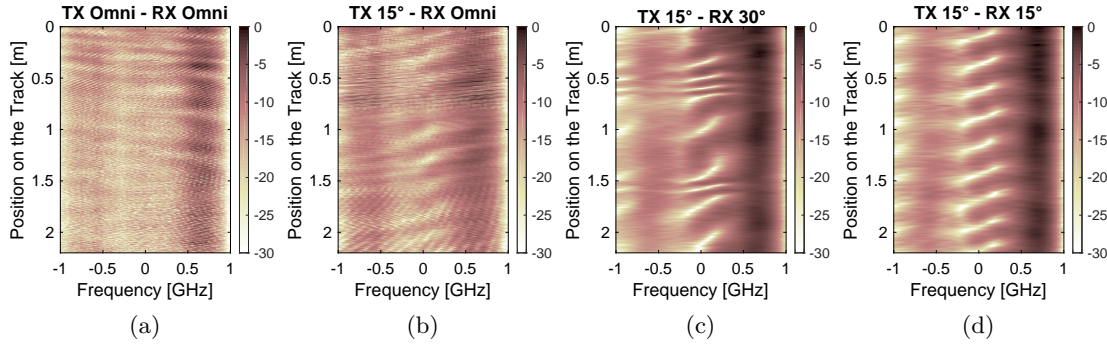


Figure 5.6: Normalized power (in dB) of the time variant frequency response of the channel during displacement with 2 GHz bandwidth for (a) TX and RX omni, (b) TX 15° and RX omni, (c) TX 15° and RX 30°, and (d) TX 15° and RX 15°.

wall) and Fig. 5.6b (many MPCs from the reflection in the wall and other scatterers).

Thus, in the presence of MPCs, every frequency component experiences a change on the amplitude during displacement. However, by considering multiple frequency components (extending the bandwidth), the total RX power tends to be more constant. This is further discussed in the analysis of fade depth.

The normalized total received power $P(t)$ is calculated as the sum of the power contribution in the delay domain or frequency domain, normalized by the overall power along the track:

$$P(t) = \frac{1}{\frac{1}{T} \sum_{\forall t} \sum_{\forall \tau} |\hat{h}(t, \tau)|^2} \sum_{\forall \tau} |\hat{h}(t, \tau)|^2. \quad (5.3)$$

The effects of directivity and bandwidth on fading can be observed in Fig. 5.7. In the first case, Fig. 5.7a shows the total received power (integrated over the bandwidth of 40 MHz) along the track: the variation of power from consecutive positions decreases considerably with an increase on the directivity. On the other hand, if we consider a bandwidth of 4 GHz as shown in Fig. 5.7b, while there is still a tendency of a decreasing RX power variability with increasing directivity, no large differences can be observed.

Similarly, Fig. 5.7c shows the RX power in LOS, using omni-directional antennas at TX and RX and different bandwidths. Also, a clear decrease of fading with increasing bandwidth can be seen. Finally, Fig. 5.7d shows the same result with high directivity at TX and RX.

This shows that the reduction of fading is originated not only by the filtering effect of the antennas, but also by the increase of bandwidth. In the time domain, it means an increase in the resolution of MPCs. In the frequency domain, it means more frequency components for diversity.

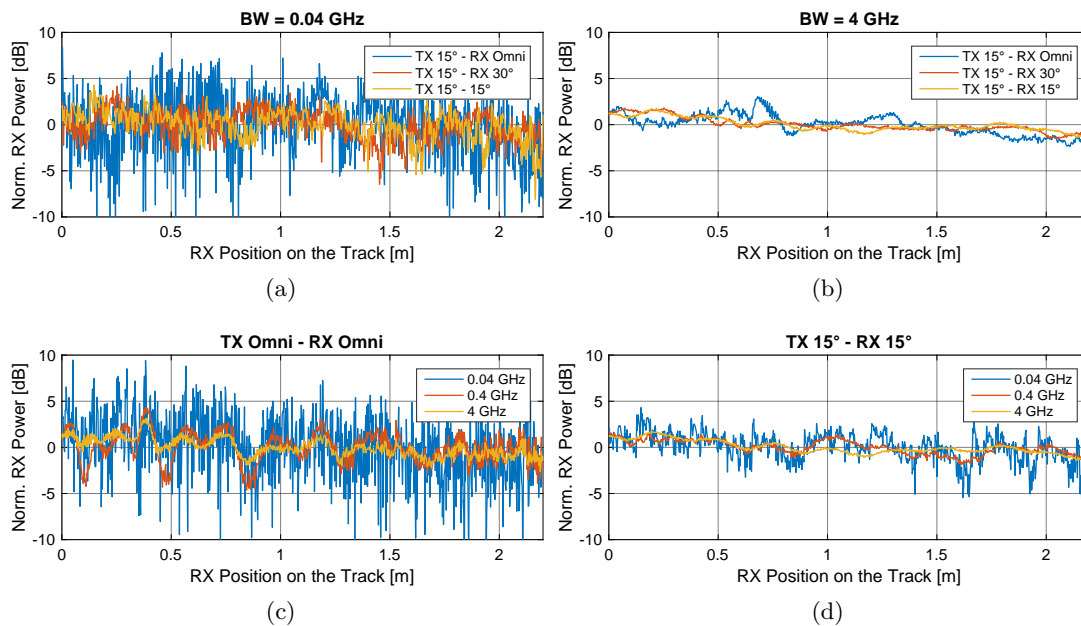


Figure 5.7: Influence of directivity on the RX power with (a) 40 MHz and (b) 4 GHz bandwidth, and influence of bandwidth with (c) omni TX and RX in LOS, and (d) 15° HPBW at TX and RX.

5.3.3 Fading Depth Estimation

The fade depth F_d is defined as the variation of the signal power along the track and it is calculated as the standard deviation σ_P of $P(t)$ expressed in dB, [92].

$$F_d = \sqrt{\frac{1}{T} \sum_{\forall t \in T} \left(P_{\text{dB}}(t) - \overline{P_{\text{dB}}(t)} \right)^2}, \quad (5.4)$$

where $P_{\text{dB}}(t) = 10 \log_{10}(P(t))$, and $\overline{P_{\text{dB}}(t)}$ is the mean value of $P_{\text{dB}}(t)$.

As seen in Fig. 5.6, for a given bandwidth, the fading characteristics along the time depend on the frequency slot we use. Therefore, we extend this analysis by calculating the fading depth with sliding window along the frequency domain. That is, given a certain bandwidth, we calculate the fading along time for the different frequency slots sweeping the complete frequency domain with such a bandwidth. Therefore, Fig. 5.8 shows the ensemble average fade depth $F = \overline{F_d}$, in which a clear trend of decreasing fade depth with increasing directivity or bandwidth, or both, can be observed.

5.3.4 Effects of Directivity on Doppler

The Doppler spectrum is the frequency domain response of the time varying channel. In a simplified model, each path arriving to the RX has a different relative velocity that originates

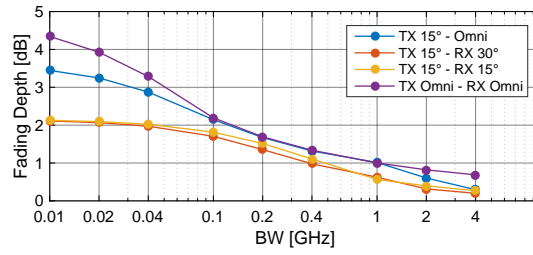
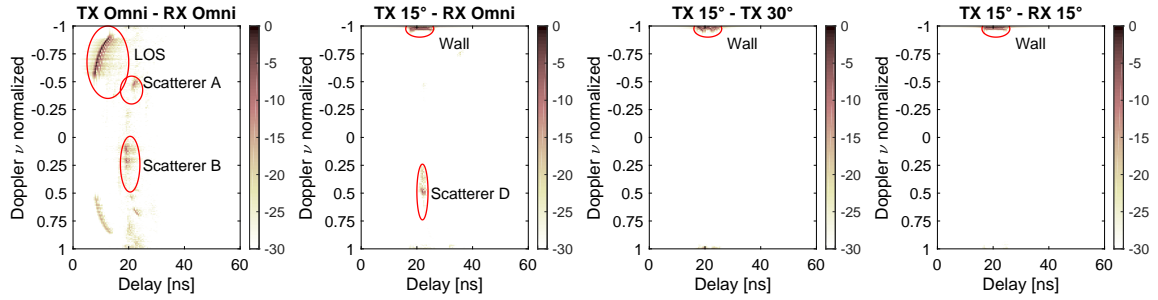


Figure 5.8: Fade depth of the different bandwidths and directivities.

Figure 5.9: Measured Doppler-delay power spectrum $|\hat{h}(\nu, \tau)|^2$ for different directivities at TX and Rx.

a discrete component in the Doppler frequency domain. However, the presence of multiple paths with different directions of arrival and relative velocities, generates several components that increase the complexity of the Doppler spectrum.

The received signal is the convolution of the transmitted spectrum with the Doppler response of the channel. In the presence of a wide Doppler response, the received signal results on a spread spectrum that differs considerably from the transmitted spectrum, as shown in Fig. B.3b. On the contrary, if the Doppler spectrum consists of few components, ideally a single strong component, the receiver sees only a shifted version of the transmitted spectrum.

The Doppler-delay spectrum $|\hat{h}(\nu, \tau)|^2$ of Fig. 5.5 is displayed in Fig. 5.9, in which the aforementioned effect of directivity is observed in the filtering of the MPCs. Therefore, as shown in the Doppler spectrum in Fig. 5.10, we expect to have a reduced Doppler on the radio-channel with directive systems. Instead of a harmful spread resulting from multi-path with a large angular dispersion, the isolation of a single path in the angular domain collapses the Doppler spectrum to a single component originating a shift effect on the Doppler domain. The latest, from implementation perspectives, is much easier to compensate, yet in the analog stage of the transceiver.

5.3.5 Influence on the Distribution of the Envelope

With high resolution in the communication systems, there is a smaller variation on the RX power as shown in Fig. 5.8. Thus, the statistical behaviour of the envelope of the signal in the radio and communication channel changes from Rayleigh to Rician [92], [93], and [90].

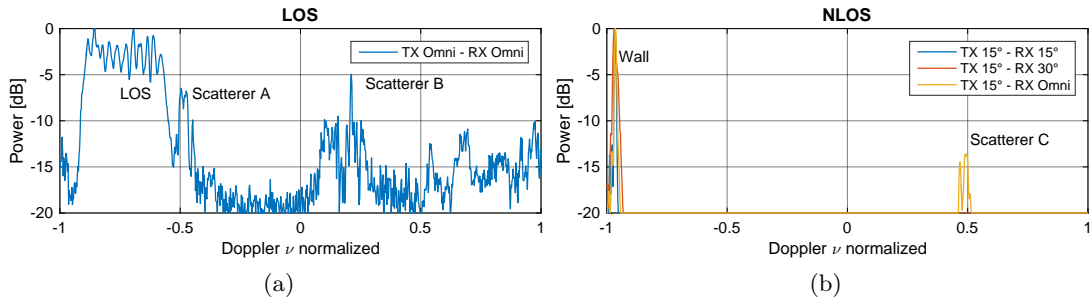


Figure 5.10: Measured Doppler power spectrum $|\hat{h}(\nu)|^2$ for (a) LOS with omni at TX and RX, and (b) NLOS with 15° at TX and different directivities Rx.

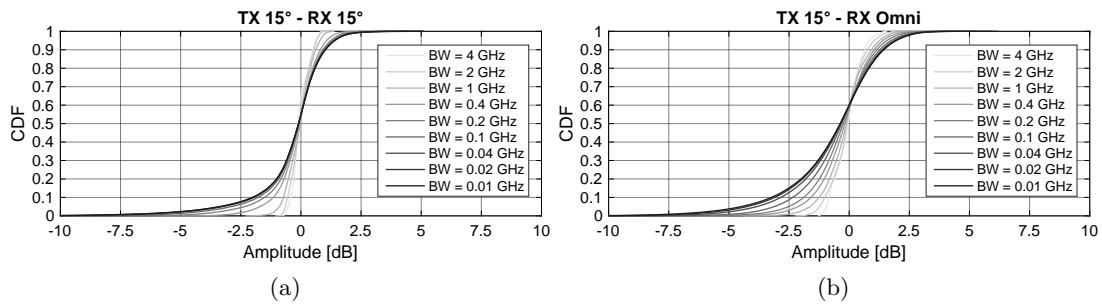


Figure 5.11: Signal level distribution and fitting for (a) TX 15° and RX 15° , and (b) TX 15° and RX Omni.

Lets define the normalized root-mean square (RMS) signal $y(t)$ as the square root of the summation of the squared absolute value of the measured CIR in the delay domain:

$$y(t) = \sqrt{\frac{1}{\frac{1}{T_w} \sum_{\forall t \in T_w} \sum_{\forall k} |h(t, k\Delta\tau)|^2} \sum_k |h(t, k\Delta\tau)|^2}, \quad (5.5)$$

where $y(t)$ is calculated using a sliding rectangular window of $T_w = 40\lambda$ samples along the complete track.

The variation of the overall received signal amplitude for different directivities and bandwidths (covering the complete measured spectrum with sliding windows with the bandwidth under test) can be seen in Fig. 5.11a for the TX 15° HPBW and Rx 15° HPBW, and Fig. 5.11b for the TX 15° HPBW and Rx Omni. In both figures, a trend of decreasing variation with increasing bandwidth is observed. Furthermore, a comparison of Fig. 5.11a with Fig. 5.11b shows a lower variation also with increasing directivity.

The K -factor was calculated using (B.13) after fitting (5.5) to the Rician distribution and extracting A and σ . The K -factor for the different system aspects investigated in this experiment are summarized in Table 5.2. There is a clear trend of increasing K with bandwidth and directivity. This is an indicator of less stochastic components, i.e. components that can't be resolve, and more deterministic components, i.e. components that can be resolved.

Table 5.2: Estimated K-factor for the different directivities and bandwidth.

Directivity	Visibility	BW [GHz]								
		0.01	0.02	0.04	0.1	0.2	0.4	1	2	4
TX 15° - RX Omni		3.47	3.83	4.54	5.98	7.56	9.01	10.88	12.98	14.71
TX 15° - TX 30°	NLOS	6.54	6.62	6.85	7.67	8.89	10.67	13.74	16.4	17.65
TX 15° - RX 15°		7.38	7.44	7.62	8.29	9.53	11.55	15.42	17.73	18.6
TX Omni - RX Omni	LOS	2.07	3.21	5.1	7.67	8.98	10.21	12.03	14.16	15.47

Finally, these results also show that in this particular example, the K -factor within a cluster is larger with high directivity on the antennas (TX 15° and RX 15° or 30°) than with LOS and isotropic characteristics at TX and RX.

5.4 Conclusions

In this chapter we have empirically shown the influence of mm-wave system aspects, as high directivity and large bandwidth, on the communication channel. This is essential to understand the differences between what the digital interfaces observe at sub-6 GHz and at mm-wave: while in the previous chapter we have seen that there are no substantial differences between the sub-6 GHz and mm-wave propagation channel (considering isotropic radiators and large bandwidths), the differences are found in the mm-wave radio-channel.

Filtering out clusters reduces large-scale and small-scale fading. Regarding the former one, a statistical analysis on a rich set of measurements in diverse scenarios has shown that with directive systems, the DS is shorter compared to low directive systems. Therefore, shorter guard intervals can be applied in multi-carrier systems with the benefits of higher efficiency.

Regarding small-scale fading, measurements have shown a considerable reduction of stochastic components in the channel by increasing either directivity or bandwidth, or both. Hence, even in NLOS, the fading distribution of the signal envelope in the radio-channel follows a Rician distribution instead of a Rayleigh.

The isolation of clusters reduces Doppler: since all the MPCs arrive from the same cluster, we have a Doppler shift instead of a spread. Moreover, the isolation of MPCs also increase the relevance of aspects as polarization: a clear polarization reduces diversity and requires a match between the TX and RX antennas.

Therefore, all the aforementioned effects need to be included in channel models: while the propagation channel doesn't show big differences over the different bands, aspects as fading, polarization, and deterministic components need to be tangible after applying directivity and increasing the system bandwidth.

6 mm-Waves, Sub-THz, and Multi-band Channel Modelling Components

“The nice thing about standards is that you have so many to choose from.”

An American Professor.

Overview

In the present chapter we introduce physical channel modelling aspects from what we have observed in the empirical part. A ground discussion on physical models and the state of the art in mm-wave channel models is introduced in Appendix C. We open the discussion on the advantages and disadvantages of geometry-based and non-geometry-based SCMs (i.e. models with and without deterministic clusters) depending on the simulation requirements. Later, we introduce different modelling aspects for multi-band and mm-wave SCMs. These components have been identified in the multi-band measurement campaigns in multiple scenarios in Chapter 4. We first address the deterministic clusters that can be tracked during the displacement of the RX units, showing their relevance in the test of applications as beamforming and localization. We also show that these clusters govern the behaviour of the LSPs. Finally, we present correlated multi-band modelling aspects taking the non-geometry based 3GPP SCMs receipt as a reference, and introducing modifications for this purpose.

6.1 Introduction

In the previous chapters, we have empirically observed that propagation at mm-wave exhibits two main differences compared to sub-6 GHz: less diffuse power and a higher isotropical path-loss. While the first characteristic originates a more specular-like channel, the second requires the utilization of highly directive radio-interfaces. This high directivity isolates clusters in the spatial domain, and therefore the digital interfaces observe a sparse channel consisting of a few number of MPCs, as observed in the DS reduction in Section 5.3. A directive radio-channel requires that the system is aware of the environment, i.e., from where does the signal come from. Moreover, during movement, systems need a constant re-orientation of the gain, and therefore, the environment must be “consistent” in models, as shown in the PDPs over distance in the measurements in multiple scenarios in Section 4.3.4, Section 4.4.3, and Section 4.5.3. This spatial consistency of the channel is not exclusive only in dynamic scenarios, but also in scenarios with multiple users, since closely located users observe the same scatterers. Applications as localization or cooperative beam-forming (exchange of “pointing” information between users) also need a consistency on the location of the clusters.

The isolation of MPCs by the utilization of directive radio interfaces reduces small-scale fading and the Doppler impairments, as shown in Section 5.3.3 and Section 5.3.4, respectively. Moreover, polarization becomes more determinant since the RX signal after beam-forming is not the superimposition of MPCs from different scattering processes, but an isolated scattering action. Hence, the polarization of the RX signal strongly depends on the TX polarization, impinging angle, and orientation of the scattering surface, as seen empirically in Section 4.3.5. Modelling aspects and further analysis on polarization are addressed in Chapter 7.

In addition, the utilization of larger bandwidths increases the resolution in the time domain. Therefore, the CIR also becomes more sparse in time-delay, reducing fading (isotropically and intra-cluster) and generating non-zero DS clusters, which can’t be modelled as the superimposition of random variables generating Rayleigh fading, as addressed in Section 5.3.5.

Regarding frequency, multi-band power profiles from measurements have shown that the scatterers are located in the same position and present similar properties across the different bands. Therefore, a similar radio-channel is observed with the same system aspects, independently of the carrier frequency¹. These scatterers, mostly specular reflections, have shown that they rule the values and behaviour of LSPs, as seen in the different measurements and environments presented in Chapter 4. Moreover, since they are common across the bands, it generates a high correlation between the isotropic LSPs at sub-6 GHz and mm-wave.

Applications as assisted inter-band beam-forming, in which a user with a transceiver including several radio interfaces can exploit the angular information from low frequencies to facilitate the pointing procedure at high frequencies, require multi-band correlated propagation channels. Therefore, frequency correlated models must consider the mm-wave system properties as high resolution, and then the sub-6 GHz channel can be computed reducing

¹Neglecting the isotropic FSPL and the diffuse power.

the system resolution by the integration of the antenna characteristics and bandwidth.

However, regarding stochastic physical spatial channel models, there are two different and divergent modelling methodologies that offer different capabilities and require also a different parametrization. In the following Section, we discuss the pros- and cons of the models in which the clusters are located randomly and the ones in which they are located deterministically in the environment.

6.2 Preliminaries: Deterministic Vs. Random Location of Clusters

As discussed in the Appendix C, there are two well established methodologies in SCMs: cluster-level (COST-type) and system-level (WINNER-type, e.g. 3GPP) models.

In the cluster-level models, the clusters are pre-located in space and then the scattered power is calculated either stochastically (e.g. COST-2100), or deterministically based on the distance and impinging and reflected angles to the scatterers, and scattering properties as reflection coefficients and roughness (e.g. Millimetre-Wave Evolution for Backhaul and Access (MiWEBA)). Therefore, a very precise and accurate channel can be obtained in the latter case, at the expense of the need a of rich data-base of scattering parameters. These models don't require the knowledge of LSPs, and therefore, there is not necessarily an agreement between the simulated and the measured LSPs. However, from our measurements in Chapter 4, we have learned that the specular scatterers are the ones that dominate the values and behaviour of the LSPs. Therefore, with a right parametrization of these scatterers, we expect to have LSPs within the range and behaviour² of the measured ones.

However, since the idea behind stochastic physical models is to have the ability of simulating different environments on each run, the problem of pre-defining the location of the clusters, is that we require an algorithm "intelligent" enough to locate them in such a way that generates a realistic environment: size of the playground, match of the scattering properties and location (ceiling, ground, vertical structures), variation on scattering properties (to avoid simulating the same playground/room on every run), addition of random components, etc.

On the other hand, system-level models generate the position of the clusters randomly. Afterwards, their powers are calculated to conform the set of correlated LSPs as DS. Later, the direction of arrival and departure are calculated to match the clusters with the angular spreads. This allows to generate completely random and different scenarios on each run, in which the isotropic LSPs are within the statistics of the ones obtained in measurements. However, this results in the generation of unrealistic scatterers in terms of position and power. Furthermore, there is no deterministic relation between the change on power of the scatterers and the impinging and reflected angles, or polarization. Moreover, two different users closely located observe similar LSPs, e.g. DS, but the direction of arrival and departure,

²By behaviour, we refer to the distribution of the LSPs in the scenario and their dynamics while movement. Examples are the correlation of angular spreads and DS, and the inverted "U" shape vs distance in environments limited by walls or structures, e.g., indoors and street canyons with buildings at the end of the street, as seen in Fig. 4.20a, Fig. 4.28a, Fig. 4.28d, Fig. 4.34a, and Fig. 4.34b, and in other publications as in [94].

and distance to the clusters are calculated independently, and therefore the scatterers they observe are completely different.

Extensions considering spatial consistency have been introduced in the so called WIN-SC model and in QuaDRiGa. However, in the first case, the consistency is over the times of arrival and angles, but not on power. On the other hand, QuaDRiGa defines the spatial consistency as the correlation of the LSPs in space (3 dimensions for single- and 6 for dual-mobility), but not on their real location. This model utilizes the method of sum-of-sinusoids (SOS) to ease the computation of the correlated parameters [95]. A comparison between the spatial consistency implementations between the 3GPP and QuaDRiGa models can be found in [96].

Depending on the test scenarios and applications, each of the modelling approaches can provide different advantages and disadvantages. Pre-defining the cluster's position and calculating deterministically the power (considering reflection coefficients and impinging and reflected angles) allows a more realistic simulation platform for applications as beam-forming and positioning. The spatial consistency allows to track the scatterers and to estimate also the change on scattered power during displacement due to the difference on impinging angles and on polarization.

On the other hand, system-level models allow a simple implementation of multiple scenarios and the parametrization can be done straightforwardly from measurements or RT simulations.

6.3 Deterministic Components in Spatial Channel Models

6.3.1 Deterministic Components in Spatial Channel Models

The multi-band measurements in different scenarios presented in Chapter 4 have shown that a highly deterministic description of the environment can be observed through the propagation channel. The scattering components that generate the largest impact on the LSPs are reflections from structures that define the environment: the furniture, machinery, and walls determining the indoor space in halls, conference rooms, an industry settings; the lateral buildings in the street canyon, and lampposts, buildings, and vehicles in V2V. In addition, all these scenarios present a ground reflection component in LOS.

Therefore, the geometry of the environment and deterministic scatterers can be set in the scenario in an early step. A similar approach is followed in the map-based model in METIS [87], in the COST2100 model [97], and in MIWEBA³ [98], in which the position of the deterministic clusters and geometry of the environment are pre-defined. Differently to the latter one, we also address deterministic back reflections (BRs) which are not explicitly considered in [99], and we introduce “diffuse scatterers”, which are scatterers with multiple angle of departures for a single impinging angle.

³Details on this model are further discussed in Appendix C.4.2.

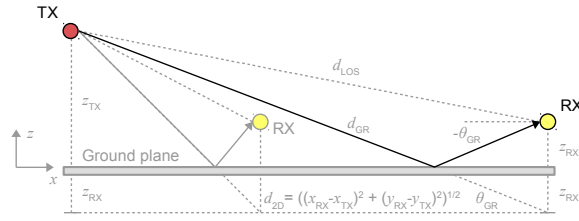


Figure 6.1: Ground reflection scheme.

Similarly to MiWEBA [98], in our approach, the deterministic scatterers define the TDoA, DoD and DoA, and the polarization of the signal. Depending on the methodology, the amplitude can be drawn from LSPs, or calculated deterministically with Fresnel equations by assigning reflection and transmission coefficients to these scatterers.

A general description of some of the most common deterministic scatterers found in the measurements, and simple modelling approaches using the method of images to incorporate them in the channel models are introduced in the following sub-sections. Finally, we compare the DS and ASA from measurements and from a simple model with deterministic scatterers.

Ground Reflection

This is a deterministic component that is always present together with the LOS and becomes more visible when there is a large difference of height and distance between the BS and the UE. Depending on the system bandwidth and directivity, GR can originate severe fading losses due to its proximity on TDoA and DoA to the LOS component. A sketch of the geometry of GR is displayed in Fig. 6.1, where $(x_{\text{TX/RX}}, y_{\text{TX/RX}}, z_{\text{TX/RX}})$ represents the TX and RX 3D Cartesian coordinates. The TDoA of the GR path can be calculated as

$$\tau_{\text{GR}} = \frac{d_{\text{GR}}}{c} = \frac{\sqrt{(z_{\text{TX}} + z_{\text{RX}})^2 + d_{2\text{D}}^2}}{c}, \quad (6.1)$$

where d_{GR} is the GR path length, c is the speed of light, z_{TX} and z_{RX} are the TX and RX heights, respectively, and $d_{2\text{D}} = \sqrt{(x_{\text{TX}} - x_{\text{RX}})^2 + (y_{\text{TX}} - y_{\text{RX}})^2}$ is the 2D distance between the TX and RX. While the AoA of the GR path ϕ_{GR} equals the AoA of the LOS path ϕ_{LOS} , the elevation of arrival (EoA) θ_{GR} is calculated as

$$\begin{aligned} \theta_{\text{GR}} &= -\arctan\left(\frac{z_{\text{TX}} + z_{\text{RX}}}{d_{2\text{D}}}\right), \\ \phi_{\text{GR}} &= \phi_{\text{LOS}}. \end{aligned} \quad (6.2)$$

The amplitude of the GR path is weighted by the reflection coefficient $\Gamma_{\text{p,s}}$ that depends on the polarization of the impinging wave, relative permittivity of the ground ε_{GR} , and incident

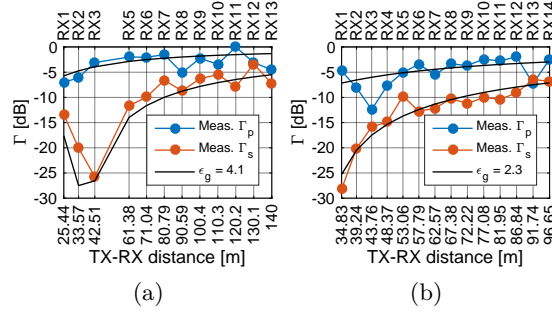


Figure 6.2: Measured RX power of the ground reflection and estimated reflection coefficient at 30 GHz in the street canyon scenario in (a) Ilmenau, and (b) Tokyo .

angle θ_{GR} . The amplitude of the reflected paths in the different polarizations is

$$\Gamma_p(\theta_{GR}) = \frac{\varepsilon_{GR} \cos(\theta_{GR}) + \sqrt{\varepsilon_{GR} - \sin^2(\theta_{GR})}}{\varepsilon_{GR} \cos(\theta_{GR}) - \sqrt{\varepsilon_{GR} - \sin^2(\theta_{GR})}},$$

$$\Gamma_s(\theta_{GR}) = \frac{\cos(\theta_{GR}) + \sqrt{\varepsilon_{GR} - \sin^2(\theta_{GR})}}{\cos(\theta_{GR}) - \sqrt{\varepsilon_{GR} - \sin^2(\theta_{GR})}}. \quad (6.3)$$

The RX power, relative to the LOS, of the GR path tracked in the measurements at 30 GHz in Ilmenau and Tokyo are shown in Fig. 6.2. The GR was extracted as the maximum component from the synthetic omni-directional PDP within a limited delay range estimated using (6.1). θ_{GR} is calculated using the set-up information and $\Gamma_{p,s}(\theta_{GR})$ are calculated by adjusting the permittivity and fitting the analytical curve to the measurements. A good match can be observed between the predicted and measured power of the GR. Results reported in [98] have also shown that GR is the second strongest component apart from the LOS in street canyon scenarios.

Side and Back Reflections

Side and back reflections have been identified in almost all the investigated scenarios: indoor, industry, outdoor, and V2V. A schematic of the street canyon scenario in Tokyo with a building at the end of the street is shown in Fig. 6.3a. Depending on the location of the TX, sides reflections might occur on the left (SRL) and right (SRR) walls, taking as a reference the RX location. The propagation distance of the n^{th} order SRL $d_{SRL,n}$ and SRR $d_{SRR,n}$ can be calculated as

$$d_{SRL/SRR,n} = \sqrt{(x_{TX} - x_{RX})^2 + d_{y,SRL/SRR,n}^2 + (z_{TX} - z_{RX})^2}, \quad (6.4)$$

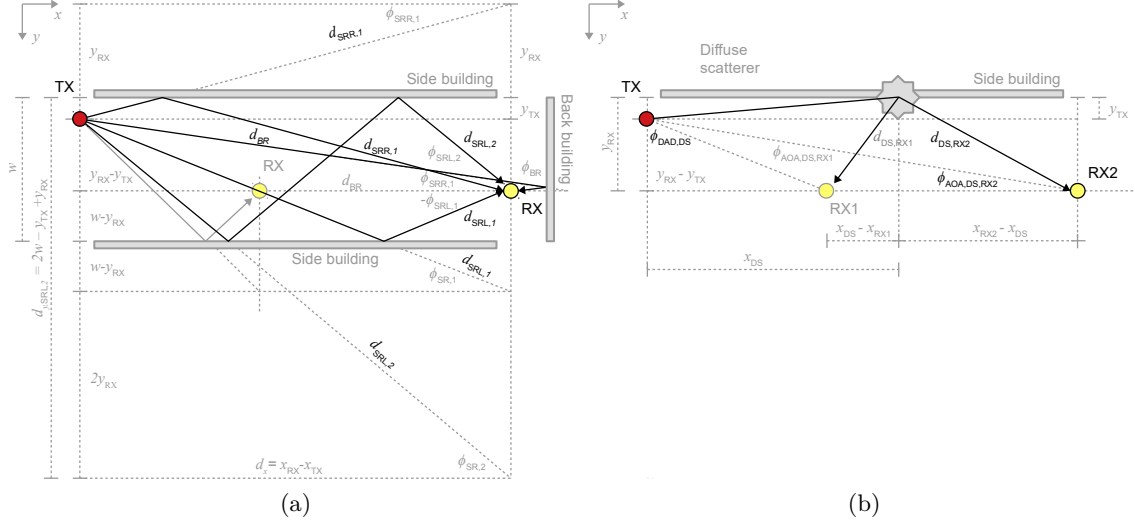


Figure 6.3: Schematic of the specular components in street canyon scenario with a building at the end.

where $d_{y,SRL/SRR}$ is calculated as

$$d_{y,SRL,n} = \begin{cases} (n+1) \cdot w - y_{TX} - y_{RX} & \text{for odd } n \\ n \cdot w - y_{TX} + y_{RX} & \text{for even } n \end{cases},$$

$$d_{y,SRR,n} = \begin{cases} (n-1) \cdot w + y_{TX} + y_{RX} & \text{for odd } n \\ n \cdot w + y_{TX} - y_{RX} & \text{for even } n \end{cases}, \quad (6.5)$$

where w is the street or scenario width.

On the other hand, the first order m^{th} BR distance can be estimated as

$$d_{BR,m} = \sqrt{(2 \cdot x_{BB,m} - x_{TX} - x_{RX})^2 + (d_{2D})^2}, \quad (6.6)$$

where $x_{BB,m}$ is the location of the m^{th} back scatterer in the x axis. The TDoAs of these components can be calculated as $\tau_{SRL/SRR,n} = \frac{d_{SRL/SRR,n}}{c}$ and $\tau_{BR,m} = \frac{d_{BR,m}}{c}$. The AoA of the side reflection (SR) $\phi_{SRL/SRR,n}$ and BR $\phi_{BR,m}$ are calculated as

$$\phi_{RX,BR,m} = 180 - \arctan\left(\frac{|y_{TX} - y_{RX}|}{|2 \cdot x_{BB,m} - x_{TX} - x_{RX}|}\right),$$

$$\phi_{RX,SRL,n} = (-1)^n \arctan\left(\frac{|d_{y,SRL,n}|}{|x_{TX} - x_{RX}|}\right),$$

$$\phi_{RX,SRR,n} = (-1)^{n+1} \arctan\left(\frac{|d_{y,SRR,n}|}{|x_{TX} - x_{RX}|}\right). \quad (6.7)$$

Diffuse Scatterers

We introduce this kind of scatterers with the particularity that for each impinging angle, there are different outgoing angles with different scattering properties, usually described by a bi-static radar cross-section.

These are last bounce scatterer (LBS). This means that under the assumption of a single side movement, e.g. RX, the DoD remains the same, but the DoA changes for the different RX positions. A more complex scenario, out of the study of this work, arises with double side mobility.

The propagation distance of the n^{th} diffuse cluster is calculated as

$$d_{\text{DS}} = \sqrt{\|\mathbf{p}_{\text{TX}} - \mathbf{p}_{\text{DS}}\|_f^2} + \sqrt{\|\mathbf{p}_{\text{DS}} - \mathbf{p}_{\text{RX}}\|_f^2}, \quad (6.8)$$

where $\mathbf{p}_{\text{TX/DS/RX}}$ is the 3D location of the TX, diffuse scatterer, and RX in the playground. The azimuth of arrival and departure are calculated as

$$\begin{aligned} \phi_{\text{AOD,DS}} &= 180 - \arctan\left(\frac{|y_{\text{TX}} - y_{\text{DS}}|}{|x_{\text{TX}} - x_{\text{DS}}|}\right), \\ \phi_{\text{AOA,DS}} &= 180 - \arctan\left(\frac{|y_{\text{RX}} - y_{\text{DS}}|}{|x_{\text{RX}} - x_{\text{DS}}|}\right). \end{aligned} \quad (6.9)$$

It is worth to mention, that the previous equations are valid for this specific geometry displayed in Fig. 6.3b. Adaptations need to be done for any position of TX, RX, and scatterers.

6.3.2 Analysis and Synthesis of Deterministic Components in Measurements

The propagation distance (or TDoA) of the strongest peaks from the synthetic omnidirectional PDP in the different positions considering a dynamic range of 40 dB at 30 GHz and 60 GHz in Tokyo is displayed with crosses in Fig. 6.4a and 6.4b, respectively. The predicted propagation distance of the SRL up to third order and 5 different BRs (building at the end of the street, back wall of side building, etc.) is overlaid with circles. A very good match between the prediction of the cluster positions and the measurements can be observed. These clusters are mostly equally visible in the different bands.

On the other hand, Fig. 6.4c and Fig. 6.4d show the Ilmenau scenario at sub-6 GHz and 30 GHz, respectively. Due to the location of the TX, there are reflections from both sides. However, differently to the Tokyo scenario, third order reflections were only visible at some positions at sub-6 GHz but not at mm-wave. The influence of the street width w is also visible on the difference on propagation distance between the different reflection orders in Ilmenau and Tokyo.

However, there are some positions in which the predicted clusters were shadowed in the measurements. This is because of the irregular facades of the buildings with different scat-

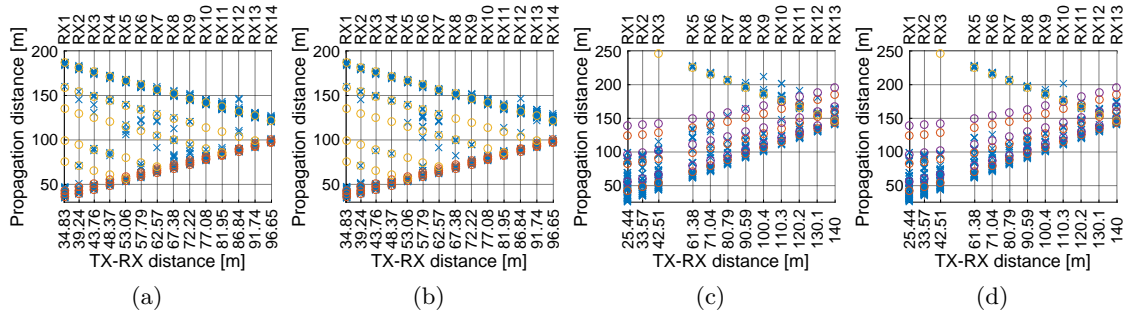


Figure 6.4: Measured (blue crosses) and estimated SRL (red circles), SRR (violet circles), and BR (orange circles) TDoA of the deterministic components in the Tokyo scenario at (a) 30 GHz, (b) 60 GHz, in Ilmenau at (c) 6.75 GHz, and (d) 30 GHz.

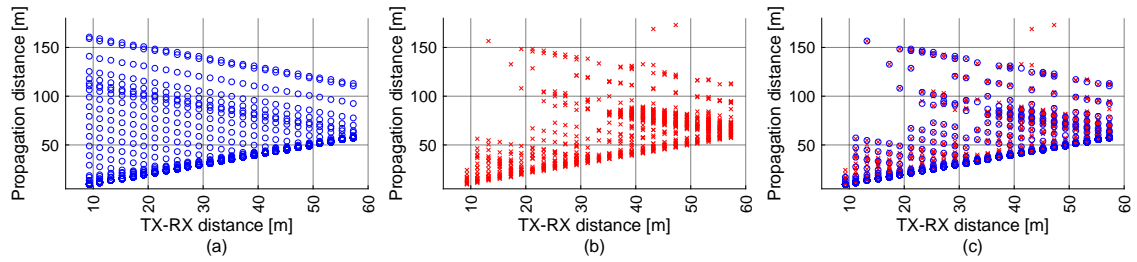


Figure 6.5: (a) delay skeleton from deterministic clusters, (b) peaks from measurements at 30 GHz in corridor scenario, and (c) delay skeleton with overlaid measurements after switching on and off the clusters.

tering properties and trees in the environment. In our simulations, to compare with the measurements, we have switched on and off the scatterers according to the measurements. Investigations on the derivation of stochastic parameters to model the shadowing behaviour of these clusters that appear and disappear in the different positions can be found in [98]. The angular characteristics cannot be contrasted with the measurements due to the coarse angular resolution of 30° .

The same modelling methodology is applied in the indoor large corridor scenario introduced in Section 4.3.4. In this case, a regular structure of scattering objects located every 5 m on the back, side reflections, and the stairs at the end of the corridor were simulated. A good match between the measured and simulated TDoAs can be observed in the Fig. 6.5.

While this approach allows to allocate the clusters in delay and angle, the scattering properties and distribution of the intra-clusters parameters as number of multi-path components, polarization, intra-cluster DSs, and intra-cluster ASs still needs to be investigated with different tools due to the limitations on resolution of the measurement equipment.

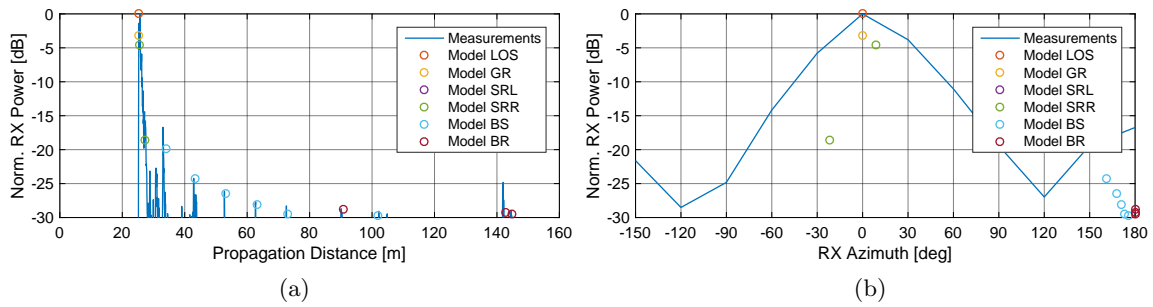


Figure 6.6: Measured and simulated (a) PDP and (b) PAP at RX in large corridor scenario at 30 GHz.

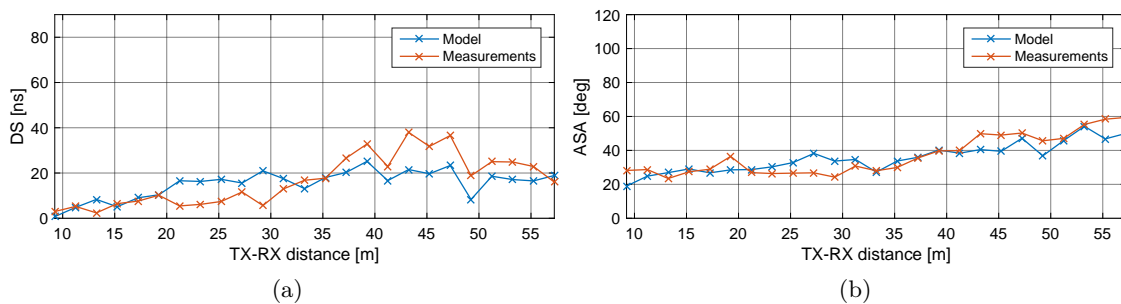


Figure 6.7: Measured and simulated (a) DS and (b) ASA in the large corridor scenario at 30 GHz.

6.3.3 Validation of Deterministic Components in Spatial Channel Models

The model has been implemented following the receipt presented in Appendix C.4.2 and parametrized as indicated in Appendix D.7. The measured and simulated PDP and PAP at the RX in the position RX 9 are displayed in Fig. 6.6.

The DS and ASA calculated from the synthesized CIR considering only the deterministic clusters in the indoor large corridor scenario are displayed in Fig. 6.7.

6.4 Non-Geometry-Based Multi-band Correlated Spatial Channel Modelling

6.4.1 Introduction

As discussed in Chapter C, system-level channel models generate stochastic LSPs based on distributions parametrized from measurements, and these LSPs are also cross-correlated to each other. Later, these values are distributed in a “physical” map applying an exponentially decaying correlation distance on the different LSPs. Thus, closely located users observe a

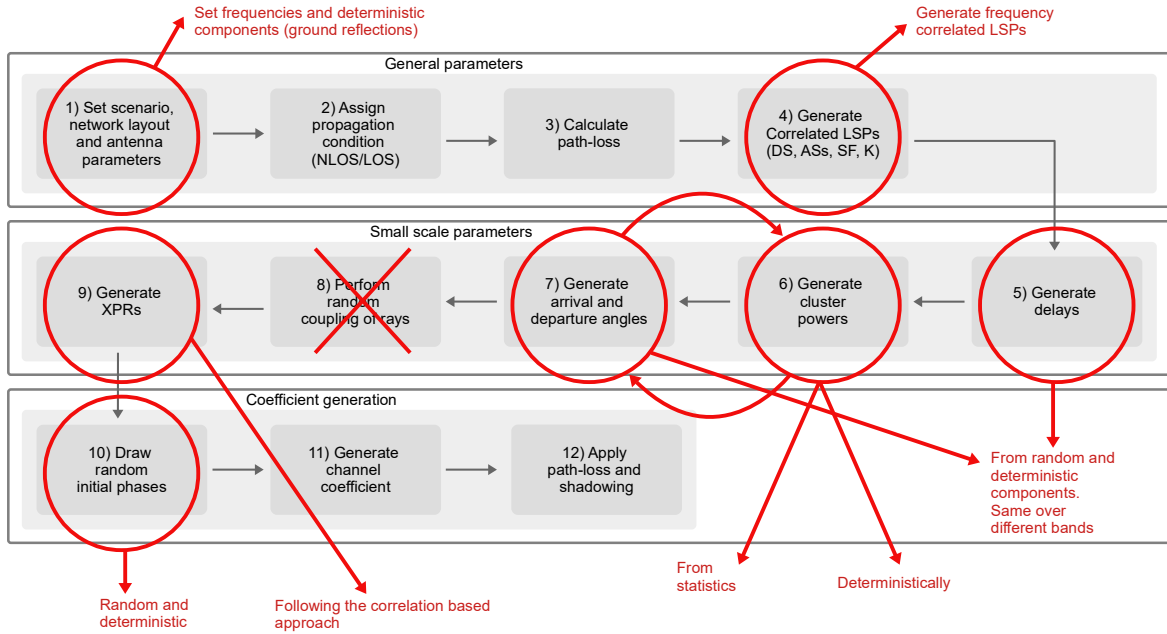


Figure 6.8: Modifications on the 3GPP SCM receipt for correlated multi-band simulations.

channel with similar LSPs, even if the scatterers are completely different (the clusters are generated individually per user in a later step). However, we have seen in Section 6.3.1 that the main scatterers are common in the different positions, and that they dominate the values of the LSPs. Furthermore, those scatterers are also, to some extent, equally visible over the different bands. Therefore, we first analyse the correlation between LSPs and then we extend this analysis to the frequency domain, i.e., how are these LSPs correlated over frequency. Finally, we introduce the synthesis scheme for inter-band correlated channels with common scatterers along frequency.

6.4.2 Modifications in the Channel Coefficient Generation Procedure

The receipt for the generation of the channel coefficients in the WINNER-type and 3GPP SCMs family is re-displayed with the necessary modifications including deterministic components to address multi-band and high resolution systems in Fig. 6.8.

All the parameters defined in Step 1 are common over the different simulated bands. Only the centre frequency, bandwidths, antenna patterns and elements allocation are specific per band. The same happens with Steps 2 and 3, in which the propagation conditions are the same over frequency, but the path-loss is calculated based on the centre frequency.

The first major modification is in the generation of correlated LSPs in Step 4, in which we also include the correlation of the parameters through the different bands. This is a completely different approach to the one followed in the 3GPP model [4]. There, the LSPs are not correlated over frequency, but their mean and variance are calculated with a frequency dependent formula. The analysis of the correlation of the LSPs over frequency based on

the measurements introduced in this work is addressed in Section 6.4.3, and the synthesis procedure in Section 6.4.4.

The next step is to calculate the delay of the clusters. We have observed in all the measurements that the main scatterers are the “limiting” walls of the environment and a group of characteristic clusters from the scenario. These components shape an skeleton in the TDoAs, DoAs, and DoDs, which are “consistently” observed over the different frequencies. Therefore, Step 5 and 6 are exchanged. In multi-band simulations, the TDoAs and directions are calculated using as an anchor the DS, and angular spreads of the lower frequency.

Later, the LSPs are used to generate the power of the different clusters over the skeleton generated in Step 5 and 6.

Another major change compared to the traditional approach is the random generation of the polarimetric ratios in step 9. We replace this step by an approach based on correlations and considering the nature of the scatterers (vertical or horizontal structures), including the parameter CPR and different XPRs. This is addressed in Chapter 7.

In the following sections, we first analyse the correlation of the different LSPs calculated from the measurements. Then we introduce the procedure for the synthesis of LSPs correlated in frequency (Step 4) and for the generation of the CIR (Step 5 to 7).

6.4.3 Analysis of the Frequency Correlation of Large-Scale Parameters

The cross-correlation between the LSPs is calculated as the Pearson correlation coefficient between the observed LSP in the different positions i , from a total of N links. In WINNER and 3GPP SCMs, the correlation is done in the logarithmic domain [4]. As an example, let us consider the correlation between the DS and ASA:

$$\rho_{\text{DS,ASA}} = \frac{1}{N-1} \sum_{n=1}^N \left(\frac{\log_{10}(\text{DS}_n) - \mu_{\text{lgDS}}}{\sigma_{\text{lgDS}}} \right) \left(\frac{\log_{10}(\text{ASA}_n) - \mu_{\text{logASA}}}{\sigma_{\text{lgASA}}} \right), \quad (6.10)$$

where μ_{lgDS} and μ_{logASA} are the mean of the logarithm of DS and ASA, and σ_{lgDS} and σ_{lgASA} are the variance.

The correlation coefficient between the different LSPs and scenarios are shown in Fig. 6.9. Independently of the value, the same trend can be observed on the LSPs in the different scenarios and visibility conditions and frequencies. There is a negative correlation between the RX power and DS, showing that DS increases when the RX power decreases. Similarly occurs with the ASA, and therefore the DS and ASA are positively correlated. On the other hand, the correlation between the RX power and the ASD is positive, meaning that the ASD increases with RX power. If we associate the RX power to the TX-RX distance, we expect to have a larger ASD with the RX close to the TX due to local scattering. When the RX moves away, the TX power is focused in the direction of the RX, reducing the local scattering closely located to the TX.

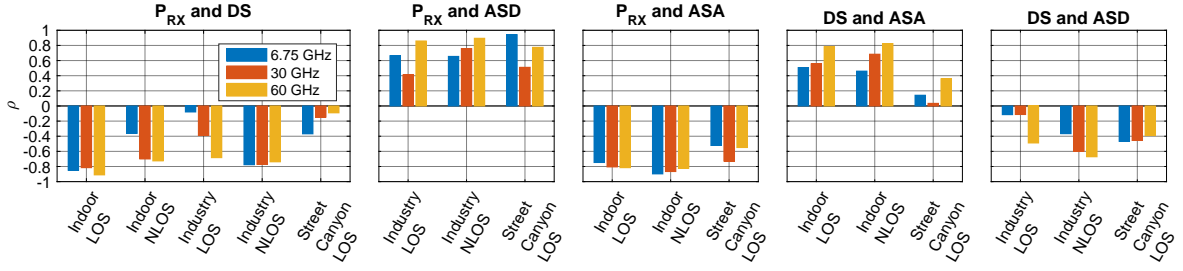


Figure 6.9: Correlation coefficient of the LSPs from multi-band measurements in different scenarios.

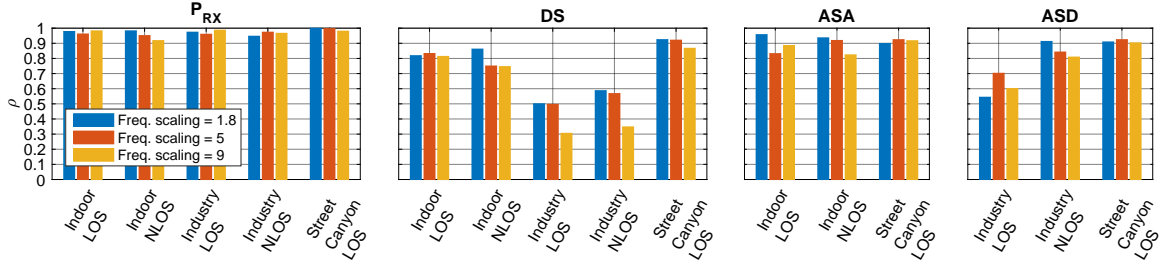


Figure 6.10: Inter-band correlation coefficient of LSPs from measurements in different scenarios, where scaling factor 1.8 corresponds to the relation between 33.75 GHz and 60.75 GHz, 5 to 6.75 GHz to 33.75 GHz, and 9 6.75 GHz to 60.75 GHz.

Our novelty, is the extension of this methodology over frequency by calculating the cross-correlation over the measured bands for each of the LSPs,

$$\rho_{\text{DS}}(f_1, f_2) = \frac{1}{N-1} \sum_{n=1}^N \left(\frac{\log_{10}(\text{DS}_{f_1, n}) - \mu_{\lg \text{DS}, f_1}}{\sigma_{\lg \text{DS}, f_1}} \right) \left(\frac{\log_{10}(\text{DS}_{f_2, n}) - \mu_{\lg \text{DS}, f_2}}{\sigma_{\lg \text{DS}, f_2}} \right), \quad (6.11)$$

where $\mu_{\lg \text{DS}, f_1}$ and $\mu_{\lg \text{DS}, f_2}$ are the mean of the logarithm of the DS in the different frequencies, and $\sigma_{\lg \text{DS}, f_1}$ and $\sigma_{\lg \text{DS}, f_2}$ are the variance.

The inter-band correlation coefficient for each scenario and visibility are displayed in Fig. 6.10. A correlation coefficient $\rho_{\text{LSP}} > 0.7$ has been observed in almost all the scenarios and parameters. Only the industrial scenario seems to show a lower correlation. While the RX power is highly correlated, the difference on the spreads (delay and angular) shows that the scatterers have a different influence over frequency. As analysed in Section 4.5.6, the difference between the diffuse and specular power ratio in the sub-6 GHz and mm-wave band might also play a significant role. On the other hand, the remaining scenarios show a high inter-band correlation between the LSPs.

6.4.4 Synthesis of Correlated Large-Scale Parameters (Step 4)

The synthesis of correlated LSPs is performed with a linear transformation: a weighted sum of independent Gaussian random processes. Thus, if the n^{th} LSP is not Gaussian distributed, a previous transformation has to be done. More details can be found in [12]. Afterwards, the

parameters needed for the calculation are the mean μ_n and variance σ_n of the n^{th} LSPs and the cross-correlation coefficient ρ between them. Let us consider the generation of N LSPs at f_1 with a vector of random independent variables $\mathbf{x} \in \mathbb{R}^{N \times 1} \sim \mathcal{N}(0, 1)$,

$$\underbrace{\begin{bmatrix} \log_{10}(\text{DS}f_1) \\ \log_{10}(\text{ASA}f_1) \\ \vdots \\ \log_{10}(\text{ASD}f_1) \end{bmatrix}}_{\hat{\mathbf{x}}_{f_1}} = \underbrace{\begin{bmatrix} L_{1,1} & 0 & \dots & 0 \\ L_{2,1} & L_{2,2} & \dots & 0 \\ \vdots & \vdots & \ddots & \vdots \\ L_{N,1} & L_{N,2} & \dots & L_{N,N} \end{bmatrix}}_{\mathbf{L}_{f_1}} \underbrace{\begin{bmatrix} x_1 \\ x_2 \\ \vdots \\ x_N \end{bmatrix}}_{\mathbf{x}_{f_1}} + \underbrace{\begin{bmatrix} \mu_{\text{lgDS}} \\ \mu_{\text{lgASA}} \\ \vdots \\ \mu_{\text{lgASD}} \end{bmatrix}}_{\mathbf{m}_{f_1}}, \quad (6.12)$$

where \mathbf{m}_{f_1} is the vector containing the mean values of the distributions of the LSPs, \mathbf{L}_{f_1} is the Cholesky decomposition of the cross-covariance matrix $\mathbf{A} \odot \mathbf{\Sigma}$ (where \odot is the element-wise multiplication),

$$\mathbf{L}_{f_1} = \text{chol}\left(\mathbf{A}_{f_1} \odot \mathbf{\Sigma}_{f_1}\right), \quad (6.13)$$

where \mathbf{A}_{f_1} contains the cross-correlation coefficients of the LSPs and $\mathbf{\Sigma}_{f_1}$ contains the multiplication of the LSPs variance:

$$\mathbf{A}_{f_1} \odot \mathbf{\Sigma}_{f_1} = \begin{bmatrix} \rho_{\text{DS}f_1, \text{DS}f_1} \cdot \sigma_{\text{lgDS}f_1} \cdot \sigma_{\text{lgDS}f_1} & \dots & \rho_{\text{DS}f_1, \text{ASD}f_1} \cdot \sigma_{\text{lgDS}f_1} \cdot \sigma_{\text{lgASD}f_1} \\ \vdots & \ddots & \vdots \\ \rho_{\text{DS}f_1, \text{ASD}f_1} \cdot \sigma_{\text{lgASD}f_1} \cdot \sigma_{\text{lgDS}f_1} & \dots & \rho_{\text{ASD}f_1, \text{ASD}f_1} \cdot \sigma_{\text{lgASD}f_1} \cdot \sigma_{\text{lgASD}f_1} \end{bmatrix}. \quad (6.14)$$

Finally, the LSPs used for the synthesis of the CIRs are transformed to the linear scale by $10^{\hat{\mathbf{x}}_{f_1}}$.

The generation of correlated LSPs between M different frequencies is made by extending (6.12) with the inter-band cross-correlation coefficients:

$$\underbrace{\begin{bmatrix} \hat{\mathbf{x}}_{f_1} \\ \hat{\mathbf{x}}_{f_2} \\ \vdots \\ \hat{\mathbf{x}}_{f_M} \end{bmatrix}}_{\hat{\mathbf{x}}} = \mathbf{L}_{f_M, f_M} \underbrace{\begin{bmatrix} \mathbf{x}_{f_1} \\ \mathbf{x}_{f_2} \\ \vdots \\ \mathbf{x}_{f_M} \end{bmatrix}}_{\mathbf{x}} + \underbrace{\begin{bmatrix} \mathbf{m}_{f_1} \\ \mathbf{m}_{f_2} \\ \vdots \\ \mathbf{m}_{f_M} \end{bmatrix}}_{\mathbf{m}}, \quad (6.15)$$

where $\mathbf{L}_{f_M, f_M} = \text{chol}\left(\mathbf{A} \odot \mathbf{\Sigma}\right) \in \mathbb{R}^{NM \times NM}$ is the cholesky decomposition of

$$\mathbf{A} \odot \mathbf{\Sigma} = \begin{bmatrix} \mathbf{A}_{f_1, f_1} \odot \mathbf{\Sigma}_{f_1, f_1} & \mathbf{A}_{f_1, f_2} \odot \mathbf{\Sigma}_{f_1, f_2} \dots & \mathbf{A}_{f_M, f_M} \odot \mathbf{\Sigma}_{f_M, f_M} \\ \mathbf{A}_{f_2, f_1} \odot \mathbf{\Sigma}_{f_2, f_1} & \mathbf{A}_{f_2, f_2} \odot \mathbf{\Sigma}_{f_2, f_2} \dots & \mathbf{A}_{f_M, f_M} \odot \mathbf{\Sigma}_{f_M, f_M} \\ \vdots & \ddots & \vdots \\ \mathbf{A}_{f_M, f_M} \odot \mathbf{\Sigma}_{f_M, f_M} & \mathbf{A}_{f_M, f_2} \odot \mathbf{\Sigma}_{f_M, f_2} \dots & \mathbf{A}_{f_M, f_M} \odot \mathbf{\Sigma}_{f_M, f_M} \end{bmatrix}, \quad (6.16)$$

and the internal sub-matrices are composed of the cross-correlation factors and the standard

deviation of LSPs

$$\mathbf{A}_{f_i, f_j} \odot \boldsymbol{\Sigma}_{f_i, f_j} = \begin{bmatrix} \rho_{DSf_i, DSf_j} \cdot \sigma_{lgDSf_i} \cdot \sigma_{lgDSf_j} & \cdots & \rho_{DSf_i, ASDf_j} \cdot \sigma_{lgDSf_i} \cdot \sigma_{lgASDf_j} \\ \vdots & \ddots & \vdots \\ \rho_{DSf_i, ASDf_j} \cdot \sigma_{lgDSf_i} \cdot \sigma_{lgASDf_j} & \cdots & \rho_{ASDf_i, ASDf_j} \cdot \sigma_{lgASDf_i} \cdot \sigma_{lgASDf_j} \end{bmatrix}. \quad (6.17)$$

It is worth to mention, that this approach needs for the parametrization, the cross-correlation of the different LSPs over frequency, which is not always simple to obtain from measurements. On the other hand, since it is not based on correlations, the approach followed in the 3GPP SCMs doesn't need these cross-correlation factors over frequency, which allows a simpler implementation.

6.4.5 Synthesis of Correlated Channel Impulse Responses (Step 5-7)

Let's consider the synthesis of correlated channels in F different frequencies. Since the clusters are assumed to be the same over frequency, delays, DoD, and DoA are calculated only once and then used to generate the power of the clusters in the different frequencies.

The frequency correlated LSPs are generated using (6.17). Afterwards, the delay and directions to calculate the clusters power are calculated using the spreads of the lowest frequency, as introduced in [4]:

$$\tau'_n = -r \cdot DS(1) \ln(X_n), \quad (6.18)$$

where $X_n \sim \text{unif}(0, 1)$. The AoA and azimuth of departure (AoD) are calculated as

$$\begin{aligned} \phi'_{\text{AOA}, n} &= \arg \left(\exp \left(-j \cdot r \cdot \text{ASA}(1) \cdot X_n^{\text{AOA}} \right) \right), \\ \phi'_{\text{AOD}, n} &= \arg \left(\exp \left(-j \cdot r \cdot \text{ASD}(1) \cdot X_n^{\text{AOD}} \right) \right), \end{aligned} \quad (6.19)$$

where $X_n^{\text{AOA}} \sim \mathcal{N}(0, 1)$ and $X_n^{\text{AOD}} \sim \mathcal{N}(0, 1)$. The EoA and elevation of departure (EoD) are calculated as

$$\begin{aligned} \theta'_{\text{EOA}, n} &= \arg \left(\exp \left(-j \cdot r \cdot \text{ESA}(1) \cdot \text{sgn} \left(X_n^{\text{EOA}} - 0.5 \right) \ln \left(1 - 2|X_n^{\text{EOA}} - 0.5| \right) / \sqrt{2} \right) \right), \\ \theta'_{\text{EOD}, n} &= \arg \left(\exp \left(-j \cdot r \cdot \text{ESD}(1) \cdot \text{sgn} \left(X_n^{\text{EOD}} - 0.5 \right) \ln \left(1 - 2|X_n^{\text{EOD}} - 0.5| \right) / \sqrt{2} \right) \right) \end{aligned} \quad (6.20)$$

where $X_n^{\text{EOA}} \sim \text{unif}(0, 1)$ and $X_n^{\text{EOD}} \sim \text{unif}(0, 1)$. In LOS, the first components of the delay, direction of arrival, and departure are set to zero: $\tau'_1 = 0$, $\phi'_{\text{AOA}, 1} = 0$, $\phi'_{\text{AOD}, 1} = 0$, $\theta'_{\text{EOA}, 1} = 0$, and $\theta'_{\text{EOD}, 1} = 0$.

The first difference to the 3GPP model is the calculation of the clusters power in the different

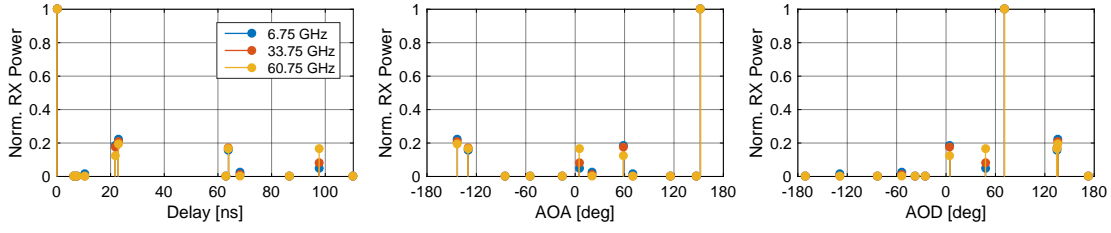


Figure 6.11: Single realization of the multi-band correlated CIR.

frequencies f ,

$$P'_n(f) = S_n \cdot e^{-\tau'_n \frac{r-1}{rDS(f)} - \frac{1}{2} \phi_{\text{AOA},n}^2 \frac{r^2-1}{r^2 \text{ASA}(f)^2} - \frac{1}{2} \phi_{\text{AOD},n}^2 \frac{r^2-1}{r^2 \text{ASD}(f)^2} - \sqrt{2} |\theta'_{\text{AOA},n}| \frac{r-1}{r \text{ESA}(f)} - \sqrt{2} |\theta'_{\text{AOD},n}| \frac{r-1}{r \text{ESD}(f)}}, \quad (6.21)$$

where $S_n = 10^{-Q_n/10}$ and $Q_n \sim \mathcal{N}(0, \zeta^2)$ is the per-cluster shadowing. Afterwards, the power is normalized in NLOS to

$$P_n = \frac{P'_n}{\sum_{n=1}^N P'_n}, \quad (6.22)$$

or in LOS as

$$P_n = \frac{K}{K+1} \frac{P'_{n=1}}{P'_{n=1}} + \frac{1}{K+1} \frac{P'_{n=2\dots N}}{\sum_{n=2}^N P'_{n=2\dots N}}, \quad (6.23)$$

where K is the K-factor in linear scale. Finally, the delays, directions of arrival and departure are calculated depending on the whether the visibility is LOS or NLOS,

$$\begin{aligned} \tau_n &= \begin{cases} \tau'_n & \text{in NLOS,} \\ \sqrt{1 + \frac{K}{2}} \tau'_n & \text{in LOS,} \end{cases} \\ \phi_{\text{AOA},n} &= \begin{cases} \phi'_{\text{AOA},n} + \phi_{\text{AOA,LOS}} & \text{in NLOS,} \\ \sqrt{1 + K} \phi'_{\text{AOA},n} + \phi_{\text{AOA,LOS}} & \text{in LOS,} \end{cases} \\ \phi_{\text{AOD},n} &= \begin{cases} \phi'_{\text{AOD},n} + \phi_{\text{AOD,LOS}} & \text{in NLOS,} \\ \sqrt{1 + K} \phi'_{\text{AOD},n} + \phi_{\text{AOD,LOS}} & \text{in LOS,} \end{cases} \\ \theta_{\text{EOA},n} &= \begin{cases} \theta'_{\text{EOA},n} + \theta_{\text{EOA,LOS}} & \text{in NLOS,} \\ \sqrt{1 + K} \theta'_{\text{EOA},n} + \theta_{\text{EOA,LOS}} & \text{in LOS,} \end{cases} \\ \theta_{\text{EOD},n} &= \begin{cases} \theta'_{\text{EOD},n} + \theta_{\text{EOD,LOS}} & \text{in NLOS,} \\ \sqrt{1 + K} \theta'_{\text{EOD},n} + \theta_{\text{EOD,LOS}} & \text{in LOS,} \end{cases}. \end{aligned} \quad (6.24)$$

A single realization of the synthesized CIR with the parameters in Table 6.1 is displayed in Fig. 6.11 where it can be seen that the clusters are located in the same delay and azimuths along the different frequencies, and then the power is scaled independently to conform the LSPs requirements.

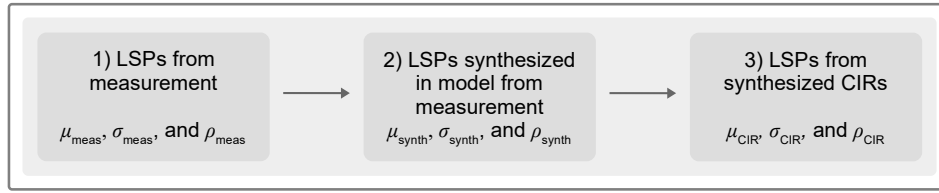


Figure 6.12: Validation methodology for 3GPP correlated multi-band SCM.

Table 6.1: Model parameters for 3GPP correlated multi-band SCM validation.

Scenario	Frequencies	Visibility	r	# Clusters ^a	K-factor ^b	ζ ^c	M
Street canyon	6.75 GHz, 33.75 GHz, and 60.75 GHz	LOS	1.5	12	$\mu_K = 3$ dB $\sigma_K = 2$ dB	0 dB	1

^aFrom 3GPP [4].

^bAssumed zero correlation to other LSPs and frequency independent.

^cPer-cluster shadow fading.

6.4.6 Validation of System-Level Correlated Multi-band Spatial Channel Models

The validation methodology is displayed in Fig. 6.12. We compare the statistics of the LSPs of the different stages: from measurements, from model synthesized, and finally, calculated from the model synthesized CIRs. For the generation of CIRs to do this comparison, we use a simplified implementation of the 3GPP receipt in [4] with the changes introduced in Fig. 6.8. This simplification isolates the CIR from external parameters and allows the comparison of the LSPs over the different frequencies.

The scenario under test is the outdoor street canyon scenario presented in Section 4.4. Since the model was generated with the available data from measurements, the analysis is only performed on DS, ASA, and ASD. Multiple parameters that introduce differences on the LSPs over frequency as number of sub-paths M , per-cluster shadowing ζ , and path-loss are neglected in the simulations. The model parameters are summarized in Table 6.1.

The statistics and correlation of the LSPs in the different steps of the generation of multi-band correlated CIRs are displayed in Fig. 6.13 and Fig. 6.14. It can be observed that the model is able to synthesize LSPs following the same statistics (first and second moment and cross-correlations) as the ones from the measurements. However, there are differences with the statistics of the LSPs calculated from the synthesized CIRs. While they follow the same trends, the mean and standard deviations are slightly different.

6.5 Conclusions

In this chapter, we have addressed modelling aspects of essential components in SCMs, which have been identified in the measurements on the previous chapters. Aspects as spatial consistency and resolution of path-level and intra-cluster properties as polarization become

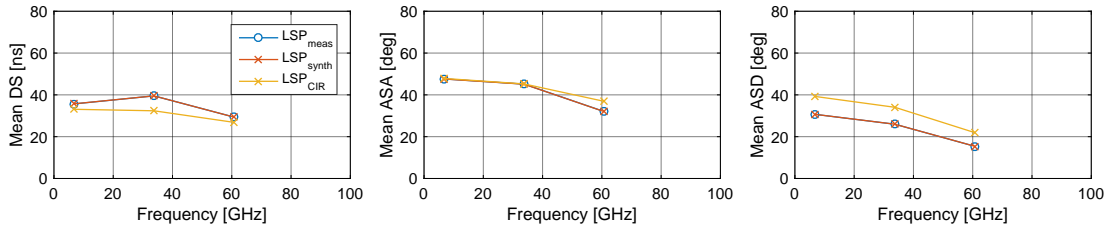


Figure 6.13: Mean of the LSPs in the different steps of the synthesis of correlated multi-band CIRs.

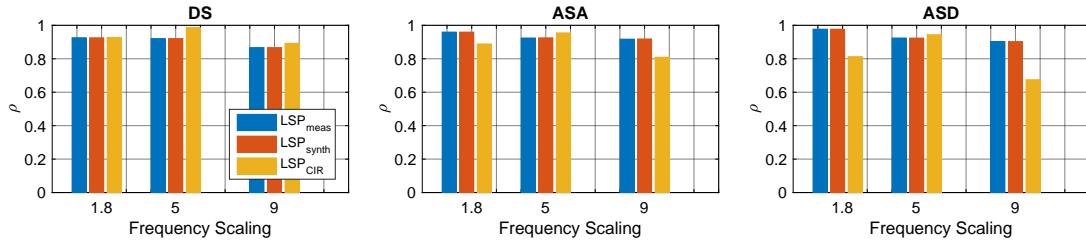


Figure 6.14: Multi-band cross-correlation factor of the different LSPs, where scaling factor 1.8 corresponds to the relation between 33.75 GHz and 60.75 GHz, 5 to 6.75 GHz to 33.75 GHz, and 9 6.75 GHz to 60.75 GHz.

more relevant if we consider the system properties at mm-wave. Depending on if the position of the clusters is pre-defined (cluster-level or COST-type) or if the position is calculated to conform the statistics of the LSPs (system-level or WINNER-type), models follow a different approach on the localization of the clusters.

The measurements have shown that the main scatterers observed during the displacement of the transceivers, or in the different positions in the environment, correspond to a well determined set of elements in the room (deterministic components). In addition, since these clusters govern the values and behaviour of the LSPs, a deterministic approach on the location and on the scattering properties (power) of those components will, at some extent, guarantee LSPs values close to the ones obtained on the measurements. However, this requires an accurate parametrization of the scattering coefficients of the different clusters and a controlled algorithm to allocate them in a certain position that originates a realistic reproduction of a real environment. Further studies need to be conducted to obtain a sufficient rich database with patterns for different impinging angles, frequencies, and polarizations, that allows the generation of channels covering a diverse group of possible environments. However, this increases considerably the required efforts on analysis and parametrization of these models. This is the approach followed in the cluster-level geometry-based stochastic channel models (GBSCMs) and in the MiWEBA models.

On the other hand, the location of clusters in WINNER-type SCMs is based on the generation of stochastic parameters from correlated distributions. Therefore, those clusters might result in the development of an environment with scatterers located in unrealistic positions, or improbable scattered power. While this approximation requires less efforts in analysis and parametrization, these models are less suitable for applications as tracking, beam-forming, and localization. However, since they are still widely used for multiple applications, we have

extended these models considering the correlation of the LSPs over frequency.

In the multi-band measurements we have observed that the clusters are the same in the different bands. The analysis of the cross-correlation between the LSPs in the different frequencies has shown that there is a high correlation over frequency, and that these processes are not independent. Therefore, system-level stochastic multi-band SCMs can be generated based on these correlations. This method allows the generation of LSPs that follow the same distributions and are correlated in frequency, as observed in the measurements. After the generation of the LSPs, the same delay and angular components of the clusters are settled over the different frequencies, and the power of each cluster is adjusted based on the LSPs. In that manner, the channel consists of the same clusters in the different bands, but with different power, as observed in the measurements.

One of the burdens of this approach, is that differences on the LSPs, e.g. DS, arises not only because of different values on the common paths, but also because of unique paths in the different bands and/or differences on diffuse multipath components (DMCs). However, this model forces the fitting of the differences on the common paths. For future investigations, once path-level information from multi-band measurements are available (or by utilizing alternative empirical methods as RT), the model needs to be adjusted by considering the statistics of common paths over frequency, and then including the unique paths.

Therefore, the correct choose of the model type, cluster-level or system-level, depends primarily on the application to be evaluated and then on the effort and available data for parametrization.

7 Polarization in Spatial Channel Models

“The world is polarized. The middle class becomes smaller. The polarization makes the difference between rich and the poor big.”

An Argentinian Pope.

Overview

In this chapter, we introduce a novel methodology to model the polarimetric coupling matrix in physical stochastic models. This model is based on the correlation of multiple parameters and mimics more accurately the physics behind the scattering process during propagation. Multiple RT simulations (contrasted with measurements) were used to analyse and parameterize this model. Finally, the influence of an inaccurate model of polarization on the estimation of polarization diversity gains is shown in a simulative analysis comparing the 3GPP approach to our model.

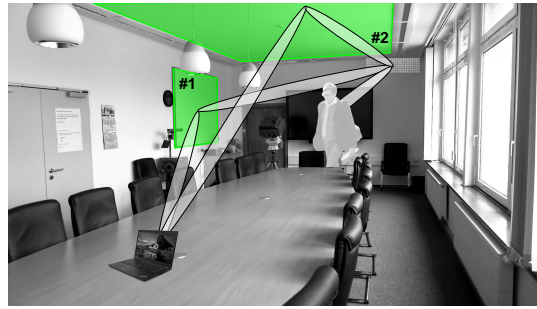


Figure 7.1: Utilization of beams to overcome human-shadowing.

7.1 Introduction

In order to compensate the increased isotropical path-loss, mm-Wave and sub-THz communication systems need to implement high directive radio-interfaces. Hence, as shown in the example in Fig. 7.1, the TX and RX are connected by sharp beams that can be easily interrupted. Shadowing losses are more severe at higher frequencies due to two reasons: penetration loss increases with frequency [54], and sharper beams generate less diffraction, as shown in our measurements in Fig. 4.4. Therefore, alternative paths (beams) have to be used for communication.

Measurements in Chapter 4 have shown that the strongest components in the propagation channel, apart from the LOS, are specular reflections. Furthermore, with increasing carrier frequency, the amount of diffuse power decreases, and therefore, these specular components become more relevant in the mm-wave and sub-THz channels. The utilization of directive radio-interfaces isolate clusters (wall, table, ceiling, etc.) from the isotropic propagation channel, becoming the scattering process in the background more visible and clear to the digital interface. Therefore, as shown in the example Fig. 7.1, the complete radio-channel consists of the scattering properties of a single or few scatterers (single cluster).

The relation of power between the different polarimetric channel components after specular reflections is described by Fresnel, (D.16). As predicted by the equations, empirical measurements in Section 4.1.2 and [100] have shown that the reflected power depends on the incident angle and polarization. We have seen in Fig. 4.2a that, independently from the angle, reflections in a vertical surface, as a concrete wall, are always stronger in the vertical polarization than in the horizontal. Similarly, as shown in Section 4.3.5, reflections in horizontal surfaces, as a table and ceiling, are stronger in the horizontal polarization than in the vertical. The ground reflection in Section 6.3.1 showed the same nature. This selectivity behaviour on polarization has a large impact on the design of communication systems.

A mismatch on the polarization can originate a complete fade in single polarized systems. This mismatch can be caused by the rotation of the antenna during operation of the terminal. Furthermore, this polarization selective response of the clusters, also originate that certain clusters are invisible to a determined polarization. Hence, single-polarized systems “see” a lower amount of clusters to be used for spatial diversity or to avoid shadowing. In addition, with polarization selective scatterers, polarization diversity within a single beam is also

affected, since one of the orthogonal components is attenuated, originating a large condition number in the polarimetric matrix.

Therefore, an accurate modelling of polarization for directive systems is crucial. Even in stochastic models, a completely random description of the polarization is not possible any more as it was for low resolution systems. Measurements have shown that, after beam-forming, the polarization has a deterministic behaviour, which is related to the nature of the scatterer. Hence, we introduce a stochastic modelling approach that considers the correlation between the different components and is parametrized from measurements and RT simulations. This intends to generate stochastic realizations of the channel, which are closer to the reality.

7.2 Limitations of the Current Modelling Approach

Polarization of paths in SCMs is usually characterized by a 2×2 complex matrix containing two orthogonal polarimetric components

$$\mathbf{\Gamma} = \begin{bmatrix} \gamma^{\phi\phi} & \gamma^{\theta\phi} \\ \gamma^{\phi\theta} & \gamma^{\theta\theta} \end{bmatrix} \in \mathbb{C}^{2 \times 2}, \quad (7.1)$$

where $\gamma^p = |\gamma^p|e^{j\Phi^p}$ is the complex channel coefficient in the TX/RX polarization defined by the tuple $p = \{\phi\phi, \theta\phi, \phi\theta, \theta\theta\}$ ¹. Let us now define the following PPRs between the channel coefficients in the different polarizations:

$$\text{XPR}_\phi = \frac{|\gamma^{\phi\theta}|^2}{|\gamma^{\phi\phi}|^2}, \quad \text{XPR}_\theta = \frac{|\gamma^{\theta\phi}|^2}{|\gamma^{\theta\theta}|^2}, \quad \text{and} \quad \text{CPR} = \frac{|\gamma^{\phi\phi}|^2}{|\gamma^{\theta\theta}|^2}. \quad (7.2)$$

These ratios are usually modelled as independent log-Normal distributions [12], [55], [101], and [102].

In most of the SCMs, e.g. in [4], [12], [103], and [87], clusters are modelled as the summation of M equally strong multi-path components that can not be resolved in time (C.2)². In these models, the polarimetric coupling matrix $\mathbf{\Gamma}_{n,m}$ of the m^{th} sub-path within the n^{th} cluster is defined as

$$\mathbf{\Gamma}_{n,m} = \begin{bmatrix} 1 \cdot e^{j\Phi_{n,m}^{\theta\theta}} & \sqrt{\text{XPR}_{n,m}} \cdot e^{j\Phi_{n,m}^{\theta\phi}} \\ \sqrt{\text{XPR}_{n,m}} \cdot e^{j\Phi_{n,m}^{\phi\theta}} & 1 \cdot e^{j\Phi_{n,m}^{\phi\phi}} \end{bmatrix}, \quad (7.3)$$

where the phase $\Phi_{n,m}^p$ of the channel coefficients $\gamma_{n,m}^p$ is obtained from independent uniform distributions, the amplitudes of the co-polar coefficients are equal $|\gamma_{n,m}^{\phi\phi}| = |\gamma_{n,m}^{\theta\theta}| = 1$ (CPR = 1), and the cross-polarized amplitudes are also assumed to be equal with $\text{XPR}_{n,m} = \text{XPR}_{\theta,n,m} = \text{XPR}_{\phi,n,m}$.

¹The variables ϕ and θ can be associated to the widely used nomenclature in polarization of horizontal and vertical, respectively.

²Please, refer to [4] and [12] for more details on the equation.

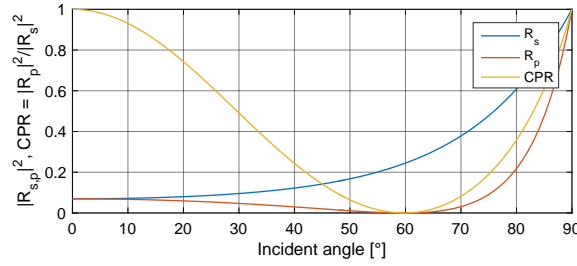


Figure 7.2: Reflection coefficient and CPR in a single layered wall with permittivity $\eta = 2.7$.

Another approach considers different XPRs for the vertical and horizontal polarizations [104], [105],

$$\mathbf{\Gamma}_{n,m} = \begin{bmatrix} 1 \cdot e^{j\Phi_{n,m}^{\theta\theta}} & \sqrt{\text{XPR}_{\theta,n,m}} \cdot e^{j\Phi_{n,m}^{\theta\phi}} \\ \sqrt{\text{XPR}_{\phi,n,m}} \cdot e^{j\Phi_{n,m}^{\phi\theta}} & 1 \cdot e^{j\Phi_{n,m}^{\phi\phi}} \end{bmatrix}, \quad (7.4)$$

where $\text{XPR}_{\theta,n,m}$ and $\text{XPR}_{\phi,n,m}$ are usually modelled as independent processes.

However, any of these models is able to mimic accurately the scattering behaviour after specular reflections. The reflection coefficient R is a function of the polarization, incident and reflected angle, and electromagnetic properties of the material. Fig. 7.2 shows the squared absolute value of the reflection coefficient $R_{s/p}$ for a wave carrying a polarization perpendicular (s) or parallel (p) to the plane containing the incident and reflected waves, and the power ratio between them (CPR), as a function of the incident/reflected angle, being the $\text{CPR} \approx 1$ only in a very short range of incident angles. For a vertical wall, s defines the vertical polarization, and p the horizontal. This is inverse in the case of ground or ceiling reflections, in which s characterizes the horizontal and p the vertical polarizations.

In the isotropic case, considering all the sub-paths within all the clusters (e.g. reflections from walls and floor/ceilings), the distribution of the CPR could possibly tend to a mean $\mu_c \rightarrow 0$ dB. However, in the isolation of a single cluster (after beam-forming), the CPR depends on the incident angles, being $\text{CPR} < 0$ dB for reflections on vertical surfaces, and $\text{CPR} > 0$ dB for horizontal surfaces, as defined in (7.2).

However, (7.3) and (7.4) assume that the power of the co-polarized components of each path is the same after scattering, which contradicts the previous statements. This approach is not so inaccurate in low resolution systems that can't resolve the intra-cluster paths and the observed channel is the complex summation of M sub-paths. This ends up in different values of power in the co-polarized components and introduces un-correlation between the different elements of $\mathbf{\Gamma}$. However, with high resolution systems, the polarization of paths and the relation between the different elements of $\mathbf{\Gamma}$ becomes more deterministic. The influence of the number of paths within the clusters on polarization diversity is study in Section 7.6.

Finally, one of the problems of considering $\text{CPR} = 0$ dB and $\text{XPR}_{\phi} = \text{XPR}_{\theta}$ is the overestimation of the polarimetric diversity obtained after beam-forming. Therefore, we introduce a novel modelling approach considering not only more realistic values of the PPRs, but also their correlations.

7.3 Novel Methodology: Correlation Based Modelling of the Polarimetric Power Ratios

A more accurate model of (7.4) can be obtained by considering different XPRs and including the CPR [104]:

$$\mathbf{\Gamma}_{n,m} = \begin{bmatrix} \sqrt{\text{CPR}_{n,m}} \cdot e^{j\Phi_{n,m}^{\phi\phi}} & \sqrt{\text{XPR}_{\theta,n,m}} \cdot e^{j\Phi_{n,m}^{\theta\phi}} \\ \sqrt{\text{CPR}_{n,m}\text{XPR}_{\phi,n,m}} \cdot e^{j\Phi_{n,m}^{\phi\theta}} & 1 \cdot e^{j\Phi_{n,m}^{\theta\theta}} \end{bmatrix}, \quad (7.5)$$

where $\text{XPR}_{\theta,\text{dB}} \sim \mathcal{N}(\mu_{\theta}, \sigma_{\theta}^2)$, $\text{XPR}_{\phi,\text{dB}} \sim \mathcal{N}(\mu_{\phi}, \sigma_{\phi}^2)$, and $\text{CPR}_{\text{dB}} \sim \mathcal{N}(\mu_c, \sigma_c^2)$. In this model, $|\gamma^{\theta\theta}| = 1$ is taken as a pivot and the power of the remaining coefficients are related to it by the polarimetric ratios from (7.2). A Frobenius normalization can be applied to $\mathbf{\Gamma}_{n,m}$ in order to scale the total power of the m^{th} sub-path.

We extended this model by considering the correlations between the different PPRs to address more realistic polarimetric matrices and obtain more accurate diversity results [106]. One of the advantages of this modelling approach is that it can be easily integrated in the current SCMs implementations, and only requires the calculation of the cross-correlation factors if the measurements of the different PPRs are available.

The correlated PPRs are generated out of a vector of random independent variables $\mathbf{x} \in \mathbb{R}^{3 \times 1} \sim \mathcal{N}(0, 1)$. The vector $\hat{\mathbf{x}} \in \mathbb{R}^{3 \times 1}$ with the correlated parameters is calculated (in dB) with

$$\underbrace{\begin{bmatrix} \text{XPR}_{\phi,n,m} \\ \text{XPR}_{\theta,n,m} \\ \text{CPR}_{n,m} \end{bmatrix}}_{\hat{\mathbf{x}}} = \underbrace{\begin{bmatrix} L_{1,1} & 0 & 0 \\ L_{2,1} & L_{2,2} & 0 \\ L_{3,1} & L_{3,2} & L_{3,3} \end{bmatrix}}_{\mathbf{L}} \underbrace{\begin{bmatrix} x_1 \\ x_2 \\ x_3 \end{bmatrix}}_{\mathbf{x}} + \underbrace{\begin{bmatrix} \mu_{\phi} \\ \mu_{\theta} \\ \mu_c \end{bmatrix}}_{\mathbf{m}}, \quad (7.6)$$

where $\mathbf{m} \in \mathbb{R}^{3 \times 1}$ contains the means from the distribution of (7.2), and \mathbf{L} is the Cholesky decomposition of the cross-covariance matrix $\mathbf{A} \odot \mathbf{\Sigma}$,

$$\mathbf{L} = \text{chol}\left(\mathbf{A} \odot \mathbf{\Sigma}\right), \quad (7.7)$$

where \mathbf{A} contains the Pearson correlation coefficient $\rho_{x,y}$ between the different PPRs with $\phi = \text{XPR}_{\phi}$, $\theta = \text{XPR}_{\theta}$, and $c = \text{CPR}$, and $\mathbf{\Sigma} = \mathbf{s} \cdot \mathbf{s}^T$ with $\mathbf{s}^T = [\sigma_{\phi} \ \sigma_{\theta} \ \sigma_c]$ contains the multiplication of the variance from the distributions of (7.2):

$$\mathbf{A} \odot \mathbf{\Sigma} = \begin{bmatrix} \rho_{\phi,\phi}\sigma_{\phi}\sigma_{\phi} & \rho_{\phi,\theta}\sigma_{\phi}\sigma_{\theta} & \rho_{\phi,c}\sigma_{\phi}\sigma_c \\ \rho_{\theta,\phi}\sigma_{\theta}\sigma_{\phi} & \rho_{\theta,\theta}\sigma_{\theta}\sigma_{\theta} & \rho_{\theta,c}\sigma_{\theta}\sigma_c \\ \rho_{c,\phi}\sigma_c\sigma_{\phi} & \rho_{c,\theta}\sigma_c\sigma_{\theta} & \rho_{c,c}\sigma_c\sigma_c \end{bmatrix}. \quad (7.8)$$

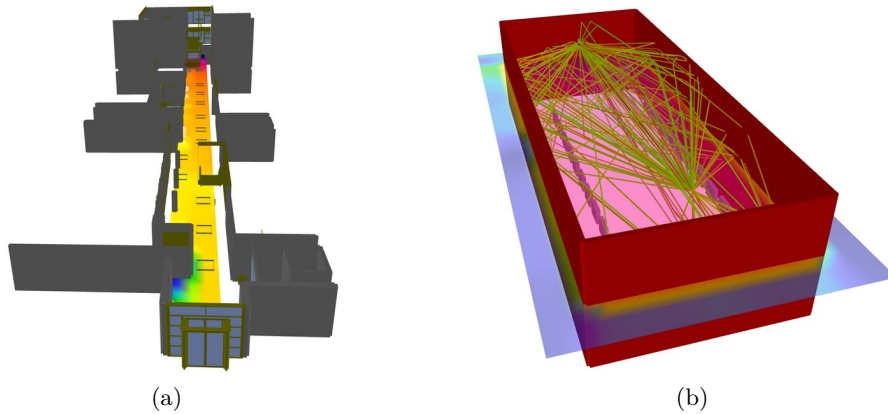


Figure 7.3: RT maps and simulations set-up for (a) large hall and (b) conference room scenarios.

7.4 Analysis and Model Parametrization

Polarization in SCMs is parametrized at path-level. However, it is difficult to obtain antenna independent parameters at that level with the current state of the art in channel measurements at mm-wave and sub-THz. Therefore, we use RT simulations to collect a rich number of antenna independent isotropic channel samples with a reasonable accuracy on the emulated physic processes.

The distribution of the PPRs is analysed using the WinProp V14.0 Ray-Tracer. The simulations were done with the large hall and conference room RT models validated in Section 4.3.4 and Section 4.3.5, respectively, and shown in Fig. 7.3. These models are parametrized with frequency dependent electromagnetic properties of the materials from a data-base. The signal level of the propagation paths and the polarization is calculated using Fresnel coefficients for transmissions and reflections, and geometrical theory of diffraction (GTD)/uniform theory of diffraction (UTD) for diffraction. These calculations are based on the permittivity, permeability, conductivity, and thickness of materials defined in the aforementioned data-base.

7.4.1 Ray-Tracing Simulations Set-Up

We have simulated an AP to UE scenario with isotropic radiators in order to obtain the isotropic characteristic of the channel. The AP (TX) was located at 2 m height and the UE (RX) at 1.6 m height. The RX positions were simulated every 0.25 m in the conference room scenario and every 1 m in the large hall. The simulated frequencies are close to the ones from the multi-band measurements presented in Chapter 4, and integer multiples from each others: $f_1 = 5$ GHz, $f_2 = 30$ GHz, and $f_3 = 60$ GHz, which are calculated as a factor of $\frac{f_2}{f_1} = 6$, $\frac{f_3}{f_1} = 12$, and $\frac{f_3}{f_2} = 2$.

Per-position, up to 100 paths were simulated within a dynamic range of 100 dB, and with a maximum of 2 transmissions, 5 reflections, 1 diffractions, and 2 reflections and diffractions.

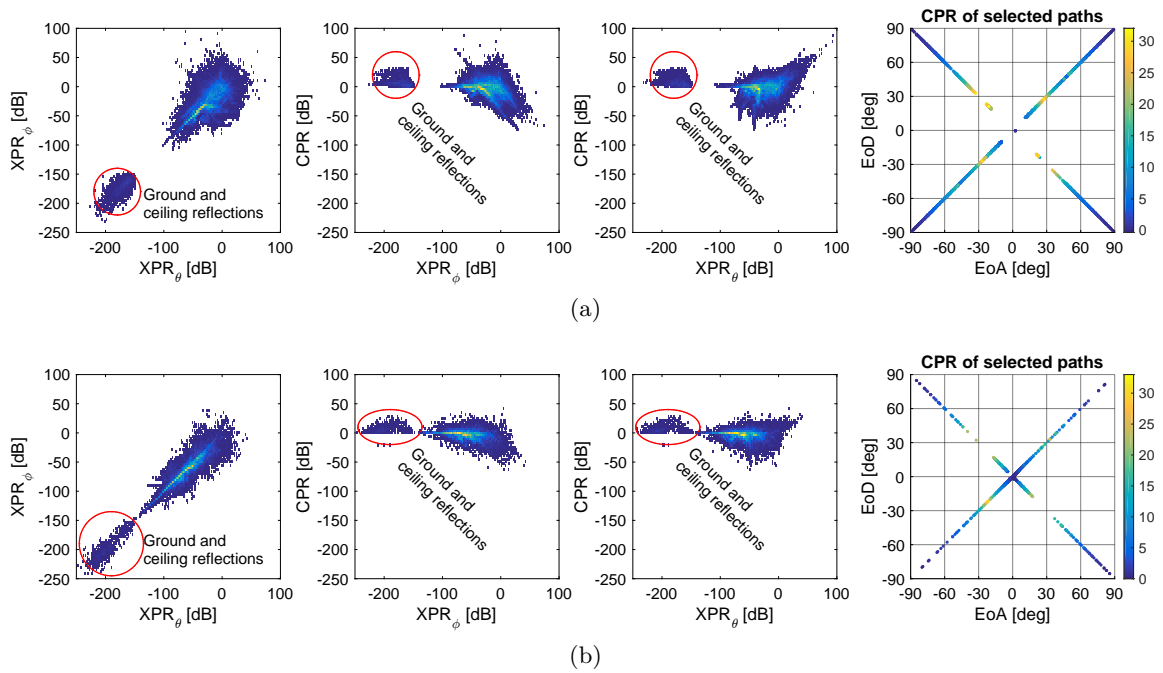


Figure 7.4: Bivariate histogram of the PPRs and ground and ceiling reflections at 60 GHz in (a) conference room scenario, and (b) large hall.

7.4.2 Distribution of the Polarimetric Power Ratios

The bivariate histogram of the PPRs in the conference room and large hall scenarios at 60 GHz are presented in Fig. 7.4. A mixture of two well separated Normal processes can be observed in the histograms of the XPRs. The samples with XPRs lower than -150 dB correspond to ground and ceiling reflections (in which extremely low cross polarization is assumed, or even neglected). These paths are not necessarily a single interaction. In addition, these paths exhibit a $\text{CPR} > 0$ dB. The EoA, EoD, and CPR of these paths are also displayed in Fig. 7.4. It is worth to notice, that in these paths, EoD always equals the EoA.

Since ground and ceiling reflections are usually treated as deterministic components within the channel, as addressed in Section 6.3.1, the analysis is focused only on the description of the remaining scatterers. All the paths with zero interactions (LOS) or with XPRs smaller than -150 dB were discarded (group of paths marked in Fig. 7.4).

The histogram of the multi-band PPRs and their fit to the Normal distribution in the conference room scenario are shown in Fig. 7.5. The parameters are summarized in Table 7.1. A slightly difference can be observed between the distributions of the XPRs, and the CPR exhibits a mean lower than 0 dB. In both scenarios and in all the simulated bands, $\mu_\phi > \mu_\theta$, indicating a larger depolarization from the horizontally polarized waves. This has also been observed in measurements in Chapter 4.

In addition, there is a clear decrease on the mean XPRs values with increasing frequency, showing that in average, the depolarization decreases with frequency. However, this is in a

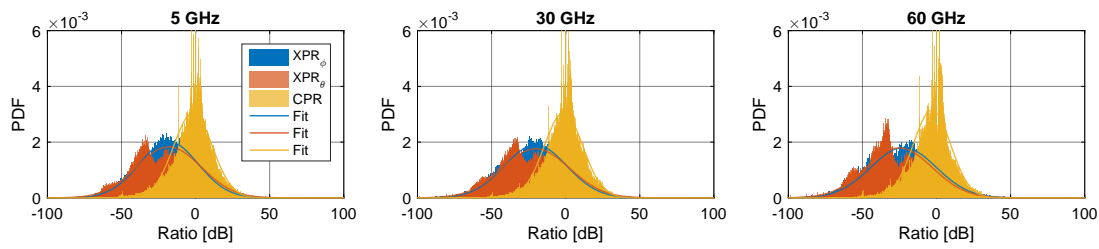


Figure 7.5: Histogram and fit to the Normal distribution of the multi-band PPRs from RT simulations in conference room scenario.

Table 7.1: Statistics of the multi-band PPRs from RT simulations.

Band	Conference Room						Large Hall					
	XPR _φ		XPR _θ		CPR		XPR _φ		XPR _θ		CPR	
	μ _φ	σ _φ	μ _θ	σ _θ	μ _c	σ _c	μ _φ	σ _φ	μ _θ	σ _θ	μ _c	σ _c
5 GHz	-18.12	19.71	-18.07	21.81	-1.81	13.09	-52.56	24.23	-56.41	23.52	-4.75	8.47
30 GHz	-20.34	20.96	-20.14	22.65	-1.45	13.07	-56.33	25.06	-59.28	24.04	-3.62	7.71
60 GHz	-22.26	22.04	-25.12	22.23	-3.12	12.69	-57.43	25.25	-60.19	24.20	-3.41	7.55

statistical point of view. A reason, is that at lower frequencies, there are more paths available by transmission and higher order reflections. A comparison through frequency considering only the common paths through bands is addressed in Section 7.4.4.

Finally, $\mu_c < 0$ dB, shows that in average, the MPCs carry more power in the vertical than in the horizontal polarization. This supports also the need of adopting the model introduced in Section 7.3. It is important to remark, that this analysis leaves aside ground and ceiling reflections, which showed a CPR larger than 0 dB in Fig. 7.4, but that are usually addressed as deterministic components in models, as discussed in Section 6.3.1.

7.4.3 Correlation of the Polarimetric Power Ratios

The relation between the different PPRs is shown in the bivariate histogram in Fig. 7.4a for the conference room and Fig. 7.4b for the large hall scenarios. The correlation factors are summarized in Table 7.2. In a large number of times, the XPR_φ and XPR_θ follow a linear relation, showing a large correlation between them. This correlation is larger in the large hall scenario, with $\rho_{\phi,\theta} \approx 0.89$ in the different frequencies. On the other hand, in the conference room, the correlation is smaller and slightly increases with frequency.

On the other hand, in both scenarios, the CPR values are mostly distributed in a line close to μ_c covering a wide range of XPR_φ and XPR_θ. This shows that the CPR is quasi-independent from the depolarization of the waves. The correlation between XPR_φ and CPR displayed in Fig. 7.4a shows $\rho_{\phi,c} \approx -0.3$ in the different scenarios and bands. For the XPR_θ and CPR case, there is almost a null correlation in the large hall scenario, but a factor from $\rho_{\theta,c} = 0.42$ to $\rho_{\theta,c} = 0.32$ in the conference room scenario.

Table 7.2: Correlation of the multi-band PPRs from RT simulations.

Band	Conference Room			Large Hall		
	$\rho_{\phi,\theta}$	$\rho_{\phi,c}$	$\rho_{\theta,c}$	$\rho_{\phi,\theta}$	$\rho_{\phi,c}$	$\rho_{\theta,c}$
5 GHz	0.59	-0.34	0.42	0.89	-0.33	-0.02
30 GHz	0.63	-0.33	0.37	0.90	-0.36	-0.09
60 GHz	0.66	-0.36	0.32	0.89	-0.36	-0.11

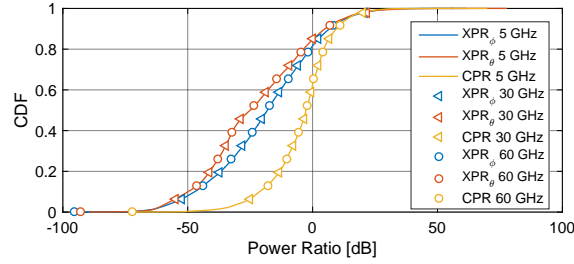


Figure 7.6: CDF of the PPRs of the common paths over frequency.

7.4.4 Analysis of Common Paths Over Frequency

Measurements and RT simulations have shown that the PPRs from isotropic channels show a frequency dependency. However, since these ratios were calculated independently, the frequency dependency can arise from multiple reasons:

- different number of paths with different polarimetric properties (more transmitted paths at lower frequencies),
- common paths exhibit different power ratios after scattering (due to the frequency dependency of the electromagnetic properties of the materials).

Therefore, we repeat the previous analysis on the common paths over frequency (without considering ground and ceiling reflections). The CDF of the PPRs in the different frequencies are displayed in Fig. 7.6. It can be observed that there are almost no differences on the distribution. Hence, the PPRs of the common paths are in these bands almost independent from frequency.

The correlation between the PPRs of the common paths over frequency is summarized in Table 7.3. The cross-correlation of the same parameter i over two frequencies f_m and f_n resulted in a full correlation ($\rho_{\text{PPR}_{i,f_m}, \text{PPR}_{i,f_n}} = 1$) and is marked in red. On the other hand, the correlation between different parameters i and j over frequencies f_m and f_n is also constant $\rho_{\text{PPR}_{i,f_m}, \text{PPR}_{j,f_m}} = \rho_{\text{PPR}_{i,f_n}, \text{PPR}_{j,f_n}}$. Therefore, the common paths over frequency seem to exhibit a similar behaviour in polarization. The differences on the statistics observed over frequency in Table 7.1 is generated by those paths that are individual to the band.

Table 7.3: Correlation of the PPRs of common paths over frequency from RT simulations.

		5 GHz			30 GHz			60 GHz		
		XPR _φ	XPR _θ	CPR	XPR _φ	XPR _θ	CPR	XPR _φ	XPR _θ	CPR
5 GHz	XPR _φ	1	0.62	-0.36	1	0.62	-0.36	1	0.62	-0.36
	XPR _θ	0.62	1	0.36	0.62	1	0.36	0.62	1	0.36
	CPR	-0.36	0.36	1	-0.37	0.36	1	-0.37	0.36	1
30 GHz	XPR _φ	1	0.62	-0.37	1	0.62	-0.36	1	0.62	-0.36
	XPR _θ	0.62	1	0.36	0.62	1	0.36	0.62	1	0.36
	CPR	-0.36	0.36	1	-0.36	0.36	1	-0.36	0.36	1
60 GHz	XPR _φ	1	0.62	-0.37	1	0.62	-0.36	1	0.62	-0.36
	XPR _θ	0.62	1	0.36	0.62	1	0.36	0.62	1	0.36
	CPR	-0.36	0.36	1	-0.36	0.36	1	-0.36	0.36	1

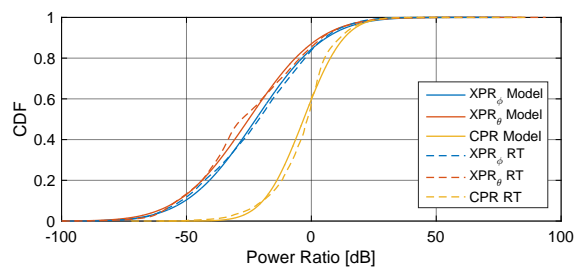


Figure 7.7: CDF of the synthesized and RT simulated PPRs at 60 GHz in conference room scenario.

7.5 Synthesis and Model Validation

The model has been validated by generating 1×10^6 polarimetric matrices and calculating the distribution and correlation of the PPRs. The CDF of the RT simulated and synthesized PPRs at 60 GHz in the conference room are displayed in Fig. 7.7. A small difference can be observed, which results from the fitting of the RT data into the Normal distribution.

Similarly, the correlation of the synthesized and the RT simulated PPRs are shown in Fig. 7.8a and Fig. 7.8b, respectively. This plot exhibits the simplifications done on the model: fitting a complex physical process into a multivariate Normal distribution. However, the objective of the model in (7.6) is to obtain a statistically accurate description of the observations done in the measurements and simulations.

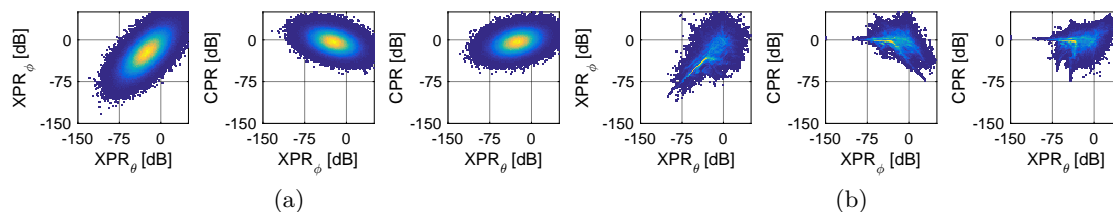


Figure 7.8: Bivariate histogram of the PPRs at 60 GHz from (a) model and (b) RT simulations in conference room.

7.6 Influence of Modelling Aspects on the Analysis of Polarization Diversity

In this section, we study the effects of the different models on the estimation of polarization diversity with high directive systems.

Let us assume a hybrid analog/digital beam-former, in which the analog part is used to compensate the isotropical path-loss. Thus, polarization diversity is applied after analog beam-forming, within a beam. Let us also assume perfect isotropic antennas at the TX and RX to avoid any extra influence rather than the polarization model under test. In addition, let us also only consider the NLOS beams, which might be the result of looking for alternative paths after human shadowing of the LOS, or in NLOS situations. We only focus on NLOS beams, since the LOS beam is the identity matrix in the polarization domain, which of course, offers the largest possible polarization diversity (neglecting antenna effects).

The system equation of polarization diversity after analog beam-forming is defined as

$$\mathbf{y} = \mathbf{H}_n \cdot \mathbf{x} + \mathbf{n}, \quad (7.9)$$

where $\mathbf{y} \in \mathbb{C}^{2 \times 1}$ is the RX signal in both polarizations, $\mathbf{H}_n = \sum_{m=1}^M \mathbf{\Gamma}_m \in \mathbb{C}^{2 \times 2}$ is the digitized channel with M sub-paths after analog beam-forming selecting the n^{th} cluster, $\mathbf{x} \in \mathbb{C}^{2 \times 1}$ are the two data streams in the different polarizations, and $\mathbf{n} \in \mathbb{C}^{2 \times 1}$ is the AWGN.

Under the assumption that the beam-former isolates a single cluster n with M sub-paths, let's define \mathbf{H}_n using the three different modelling approaches of $\mathbf{\Gamma}_n$. In the first case, let us consider the approach followed in the 3GPP SCM [4]:

$$\mathbf{H}_{n,3GPP} = \sum_{m=1}^M \begin{bmatrix} 1 & \sqrt{\text{XPR}_m} \\ \sqrt{\text{XPR}_m} & 1 \end{bmatrix} \odot \begin{bmatrix} e^{j\Phi_{n,m}^{\phi\phi}} & e^{j\Phi_m^{\theta\phi}} \\ e^{j\Phi_{n,m}^{\phi\theta}} & e^{j\Phi_m^{\theta\theta}} \end{bmatrix}. \quad (7.10)$$

In the second case, we consider different XPRs, but still no CPR:

$$\mathbf{H}_{n,3GPPM} = \sum_{m=1}^M \begin{bmatrix} 1 & \sqrt{\text{XPR}_{\theta,m}} \\ \sqrt{\text{XPR}_{\phi,m}} & 1 \end{bmatrix} \odot \begin{bmatrix} e^{j\Phi_{n,m}^{\phi\phi}} & e^{j\Phi_{n,m}^{\theta\phi}} \\ e^{j\Phi_{n,m}^{\phi\theta}} & e^{j\Phi_{n,m}^{\theta\theta}} \end{bmatrix}, \quad (7.11)$$

where, XPR_{ϕ} and XPR_{θ} can be generated either independently (less accurate, but most frequently implemented), or based on the correlations introduced in (7.6). Finally, the third case considers different XPRs, and also $\text{CPR} \neq 1$:

$$\mathbf{H}_{n,\text{TUIL}} = \sum_{m=1}^M \begin{bmatrix} \sqrt{\text{CPR}_m} & \sqrt{\text{XPR}_{\theta,m}} \\ \sqrt{\text{CPR}_m \cdot \text{XPR}_{\phi,m}} & 1 \end{bmatrix} \odot \begin{bmatrix} e^{j\Phi_{n,m}^{\phi\phi}} & e^{j\Phi_{n,m}^{\theta\phi}} \\ e^{j\Phi_{n,m}^{\phi\theta}} & e^{j\Phi_{n,m}^{\theta\theta}} \end{bmatrix}, \quad (7.12)$$

where, XPR_{ϕ} , XPR_{θ} , and CPR can also be generated either from independent Normal distributions or considering the correlations with (7.6).

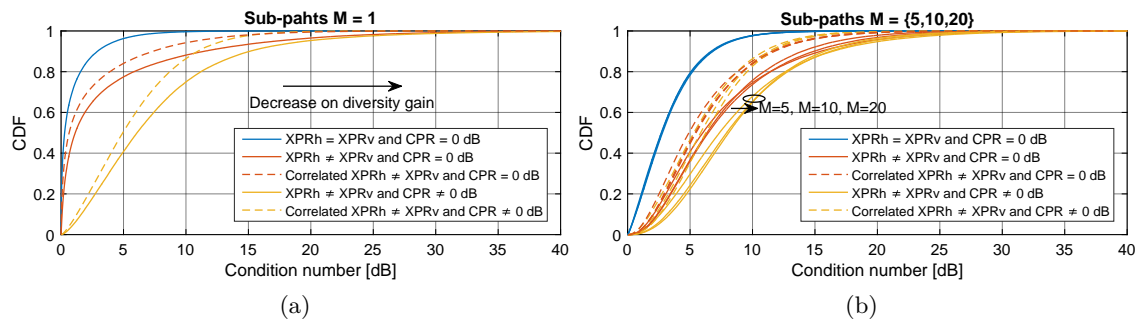


Figure 7.9: Condition number of different modelling approaches with (a) $M = 1$ sub-paths and (b) $M = \{5, 10, 20\}$ sub-paths within the clusters.

In order to evaluate the diversity gains, we use the condition number κ of \mathbf{H}_n , which is defined as the ratio

$$\kappa = \frac{\sigma_1}{\sigma_2}, \quad (7.13)$$

where σ_1 and σ_2 are the largest and smallest singular values, respectively. This ratio, describes the relation of power between the two orthogonal components in \mathbf{H}_n . A well-conditioned channel (small condition number) attain higher capacities. A condition number equal to the unity (lowest possible value) means that the two orthogonal channels in \mathbf{H}_d are equally strong. On the other hand, a large condition number means that one of the channels is stronger than the other one.

The condition number of \mathbf{H}_n with the different modelling approaches presented in (7.10)-(7.12) for 1×10^6 different clusters are presented in Fig. 7.9a with $M = 1$ sub-paths and in Fig. 7.9b for different number of sub-paths. At a first glance, it can be observed that the simplified, but less accurate, modelling approach used in $\mathbf{H}_{3\text{GPP}}$ has in average a lower condition number. This conducts to an overestimation of polarization diversity gains. As the modelling complexity increases, representing more accurately what has been observed in measurements, the condition number also increases, and therefore, the diversity gain decreases.

Furthermore, the influence of the correlation between the PPRs on the condition number of \mathbf{H}_n is displayed in dashed lines in Fig. 7.9. It can be seen that both, $\mathbf{H}_{3\text{GPPM},n}$ and $\mathbf{H}_{\text{TUILL},n}$ exhibit a lower condition number after the correlations observed in the measurements and simulations are considered in the model. However, considering a $\text{CPR} \neq 0$ dB still increases the condition number.

These results also show that the condition number depends on the number of paths within the channel after beam-forming. For a single path ($M=1$) channel, there is a large difference between the different models. However, when the number of paths increases, this difference decreases.

7.7 Conclusions and Future Work

In this chapter, we have introduced a novel modelling approach of the polarimetric channel coefficient matrix for SCMs based on three parameters calculated from correlated distributions: different XPR for horizontal and vertical polarizations, and CPR distinct to the unit. The correlation between these parameters is obtained from extensive measurements and simulations analysis.

Since path-level information is required to parametrize this model, and since there are several limitations on HRPE algorithms for UWB mm-wave and sub-THz measurements, we have used RT simulations validated with measurements to extract the model parameters. Ground and ceiling reflections showed a very deterministic description (equal EoA to EoD), extremely low XPRs, and as expected, always a CPR larger than one. Since in most of the models these components are addressed as deterministic ones, we have excluded them from the investigation. The analysis of the distributions of the PPRs have shown that the XPRs are not equally distributed. In both scenarios under test, a conference room and a large hall, and in most of the measurements introduced in this work, the vertical XPR was lower than the horizontal XPR. This means that in average, there is less leakage of power from the vertical components than from the horizontal one. Moreover, the mean value of the CPR was also lower than one.

An analysis over frequency considering all the simulated paths showed that the mean XPRs decrease with increasing frequency. On the other hand, the CPRs, while negative, didn't show any frequency dependent trend. However, the CPRs in the different frequencies were larger in the large hall scenario.

The correlation between the different PPRs was scenario dependent but not frequency dependent. In both cases, the XPRs values were highly correlated (approx. 0.6 in conference room and 0.9 in large hall). The CPR was negatively correlated to the horizontal XPR (approx. 0.33 in both scenarios), and positively correlated to the vertical XPR (0.37 in average in conference room) and almost no correlated in the large hall scenario.

The previous results were obtained considering the isotropic characteristics and all the paths. Due to propagation characteristics, not all the paths are the same in the different bands. At lower frequencies, there are more paths resulting from transmission and further scattering, and their PPRs influence the overall statistics. Therefore, an analysis of the PPRs in the common paths across the different frequencies has shown that these paths are completely correlated over frequency with the same statistics. Therefore, the differences on the statistics of XPRs and CPR over frequency arise from the non-common paths.

The model was validated generating a rich set of polarimetric parameters and comparing the statistics and correlations with the ones from the RT simulations. The results showed a good agreement on the statistics and correlations, even if the model was a simplification of the physics behind each individual scattering process.

Finally, we have conducted a simulative analysis to show the influence of the different modelling approaches on the estimation of polarization diversity. The results have shown that a

simplified model as the 3GPP, considering a single XPR value for both the vertical and horizontal polarizations, as well as neglecting the CPR, induces overestimation on the achievable polarization diversity after beam-forming, which is relevant if hybrid analog/digital architectures are under test. Therefore, our model based on correlations is encouraged.

Conclusions

8 Conclusions and Future Work

“Your faith was strong but you needed proof.”

A Canadian song-writer.

Overview

This chapter summarizes the overall conclusions obtained from the empirical observations carried out in this work. In addition, open questions and future investigations lines are also outlined.

8.1 Conclusions

The objective of this work was to prove that despite path-loss and DMC power, the isotropic propagation channel at mm-wave offers similar opportunities as the sub-6 GHz channel. The main differences arises on the system characteristics that need to be implemented to compensate the isotropic path-loss, i.e., high directive radio-interfaces. Consequently, channel models need to be re-adapted to deal with high resolution communication systems. Therefore, we first investigated the isotropic characteristics of the mm-wave and sub-THz channels, and then we analysed the effects of system aspects on the radio-channel and modelling aspects.

In most of the available research, the mm-wave and sub-THz channel was investigated by individual measurements which were later compared to previous results at lower frequencies in different scenarios and with different measurement characteristics. In addition, the lack of HRPE at higher frequencies prohibits the comparison of path-level characteristics from measurements. Most of the investigations are based on the characterization of parameters calculated from completely different measurement equipments with a large bias given by the resolutions. Hence, multiple conclusions were based on the differences, and less on the similarities. Therefore, we have introduced a different sounding methodology to characterize propagation based on the direct comparison of simultaneous measurements in different bands with similar resolution in the different domains.

The first step in this work was to validate the measurement methodology using a simulative approach in **Chapter 3**. The response of the channel sounder including the antennas was measured in the different bands in an anechoic chamber and then the results were embedded in RT simulations to emulate the sounding process. The same CIR was used over the different frequencies in order to identify the differences introduced by the measurement system. The LSPs calculated from the emulated marginal power profiles were used as a comparison metric, since they are the fundamental parameters of the most popular stochastic SCM.

Firstly, we analysed the influence of the sounder resolution. The results show that there is an intrinsic difference between the LSPs calculated directly from the measured marginal power profiles and the ones calculated from path-level data (e.g. from HRPE results). This error depends on the resolution of the channel sounder (bandwidth and directivity of the antennas). As shown in Fig. 3.4, the error is smaller in the DS, due to the large measurement bandwidth, than in the angular spreads, due to the coarse resolution of the antennas¹.

Then, since the isotropic propagation characteristic of the channel was frequently analysed, the synthesis of omni-directional (limited to the number of scans) antenna patterns from directive scans generated a low impact on the estimation of LSPs and RX power. We have shown in Fig. 3.8 that scanning steps equal to the antenna's HPBW offer an acceptable trade-off between accuracy and measurement time.

On the other hand, the multi-band validation was done by comparing the calculated LSPs

¹It is important to remark that all the parameters presented in this work, as well as the parametrization of the models, are biased by the low resolution of the measurement equipment in the angular domain. However, this is the current state of the art in the topic and results from a trade-off between measurement time and resolution.

in the different bands. As displayed in Fig. 3.4, there are systematic differences between the bands, introduced by the electronics of the measurement devices and small differences on the antenna patterns. However, these differences generated an average discrepancy of less than 10% on the DS, ASD, and ASA calculated in the different bands. The impact of this error on the inter-band analysis was considered to be minimum, validating the multi-band measurement methodology used in this work.

After validation, we have conducted systematic multi-band measurements in different scenarios of interest for 5G, with the intention of characterizing the propagation channel at high frequencies, keeping the well known sub-6 GHz channel as a reference. Most of this characterization has been empirically done in **Chapter 4**.

The results of the identification of scatterer in the environment, analysis of marginal power profiles, and LSPs, have shown that there is a large influence of the geometry of the environment: limiting walls (and buildings) are the dominating scatterers in all the scenarios. In addition, multiple relevant scenario dependent scatterers have been identified: furniture and windows in indoor, machines in industry, parked and circulating vehicles in V2V, and building facades and vegetation in outdoor scenarios. These dominant deterministic scatterers generate a high correlation on the dynamics of the LSPs: DS and ASs are well defined by the geometry of the scenarios, as shown in Fig. 4.11, Fig. 4.20, and Fig. 4.28. Moreover, Fig. 6.7 shows that the evolution of the LSPs observed in the measurements can be emulated with a deterministic location of the dominant scatterers in hybrid deterministic/stochastic models.

Measurements in V2V scenarios presented in Section 4.6 have shown the presence of a rich number of MPCs in the environment. Moreover, we have seen that vehicles simultaneously act as strong scatterers and blockers (Section 4.6.5). This introduces a high dynamics on the appearance and disappearance of the clusters during displacement of the vehicles in the surrounding environment, as seen in Fig. 4.47. Furthermore, we have observed a large impact of the vehicle size on the blockage loss and on the isotropic LSPs under blockage (Fig. 4.53). Measurements displayed in Fig. 4.48 have also shown that blockage loss increases with frequency, and depends on the distance of the blocker to the TX and/or RX.

In addition, we have observed that reflections from far buildings are within an acceptable dynamic range (Fig. 4.26 and Fig. 4.39), showing that if path-loss is correctly compensated in the radio-interface, mm-wave can cover a large distance range in outdoor applications. Moreover, the main scatterers in all the investigated scenarios are common over frequency and are traceable during displacement (Fig. 4.10, Fig. 4.32, and Fig. 4.51). This points out the real necessity of spatial consistency in channel models to test applications as localization and beam-forming.

The utilization of high directive radio-interfaces isolates scatterers/clusters in the channel. Thus, as investigated in **Chapter 5**, the radio-channel consists of a few MPCs. This results in an overall reduction in DS that depends on the scenario, frequency, and directivity, as shown in Fig. 5.3. Also, the isolation of few of MPCs produces that Doppler tends to a shift rather than spread (Fig. 5.10), which is easier to compensate with analog circuits.

Moreover, a larger bandwidth allows the resolution of paths in the delay domain. We have empirically shown that with increasing directivity and bandwidth the overall fading is re-

duced, as observed in Fig. 5.8. The statistics of small scale fading changes from Rayleigh to a distribution with deterministic components as Rician (Fig. 5.11), and the ratio of stochastic (unresolved) to deterministic (resolved) power depends on the bandwidth and directivity, as listed in Table 5.2.

On the other hand, the utilization of high directive radio-interfaces results in a link more susceptible to human shadowing. Obstruction is more severe with increasing frequency and directivity, as shown in Fig. 4.4. Therefore, the utilization of alternative beams to counteract these effects is necessary. However, these NLOSs beams result on the isolation of clusters, and the channel is defined by the scattering properties of a single scatterer, e.g., a concrete wall.

Item-level measurements have shown that with high resolution systems, the received power and polarization of specular reflections in a wall exhibits a deterministic behaviour (analytically predictable), as shown in Fig. 4.2. Here, the power in the vertical polarization is stronger than in the horizontal polarization, generating a CPR different to the unit. Moreover, measurements in a complex indoor scenario in Section 4.3.5 showed the same behaviour. The amplitude of the different polarimetric components in the channel matrix can be accurately predicted with Fresnel equations: the polarization depends on the orientation of the structures, impinging and reflected angles, and electromagnetic properties of the material. Most of the current SCMs, e.g. [4], [97], and [103], don't consider CPR as a tuning parameter and offer inaccurate realizations of the polarimetric channel matrix, which results in an over-estimation of diversity gains after beam-forming. Therefore, we have introduced in **Chapter 7** a novel modelling approach based on XPRs, CPRs, and their correlations, which generates more accurate results.

This polarimetric selective response of the scatterers causes a power imbalance of the orthogonal polarimetric channels within a NLOS beam, reducing the possible achievable gains on polarization diversity. In addition, the amount of available scatterers in the environment for spatial diversity also depends on the polarization at TX and RX. Therefore, the utilization of dual-polarized radio-interfaces increases the number of possible alternative beams, and also can be used to compensate losses due to miss-alignments of the polarimetric plane of the antennas.

Regarding multi-band modelling, the measurements have shown that the structure of the isotropic propagation channel in all the scenarios under investigation was similar in the delay and angular domain over frequencies, both in LOS and NLOS. The main scatterers are present in the different bands, with similar power, forming a common skeleton over frequency (Fig. 4.10, Fig. 4.32, and Fig. 4.51). While the “bones” are the same, more “flesh” can be found at lower frequencies product of the presence of more diffuse MPCs (Fig 4.36) and unique paths from transmission through walls. Significant reduction of DMC power with increasing frequency has been empirically observed in Section 4.5.6. The measurements in the industry scenario have shown that the difference over frequency of diffuse power was larger than the difference of specular power. Hence, a higher ratio of specular to diffuse power is observed at higher frequency.

This similar structure in the different bands generates a correlation on the LSPs over frequency. In the measurements and simulations we have observed that while the values of the

LSPs differ over frequency, they follow a similar trend on the different positions. This is the consequence of the influence of the common dominant scatterers. Therefore, we have extended the 3GPP SCM for correlated multi-band simulations in **Chapter 6**, with an approach based on the correlation of the LSPs over frequency.

8.2 Open Discussions and Future Work

There are multiple aspects that need to be further investigated once HRPE is available at mm-wave in a multi-band approach. One of these aspects are the intra-cluster characteristics: from our measurements we have seen that the main clusters are present in the different band, however, how does the inner cluster structure changes over band?

Regarding multi-band models following the 3GPP SCM guidelines, in this work and in [4], the delay and angles of the clusters are common over the different bands. Afterwards, the power of each cluster is calculated from the LSPs. However, this is accurate only if those LSPs were obtained from channels in which the clusters were exactly the same over the different bands. Therefore, a statistical analysis of common and individual clusters over frequency must be conducted in order to validate this approach, or to introduce “band-dependent” clusters. Example of individual clusters are MPCs from transmission through walls that are extremely attenuated at high frequencies, but present at sub-6 GHz. After including these individual clusters in the model with their corresponding delays and angles of arrival and departure, the influence on the LSPs needs to be evaluated. Or inversely, how to estimate from the LSPs, which portion is product of common and which one of individual clusters. Extensive RT simulations with frequency dependent parametrization in different scenarios can be used to conduct such analysis.

Finally, modelling aspects of polarization within stochastic models can be further improved by defining different nature of clusters: vertical or horizontal scatterers. The number of each of them according to scenario, visibility, band, etc, and the statistics of the PPRs individually per scatterer type also needs to be further analysed.

Bibliography

- [1] A. Osseiran, V. Braun, T. Hidekazu, P. Marsch, H. Schotten, H. Tullberg, M. A. Uusitalo, and M. Schellman, “The Foundation of the Mobile and Wireless Communications System for 2020 and Beyond: Challenges, Enablers and Technology Solutions,” in *IEEE 77th Vehicular Technology Conference (VTC Spring), 2013*, (Piscataway, NJ), pp. 1–5, IEEE, 2013.
- [2] Cisco, “Cisco Visual Networking Index: Global Mobile Data Traffic Forecast Update, 2016–2021: White Paper,” 2017.
- [3] S. Salous, V. Degli Esposti, F. Fuschini, R. S. Thomae, R. Mueller, D. Dupleich, K. Haneda, J.-M. Molina Garcia-Pardo, J. Pascual Garcia, D. P. Gaillot, S. Hur, and M. Nekovee, “Millimeter-Wave Propagation: Characterization and modeling toward fifth-generation systems. [Wireless Corner],” *IEEE Antennas and Propagation Magazine*, vol. 58, no. 6, pp. 115–127, 2016.
- [4] European Telecommunications Standards Institute, “Study on channel model for frequencies from 0.5 to 100 GHz: 3GPP TR 38.901 version 15.0.0 Release 15,” 2018.
- [5] N. Guo, R. C. Qiu, S. S. Mo, and K. Takahashi, “60-GHz Millimeter-Wave Radio: Principle, Technology, and New Results,” *EURASIP Journal on Wireless Communications and Networking*, vol. 2007, no. 1, p. 068253, 2006.
- [6] M. Kyro, J. Simola, K. Haneda, S. Ranvier, P. Vainikainen, and K.-i. Takizawa, “60 GHz Radio Channel Measurements and Modeling in a Shielded Room,” in *IEEE 71st Vehicular Technology Conference (VTC 2010-Spring), 2010*, (Piscataway, NJ), pp. 1–5, IEEE, 2010.
- [7] A. P. Garcia, W. Kotterman, U. Trautwein, D. Brückner, J. Kunisch, and R. S. Thomä, “60 GHz time-variant shadowing characterization within an Airbus 340,” in *Proceedings of the Fourth European Conference on Antennas and Propagation*, pp. 1–5, 2010.
- [8] A. P. Garcia Ariza, R. Mueller, F. Wollenschlager, A. Schulz, M. Elkhoully, Y. Sun, S. Glisic, U. Trautwein, R. Stephan, J. Muller, R. S. Thomae, and M. Hein, “60 GHz Ultrawideband Polarimetric MIMO Sensing for Wireless Multi-Gigabit and Radar,” *IEEE Transactions on Antennas and Propagation*, vol. 61, no. 4, pp. 1631–1641, 2013.
- [9] Y. Lostanlen, Y. Corre, Y. Louet, Y. Le Helloco, S. Collonge, and G. El-Zein, “Comparison of measurements and simulations in indoor environments for wireless local networks at 60 GHz,” in *IEEE 55th Vehicular Technology Conference*, (Piscataway,

- NJ), pp. 389–393, IEEE, 2002.
- [10] T. S. Rappaport, Shu Sun, R. Mayzus, Hang Zhao, Y. Azar, K. Wang, G. N. Wong, J. K. Schulz, M. Samimi, and F. Gutierrez, “Millimeter Wave Mobile Communications for 5G Cellular: It Will Work!,” *IEEE Access*, vol. 1, pp. 335–349, 2013.
- [11] H. T. Friis, “A Note on a Simple Transmission Formula,” *Proceedings of the IRE*, vol. 34, no. 5, pp. 254–256, 1946.
- [12] P. Kyosti et al., “WINNER II Channel Models: IST-4-027756 WINNER II D1.1.2 V1.1,” 2007.
- [13] W. Liu, “Wideband beamforming for multipath signals based on frequency invariant transformation,” *International Journal of Automation and Computing*, vol. 9, no. 4, pp. 420–428, 2012.
- [14] A. Richter, *Estimation of radio channel parameters: Models and algorithms*. Ilmenau: ISLE, 2005.
- [15] P. Koivumäki, S. L. H. Nguyen, K. Haneda, and G. Steinbock, “A Study of Polarimetric Diffuse Scattering at 28 GHz for a Shopping Center Facade,” in *2018 IEEE International Symposium on Personal, Indoor and Mobile Radio Communications*.
- [16] E. M. Vitucci, M. Zoli, K. Guan, B. Peng, F. Fuschini, M. Barbiroli, T. Kürner, and V. Degli Esposti, “Tri-Band Mm-wave Directional Channel Measurements in Indoor Environment,” in *2018 IEEE International Symposium on Personal, Indoor and Mobile Radio Communications*.
- [17] M. Zoli, *Radio Channel Characterization for Future Wireless Networks and Applications*. 2018.
- [18] J. Lee, K.-W. Kim, M.-D. Kim, J.-J. Park, Y. K. Yoon, and Y. J. Chong, “Measurement-Based Millimeter-Wave Angular and Delay Dispersion Characteristics of Outdoor-to-Indoor Propagation for 5G Millimeter-Wave Systems,” *IEEE Access*, vol. 7, pp. 150492–150504, 2019.
- [19] J. H. Winters, “Optimum combining in digital mobile radio with cochannel interference,” *IEEE Transactions on Vehicular Technology*, vol. 33, no. 3, pp. 144–155, 1984.
- [20] M. Agiwal, A. Roy, and N. Saxena, “Next Generation 5G Wireless Networks: A Comprehensive Survey,” *IEEE Communications Surveys & Tutorials*, vol. 18, no. 3, pp. 1617–1655, 2016.
- [21] D. Molina Bravo, *Polarimetric Wideband Beam-forming for Millimeter Wave Applications*. 2018.
- [22] D. Dupleich, *WSA 2016: 20th International ITG Workshop on Smart Antennas, March 9-11, 2016, Munich, Germany*. ITG-Fachbericht, 2016.

- [23] S. Sun, T. S. Rappaport, R. W. Heath, A. Nix, and S. Rangan, “MIMO for Millimeter-Wave Wireless Communications: Beamforming, Spatial Multiplexing, or Both?,” *IEEE Communications Magazine*, 2014.
- [24] “5G empowering vertical industries: 5G vertical sectors,” 2016.
- [25] *The 11th European Conference on Antennas and Propagation (EuCAP 2017) (EuCAP 2017)*, (Paris, France), 2017.
- [26] C. Campolo, A. Molinaro, A. Iera, and F. Menichella, “5G Network Slicing for Vehicle-to-Everything Services,” *IEEE Wireless Communications*, vol. 24, no. 6, pp. 38–45, 2017.
- [27] 5G mmWave Channel Model Alliance, “5G mmWave Channel Model Alliance - Modeling Approaches for mmWave,” 2019.
- [28] R. Mueller, R. Herrmann, D. A. Dupleich, C. Schneider, and R. S. Thomae, “Ultrawideband multichannel sounding for mm-wave,” in *2014 8th European Conference on Antennas and Propagation (EuCAP)*, pp. 817–821.
- [29] R. Herrmann and J. Sachs, “M-sequence-based ultra-wideband sensor network for vitality monitoring of elders at home,” *IET Radar, Sonar & Navigation*, vol. 9, no. 2, pp. 125–137, 2015.
- [30] F. o. E. E. Internationales Wissenschaftliches Kolloquium. Technische Universität Ilmenau, I. Technology, and . . . 07-10, “Information technology and electrical engineering - devices and systems, materials and technologies for the future,” 2009.
- [31] R. Zetik and R. S. Thoma, “Ultra-Wideband channel sounder — Design, construction and selected applications,” in *20th Telecommunications Forum (TELFOR), 2012*, (Piscataway, NJ), pp. 975–978, IEEE, 2012.
- [32] M. Haardt, *Efficient one-, two-, and multidimensional high-resolution array signal processing: Zugl.: München, Univ., Diss., 1996*. Berichte aus dem Lehrstuhl für Netzwerktheorie und Schaltungstechnik der Technischen Universität München, Aachen: Shaker, als ms. gedr ed., 1997.
- [33] B. H. Fleury, M. Tschudin, R. Heddergott, D. Dahlhaus, and K. Ingeman Pedersen, “Channel parameter estimation in mobile radio environments using the SAGE algorithm,” *IEEE Journal on Selected Areas in Communications*, vol. 17, no. 3, pp. 434–450, 1999.
- [34] K. Haneda and J. Takada, “An application of SAGE algorithm for UWB propagation channel estimation,” in *2003 IEEE Conference on Ultra Wideband Systems and Technologies*, (Piscataway, N.J), pp. 483–487, IEEE, 2003.
- [35] R. Schmidt, “Multiple emitter location and signal parameter estimation,” *IEEE Transactions on Antennas and Propagation*, vol. 34, no. 3, pp. 276–280, 1986.

- [36] M. Steinbauer, D. Hampicke, G. Sommerkorn, A. Schneider, A. F. Molisch, R. Thoma, and E. Bonek, "Array measurement of the double-directional mobile radio channel," in *VTC 2000 - Spring*, (Piscataway, NJ), pp. 1656–1662, IEEE, 2000.
- [37] R. Muller, M. Kaske, P. Rauschenbach, G. Sommerkorn, C. Schneider, F. Wollenschlager, S. Hafner, and R. S. Thoma, "Design of a circular antenna array for MIMO channel sounding application at 2.53 GHz," in *8th European Conference on Antennas and Propagation (EuCAP), 2014*, (Piscataway, NJ), pp. 239–243, IEEE, 2014.
- [38] S. Haefner and R. Thomä, "High Resolution Estimation of AoA, AoD and TdoA from MIMO Channel Sounding Measurements with Virtual Antenna Arrays: Maximum-Likelihood vs. Unitary Tensor-ESPRIT," in *International Journal of Advances in Telecommunications, Electrotechnics, Signals and Systems*.
- [39] R. Sun, P. B. Papazian, J. Senic, C. Gentile, and K. A. Remley, "Angle- and Delay-dispersion Characteristics in a Hallway and Lobby at 60 GHz," in *EuCAP 2018*, ([S. l.]), pp. 360 (5 pp.)–360 (5 pp.), EurAAP = European Association for Antennas and Propagation, 2018.
- [40] B. Hanssens, E. Tanghe, D. P. Gaillot, M. Liénard, C. Oestges, D. Plets, L. Martens, and W. Joseph, "An extension of the RiMAX multipath estimation algorithm for ultra-wideband channel modeling," *EURASIP Journal on Wireless Communications and Networking*, vol. 2018, no. 1, p. 164, 2018.
- [41] R. Herrmann Dr.-Ing., *M-sequence based ultra-wideband radar and its application to crack detection in salt mines*. PhD thesis, 2011.
- [42] D. Dupleich, R. Müller, and R. Thomä, "Practical Aspects on the Noise Floor Estimation and Cut-off Margin in Channel Sounding Applications," in *2021 15th European Conference on Antennas and Propagation (EuCAP)*, pp. 1–5, 2021.
- [43] D. He, K. Guan, A. Fricke, B. Ai, R. He, Z. Zhong, A. Kasamatsu, I. Hosako, and T. Kurner, "Stochastic Channel Modeling for Kiosk Applications in the Terahertz Band," *IEEE Transactions on Terahertz Science and Technology*, vol. 7, no. 5, pp. 502–513, 2017.
- [44] N. Boujnah, S. Ghafoor, and A. Davy, "Modeling and Link Quality Assessment of THz Network Within Data Center," in *2019 European Conference on Networks and Communications (EuCNC)*, (Piscataway, NJ), pp. 57–62, IEEE, 2019.
- [45] R. W. Heath, "Going Toward 6G [From the Editor]," *IEEE Signal Processing Magazine*, vol. 36, no. 3, pp. 3–4, 2019.
- [46] K. Haneda, S. L. H. Nguyen, A. Karttunen, J. Järveräinen, A. Bamba, R. D'Errico, J. Medbo, F. Undi, S. Jaeckel, N. Iqbal, J. Luo, M. Rybakowski, C. Diakhate, J.-M. Conrat, A. Naehring, S. Wu, A. Goulios, and E. Mellios, "Measurement results and final mmagic channel models: Specular wall reflections and diffused scattering measurements," in *Millimetre-Wave Based Mobile Radio Access Network for Fifth*

Generation Integrated Communications (mmMAGIC).

- [47] F. Fuschini, S. Häfner, M. Zoli, R. Müller, E. M. Vitucci, D. Dupleich, M. Barbiroli, J. Luo, E. Schulz, V. Degli-Esposti, and R. S. Thomä, “Item level characterization of mm-wave indoor propagation,” *EURASIP Journal on Wireless Communications and Networking*, vol. 2016, no. 1, p. 27, 2016.
- [48] P. Karadimas, B. Allen, and P. Smith, “Human Body Shadowing Characterization for 60-GHz Indoor Short-Range Wireless Links,” *IEEE Antennas and Wireless Propagation Letters*, vol. 12, pp. 1650–1653, 2013.
- [49] G. R. MacCartney, T. S. Rappaport, and S. Rangan, “Rapid Fading Due to Human Blockage in Pedestrian Crowds at 5G Millimeter-Wave Frequencies,” in *2017 IEEE Global Communications Conference (GLOBECOM)*, (Piscataway, NJ), pp. 1–7, IEEE, 2017.
- [50] M. Jacob, *The 60 GHz indoor radio channel: Overcoming the challenges of human blockage: Zugl.: @Braunschweig, Techn. Univ., Diss., 2013*, vol. 34 of *Mitteilungen aus dem Institut für Nachrichtentechnik der Technischen Universität Braunschweig*. Braunschweig and Aachen: Univ.-Bibl and Shaker, 2014.
- [51] K. Haneda, S. H. Le Nguyen, J. Jarvelainen, and J. Putkonen, “Estimating the omnidirectional pathloss from directional channel sounding,” in *2016 10th European Conference on Antennas and Propagation (EuCAP)*, pp. 1–5.
- [52] G. R. MacCartney, S. Deng, S. Sun, and T. S. Rappaport, “Millimeter-Wave Human Blockage at 73 GHz with a Simple Double Knife-Edge Diffraction Model and Extension for Directional Antennas,” in *2016 IEEE 84th Vehicular Technology Conference (VTC-Fall)*, pp. 1–6, IEEE, 2016.
- [53] W. Qi, J. Huang, J. Sun, Y. Tan, C.-X. Wang, and X. Ge, “Measurements and modeling of human blockage effects for multiple millimeter Wave bands,” in *IWCMC 2017*, (Piscataway, NJ), pp. 1604–1609, IEEE, 2017.
- [54] U. T. Virk and K. Haneda, “Modeling Human Blockage at 5G Millimeter-Wave Frequencies,” in *2018 7th MC meeting and 7th technical meeting*.
- [55] D. Dupleich, S. Haefner, C. Schneider, R. Mueller, R. S. Thoma, J. Luo, E. Schulz, X. Lu, and G. Wang, “Double-Directional and Dual-Polarimetric Indoor Measurements at 70 GHz,” *2015 IEEE 26th International Symposium on Personal Indoor and Mobile Radio Communications (PIMRC)*, 2015.
- [56] S. Haefner, D. Dupleich, R. Mueller, C. Schneider, R. S. Thoma, J. Luo, E. Schulz, X. Lu, and T. Wang, “Characterisation of Channel Measurements at 70GHz in Indoor Femtocells,” *2015 IEEE 81st Vehicular Technology Conference*, 2015.
- [57] G. R. MacCartney, T. S. Rappaport, S. Sun, and S. Deng, “Indoor Office Wideband Millimeter-Wave Propagation Measurements and Channel Models at 28 and 73 GHz

- for Ultra-Dense 5G Wireless Networks,” *IEEE Access*, vol. 3, pp. 2388–2424, 2015.
- [58] K. Haneda, J. Jarvelainen, A. Karttunen, M. Kyro, and J. Putkonen, “A Statistical Spatio-Temporal Radio Channel Model for Large Indoor Environments at 60 and 70 GHz,” *IEEE Transactions on Antennas and Propagation*, p. 1, 2015.
- [59] C. Gustafson, K. Haneda, S. Wyne, and F. Tufvesson, “On mm-Wave Multipath Clustering and Channel Modeling,” *IEEE Transactions on Antennas and Propagation*, vol. 62, no. 3, pp. 1445–1455, 2014.
- [60] S. Nie, G. R. MacCartney, S. Sun, and T. S. Rappaport, “72 GHz Millimeter Wave Indoor Measurements for Wireless and Backhaul Communications,” *IEEE 24th International Symposium on Personal, Indoor and Mobile Radio Communications: Mobile and Wireless Networks*, 2013.
- [61] L. Pometcu and R. D’Errico, “Characterization of sub-THz and mmWave Propagation Channel for Indoor Scenarios,” in *EuCAP 2018*, ([S. l.]), pp. 632 (4 pp.)–632 (4 pp.), EurAAP = European Association for Antennas and Propagation, 2018.
- [62] D. Dupleich, R. Müller, S. Skoblikov, C. Schneider, J. Luo, G. Del Galdo, and R. Thomä, “Multi-band Indoor Propagation Characterization by Measurements from 6 to 60 GHz,” in *Submitted to 13th European Conference on Antennas and Propagation (EuCAP 2019)*.
- [63] D. Dupleich, R. Muller, S. Skoblikov, J. Luo, G. Del Galdo, and R. S. Thoma, “Multi-band Double-directional 5G Street Canyon Measurements in Germany,” in *2019 European Conference on Networks and Communications (EuCNC)*, (Piscataway, NJ), pp. 123–127, IEEE, 2019.
- [64] S. Priebe, C. Jastrow, M. Jacob, T. Kleine-Ostmann, T. Schrader, and T. Kurner, “Channel and Propagation Measurements at 300 GHz,” *Antennas and Propagation, IEEE Transactions on*, vol. 59, no. 5, pp. 1688–1698, 2011.
- [65] S. Nguyen, J. Jarvelainen, A. Karttunen, K. Haneda, and J. Putkonen, “Comparing Radio Propagation Channels Between 28 and 140 GHz Bands in a Shopping Mall,” in *EuCAP 2018*, ([S. l.]), pp. 515 (5 pp.)–515 (5 pp.), EurAAP = European Association for Antennas and Propagation, 2018.
- [66] S. L. H. Nguyen, J. Medbo, M. Peter, A. Karttunen, K. Haneda, A. Bamba, R. D’Errico, N. Iqbal, C. Diakhate, and J.-M. Conrat, “On the Frequency Dependency of Radio Channel’s Delay Spread: Analyses and Findings From mmMAGIC Multi-frequency Channel Sounding,” in *2018 12th European Conference on Antennas and Propagation (EuCAP)*.
- [67] U. T. Virk, S. L. H. Nguyen, and K. Haneda, “Multi-frequency power angular spectrum comparison for an indoor environment,” in *2017 11th European Conference on Antennas and Propagation (EUCAP)*, (Piscataway, NJ), pp. 3389–3393, IEEE, 2017.

- [68] E. M. Vitucci, M. Zoli, F. Fuschini, M. Barbiroli, V. Degli-Esposti, K. Guan, B. Peng, and T. Kuerner, "Tri-Band Mm-wave Directional Channel Measurements in Indoor Environment," in *2018 IEEE 29th Annual International Symposium on Personal, Indoor, and Mobile Radio Communications (PIMRC)*, (Piscataway, NJ), pp. 205–209, IEEE, 2018.
- [69] S. Sun, T. S. Rappaport, T. A. Thomas, A. Ghosh, H. C. Nguyen, I. Z. Kovacs, I. Rodriguez, O. Koymen, and A. Partyka, "Investigation of Prediction Accuracy, Sensitivity, and Parameter Stability of Large-Scale Propagation Path Loss Models for 5G Wireless Communications," *IEEE Transactions on Vehicular Technology*, vol. 65, no. 5, pp. 2843–2860, 2016.
- [70] X. Raimundo, S. El-Faitori, and S. Salous, "Multi-band Outdoor Measurements in a Residential Environment for 5G Networks," in *2018 12th European Conference on Antennas and Propagation (EuCAP)*.
- [71] M. Sasaki, M. Nakamura, W. Yamada, N. Kita, Y. Takatori, Inomta, minoru, K. Kitao, and T. Imai, "Path Loss Characteristics From 2 to 66 GHz in Urban Macrocell Environments Based on Analysis using ITU-R Site-General Models," *12th European Conference on Antennas and Propagation (EuCAP)*, 2018.
- [72] T. S. Rappaport, F. Gutierrez, E. Ben Dor, J. N. Murdock, Q. Yijun, and J. I. Tamir, "Broadband Millimeter-Wave Propagation Measurements and Models Using Adaptive-Beam Antennas for Outdoor Urban Cellular Communications," *Antennas and Propagation, IEEE Transactions on*, vol. 61, no. 4, pp. 1850–1859, 2013.
- [73] T. S. Rappaport, G. R. MacCartney, M. K. Samimi, and S. Sun, "Wideband Millimeter-Wave Propagation Measurements and Channel Models for Future Wireless Communication System Design," *IEEE Transactions on Communications*, vol. 63, no. 9, pp. 3029–3056, 2015.
- [74] S. Hur, S. Baek, B. Kim, Y. Chang, A. F. Molisch, T. S. Rappaport, K. Haneda, and J. Park, "Proposal on Millimeter-Wave Channel Modeling for 5G Cellular System," *IEEE Journal of Selected Topics in Signal Processing*, vol. 10, no. 3, pp. 454–469, 2016.
- [75] R. J. Weiler, M. Peter, T. Kühne, M. Wisotzki, and W. Keusgen, "Simultaneous millimeter-wave multi-band channel sounding in an urban access scenario," in *2015 9th European Conference on Antennas and Propagation (EuCAP)*, pp. 1–5, 2015.
- [76] F. Griffiths and M. Ooi, "The fourth industrial revolution - Industry 4.0 and IoT [Trends in Future I&M]," *IEEE Instrumentation & Measurement Magazine*, vol. 21, no. 6, pp. 29–43, 2018.
- [77] J. Narrainen and R. D'Errico, "Channel characterization in industrial environment with high clutter," in *CA15104 TD(19)10034*.
- [78] E. Tanghe, W. Joseph, L. Verloock, L. Martens, H. Capoen, K. Herwegen, and

- W. Vantomme, "The industrial indoor channel: large-scale and temporal fading at 900, 2400, and 5200 MHz," *IEEE Transactions on Wireless Communications*, vol. 7, no. 7, pp. 2740–2751, 2008.
- [79] S. Jaeckel, T. Heyn, N. Turay, L. Raschkowski, L. Thiele, R. Vuoltoniemi, M. Sonkki, V. Hovinen, F. Burkhardt, and P. Karunakaran, "Industrial Indoor Measurements from 2-6 GHz for the 3GPP-NR and QuaDRiGa Channel Model," in *2019 IEEE 90th Vehicular Technology Conference (VTC2019-Fall)*, pp. 1–7, IEEE, 9/22/2019 - 9/25/2019.
- [80] D. Solomitchii, A. Orsino, S. Andreev, Y. Koucheryavy, and M. Valkama, "Characterization of mmWave Channel Properties at 28 and 60 GHz in Factory Automation Deployments," in *2018 IEEE Wireless Communications and Networking Conference (WCNC)* (I. WCNC, ed.), (Piscataway, NJ), pp. 1–6, IEEE, 2018.
- [81] E. M. Vitucci, V. Degli-Esposti, F. Mani, F. Fuschini, M. Barbiroli, M. Gan, C. Li, J. Zhao, and Z. Zhong, "Tuning Ray Tracing for Mm-wave Coverage Prediction in Outdoor Urban Scenarios," *Radio Science*, vol. 54, no. 11, pp. 1112–1128, 2019.
- [82] D. Dupleich, R. Muller, S. Skoblikov, C. Schneider, J. Luo, M. Boban, G. Del Galdo, and R. Thoma, "Multi-band Characterization of Path-loss, Delay, and Angular Spread in V2V Links," in *2018 IEEE 29th Annual International Symposium on Personal, Indoor, and Mobile Radio Communications (PIMRC)*, (Piscataway, NJ), pp. 85–90, IEEE, 2018.
- [83] D. Dupleich, F. Fuschini, R. Mueller, E. Vitucci, C. Schneider, V. Degli Esposti, and R. S. Thoma, "Directional characterization of the 60 GHz indoor-office channel," in *2014 XXXIth URSI General Assembly and Scientific Symposium (URSI GASS)*, pp. 1–4.
- [84] D. Dupleich, R. Mueller, S. Skoblikov, C. Schneider, J. Luo, G. Del Galdo, and R. S. Thoma, "Multi-band Indoor Propagation Characterization by Measurements from 6 to 60 GHz," in *European Conference on Antennas and Propagation, European Association on Antennas and Propagation (EuCAP 2019)*.
- [85] M. Giordani, A. Zanella, and M. Zorzi, "Millimeter wave communication in vehicular networks: Challenges and opportunities," in *2017 6th International Conference on Modern Circuits and Systems Technologies (MOCAS)*, (Piscataway, NJ), pp. 1–6, IEEE, 2017.
- [86] M. Boban, D. Dupleich, N. Iqbal, J. Luo, C. Schneider, R. Muller, Z. Yu, D. Steer, T. Jamsa, J. Li, and R. S. Thoma, "Multi-Band Vehicle-to-Vehicle Channel Characterization in the Presence of Vehicle Blockage," *IEEE Access*, vol. 7, pp. 9724–9735, 2019.
- [87] V. Nurmela, A. Karttunen, A. Roivainen, L. Raschkowski, T. Imai, J. Jarvelainen, J. Medbo, J. Vihriala, J. Meinila, K. Haneda, V. Hovinen, J. Ylitalo, N. Omaki, K. Kusume, P. Kyosti, T. Jamsa, A. Hekkala, R. Weiler, and M. Peter, "METIS Channel Models: Deliverable D1.4," 2015.

- [88] M. K. Samimi, G. R. MacCartney, S. Sun, and T. S. Rappaport, “28 GHz Millimeter-Wave Ultrawideband Small-Scale Fading Models in Wireless Channels,” in *2016 IEEE 83rd Vehicular Technology Conference (VTC Spring)*, pp. 1–6.
- [89] E. Zöchmann, S. Caban, C. F. Mecklenbräuker, S. Pratschner, M. Lerch, S. Schwarz, and M. Rupp, “Better than Rician: Modelling millimetre wave channels as Two-Wave with Diffuse Power,” 2018.
- [90] N. Iqbal, J. Luo, C. Schneider, D. Dupleich, S. Haefner, R. Müller, and R. S. Thomä, “Frequency and Bandwidth Dependence of Millimeter Wave Ultra-Wide-Band Channels,” in *2017 11th European Conference on Antennas and Propagation (EUCAP) (EuCAP 2017)*, (Paris, France), 2017.
- [91] D. Dupleich, R. Müller, S. Skoblikov, C. Schneider, M. Boban, J. Luo, G. Del Galdo, and R. S. Thomä, “Multi-band Spatio-Temporal Characterization of a V2V Environment Under Blockage,” in *EuCAP 2018*, ([S. 1.]), pp. 366 (5 pp.)–366 (5 pp.), EurAAP = European Association for Antennas and Propagation, 2018.
- [92] B. Allen, W. Q. Malik, and D. J. Edwards, “Bandwidth-dependent modelling of small-scale fade depth in wireless channels,” *IET Microwaves, Antennas & Propagation*, vol. 2, no. 6, pp. 519–528, 2008.
- [93] D. Dupleich, N. Iqbal, C. Schneider, S. Haefner, R. Müller, S. Skoblikov, J. Luo, and R. S. Thomä, “Investigations on Fading Scaling with Bandwidth and Directivity at 60 GHz,” in *The 11th European Conference on Antennas and Propagation (EuCAP 2017) (EuCAP 2017)*, (Paris, France), 2017.
- [94] F. D. Cardoso, M. M. Ferreira, S. J. Ambroziak, and L. M. Correia, “A Wideband Channel Model for Body Area Networks in Circular Metallic Indoor Environments,” *IEEE Access*, vol. 9, pp. 73791–73798, 2021.
- [95] S. Jaeckel, L. Raschkowski, F. Burkhardt, and L. Thiele, “Efficient Sum-of-Sinusoids-Based Spatial Consistency for the 3GPP New-Radio Channel Model,” in *2018 IEEE Globecom Workshops (GC Wkshps)*, pp. 1–7, 2018.
- [96] M. Kurras, S. Dai, S. Jaeckel, and L. Thiele, “Evaluation of the Spatial Consistency Feature in the 3GPP Geometry-Based Stochastic Channel Model,” in *2019 IEEE Wireless Communications and Networking Conference (WCNC)*, pp. 1–6, 2019.
- [97] L. Liu, C. Oestges, J. Poutanen, K. Haneda, P. Vainikainen, F. Quitin, F. Tufvesson, and P. Doncker, “The COST 2100 MIMO channel model,” *IEEE Wireless Communications*, vol. 19, no. 6, pp. 92–99, 2012.
- [98] A. Maltsev, A. Puduev, I. Bolotin, G. Morozov, I. Karls, M. Faerber, I. Siaud, A.-M. Ulmer-Moll, J.-M. Conrat, R. Weiler, M. Peter, and W. Keusgen, “WP5: Propagation, Antenna and Multi-Antenna Techniques: D5.1: Channel Modeling and Characterization,” 2014.

- [99] A. Maltsev, A. Pudeyev, I. Bolotin, G. Morozov, I. Karls, M. Faerber, I. Siaud, A.-M. Ulmer-Moll, J.-M. Conrat, R. J. Weiler, M. Peter, and W. Keusgen, “WP5: Propagation, Antennas and Multi-Antenna Techniques: D5.1: Channel Modelling and Characterization.”
- [100] K. Sato, T. Manabe, T. Ihara, H. Saito, S. Ito, T. Tanaka, K. Sugai, N. Ohmi, Y. Murakami, M. Shibayama, Y. Konishi, and T. Kimura, “Measurements of reflection and transmission characteristics of interior structures of office building in the 60-GHz band,” *IEEE Transactions on Antennas and Propagation*, vol. 45, no. 12, pp. 1783–1792, 1997.
- [101] A. Karttunen, C. Gustafson, A. F. Molisch, J. Jarvelainen, and K. Haneda, “Censored Multipath Component Cross-Polarization Ratio Modeling,” *IEEE Wireless Communications Letters*, p. 1, 2016.
- [102] C. Gustafson, D. Bolin, and F. Tufvesson, “Modeling the Polarimetric mm-Wave Propagation Channel Using Censored Measurements,” in *2016 IEEE Global Communications Conference (GLOBECOM)*, (Piscataway, NJ), pp. 1–6, IEEE, 2016.
- [103] S. Jaeckel, L. Raschkowski, K. Borner, and L. Thiele, “QuaDRiGa: A 3-D Multi-Cell Channel Model With Time Evolution for Enabling Virtual Field Trials,” *IEEE Transactions on Antennas and Propagation*, vol. 62, no. 6, pp. 3242–3256, 2014.
- [104] C. Oestges, B. Clerckx, M. Guillaud, and M. Debbah, “Dual-polarized wireless communications: From propagation models to system performance evaluation,” *IEEE Transactions on Wireless Communications*, vol. 7, no. 10, pp. 4019–4031, 2008.
- [105] S. Jaeckel, K. Borner, L. Thiele, and V. Jungnickel, “A Geometric Polarization Rotation Model for the 3-D Spatial Channel Model,” *IEEE Transactions on Antennas and Propagation*, vol. 60, no. 12, pp. 5966–5977, 2012.
- [106] D. Dupleich, R. Müller, N. Han, S. Häfner, C. Schneider, J. Luo, G. Del Galdo, and R. S. Thoma, “Polarization in Spatial Channel Models at mm-Waves: a Correlation Based Approach,” in *2019 13th European Conference on Antennas and Propagation*.
- [107] P. Bello, “Characterization of Randomly Time-Variant Linear Channels,” *IEEE Transactions on Communications*, vol. 11, no. 4, pp. 360–393, 1963.
- [108] B. H. Fleury, “First- and second-order characterization of direction dispersion and space selectivity in the radio channel,” *IEEE Transactions on Information Theory*, vol. 46, no. 6, pp. 2027–2044, 2000.
- [109] G. Del Galdo, “Geometry-Based Channel Modeling for Multi-User MIMO Systems and Applications,” 2008.
- [110] A. F. Molisch, “Ultrawideband Propagation Channels-Theory, Measurement, and Modeling,” *IEEE Transactions on Vehicular Technology*, vol. 54, no. 5, pp. 1528–1545, 2005.

- [111] B. Sklar, "Rayleigh fading channels in mobile digital communication systems .I. Characterization," *IEEE Communications Magazine*, vol. 35, no. 7, pp. 90–100, 1997.
- [112] ITU-R, "Effects of building materials and structures on radiowave propagation above about 100 MHz: Recommendation ITU-R P.2040-1,"
- [113] T. S. Rappaport, Q. Yijun, J. I. Tamir, J. N. Murdock, and E. Ben Dor, "Cellular broadband millimeter wave propagation and angle of arrival for adaptive beam steering systems (invited paper)," in *Radio and Wireless Symposium (RWS), 2012 IEEE*, pp. 151–154, 2012.
- [114] S. Sun, T. S. Rappaport, T. A. Thomas, and A. Ghosh, "A Preliminary 3D mmWave Indoor Office Channel Model," *International Workshop on Emerging MIMO Technologies with 2D Antenna Array for 4G LTE-Advanced and 5G, ICNC Workshop*, 2015.
- [115] W. C. Y. Lee, *Mobile cellular telecommunications systems: Analog and digital systems*. New York u.a.: McGraw-Hill, 2. ed. ed., 1995.
- [116] G. D. Durgin, T. S. Rappaport, and D. A. de Wolf, "New analytical models and probability density functions for fading in wireless communications," *IEEE Transactions on Communications*, vol. 50, no. 6, pp. 1005–1015, 2002.
- [117] P. Almers, E. Bonek, A. Burr, N. Czink, M. Debbah, V. Degli-Esposti, H. Hofstetter, P. Kyösti, D. Laurenson, G. Matz, A. F. Molisch, C. Oestges, and H. Özcelik, "Survey of Channel and Radio Propagation Models for Wireless MIMO Systems," *EURASIP Journal on Wireless Communications and Networking*, vol. 2007, no. 1, p. 019070, 2007.
- [118] 3rd Generation Partnership Project, "Spatial channel model for Multiple Input Multiple Output (MIMO) simulations (Release 9): 3GPP TR 25.996 V9.0.0," 2009.
- [119] R. J. Weiler, M. Peter, W. Keusgen, A. Maltsev, I. Karls, A. Pudueyev, I. Bolotin, I. Siaud, and A.-M. Ulmer-Moll, "Quasi-deterministic millimeter-wave channel models in MiWEBA," *EURASIP Journal on Wireless Communications and Networking*, vol. 2016, no. 1, p. 74, 2016.
- [120] 5G mmWave Channel Model Alliance, "Verification Techniques for mmWave Channel Sounders: Activities of the 5G mmWave Channel Model Alliance," 2019.
- [121] V. Degli-Esposti and H. L. Bertoni, "Evaluation of the role of diffuse scattering in urban microcellular propagation," in *1999 IEEE 50th Vehicular Technology Conference, (Piscataway)*, pp. 1392–1396, I E E E, Sept. 1999.
- [122] V. Degli-Esposti, F. Fuschini, E. M. Vitucci, and G. Falciasecca, "Measurement and Modelling of Scattering From Buildings," *Antennas and Propagation, IEEE Transactions on*, vol. 55, no. 1, pp. 143–153, 2007.
- [123] F. Mani, E. M. Vitucci, M. Barbiroli, F. Fuschini, V. Degli Esposti, M. Gan, C. Li,

- J. Zhao, and Z. Zhong, “26GHz ray-tracing pathloss prediction in outdoor scenario in presence of vegetation,” in *EuCAP 2018*, ([S. l.]), pp. 25 (5 pp.)–25 (5 pp.), EurAAP = European Association for Antennas and Propagation, 2018.
- [124] A. Saleh and R. Valenzuela, “A Statistical Model for Indoor Multipath Propagation,” *IEEE Journal on Selected Areas in Communications*, vol. 5, no. 2, pp. 128–137, 1987.
- [125] A. O. Martinez, P. Eggers, and E. d. Carvalho, “Geometry-Based Stochastic Channel Models for 5G: Extending Key Features for Massive MIMO,” *CoRR*, vol. abs/1609.05639, 2016.
- [126] D. Dupleich, E. Schäfer, G. Del Galdo, and R. Thomä, “Influence of System Aspects in Propagation Based Evaluation of Beam-forming at mm-Waves,” in *EuCAP 2018*, ([S. l.]), pp. 404 (5 pp.)–404 (5 pp.), EurAAP = European Association for Antennas and Propagation, 2018.
- [127] D. Dupleich, R. Muller, C. Schneider, S. Skoblikov, J. Luo, M. Boban, G. Del Galdo, and R. Thoma, “Multi-Band Vehicle to Vehicle Channel Measurements from 6 GHz to 60 GHz at "T" Intersection,” in *2019 IEEE 2nd Connected and Automated Vehicles Symposium (CAVS)*, pp. 1–5, 2019.
- [128] S. Jaeckel, L. Raschkowski, S. Wu, L. Thiele, and W. Keusgen, “An Explicit Ground Reflection Model for mm-Wave Channels,” in *2017 IEEE Wireless Communications and Networking Conference Workshops (WCNCW)*, pp. 1–5, 2017.
- [129] A. Maltsev, V. Erceg, E. Perahia, C. Hansen, R. Maslennikov, A. Lomayev, A. Sevastyanov, A. Khoryaev, G. Morozov, M. Jacob, S. Priebe, T. Kürner, K. Sato, H. Sawada, and H. Harada, “Channel Models for 60 GHz WLAN Systems,” *IEEE802.11ad 09/0334r8*, 2010.
- [130] A. Maltsev, R. Maslennikov, A. Lomyev, A. Sevasytanov, and A. Khoryaev, “Statistical Channel Model for 60 GHz WLAN Systems in Conference Room Environment,” *Radioengineering*, vol. 20, no. 2, June 2011.
- [131] R. Sun, P. B. Papazian, J. Senic, Y. Lo, J.-K. Choi, K. A. Remley, and C. Gentile, “Design and calibration of a double-directional 60 GHz channel sounder for multipath component tracking,” in *2017 11th European Conference on Antennas and Propagation (EUCAP)*, (Piscataway, NJ), pp. 3336–3340, IEEE, 2017.
- [132] J. Sachs, R. Herrmann, and M. Kmec, “Time and range accuracy of short-range ultra-wideband pseudo-noise radar,” *Applied Radio Electronics*, vol. 12, pp. 105–113, 2013.
- [133] H. Niu, D. Dupleich, R. Mueller, S. Skoblikov, C. Schneider, G. Del Galdo, and R. Thomae, “Hybrid Ray Tracing Method for Millimeter Wave Propagation Simulation in Large Indoor Scenarios,” in *WSA 2019; 23rd International ITG Workshop on Smart Antennas*, pp. 1–6, 2019.

A The Multipath Propagation and Radio Channel

Overview

This chapter addresses the fundamental description of propagation and radio channels. Firstly, we introduce the basic terminology and equations describing propagation. Secondly, we describe the effects of considering antennas on the description of the channel. We finally conclude this chapter with an example showing the impairments of multi-path propagation and the effect of considering different system aspects as antenna directivity, polarization, and bandwidth.

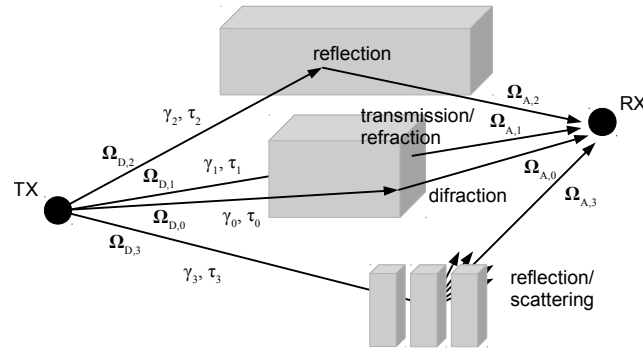


Figure A.1: Propagation mechanisms and multi-path channel.

A.1 Propagation Mechanisms

While the propagation of electromagnetic waves can be described using Maxwell equations, normally we appeal to some simplifications in order to reduce models complexity and also computation time. Let us approximate spherical waves to plane waves in the far field (at distances larger than the Fraunhofer distance). Under this assumption, we can define the wave-front as a locus in which the electromagnetic field has constant phase. Let us now denominate *ray* to the curve that is perpendicular to the wave-front. A ray describes the *path* that a wave-front follows during propagation. While in free-space rays are rectilinear, in presence of obstacles rays are piecewise rectilinear.

Considering the aforementioned simplification, we can describe the propagation between two points by means of a multi-path channel as shown in Fig. A.1. The shortest physical path is called the LOS component. It worth to remark, that the LOS component can be partially obstructed or completely blocked. In those scenarios, we refer to OLOS and NLOS, respectively. The interactions between the electromagnetic waves and the scatterers can be classified as follows:

Reflection, refraction, and transmission When an electromagnetic wave encounters a smooth interface (border region between two isotropic media), one part of the signal is reflected back to the incident media, and the other part is refracted (transmitted) inside of the media. Specular reflections generate SMC. Fresnel's equations describe which part is reflected and which part is refracted (transmitted).

Specular reflections occur when the reflected angle ϕ_r equals the incident angle ϕ_i . On the other hand, there is a change on the direction of the electromagnetic wave travelling inside of the media which is defined by Snell's law: the relation of the incident and refracted (transmitted) angles, ϕ_i and ϕ_t respectively, can be calculated as

$$n_i \sin(\phi_i) = n_t \sin(\phi_t), \quad (\text{A.1})$$

where n_i and n_t are the refractive coefficients of the isotropic media in the interface.

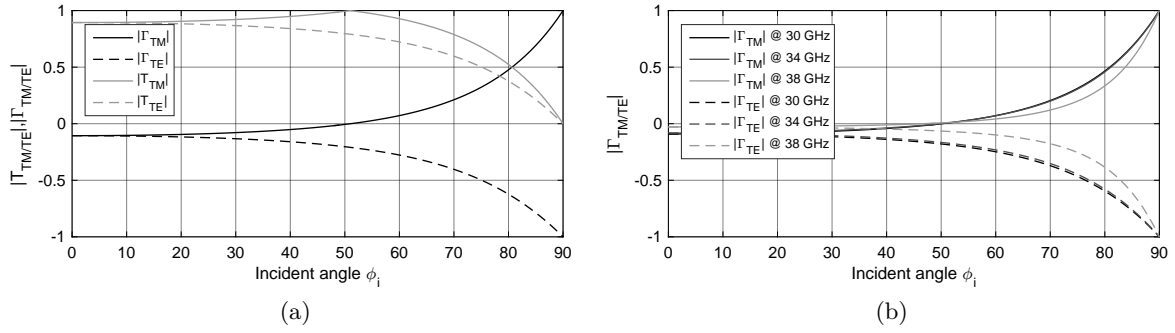


Figure A.2: Reflection and transmission coefficients for air to concrete interface (a) at 26.5 GHz, and (b) reflection coefficient for different carrier frequency.

Electromagnetic waves are attenuated by passing through different media. This attenuation depends, between others, on the material properties, incident angle, polarization, and wavelength of the impinging waves. The polarization of the electric field of the electromagnetic wave is defined as perpendicular (TE) to the plane containing the incident, reflected, and refracted rays, or parallel (TM) to the aforementioned plane. In lossless materials, due to the law of energy conservation, what is not transmitted is reflected back:

$$T_{TE/TM}^2 = 1 - \Gamma_{TE/TM}^2, \quad (\text{A.2})$$

where $T_{TE/TM}$ and $\Gamma_{TE/TM}$ are the transmission and reflection coefficients, respectively. On the other hand, in lossy materials, part of the energy is dissipated inside of the material. Fig. A.2 shows the theoretical variation of the coefficients for different incident angles and polarizations. It worth to point out the role of polarization: two signals with the same incident angle into the same medium, but different polarizations, reflect different power. Empirical results in a controlled environment validating these behaviour at 70 GHz are introduced in Section 4.1.2, and the influence in complex indoor scenarios at different frequencies are addressed in Section 4.3.4 and Section 4.3.5.

Furthermore, there is a specific incident angle in which $\Gamma_{TM}(\phi_i) = 0$. This angle is known as the Brewster's angle, and depends on the refraction index of the media in the interface:

$$\phi_B = \tan^{-1}(n_t/n_i). \quad (\text{A.3})$$

A TM polarized wave impinging at this angle will not be reflected. In the example in Fig. A.2, this angle is close to 50° in the different frequencies. This filtering phenomena is known as *polarization by reflection*

Since one of the conditions for specular reflections is a smooth surface, it is expected an increment on the number of reflections with increasing frequencies (shorter wavelength), since more objects become smooth to the wave-fronts. Furthermore, since specular reflections are the strongest in terms of power, the mm-wave channel is expected to be dominated by SMC. An empirical comparison between the ratio of SMC and DMC power at sub-6 GHz and mm-wave in industrial scenarios is introduced in Section 4.5.6.

Furthermore, as transmission loss of most of the materials increases with the wavelength, mm-wave communications are mostly limited to intra-room communications. Measurements of the blockage loss at 70 GHz of different items are introduced in Section 4.1.3.

Diffraction In order to be diffracted, electromagnetic waves need to encounter an obstacle or slit comparable to the wavelength. It is generated by the interference of waves following the Huygens-Fresnel principle. Diffraction is the reason why waves bent around edges facilitating coverage in NLOS conditions. Measurements in indoor and outdoor scenarios showing this effect are introduced in Section 4.3.4 and Section 4.6.2, respectively.

Scattering When an electromagnetic wave encounters a rough surface, it is not only reflected as a specular component, but it is also scattered in multiple directions. Since the roughness of a surface depends on the wavelength of the impinging wave, between others, less scattering is expected at mm-wave: objects that at low frequencies show a rough surface, are seen as a smooth surfaces at mm-wave. An empirical comparison between specular and diffuse scattering at 70 GHz is introduced in Section 4.1.1.

A.2 The Multi-path Propagation Channel

The propagation mechanisms mentioned in the previous section are summarized in Fig. A.1. We can observe that the radio waves reach the RX by multiple paths. Each of these paths has the following properties:

- propagation delay, also known as TDoA τ ,
- complex gain resulting of reflection/scattering, diffraction, or transmission γ ,
- DoD Ω_D and DoA Ω_A , and
- Doppler shift ν experienced by the mobility of the TX, RX, or scatterers.

The RX signal $x(t)$ is the vectorial summation (amplitude and phase) of multiple scaled, delayed, and phase shifted copies of the TX signal $s(t)$:

$$\begin{aligned}
 x(t) &= \gamma_0 \cdot s(t - \tau_0) \cdot e^{j2\pi\nu_1 t} + \dots + \gamma_3 \cdot s(t - \tau_3) \cdot e^{j2\pi\nu_3 t}, \\
 &= \sum_{l=1}^L \gamma_l \cdot s(t - \tau_l) \cdot e^{j2\pi\nu_l t}, \\
 &= \int_{\mathbb{R}} s(t) \cdot \sum_{l=0}^{L-1} \gamma_l \cdot e^{j2\pi\nu_l t} \cdot \delta(t - \tau_l) d\tau, \\
 &= s(t) * h(t, \tau),
 \end{aligned} \tag{A.4}$$

where $h(t, \tau)$ is the so called time varying CIR, consisting of a train of delta functions. This

models the time dispersion (propagation delay) characteristic of the channel as a consequence of the multi-path nature of the propagations. $h(t, \tau)$ is normally described as a time varying CIR consisting of L MPC:

$$h(t, \tau) = \sum_{l=0}^{L-1} \gamma_l \delta(\tau - \tau_l) e^{j2\pi\nu_l t}. \quad (\text{A.5})$$

Although being (A.4) a discrete and very simplified representation of a more complex continuous physic phenomena, it is still widely used and offers a good framework to analyse communication systems. This model contains all the different propagation mechanisms aforementioned, and is suitable to be parametrized with channel predictions from tools as RT or measurements.

In the next subsection, the duality between spreading and selectivity are analysed in the different domains of the propagation channel.

A.2.1 Deterministic Description of the Propagation Channel: First Set of Bello Equations

Spreading Functions

Bello introduced in his seminal work in the 60's a framework for the characterization of single-input/single-output (SISO) linear time variant systems, [107]. By that time, the propagation channel was represented only in the time and propagation delay domains. The input/output relation of the time dispersive channel $h(t, \tau)$ is computed by the system equation

$$x(t) = \int_{\mathbb{R}} h(t, \tau) s(t - \tau) d\tau. \quad (\text{A.6})$$

In the presence of a stationary channel, the system becomes LTI and (A.6) can be re-written as

$$x(t) = \int_{\mathbb{R}} h(\tau) s(t - \tau) d\tau, \quad (\text{A.7})$$

which is the convolution of the channel with the TX signal. In most of the applications, for a simplified and more harmonious mathematical description, the channel is considered time-invariant during the observation time. The Fourier transform and inverse transform of the propagation channel in the different domains defines the 4 equations of the original set of Bello functions:

$$\begin{aligned} h(t, f) &= \int_{\mathbb{R}} h(t, \tau) e^{j2\pi f\tau} d\tau, \\ h(\nu, f) &= \int_{\mathbb{R}} h(t, f) e^{-j2\pi\nu t} dt, \end{aligned}$$

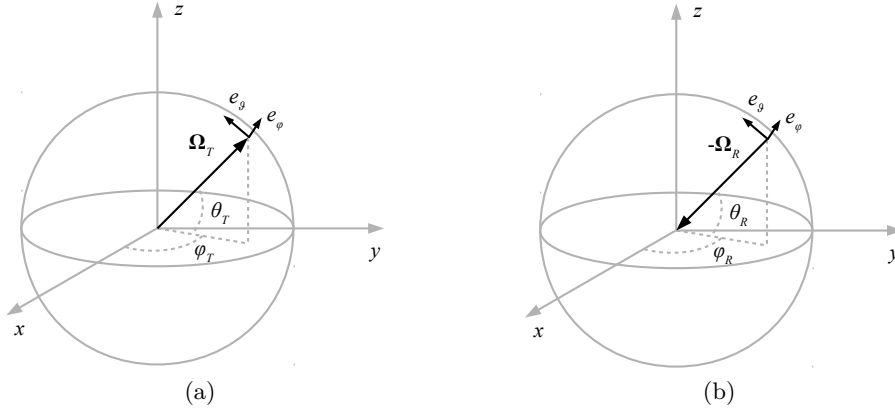


Figure A.3: Spherical coordinate system and polarization at (a) TX and (b) RX.

$$\begin{aligned}
 h(\nu, \tau) &= \int_{\mathbb{R}} h(\nu, f) e^{j2\pi f\tau} df, \\
 h(t, \tau) &= \int_{\mathbb{R}} h(\nu, \tau) e^{j2\pi\nu t} d\nu.
 \end{aligned} \tag{A.8}$$

With the advent of multi-antenna systems, the spatial information became necessary to fully characterize the propagation channel. Furthermore, several applications were now capable of utilizing directions of arrival and departure of the electromagnetic waves with different purposes, from channel sounding to beam-forming. Fleury was who extended in the early 2000's this set of equations considering the spatial domain, [108]. While in his work he only addressed the angular domain at the RX side of the link, [109] considers the spatial properties at both sides of the link.

Let us extend the multi-path CIR in (A.5) considering the DoD and DoA assuming isotropic radiators:

$$h(t, \tau, \mathbf{\Omega}_D, \mathbf{\Omega}_A) = \sum_{l=0}^{L-1} \gamma_l \delta(\tau - \tau_l) \delta(\mathbf{\Omega}_D - \mathbf{\Omega}_{D,l}) \delta(\mathbf{\Omega}_A - \mathbf{\Omega}_{A,l}) e^{j2\pi\nu_l t}, \tag{A.9}$$

where $\mathbf{\Omega}_{D,l}$ is the DoD and $\mathbf{\Omega}_{A,l}$ is DoA the l^{th} MPC. The directional dimension is described by the vector $\mathbf{\Omega} \in \mathcal{S}^2 \subset \mathbb{R}^3$:

$$\mathbf{\Omega} = [\cos(\theta) \cdot \cos(\phi), \quad \cos(\theta) \cdot \sin(\phi), \quad \sin(\theta)]^T, \tag{A.10}$$

which is the transformation from the spherical coordinate system \mathcal{S}^2 with $\Omega = \{\phi, \theta\}$ being the azimuth and elevation, to Cartesian coordinates, where $\mathbf{\Omega} = \{x, y, z\} \in \mathbb{R}^3$ satisfies the condition $\|\mathbf{\Omega}\|_F^2 = 1$. A more clear representation is shown in Fig. A.3.

The spatial domain is related to the angular domain also by the multidimensional Fourier transform:

$$h(t, \tau, \mathbf{p}_T, \mathbf{p}_R) = \int_{\mathcal{S}^2} \int_{\mathcal{S}^2} h(t, \tau, \mathbf{\Omega}_D, \mathbf{\Omega}_A) e^{j\frac{2\pi}{\lambda} \mathbf{\Omega}_D^T \cdot \mathbf{p}_T} e^{j\frac{2\pi}{\lambda} \mathbf{\Omega}_A^T \cdot \mathbf{p}_R} d\mathbf{\Omega}_D d\mathbf{\Omega}_A, \tag{A.11}$$

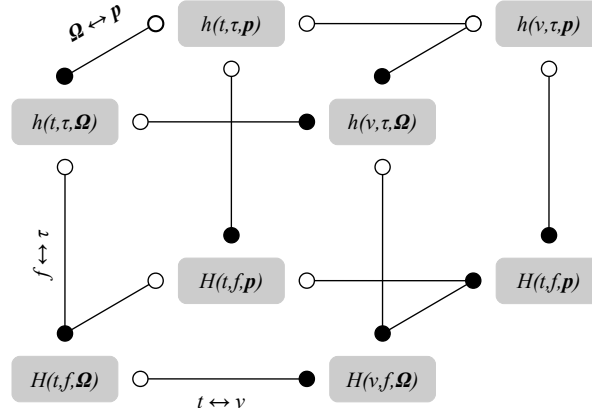


Figure A.4: Fourier relationships between the different Bello functions.

where \mathbf{p}_T and \mathbf{p}_R are the local Cartesian coordinates at the TX and RX, respectively. The angular spreading function can be computed back from (A.12) by its inverse Fourier transform:

$$h(t, \tau, \boldsymbol{\Omega}_D, \boldsymbol{\Omega}_A) = \frac{1}{\lambda} \frac{1}{\lambda} \int_{\mathbb{R}} \int_{\mathbb{R}} h(t, \tau, \mathbf{p}_T, \mathbf{p}_R) e^{-j \frac{2\pi}{\lambda} \boldsymbol{\Omega}_D^T \cdot \mathbf{p}_T} e^{-j \frac{2\pi}{\lambda} \boldsymbol{\Omega}_A^T \cdot \mathbf{p}_R} d\mathbf{p}_T d\mathbf{p}_R. \quad (\text{A.12})$$

The equations (A.8) and (A.11)-(A.12) complete the first set of Bello equations. These functions and their corresponding Fourier pairs can be seen in Fig. A.4.

Let us now consider the multi-dimensional multi-path propagation channel introduced in (A.9) in the Doppler domain:

$$h(\nu, \tau, \boldsymbol{\Omega}_D, \boldsymbol{\Omega}_A) = \sum_{l=0}^{L-1} \gamma_l \delta(\tau - \tau_l) \delta(\boldsymbol{\Omega}_D - \boldsymbol{\Omega}_{D,l}) \delta(\boldsymbol{\Omega}_A - \boldsymbol{\Omega}_{A,l}) \delta(\nu - \nu_l). \quad (\text{A.13})$$

We can observe in (A.13) that all the dimensions are dispersive, in the sense that they expand these domains through trains of impulses. If we Fourier transform each of these dimensions, we have

$$h(t, f, \mathbf{p}_T, \mathbf{p}_R) = \sum_{l=0}^{L-1} \gamma_l e^{-j2\pi f \tau_l} e^{j \frac{2\pi}{\lambda} \boldsymbol{\Omega}_{D,l}^T \cdot \mathbf{p}_T} e^{j \frac{2\pi}{\lambda} \boldsymbol{\Omega}_{A,l}^T \cdot \mathbf{p}_R} e^{j2\pi \nu_l t}. \quad (\text{A.14})$$

While the spreading characteristic in the angular domain can be observed in (A.9), the selectivity is observed in (A.12). Thus, the channel in each frequency component f is the result of a scaled vectorial summation of the MPCs. The condensation of these coefficients introduces *small-scale fading*, process that is analysed in Chapter B. The same happens in the other selective dimensions: time and space. The the Doppler dispersion results in a time selective process, and the angular in a spatial selective. As mentioned in [109], the main contribution of Bello was the identification of the dispersion/selectivity relation as a part of the same process, as summarized in Table A.1. The dispersion in a given dimension

Table A.1: Dispersive/selective relation between the different dimensions.

Dispersive		Selective
Doppler	•—○	time
delay	○—•	frequency
angular	•—○	spatial

(modelled as a train of delta impulses), corresponds a selectivity in its Fourier transformed dimension. Usually, the negative effects of selectivity are counteracted by means of diversity. More on this is addressed in Chapter B and a comprehensive analysis based on simulations of the channel in the different domains can be found in the Appendix D.4. Moreover, for measurement purposes, the channel is usually sampled in the selective domains, namely time, frequency, and space.

Marginal Spreading Functions

The spreading function $h(\nu, \tau, \boldsymbol{\Omega}_D, \boldsymbol{\Omega}_A)$ depicts how the multi-path channel disperses the propagated electromagnetic waves in the Doppler, delay, and angular (at TX and RX) domains. By means of the marginal spreading functions, we can derive the representation of the propagation channel in the dimension of interest. The four marginal spreading functions are calculated by condensing (integrating) the $h(\nu, \tau, \boldsymbol{\Omega}_D, \boldsymbol{\Omega}_A)$ in the remaining spreading domains:

$$h(\tau) = \int_{\mathbb{R}} \int_{\mathcal{S}^2} \int_{\mathcal{S}^2} h(\nu, \tau, \boldsymbol{\Omega}_D, \boldsymbol{\Omega}_A) d\boldsymbol{\Omega}_D d\boldsymbol{\Omega}_A d\nu, \quad (\text{A.15})$$

$$h(\nu) = \int_{\mathbb{R}} \int_{\mathcal{S}^2} \int_{\mathcal{S}^2} h(\nu, \tau, \boldsymbol{\Omega}_D, \boldsymbol{\Omega}_A) d\boldsymbol{\Omega}_D d\boldsymbol{\Omega}_A d\tau, \quad (\text{A.16})$$

$$h(\boldsymbol{\Omega}_A) = \int_{\mathbb{R}} \int_{\mathbb{R}} \int_{\mathcal{S}^2} h(\nu, \tau, \boldsymbol{\Omega}_D, \boldsymbol{\Omega}_A) d\boldsymbol{\Omega}_D d\tau d\nu, \quad (\text{A.17})$$

$$h(\boldsymbol{\Omega}_D) = \int_{\mathbb{R}} \int_{\mathbb{R}} \int_{\mathcal{S}^2} h(\nu, \tau, \boldsymbol{\Omega}_D, \boldsymbol{\Omega}_A) d\boldsymbol{\Omega}_A d\tau d\nu. \quad (\text{A.18})$$

The previous equations can also be calculated evaluating the selective domains in zero:

$$h(\tau) = h(t, \tau, \mathbf{p}_T, \mathbf{p}_R)|_{t=0, \mathbf{p}_T=\mathbf{0}, \mathbf{p}_R=\mathbf{0}} \quad (\text{A.19})$$

$$h(\nu) = h(\nu, f, \mathbf{p}_T, \mathbf{p}_R)|_{f=0, \mathbf{p}_T=\mathbf{0}, \mathbf{p}_R=\mathbf{0}} \quad (\text{A.20})$$

$$h(\boldsymbol{\Omega}_A) = h(t, t, \mathbf{p}_D, \boldsymbol{\Omega}_A)|_{t=0, f=0, \mathbf{p}_T=\mathbf{0}} \quad (\text{A.21})$$

$$h(\boldsymbol{\Omega}_D) = h(t, f, \boldsymbol{\Omega}_D, \mathbf{p}_R)|_{t=0, f=0, \mathbf{p}_R=\mathbf{0}}. \quad (\text{A.22})$$

Full Characterization of the Multi-path Propagation Channel Considering Polarization

The characterization of the propagation channel is not yet complete without considering the polarization of each multi-path component. Let us extend (A.9) as

$$\mathbf{H}(t, \tau, \boldsymbol{\Omega}_D, \boldsymbol{\Omega}_A) = \sum_{l=0}^{L-1} \boldsymbol{\Gamma}_l \delta(\tau - \tau_l) \delta(\boldsymbol{\Omega}_T - \boldsymbol{\Omega}_{T,l}) \delta(\boldsymbol{\Omega}_R - \boldsymbol{\Omega}_{R,l}) e^{-j2\pi\nu_l t}, \quad (\text{A.23})$$

where $\boldsymbol{\Gamma}_l \in \mathbb{C}^{2 \times 2}$ is the polarimetric scattering matrix:

$$\boldsymbol{\Gamma}_l = \begin{bmatrix} \gamma^{\phi\phi} & \gamma^{\phi\theta} \\ \gamma^{\theta\phi} & \gamma^{\theta\theta} \end{bmatrix}. \quad (\text{A.24})$$

This is the most complete characterization of the spreading functions of the propagation channel considering their multiple dimensions and their Fourier relationships: time (Doppler), delay (frequency), angular (spatial), and polarization. This representation is also very useful since it combines in a single equation, all the path properties that are frequently predicted in simulation tools as RT or extracted with HRPE from measurements.

The polarimetric scattering matrix $\boldsymbol{\Gamma}_l(\tau) \rightarrow \boldsymbol{\Gamma}_l(f)$ is frequency dependent, specially if large bandwidths are considered. For example, the reflection coefficient of temperad glass changes from 0.9 to 0.65 from 7.5 GHz to 10.5 GHz, [110]. However, for sake of simplicity, in this work we neglect this effect and assume constant scattering properties along the considered bandwidth.

A.2.2 Stochastic Description of the Propagation Channel: Second Set of Bello Equations

If we treat the channel as a random process, the autocorrelation functions of the deterministic description of the channel provides the basis for the stochastic representation of the propagation channel.

Wide-Sense Stationary (WSS) Process

In statistics, a stochastic process whose first (mean) and second (variance) order moments are independent from the time is defined as a stationary process in a strict sense. That means that the statistics remain invariant to time shifts.

$$\begin{aligned} \mu_h(t) &= \mu_h \\ \sigma_h^2(t) &= \sigma_h^2 \\ C_{h,h}(t, t') &= C_{h,h}(t, \Delta t) = \mathbb{E}\{(h(t) - \mu_h(t))^* (h(t + \Delta t) - \mu_h(t + \Delta t))\} \\ R_{h,h}(t, t') &= \mathbb{E}\{h^*(t)h(t + \Delta t)\}. \end{aligned} \quad (\text{A.25})$$

However, since there are no stationary propagation channels in real world applications, the stationary conditions can be softened, giving place to the so called wide-sense stationary (WSS) process. A WSS random process only requires that the first moment (mean) and autocorrelation do not vary with time:

$$\begin{aligned}\mu_h(t) &= \mu_h \\ R_{h,h}(t, t') &= \mathbb{E}\{h^*(t)h(t + \Delta t)\} = R_{h,h}(\Delta t).\end{aligned}\tag{A.26}$$

Uncorrelated Scattering (US)

This condition establishes that the scattering resulting from the propagation is uncorrelated, meaning that the MPCs from the scatterer τ_1 are uncorrelated to the MPCs from scatterer τ_2 . Defining the delay difference $\Delta\tau = \tau_2 - \tau_1$ as the difference in delay between the different scattered MPCs, the autocorrelation function under uncorrelated scattering (US) assumption is

$$R_{h,h}(\Delta\tau) = \mathbb{E}\{h^*(\tau)h(\tau + \Delta\tau)\} = 0 \quad \forall \Delta\tau \neq 0.\tag{A.27}$$

Wide-Sense Stationary Uncorrelated Scattering (WSSUS)

Combining both previous conditions, we obtain the conditions for a wide-sense stationary uncorrelated scattering (WSSUS) process. The autocorrelation of the *spreading function* of the channel is calculated as the expectation in the different orthogonal domains.

$$R_{h,h}(\nu, \tau, \boldsymbol{\Omega}_D, \boldsymbol{\Omega}_A) = \mathbb{E}\{|h(\nu, \tau, \boldsymbol{\Omega}_D, \boldsymbol{\Omega}_A)|^2\}\tag{A.28}$$

On the other hand, the autocorrelation in the WSS domains depend on the different lags:

$$R_{h,h}(\Delta t, \Delta f, \Delta \mathbf{p}_T, \Delta \mathbf{p}_R) = \mathbb{E}\{|h^*(t, f, \mathbf{p}_T, \mathbf{p}_R)h(t + \Delta t, f + \Delta f, \mathbf{p}_T + \Delta \mathbf{p}_T, \mathbf{p}_R + \Delta \mathbf{p}_R)|^2\}\tag{A.29}$$

Marginal Power Profiles and Spreading Factors

The marginal power profiles represent the distribution of power in the different domains. Similarly to (A.18), we can characterize the propagation in different domains by integrating (A.28) in the dimensions of no interest, or setting the lags to zero in (A.29).

Power Delay Profile and RMS Delay Spread The PDP defines the distribution of the power along the delay domain:

$$\text{PDP}(\tau) = \mathbb{E}\{|h(\tau)|^2\}$$

$$\begin{aligned}
&= \int_{\mathbb{R}} \int_{\mathcal{S}^2} \int_{\mathcal{S}^2} R_{h,h}(\nu, \tau, \boldsymbol{\Omega}_D, \boldsymbol{\Omega}_A) d\nu d\boldsymbol{\Omega}_D d\boldsymbol{\Omega}_A \\
&= R_{h,h}(\Delta t, \tau, \boldsymbol{\Delta p}_T, \boldsymbol{\Delta p}_R) |_{\Delta t=0, \boldsymbol{\Delta p}_T=\mathbf{0}, \boldsymbol{\Delta p}_R=\mathbf{0}}
\end{aligned} \tag{A.30}$$

The DS is a measure of the richness of MPCs in the propagation channel. It shows how much the MPCs spread generating inter-symbol interference (ISI) in wideband single carrier systems. It has been seen in practice, that with a larger DS, the channel becomes more frequency selective and harder to equalize. In multi-carrier systems as OFDM, it defines the length of the guard-interval. The most common metric used to quantify the DS is the RMS-DS (from now on we refer to it simply as DS) and is calculated using the PDP:

$$\text{DS} = \sqrt{\frac{\int_{\tau} \tau^2 \cdot \text{PDP}(\tau) d\tau}{\int_{\tau} \text{PDP}(\tau) d\tau} - \left(\frac{\int_{\tau} \tau \text{PDP}(\tau) d\tau}{\int_{\tau} \text{PDP}(\tau) d\tau} \right)^2}. \tag{A.31}$$

The measurement of the DS is influenced by several factors, being the DR and bandwidth of the channel sounder, and directivity of the antenna the most significant ones. Such influence is addressed in Section 2.2.

Another metric widely used to describe the length of the CIR is the excess delay (ED). This is calculated as the delay range between the first and last components in the PDP within a considered dynamic range:

$$\text{ED} = \underset{\tau}{\text{argmax}}\{\text{PDP}(\tau) \neq 0\} - \underset{\tau}{\text{argmin}}\{\text{PDP}(\tau) \neq 0\}. \tag{A.32}$$

The ED together with the dynamic range conform the rectangular delay window.

Power Angular Profile and Angular Spreads These profiles describe the distribution of the propagation power in the angular domain. It can be calculated at the TX or RX, and decomposed in PAP and power elevation profile (PEP). Let us define the joint PAEP of departure as:

$$\begin{aligned}
\text{PAEP}(\boldsymbol{\Omega}_D) &= \mathbb{E}\{|h(\boldsymbol{\Omega}_D)|^2\} \\
&= \int_{\mathbb{R}} \int_{\mathbb{R}} \int_{\mathcal{S}^2} R_{h,h}(\nu, \tau, \boldsymbol{\Omega}_D, \boldsymbol{\Omega}_A) d\nu d\tau d\boldsymbol{\Omega}_A.
\end{aligned} \tag{A.33}$$

Now we can decompose (A.33) in its elevation and azimuth domains using the following relation:

$$\int_{\mathcal{S}^2} f(\boldsymbol{\Omega}) d\boldsymbol{\Omega} = \int_{-\pi}^{+\pi} \int_{-\frac{\pi}{2}}^{+\frac{\pi}{2}} f(\phi, \theta) \cdot \sin(\theta) d\phi d\theta. \tag{A.34}$$

Finally, the PAP and PEP are calculated in the orthogonal stochastic measure (OSM) do-

mains as:

$$\begin{aligned} \text{PAP}(\phi_D) &= \int_{-\frac{\pi}{2}}^{+\frac{\pi}{2}} \text{PAEP}(\boldsymbol{\Omega}_D) \cdot \sin(\theta_D) d\theta_D \\ &= \int_{\mathbb{R}} \int_{\mathbb{R}} \int_{\mathcal{S}^2} \int_{-\frac{\pi}{2}}^{+\frac{\pi}{2}} R_{h,h}(\nu, \tau, \boldsymbol{\Omega}_D, \boldsymbol{\Omega}_A) \cdot \sin(\theta_D) d\theta_D d\nu d\tau d\boldsymbol{\Omega}_A, \end{aligned} \quad (\text{A.35})$$

and

$$\begin{aligned} \text{PEP}(\theta_D) &= \int_{-\pi}^{+\pi} \text{PAEP}(\boldsymbol{\Omega}_D) \cdot \sin(\theta_D) d\phi_D \\ &= \int_{\mathbb{R}} \int_{\mathbb{R}} \int_{\mathcal{S}^2} \int_{-\pi}^{+\pi} R_{h,h}(\nu, \tau, \boldsymbol{\Omega}_D, \boldsymbol{\Omega}_A) \cdot \sin(\theta_D) d\phi_D d\nu d\tau d\boldsymbol{\Omega}_A. \end{aligned} \quad (\text{A.36})$$

The same methodology can be applied at the RX to derive the power angular profiles of arrival.

Similarly to the DS, we can characterize the angular domain of a propagation channel by its spread factors. The AS and ES are calculated using the profiles defined in (A.35) and (A.36), respectively:

$$\text{ASD} = \sqrt{\frac{\int_{\phi_D} \phi_D^2 \text{PAP}_T(\phi_D)}{\int_{\phi_D} \text{PAP}_T(\phi_D)} - \left(\frac{\int_{\phi_D} \phi_D \text{PAP}_T(\phi_D)}{\int_{\phi_D} \text{PAP}_T(\phi_D)} \right)^2}, \quad (\text{A.37})$$

and

$$\text{ESD} = \sqrt{\frac{\int_{\theta_D} \phi_D^2 \text{PEP}_T(\theta_D)}{\int_{\theta_D} \text{PEP}_T(\theta_D)} - \left(\frac{\int_{\theta_D} \theta_D \text{PEP}_T(\theta_D)}{\int_{\theta_D} \text{PEP}_T(\theta_D)} \right)^2}. \quad (\text{A.38})$$

For the ASA and ESA, ϕ_D is replaced by ϕ_A , PAP_T by PAP_R , θ_D by θ_A , and PEP_T by PEP_R . Furthermore, when the whole azimuthal circumference is measured, the periodicity must be considered into the calculation of the spreads.

A.3 The Multi-path Radio Channel

As soon as the antennas are introduced in the model in (A.23), or in the measurements in the real world, the directional and polarimetric information is lost since the antenna integrates over these dimensions. If we want to retrieve back the directional information of the MPC, we need diversity in the directional and polarimetric domain.

A.3.1 Signal Model Considering Single Polarized Antennas

Let us now consider the antenna effects on the multi-path propagation channel. Under the assumption of single polarized (single port) antennas, the signal measured at the antenna port in (A.23) can be calculated as

$$\begin{aligned}\tilde{h}(t, \tau) &= \int_{S^2} \int_{S^2} \mathbf{g}_R^T(\boldsymbol{\Omega}_A) \mathbf{H}(t, \tau, \boldsymbol{\Omega}_A, \boldsymbol{\Omega}_D) \mathbf{g}_T(\boldsymbol{\Omega}_D) d\boldsymbol{\Omega}_D d\boldsymbol{\Omega}_A \\ &= \sum_l \left[\int_{S^2} \int_{S^2} \mathbf{g}_R^T(\boldsymbol{\Omega}_A) \boldsymbol{\Gamma}_l \mathbf{g}_T(\boldsymbol{\Omega}_D) \delta(\boldsymbol{\Omega}_A - \boldsymbol{\Omega}_{A,l}) \delta(\boldsymbol{\Omega}_D - \boldsymbol{\Omega}_{D,l}) d\boldsymbol{\Omega}_D d\boldsymbol{\Omega}_A \right] e^{-j2\pi\nu t} \delta(\tau - \tau_l), \\ &= \sum_l \underbrace{\mathbf{g}_R^T(\boldsymbol{\Omega}_{A,l}) \boldsymbol{\Gamma}_l \mathbf{g}_T(\boldsymbol{\Omega}_{D,l})}_{a_l} e^{-j2\pi\nu t} \delta(\tau - \tau_l),\end{aligned}\quad (\text{A.39})$$

where $a_l \in \mathbb{C}$ is the radio-channel coefficient of the l^{th} multipath component, $\mathbf{g}_R(\boldsymbol{\Omega}_A) = [g^\phi(\boldsymbol{\Omega}_A), g^\theta(\boldsymbol{\Omega}_A)]^T$ and $\mathbf{g}_T(\boldsymbol{\Omega}_D) = [g^\phi(\boldsymbol{\Omega}_D), g^\theta(\boldsymbol{\Omega}_D)]^T$ are the RX and TX antenna patterns in the ϕ and θ polarization, respectively. We assume frequency independent antennas for sake of simplicity. However, as shown in Appendix D, all the antennas have large variations within the bandwidth of interest.

A.3.2 Extension to Dual-polarized Antennas

Dual-polarized measurements are necessary to capture the complete 3D characteristic of the channel. In this case, (A.5) can be re-written as

$$\begin{aligned}\tilde{\mathbf{H}}(t, \tau) &= \int_{S^2} \int_{S^2} \mathbf{G}_R^T(\boldsymbol{\Omega}_A) \mathbf{H}(t, \tau, \boldsymbol{\Omega}_A, \boldsymbol{\Omega}_D) \mathbf{G}_T(\boldsymbol{\Omega}_D) d\boldsymbol{\Omega}_D d\boldsymbol{\Omega}_A \\ &= \sum_l \underbrace{\mathbf{G}_R^T(\boldsymbol{\Omega}_{A,l}) \boldsymbol{\Gamma}_l \mathbf{G}_T(\boldsymbol{\Omega}_{D,l})}_{\mathbf{A}_l} e^{-j2\pi\nu t} \delta(\tau - \tau_l),\end{aligned}\quad (\text{A.40})$$

where $\mathbf{A}_l \in \mathbb{C}^{2 \times 2}$ is the measured antenna-dependent polarimetric scattering matrix of the l^{th} path, $\mathbf{G}_R(\boldsymbol{\Omega}_A) \in \mathbb{C}^{2 \times 2}$ and $\mathbf{G}_T(\boldsymbol{\Omega}_D) \in \mathbb{C}^{2 \times 2}$ are two-ports RX and TX antenna patterns, respectively:

$$\mathbf{G}(\boldsymbol{\Omega}) = \begin{bmatrix} g^{\phi\phi}(\boldsymbol{\Omega}) & g^{\phi\theta}(\boldsymbol{\Omega}) \\ g^{\theta\phi}(\boldsymbol{\Omega}) & g^{\theta\theta}(\boldsymbol{\Omega}) \end{bmatrix}. \quad (\text{A.41})$$

The polarimetric characteristics of the MPCs can only be recovered unaltered if $\mathbf{G}(\boldsymbol{\Omega}) = \mathbf{I}_{2 \times 2} \forall \boldsymbol{\Omega}$. This means that the cross-polarization discrimination (XPD) of the antenna has to be $\text{XPD} = \infty \forall \boldsymbol{\Omega}$, which is non-practical.

If no polarimetric analysis is performed, the contribution of each polarization is summed in the power domain:

$$|\tilde{h}(\tau, \boldsymbol{\Omega}_A, \boldsymbol{\Omega}_D)|^2 = \|\tilde{\mathbf{H}}(\tau, \boldsymbol{\Omega}_A, \boldsymbol{\Omega}_D)\|_F^2. \quad (\text{A.42})$$

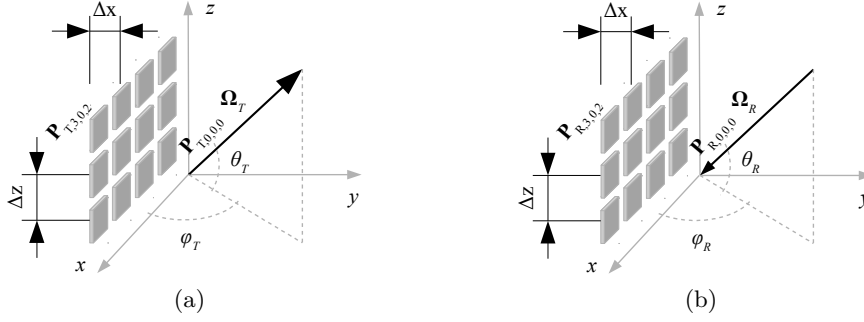


Figure A.5: MIMO coordinate system at (a) TX and (b) RX.

A.4 The Multi-path MIMO Propagation and Radio Channel

The MIMO representation of the propagation and radio channel introduced in (A.12) and (A.44), respectively, is straight forward under certain assumptions. Let us assume planar waves at the sampling points \mathbf{p}_{m_x, m_z} uniformly distributed in a rectangular area on the xz plane, where $m_x = \{0, \dots, M_x - 1\} \in \mathbb{Z}$ and $m_z = \{0, \dots, M_z - 1\} \in \mathbb{Z}$. To fulfil Nyquist, the sampling points have to be, maximum, separated $\Delta = \frac{\lambda_c}{2}$, where λ_c is the carrier frequency. If we consider a wideband system, we have to sample $\Delta = \frac{\lambda_H}{2}$, being $\lambda_L = \frac{c}{f_c + B/2}$ the shortest wavelength.

There are in total $M = M_x + M_z$ sampling points as shown in Fig. A.5, and their coordinates are determined as:

$$\mathbf{p}_{m_x, m_z} = [x \cdot \Delta_x \cdot m_x, 0, z \cdot \Delta_z \cdot m_z]^T. \quad (\text{A.43})$$

By doing the same on the other side of the link, the sampled spatial channel introduced in (A.12) can be arranged in a channel matrix $\mathbf{H}(t, \tau) \in \mathbb{C}^{M_R \times M_T}$, whose elements represent the propagation channel between the m_T^{th} and m_R^{th} isotropic TX and RX antenna element:

$$h_{m_R, m_T}(t, \tau) = \sum_{l=0}^{L-1} \gamma_l \cdot e^{-j \frac{2\pi}{\lambda} \boldsymbol{\Omega}_{D,l}^T \cdot \mathbf{p}_{T, m_T}} \cdot e^{-j \frac{2\pi}{\lambda} \boldsymbol{\Omega}_{A,l}^T \cdot \mathbf{p}_{R, m_R}} \cdot e^{-j 2\pi \nu_l t} \cdot \delta(\tau - \tau_l), \quad (\text{A.44})$$

where $m_R = \{0, \dots, M_{R,x} + M_{R,z} - 1\}$ and $m_T = \{0, \dots, M_{T,x} + M_{T,z} - 1\}$.

Let us now consider that the sampling points are antennas allocated in a uniform rectangular array (URA). The MIMO radio channel $\tilde{\mathbf{H}}(t, \tau) \in \mathbb{C}^{M_R \times M_T}$ is an extension of (A.44) considering polarization and antenna patterns:

$$\begin{aligned} \tilde{h}_{m_R, m_T}(t, \tau) = & \sum_{l=0}^{L-1} \mathbf{g}_{R, m}^T(\boldsymbol{\Omega}_{A,l}) \cdot \boldsymbol{\Gamma}_l \cdot \mathbf{g}_{T, n}(\boldsymbol{\Omega}_{D,l}) \cdot e^{-j \frac{2\pi}{\lambda} \boldsymbol{\Omega}_{D,l}^T \cdot \mathbf{p}_{T, m_T}} \dots \\ & \dots e^{-j \frac{2\pi}{\lambda} \boldsymbol{\Omega}_{A,l}^T \cdot \mathbf{p}_{R, m_R}} \cdot e^{-j 2\pi \nu_l t} \cdot \delta(\tau - \tau_l), \end{aligned} \quad (\text{A.45})$$

where $\mathbf{g}_{T, m_T}(\boldsymbol{\Omega}_D)$ and $\mathbf{g}_{R, m_R}(\boldsymbol{\Omega}_A)$ are the m_T^{th} and m_R^{th} TX and RX antenna patterns,

respectively. Although large, this system equation has several advantages: under the assumption of planar waves, the radio channel can be described for any kind of array shape and antenna patterns. The array shape is given by the location of the antenna elements in the \mathbf{p}_{T,m_T} and \mathbf{p}_{R,m_R} vectors.

The extension to dual-polarized antennas is straightforward:

$$\begin{aligned} \tilde{\mathbf{H}}_{m_R,m_T}(t,\tau) = & \sum_{l=0}^{L-1} \mathbf{G}_{R,m}^T(\boldsymbol{\Omega}_{A_l}) \cdot \boldsymbol{\Gamma}_l \cdot \mathbf{G}_{T,n}(\boldsymbol{\Omega}_{D,l}) \cdot e^{-j\frac{2\pi}{\lambda}\boldsymbol{\Omega}_{D,l}^T \cdot \mathbf{p}_{T,m_T}} \dots \\ & \dots e^{-j\frac{2\pi}{\lambda}\boldsymbol{\Omega}_{A,l}^T \cdot \mathbf{p}_{R,m_R}} \cdot e^{-j2\pi\nu_l t} \cdot \delta(\tau - \tau_l). \end{aligned} \quad (\text{A.46})$$

B Fading in Wireless Mobile Channels

Overview

This chapter provides the theoretical background of fading, focusing in the different causes, dimensions, and models. Empirical results in large-scale fading are found in Chapter 4, and in small-scale fading in Chapter 5.

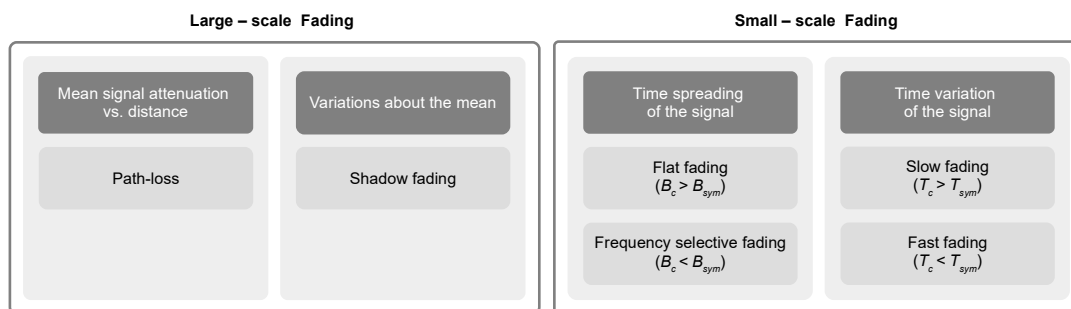


Figure B.1: Classification of fading and its relation to the different dimensions.

B.1 Introduction

Fading is one of the most harmful effects in wireless mobile communications. It is the attenuation that signals encounter as a consequence of the interaction of the multiple paths that the signal experience between the TX and RX. Thus, if there are no MPCs, the signal experiences only free-space attenuation over distance (or the attenuation given by any of the propagation mechanisms discussed in Section A.1) and consequently no fading. Thus, considering the system characteristics at mm-wave as larger bandwidth and high directivity that isolates MPCs, we focus our interest on describing fading since it might experience a different behaviour compared to systems with low directivity.

Moreover, as discussed in Section A.2.1, the utilization of diversity in the selective domains (namely time, frequency, and space) alleviates the deterioration of the signal quality. Therefore, with system aspects as large bandwidths, implying the possibility to use higher orders of frequency diversity in OFDM systems, the total attenuation of the signal is also reduced.

Fading can be classified into *large-scale* and *small-scale* [111], depending the length of the displacement area under consideration: the former deals with the average attenuation over large areas (compared to the wavelength) and the latter, over small areas (typically between 20 and 40 wavelengths). Furthermore, as shown in Fig. B.1, small-scale fading can be classified depending on the dimension it occurs: in frequency as *flat* or *frequency selective fading* or in time as *slow* or *fast fading*.

B.2 Large-Scale Fading

Large-scale fading accounts for the variation of the RX envelope during the displacement over large distances, occasioned by the attenuation over free-space propagation and the shadowing of scatterers as trees, buildings, etc. There are mainly two components to be characterized: the mean signal attenuation over distance, and the variations about the mean. In free space, the signal attenuates inversely proportional to the square of the distance, which results in a logarithmic slope with decay 2. If we add scatterers (multi-paths), the addition (or subtraction) of the MPCs changes in average the slope of the attenuation curve. This is normally modelled by an exponent n called PLE (with $n = 2$ in the FSPL). In addition, the

variation over the mean is modelled as a Gaussian random variable, whose magnitude in decibels are described with a *log-normal* distribution. These two effects in large-scale fading are usually modelled with empirical path-loss models.

B.2.1 Free Space Path-loss

During propagation, electromagnetic waves attenuate proportionally to the square of the distance between the emitter and receiver. The power density (power flow per unit area) is defined as

$$P_0 = \frac{P_T}{4\pi d^2}, \quad (\text{B.1})$$

where P_T is the power in Watts and d the separation distance between emitter and receiver. A RX antenna collects power proportionally to the effective aperture A_{eff} :

$$P_R = P_0 A_{\text{eff}}, \quad (\text{B.2})$$

being the effective aperture of a lossless isotropic radiator $A_{\text{eff}} = \frac{\lambda^2}{4\pi}$. From (B.1) and (B.2):

$$P_R = \underbrace{\left(\frac{P_T}{4\pi d^2} \right)}_{\text{TX power density}} \underbrace{\left(\frac{\lambda^2}{4\pi} \right)}_{\text{RX effective aperture}}. \quad (\text{B.3})$$

In telecommunications, one of the most widely used formulas to calculate the received power at a given distance is the Friis transmission equation, [11]. This formula relates the TX power of an isotropic radiator and the received power considering the effective aperture of the RX antenna. Differently to the equation originally proposed in [11], in which the directivity of the antennas were taken into account, (B.3) is more popularly defined nowadays in terms of the TX and RX antenna gains (with respect to isotropic radiators) G_T and G_R , respectively:

$$P_R = P_T G_T G_R \left(\frac{c}{4\pi f d} \right)^2, \quad (\text{B.4})$$

where $\lambda = \frac{c}{f}$ and c is the speed of light. The FSPL is calculated as the TX-RX power ratio with unitary gain at TX and RX antennas:

$$\text{FSPL} = \frac{P_R}{P_T} = \left(\frac{c}{4\pi f d} \right)^2. \quad (\text{B.5})$$

At a first glance, (B.4) shows that the free-space path-loss depends on the wavelength. However, from (B.3), we can observe that the power density is independent from the wavelength. What introduces the dependency to the frequency is the effective aperture of the antenna, which depends on its physical size. Therefore, the area can be increased by combining multiple antennas to compensate FSPL.

B.2.2 Empirical Path-loss and Shadowing Models

Empirical path-loss models are extensively used in propagation channel models due to their simplicity and practicability to make estimations direct in the link-layer. The most frequently used path-loss models are stochastic models parametrized by fitting curves from several measurements. These measurements are generally divided accordingly to the visibility conditions (LOS, OLOS, NLOS, etc.) and further classified depending on the scenarios (indoor, office, street-canyon, etc.). There are mainly two models being covered in the current literature: FI and CI. The first one is also known as alpha-beta (AB) model since they are the two parameters to be fitted. The equation is as follows:

$$PL_{AB,dB}(d) = 10 \cdot \alpha_{AB} \cdot \log_{10} \left(\frac{d}{d_0} \right) + \beta_{AB} + X_{\sigma_{AB}}, \quad (\text{B.6})$$

where d is the distance to the reference distance d_0 (typically 1 m). The parameter α_{AB} is the PLE and determines the slope of the curve or change rate of power over distance. The second parameter β_{AB} is the reference path-loss at the distance d_0 , which in contrast to the CI model, has no real physical meaning. The variable $X \in \mathcal{N}(0, \sigma_{AB})$ is a zero-mean log-normal distributed variable that models the power variations given by the environment (scattering, fading, and shadowing of scatterers in different positions).

On the other hand, the CI model has a physical anchor given by the parameter β_{CI} :

$$PL_{CI,dB}(d) = 10 \cdot \alpha_{CI} \cdot \log_{10} \left(\frac{d}{d_0} \right) + \beta_{CI} + X_{\sigma_{CI}}, \quad (\text{B.7})$$

where $\beta_{CI} = 10 \log_{10} \left(\frac{4\pi f_0 d_0}{c_0} \right)^2$ is the FSPL at the reference distance d_0 . If we compare both models, the main difference is that β_{CI} accounts for the FSPL (PLE = 2), and β_{AB} can take any value (PLE $\in \mathbb{R}$). Thus, the only tunable parameter in the CI model is the exponent α_{CI} .

The anchor β_{CI} with physical meaning turns the CI model more realistic. However, is that anchor the one that limits the applicability of such a model in NLOS scenarios, since it overestimates path-loss at larger distances, and underestimates it at closer TX-RX distances because of the “need” to anchor the fitting curve to the FSPL at d_0 .

B.2.3 Empirical Multi-band Path-loss Models

The need of multi-band path-loss models has been boosted with the consideration of the mm-wave spectrum. This big step on the carrier frequency affects considerably the isotropic path-loss. Furthermore, the co-existence of multiple technologies with different carrier frequencies co-operating in a single device increases the demand for prediction tools. In that regard, there has been lately a lot of efforts in the community to extend the previous models considering the complete spectrum [4], [112], [73], etc.

The AB model in (B.6) has been extended to the so-called alpha-bega-gamma (ABG) model,

which includes a parameter γ_{ABG} to introduce the inter-band relation

$$PL_{\text{ABG,dB}}(d, f_c) = 10 \cdot \alpha_{\text{ABG}} \cdot \log_{10} \left(\frac{d}{d_0} \right) + \beta_{\text{ABG}} + 10 \cdot \gamma_{\text{ABG}} \cdot \log_{10}(f_c) + X_{\sigma_{\text{ABG}}}, \quad (\text{B.8})$$

where f_c is normally given in GHz. It is clear to observe that if we set $\gamma = 2$ (no frequency dependence on the model), (B.8) turns into (B.6), and if we later set $\beta_{\text{AB}} = \text{FSPL}$, (B.6) turns into (B.7).

The CI model has also been extended to address multi-band models. In that case, the PLE is also anchored to 2:

$$PL_{\text{CI,dB}}(d, f_c) = 10 \cdot \alpha_{\text{CI}} \cdot \log_{10} \left(\frac{d}{d_0} \right) + 32.44 + 10 \cdot 2 \cdot \log_{10}(f_c) + X_{\sigma_{\text{CI}}}, \quad (\text{B.9})$$

where f_c is in GHz and $32.44 = 20 \cdot \log_{10} \left(\frac{4\pi \cdot 1 \cdot \text{E}^9}{c_0} \right)$.

The methodology to estimate the parameters of the single and multi-band empirical path-loss model from directive measurements is introduced in Chapter 2 and parameters from measurements in a large set of scenarios and visibility conditions in Chapter 4.

B.2.4 Directional and Omni-directional Path-loss

Traditionally, path-loss was modelled considering omni-directional systems. However, with the trend of directive systems at mm-wave, the idea of including the spatial filtering effects of beam-forming in the path-loss has gained certain impulse in the latest years [113, 72, 73]. This is also convenient since communication systems with antenna arrays and beam-steering capabilities match the antenna characteristics that are normally used during channel measurements. On the other hand, such models are not flexible since they are only applicable to systems with the same directivity as the channel sounder, and lack of the possibility to define a fine steering direction, since the parameters are frequently obtained from a pre-defined grid of directions.

In the current literature, such as in [114], the directive path-loss is derived using the strongest peak from the synthetic omni-directional PDP. This assumes that the system is flexible enough to steer the gain in any direction and isolate a single path from the complete propagation environment. In contrast, in this work we select the scanning direction from a pre-defined grid of pointing directions (defined during the channel measurements) that delivers the highest power to the RX, including the effects of all the clusters within the beam.

If we consider only the spatial filtering given by the directivity of the antenna, we expect that the parameter from the path-loss models that is most affected is the shadow fading $\sigma_{\text{CI}/\text{FI}}$. With omni-directional antennas, the antennas integrate all the scatterers in the environment, introducing larger variations during large displacements due to the appearance and disappearance of scatterers. On the other hand, with directive antennas pointing in the direction that delivers the highest energy to the RX, filter out multiple scatterers reducing the variation of signal power in consecutive positions.

B.3 Small-Scale Fading

Small-scale fading describes the variations of signal amplitude in short distances (usually at some wavelengths level). It is generated by two mechanisms: time-delay spreading due to multi-path propagation, and time-variation due to motion. While the first one characterizes propagation in wireless channels, the later appears during the displacement of at least one of the communication entities or objects in the environment.

B.3.1 Time Spreading of the Signal and Frequency Selectivity

Following the analogy between dispersion and selectivity introduced in Table A.1, the multi-path propagation channel introduces a time-delay dispersion of the TX signal and a frequency selectivity in the frequency domain, as shown in Fig. B.2. Let us call τ_{\max} to the excess delay, i.e. the time difference between the first and latest path within a dynamic range, and $T_{\text{sym}} = 1/B_{\text{sym}}$ as the symbol length, inversely proportional to signal bandwidth. Let us also consider as reference a digital RX system that samples the signal at a frequency f_s , proportional to the transmission bandwidth $f_s = n \cdot B_{\text{sym}}$ for $n \in \mathcal{N}$. The digitization results in a discrete CIR composed by channel taps separated $\Delta\tau_s = 1/f_s$.

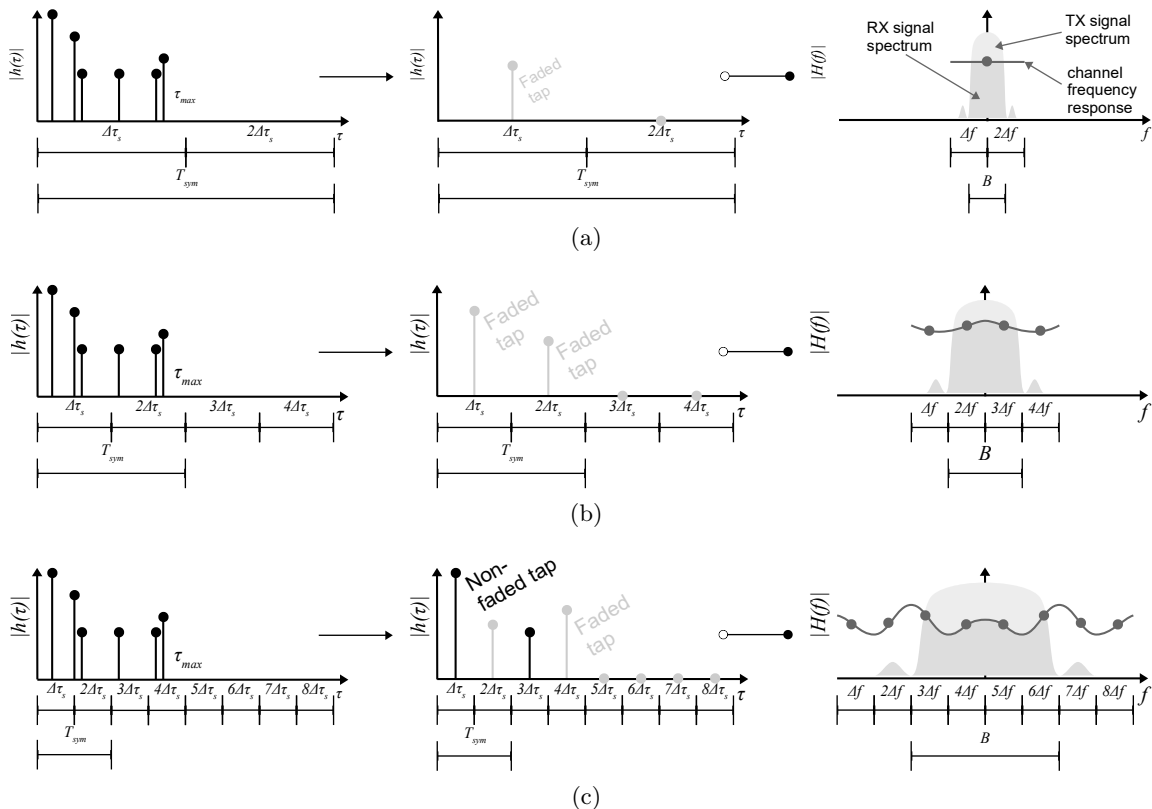


Figure B.2: Multi-path propagation channel, equivalent after digitization, and Fourier transform for (a) single tap flat fading channel, (b) 2-taps frequency-selective fading channel, and (c) frequency-selective channel with faded and non-faded taps.

Depending on the relative duration of τ_{\max} and T_{sym} , the channel experiences flat or frequency selective fading. Usually, the RMS DS is used instead of the τ_{\max} to characterize how frequency flat or selective is the channel. If $T_{\text{sym}} > \text{DS}$, all the MPCs fall within a single sample of the symbol and they can't be resolve. Hence, the channel is a single tap frequency-flat, otherwise, it consists of multiple taps and becomes frequency selective.

The DS is related to the coherence bandwidth in the frequency domain by

$$B_c \approx \frac{1}{c \cdot \text{DS}}, \quad (\text{B.10})$$

where c is a constant that depends on the metric used. For example, if we define the portion of spectrum in which the complex frequency response of the channel has a correlation of 0.9, then $c \approx 50$ [115]. For instance, if $B_{\text{sym}} < B_c$, then the channel is frequency flat, otherwise, frequency selective.

Frequency Flat Fading

If the duration of the transmitted signal T_{sym} is larger than τ_{\max} , the channel collapses to a single impulse whose amplitude results from the combination of all the paths within T_{sym} . Accordingly to their relative phases, this combination can be constructive or destructive, producing the latter a degradation in SNR. The single impulse channel in time domain is seen as a flat spectrum in the frequency domain, meaning that all the frequency components of the TX signal undergo the same gain or attenuation.

If all the MPCs fall within a single delay tap ($\tau_{\max} < 1/f_s$) as shown in Fig. B.2a, the system can't resolve them any more. The channel in (A.39) becomes a single tap channel $\tilde{h}(t, \tau) \rightarrow h(t) = a_k$ with a flat frequency response. The distribution of the amplitude of the channel in flat fading is frequently modelled as a stochastic process with Rayleigh or Rician distributions, depending on the number of MPCs and their relative amplitudes and phases.

Rayleigh fading Let us assume a large number of equally strong MPCs arriving from a wide range of directions, usual situation in rich scattering propagation environments in NLOS and with isotropic antennas, the complex amplitude of the channel tap over time becomes complex Gaussian due to the central limit theorem. Hence, if $h(t) \in \mathbb{C} \sim \mathcal{N}(\mu, \sigma^2)$, then $x = |h(t)|$ is Rayleigh distributed, with the following probability distribution function (PDF):

$$p_x(x) = \frac{x}{\sigma^2} e^{-\frac{x^2}{2\sigma^2}}. \quad (\text{B.11})$$

Rician fading In the presence of a strong path in comparison to the other ones, usual situation in LOS propagation scenarios, $x = |h(t)|$ follows a Rician distribution with the following PDF:

$$p_x(x) = \frac{x}{\sigma^2} e^{-\frac{(x^2 + \rho^2)}{2\sigma^2}} I_0\left(\frac{x\rho}{\sigma^2}\right), \quad (\text{B.12})$$

where $I_0(\cdot)$ is the modified Bessel function of the first kind with zero order. The ratio of power between the strongest and the scattered paths is defined by the Rician fading K -factor:

$$k = \frac{\rho^2}{2\sigma^2}. \quad (\text{B.13})$$

It worth to remark that when there is no stronger constant components in comparison to the other ones, $\rho \rightarrow 0$, $k \rightarrow 0$, and $I_0(\frac{x\rho}{\sigma^2} \rightarrow 0) = 1$. Hence, (B.12) converges to (B.11). Even if the Rician distribution is usually used to model LOS scenarios with isotropic antennas, it can also be used to model strong reflections in NLOS. As discussed empirically in Section 5.3.5, this can be the result of using directive antennas that amplifies a bundle of MPCs and filter-out the remaining ones.

TWDP fading In the recent years, the TWDP has also been used to model fading, [89]. If we add a second specular component to the Rician model, we end up in the TWDP that describes two constant amplitude components plus a large number of small components with random phases. The absolute value of the base-band signal is

$$x = |V_1 \cdot e^{j\phi_1} + V_2 \cdot e^{j\phi_2} + X + j \cdot Y|, \quad (\text{B.14})$$

where ϕ_1 and ϕ_2 are independent uniform random variables distributed in $[0, 2\pi)$, and X and Y are zero-mean Gaussian random variables with variance σ^2 . The PDF of the TWDP fading is characterized by three components

$$\Omega = V_1^2 + V_2^2 + 2\sigma^2, \quad K = \frac{V_1^2 + V_2^2}{2\sigma^2}, \quad \Delta = \frac{2V_1V_2}{V_1^2 + V_2^2}, \quad (\text{B.15})$$

where $\Omega = \mathbb{E}\{x^2\}$ is the average power ratio, K is the key factor describing the specular to diffuse components ratio, and Δ is the disparity between specular components. If the two specular components are similar, $\Delta \rightarrow 1$. In the opposite case, $\Delta \rightarrow 0$ and TWDP converges to the Rician fading scenario with a single specular component.

Three parameters need to be estimated from the set of measured absolute values of the RX signal in order to obtain the parametrized TWDP distribution. Since there is no closed form solution for the PDF, [116] introduces the following definite integral

$$p_x(x) = x \int_0^\infty J_0(x\nu) J_0(V_1\nu) J_0(V_2\nu) e^{-\frac{\nu^2\sigma^2}{2}} \nu \, d\nu, \quad (\text{B.16})$$

and related work on how to solve it can be found in [89].

Frequency-selective Fading

Increasing the bandwidth $\uparrow B_{\text{sym}}$ results in the reduction of the symbol length T_{sym} . Hence, if $T_{\text{sym}} < \tau_{\text{max}}$, then (A.39) becomes a multiple tap channel with a frequency selective response in the frequency domain, as shown in Fig. B.2b and Fig. B.2c. This distorts the pulse shape

and introduces ISI, increasing the bit error rate (BER).

Depending on B_{sym} and f_s , the number of paths L_k falling into the k^{th} tap increases or decreases as shown in Fig. B.2b and Fig. B.2c. In the case of a large number of equally strong paths arriving at the same tap k , $x = |h(t, k\Delta\tau)|$ can still be modelled as Rayleigh using (B.11). On the other hand, if there is a remarkable stronger path in comparison to the other ones within a tap, it can be modelled as Rician with (B.12). In extreme cases, with infinite bandwidth and/or angular resolution, each channel tap consists of a single path. The number of paths per tap depends, among others, on the spatial and time resolution, and is the subjects of investigations in Section 5.3.

Usually, OFDM systems are modelled as a collection of single-taps flat-fading channels, since each of the sub-carriers is seen as an independent narrowband channel experiencing either Rician or Rayleigh fading, depending on if they are in LOS or NLOS, respectively.

B.3.2 Time Variance of the Signal and Frequency Spreading

The time dispersion of the channel in the delay domain originated a frequency selection in the frequency domain, both related by the Fourier transform. In the time variance case, we have a time selective process, which originates a frequency (Doppler) dispersion. Let us characterize the RX signal $x(t)$ as the convolution between the channel $h(t, \tau)$ and TX signal $s(t)$:

$$x(t) = \int_{\mathbb{R}} h(\tau, t) s(t - \tau) d\tau. \quad (\text{B.17})$$

The spectrum of the received signal $X(f)$ is then calculated by the multidimensional convolution between the spectrum of the TX signal $S(f)$ and the frequency/Doppler response of the channel $H(\nu, f)$ from (A.8):

$$\begin{aligned} X(f) &= \int_{\mathbb{R}} H(f - \nu, \nu) S(f - \nu) d\nu \\ &= S(f) * H(f, \nu). \end{aligned} \quad (\text{B.18})$$

If $H(\nu, f)$ consists of a single component as shown in Fig. B.3a, or a remarkable strong one in comparison to the rest, then the complete spectrum of the RX signal is shifted: each frequency component of the TX signal is equally shifted away from the carrier in the direction of the dominant Doppler component. This is easier to compensate, since only a frequency shift is needed, which can be obtained by an adjustment on the oscillators in the up/down converters. On the other hand, if $H(\nu, f)$ consists of multiple strong components as depicted in Fig. B.3b, the convolution in (B.18) originates a Doppler spread, mixing the different frequency components of $S(f)$. This creates a broadening of the original spectrum which is more complicated to correct.

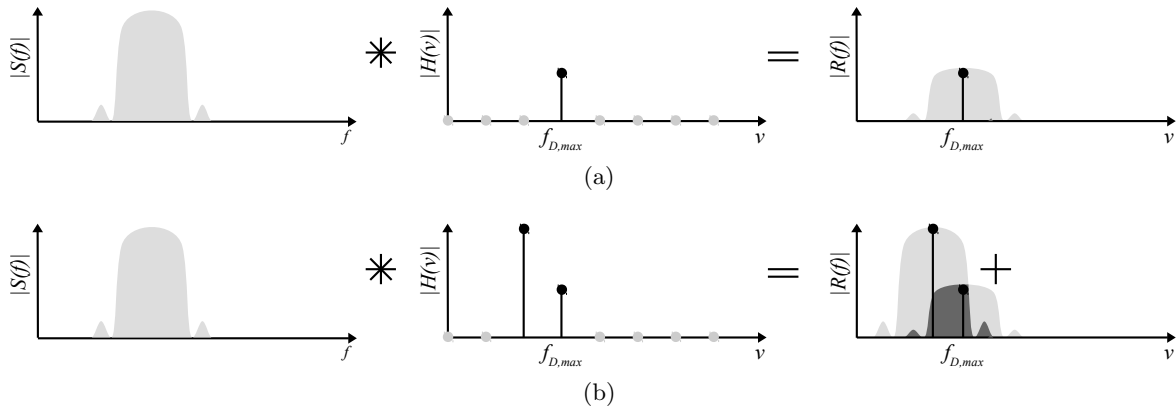


Figure B.3: (a) Doppler shift with single component, and (b) Doppler spread due to multipath propagation. The overlapped region of the spectrum in dark gray.

Slow Fading

Let us analyse the autocorrelation function $R_{h,h}(\Delta t)$ of a single frequency component of the channel ($\Delta f = 0$). The time instant T_c is denominated *coherent time* and accounts for the portion of time for which the channel remains completely or to an extent, invariant. It is normally estimated as a

$$T_c \approx \frac{1}{c \cdot \nu_{\max}}, \quad (\text{B.19})$$

where c is a constant and ν_{\max} is the maximum Doppler frequency, depending between others, on the relative displacement velocity and direction. In a wireless static channel, $\nu_{\max} \rightarrow 0$ and for instance $T_c \rightarrow \infty$. However, when something changes in the channel, either TX, RX, or scatterers position, T_c is reduced, introducing a degradation in the channel, that can be classified depending on the relation of T_c to T_{sym} as *slow* and *fast-fading*.

In this case, the symbol length T_{sym} is shorter than the coherence time of the channel T_c . That means that the channel is correlated (remains unchanged) in time during the transmission of a symbol and for instance there is no distortion in the signal, only a degradation of the SNR, similar to the flat-fading consequences.

Fast Fading

If the symbol duration T_{sym} is larger than the coherence time of the channel T_c , the channel varies during the transmission of a single symbol, introducing serious distortions in the signal shape that need to be repaired. Contrary to slow fading that causes only SNR degradation, this effect induces a severe BER deterioration.

B.4 Summary

Summarizing the small-scale fading effects, we can see that to obtain flat-fading, we increase T_{sym} larger than the DS. However, by enlarging the symbol duration, we increase the probability that $T_{\text{sym}} > T_c$. This is one of the trade-off in OFDM modulation, in which a wideband signal that experiences frequency-selective fading, is distributed in multiple narrowband signals, that experience flat fading individually. However, the mobility is limited due to the susceptibility to fast-fading. Since mm-wave systems implement high directive radio channels, the influence of such a system aspect in fading is addressed in Chapter 5. We empirically show that by limiting the number of MPCs the shadowing factor in path-loss decreases, as well as the Doppler spread, and frequency selectivity. In addition, by increasing the bandwidth, the channel also becomes more deterministic with lower variations of total RX power. All these results are supported by simulations in Appendix D.4.

C State of the Art in Physical Channel Models

Overview

In this chapter, we intend to provide an overview on channel modelling and the current state of the art for mm-wave and multi-band models. Since the main objective of this work is to characterize multi-band propagation and the influence of system aspects on channel models, we focus on the description of physical channels, most specifically, in SCMs based on the 3GPP standards and the quasi-deterministic approach in MiWEBA. We first point out the limitations of the current modelling approach, and then we propose modifications to address mm-wave and multi-band simulations. These recommendations are later supported by measurements in Chapter 4 and Chapter 5, and introduced in Chapter 6 and Chapter 7.

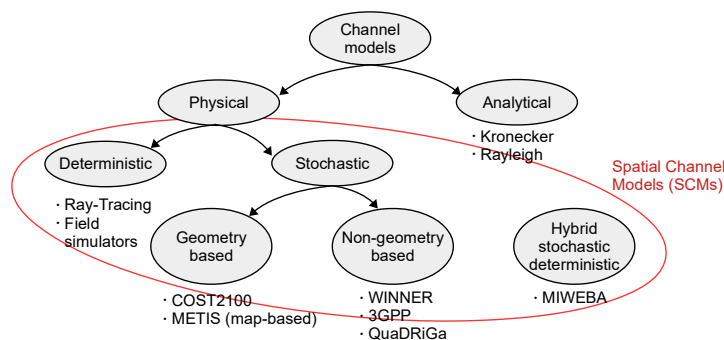


Figure C.1: Classification of channel models according to their nature.

C.1 Introduction

Channel models are one of the most important tools for the design and development of wireless communication systems. It allows to predict the channel behaviour under multiple situations and test system concepts and algorithms. Therefore, model complexities scale accordingly to the system properties under test. For example, if the evaluation parameters are the SNR, coverage, etc., empirical path-loss models as the one treated in Section B.2 offer a good trade-off between complexity and accuracy. On the other hand, if more complex features as beam-forming or coding algorithms are under test, models must offer between others, the information of propagation parameters as DoA and DoD. In addition, if mobility is supported by the terminals, aspects as Doppler and spatial consistency come to the scene.

As shown in Fig. C.1, channel models are frequently classified as physical and analytical, [117]. *Physical* models characterize the environment in terms of the propagation of electromagnetic waves and generate a CIR with parameters that correspond to realistic propagation. These models are antenna independent and frequently assume infinite bandwidth. This makes physical models more flexible, since different antenna characteristics as aperture, array geometry, patterns, etc., and system aspects as bandwidth can be easily embedded for testing. Moreover, physical models are also sub-divided into deterministic and stochastic models, and the latter into geometry-based, non-geometry-based, and a hybrid methodology combining stochastic and deterministic components. All these models, can also be classified as SCMs if they mimic the temporal and angular characteristics of the scatterers in the environment.

On the other hand, *analytical* models characterize the CIR in a mathematical way without considering explicitly propagation phenomena in the background. A set of these models are the correlation-based stochastic channel models (CBSCMs), that generate the MIMO channel coefficients (most frequently in the frequency domain), based on statistics of parameters as correlation properties between antennas. Examples of these models are the Kronecker correlation model, keyhole model, and Rayleigh i.i.d models.

In this work, we focus on physical SCMs. We utilize deterministic models as RT to facilitate the interpretation of measurements and to generate a statistically rich data-set, together with measurements, for parametrization of stochastic models. In addition, in Chapter 6 we extend stochastic models to address multi-band simulations and high resolution systems.

C.2 Deterministic vs Stochastic Physical Channel Modelling

Physical models can be sub-classified into deterministic or stochastic. The main difference is that while the former ones provide the same result every time they are executed, the latter ones generate a completely different channel realization every time they are run, since the output is randomly drawn from statistic distributions. This allows the test of wireless systems under different channels and conditions. Therefore, it is also usual that while the deterministic models are used to analyse specific features under controlled circumstances, the results obtained with stochastic models are based on the analysis of statistics.

The stochastic or deterministic term is applied here to the nature of the model itself, and not to the components inside of the model, since stochastic models can also have deterministic components inside. Examples are the map-based models in METIS [87], the quasi-deterministic models in MiWEBA [99], and the inclusion of explicit components as ground reflection within the 3GPP SCM family [4]. All these simulators produce a different channel every time they are run.

RT is an example of deterministic models. The channel in these cases account with more realistic characteristics and considers detailed physic processes. RT offers a very accurate prediction of the propagation at expenses of high computational needs. However, the accuracy of the results highly depends on the level of details used to describe the scenario, i.e. amount and shape of objects and their electromagnetic properties. The high complexity and computation costs, together with the site and scenario specificity, limits the applicability of deterministic models.

On the other hand, physical stochastic models are pertinent for the generalization of results. They don't necessarily represent a realistic case in a single realization, but the ensemble statistics of multiple repetitions fit with the statistics of real scenarios. Thus, stochastic models don't relate the propagation parameters of the MPCs to particular scatterers, but the parameters are drawn from multi-dimensional random processes, whose distributions are obtained from extensive measurement campaigns. This means that the CIR doesn't correspond to a particular propagation environment, but its statistics do, providing realistic propagation properties to imaginary scatterers. In contrast to deterministic models, physical stochastic models offer high flexibility of generating CIRs for multiple scenarios, being much lighter in terms of computation, but at expenses of reduced accuracy.

Examples of stochastic models are the WIN-II [12], the 3GPP SCM [118], COST 2100 [13], METIS [87], and MiWEBA [119], between others. A further classification and description of physical stochastic models can be found in [120].

In the following sections we address RT as a deterministic modelling approach, and then we focus on statistic models, most specifically, on non-geometry-based and hybrid models.

C.3 Ray-Tracing for mm-wave and Sub-THz Simulations

RT is a deterministic modelling methodology based on the geometrical theory of propagation (GTP), which is an extension of geometrical optics (GO) that accounts for diffraction by introducing GTD. GTP is a high frequency approximation of basic electromagnetic theory based on the concept of ray to treat the different propagation mechanisms described in Section A.1: reflection and transmission on plane surfaces and diffraction on edges.

There are two main basic assumptions in RT: far-field and high frequency. While the first one allows the treatment of the electromagnetic waves as plane waves, the latter considers a small wavelength compared to the dimensions of the objects in the environment.

One of the main motivations to use RT in mm-wave is the accuracy on modelling the directional characteristics of the channel (including polarization). Furthermore, the output of the model is antenna independent and has infinite resolution in the time domain (infinite bandwidth), being more flexible to adapt to different system aspects. On the other hand, between the main limitations of RT we can mention that is a site specific solution whose accuracy highly depends on the good characterization of the environment. A good parametrization of the electromagnetic properties of the constructive materials and a high definition on the shape of objects and details is sometimes not possible. There is always a trade off between the efforts and resources dedicated to the parametrization and the expected accuracy.

RT is usually extended with different methods to treat diffuse scattering. In [121], the authors have introduced a method based on the effective roughness of the surface, in which the scattered components follow a Lambertian scattering pattern, independently of the incident angle. The parameters for this model are obtained experimentally [17]. [122] has extended this method by orienting this Lambertian lobe into the specular direction. The results show that by adopting a single lobe scattering pattern and reshaping it, the simulations agree more satisfactory with the measurements at sub-6 GHz. Recent results at mm-wave have shown that non-specular components in NLOS are much more relevant than expected, since a good agreement between measurements at 26 GHz and the simulations was found only after considering diffuse scattering, [123].

C.4 Review of Stochastic Spatial Channel Models

SCMs are based on the concept of clusters as shown in Fig. C.2: a set of MPCs that are closely related by the propagation distance and angle of arrival and departure. The most popular time delay cluster model is the Saleh-Valenzuela [124]:

$$h(\tau) = \sum_{n=1}^N \sum_{m=1}^M \gamma_{m,n} \cdot \delta(\tau - \tau_n - \tau_{n,m}), \quad (\text{C.1})$$

where $\gamma_{m,n}$ is the complex channel coefficient that describes a MPC arriving at the time τ_n (arriving time of the n^{th} cluster from N) which is subdivided into M sub-paths. SCMs have extended (C.1) including the angular information of each path. The ability of the system

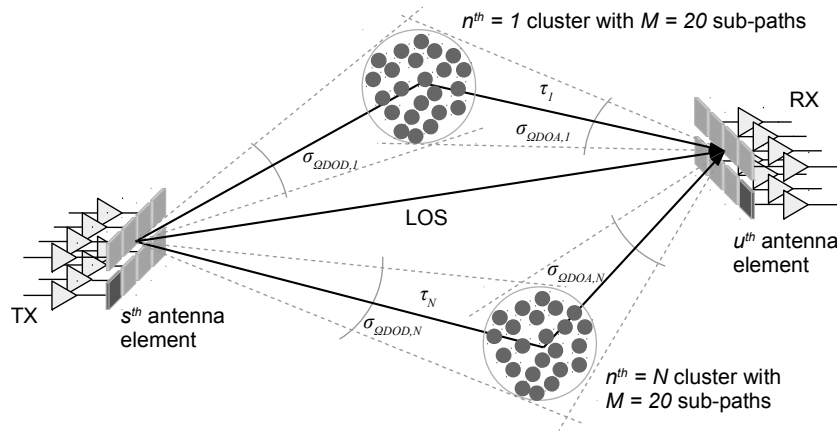


Figure C.2: WINNER representation of clusters with sub-paths.

to resolve the different number of MPCs within the cluster depends on the bandwidth and angular resolution, which is addressed in Section 2.2.

Depending on the authors, stochastic SCM can be divided into two categories: non-geometry-based and geometry-based [120], system-level and cluster-level [97], or Wireless World Initiative New Radio (WINNER)- and European cooperation in science and technology (COST)-type [125], respectively. The former ones generate the multipath components in the parametric domain and they are not related to particular scatterers. Hence, the position of scatterers are defined by the DoD and DoA from the terminal perspective. These models are easily scalable with regard to scenarios, since only the statistics of the LSPs for the different environments are required to parametrize the model. However, as discussed later in this chapter, the scalability in frequency requires modifications in the modelling approach to address the system aspects targeted for high frequencies. Popular examples of these modelling approach are the 3GPP SCMs, WIN-I, WIN-II, and WIN+ models, QuaDRiGa, and METIS.

On the other hand, the latter defines a particular position of the scatterers, which can be placed in a circle, an ellipsoid, or 3D coordinates. The position of the scatterers is defined previous to the simulation. Afterwards, a simplified RT engine is used to define the TDoA and DoA and DoD of the MPCs. The amplitude of the MPCs is defined by the path-loss and the large-scale properties of the corresponding cluster. The concept of visibility region is used to “activate” or “deactivate” the different clusters according to the position of the UE. The randomness of the channel is given by the different number of active clusters from the visibility regions, which also governs the LSPs. Popular examples of such models are COST 273 and COST 2100.

Finally, with the advent of mm-wave communications, a third category of stochastic SCMs has obtained more attention. Hybrid stochastic deterministic models as MiWEBA are stochastic models (they produce a different result on every run) with deterministic components (the main scatterers are treated as in RT). The rest of the scatterers are drawn from stochastic processes.

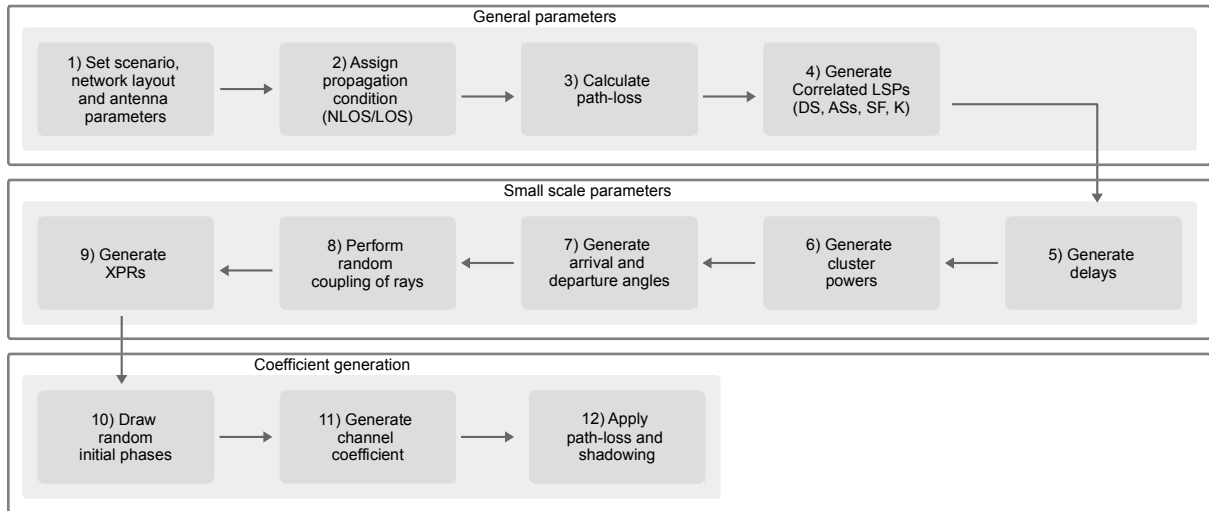


Figure C.3: Channel generation procedure of the 3GPP SCM.

C.4.1 Non-geometry-based Spatial Channel Models: Channel Equation and Channel Impulse Response Generation

System-level models have a similar receipt for the generation of the channel coefficients based on a channel equation (C.5) with variables generated from distributions. Apart from small modifications, they all follow the same structure. Hence, let us consider the latest 3GPP SCM procedure showed in Fig. C.3 ([4], [12]) as a reference to analyse the generation of the channel coefficients.

These models separate parameters into LSPs and small scale parameter (SSP). The first ones are DS, ASs, K-factor, and shadowing. The latter ones correspond to the TDoA, DoA, DoD, and power. While the LSPs are drawn from tabulated distribution functions, the SSPs are drawn also randomly, but using the previously generated LSPs as input to the random distributions.

At a higher level, system-level models generate maps of correlated LSPs with the purpose that different terminals that are closely located, experience similar large-scale values. However, this correlation is only from a statistical point of view, since two closely located terminals will have similar angular spreads, but there is no guarantee that they observe the same physical cluster. Contrarily, cluster-level models predefine the cluster position, and then the terminals observe the clusters based on visibility regions. Once the large-scale parameters are generated in the step 4, they are used to draw the variables from distributions to be used for small-scale fading.

At low level, the small-scale parameter are generated in the following manner: the first step is to generate the cluster delays τ_n from the tabulated DS (step 5). Second, in step 6 the per cluster power P_n is generated using the DS and assuming an exponential delay distribution. Then, the per-cluster DoA and DoD are generated from their respective spreads in step 7. The per sub-paths angles $\phi_{A,n,m}$, $\phi_{D,n,m}$, $\theta_{A,n,m}$, and $\theta_{D,n,m}$ are calculated using fixed offsets to the cluster angles, then the angles are randomly assigned to each sub-path in step

8. The per sub-path XPR $\kappa_{n,m}$ is drawn randomly from a log-normal distribution in step 9. Finally, the initial random phases of each sub-path are $\Phi_{n,m}$ are calculated from a uniform distribution in step 10, and the channel coefficient is generated with (C.5) in step 11.

The CIR is then obtained using the following channel equation:

$$\begin{aligned}
H_{u,s,n}^{\text{NLOS}}(t) &= \sum_{m=1}^M H_{u,s,n,m}^{\text{NLOS}}(t) \\
&= \sum_{m=1}^M \sqrt{\frac{P_n}{M}} \begin{bmatrix} g_{R,u}^{\theta}(\theta_{A,n,m}, \phi_{A,n,m}) \\ g_{R,u}^{\phi}(\theta_{A,n,m}, \phi_{A,n,m}) \end{bmatrix}^T \underbrace{\begin{bmatrix} e^{j\Phi_{n,m}^{\theta\theta}} & \sqrt{\kappa_{n,m}^{-1}} \cdot e^{j\Phi_{n,m}^{\theta\phi}} \\ \sqrt{\kappa_{n,m}^{-1}} \cdot e^{j\Phi_{n,m}^{\phi\theta}} & e^{j\Phi_{n,m}^{\phi\phi}} \end{bmatrix}}_{\mathbf{\Gamma}_{n,m}} \cdots \\
&\cdots \begin{bmatrix} g_{T,s}^{\theta}(\theta_{D,n,m}, \phi_{D,n,m}) \\ g_{T,s}^{\phi}(\theta_{D,n,m}, \phi_{D,n,m}) \end{bmatrix} e^{j\frac{2\pi}{\lambda_0} \mathbf{p}_{T,s}^T \cdot \boldsymbol{\Omega}_{D,n,m}} \cdot e^{j\frac{2\pi}{\lambda_0} \mathbf{p}_{R,u}^T \cdot \boldsymbol{\Omega}_{A,n,m}} \cdot e^{j\frac{2\pi}{\lambda_0} \mathbf{p}_{R,u}^T \cdot \mathbf{v}t}, \quad (\text{C.2})
\end{aligned}$$

where $\frac{\mathbf{p}_{R,u}^T \cdot \mathbf{v}}{\lambda_0} = \nu_{n,m}$ is the Doppler component that depends on the DoA and velocity vector

$$\mathbf{v} = v \cdot \begin{bmatrix} \sin(\theta_v) \cos(\phi_v) & \sin(\theta_v) \sin(\phi_v) & \cos(\theta_v) \end{bmatrix}^T, \quad (\text{C.3})$$

being v the relative velocity of motion.

In LOS, the deterministic channel component is given by:

$$\begin{aligned}
H_{u,s,1}^{\text{LOS}}(t) &= \begin{bmatrix} g_{R,u}^{\theta}(\theta_{A,LOS}, \phi_{A,LOS}) \\ g_{R,u}^{\phi}(\theta_{A,LOS}, \phi_{A,LOS}) \end{bmatrix}^T \begin{bmatrix} 1 & 0 \\ 0 & -1 \end{bmatrix} \begin{bmatrix} g_{T,s}^{\theta}(\theta_{D,LOS}, \phi_{D,LOS}) \\ g_{T,s}^{\phi}(\theta_{D,LOS}, \phi_{D,LOS}) \end{bmatrix} \cdots \\
&\cdots e^{j\frac{2\pi}{\lambda_0} \mathbf{p}_{T,s}^T \cdot \boldsymbol{\Omega}_{D,LOS}} \cdot e^{j\frac{2\pi}{\lambda_0} \mathbf{p}_{R,u}^T \cdot \boldsymbol{\Omega}_{A,LOS}} \cdot e^{\frac{2\pi}{\lambda_0} \mathbf{p}_{R,u}^T \cdot \mathbf{v}t}, \quad (\text{C.4})
\end{aligned}$$

and is finally added to (C.2) to generate the CIR:

$$H_{u,s}^{\text{LOS}}(t, \tau) = \sqrt{\frac{K_R}{K_R + 1}} H_{u,s,1}^{\text{LOS}}(t) \delta(\tau - \tau_1) + \sqrt{\frac{1}{K_R + 1}} H_{u,s}^{\text{NLOS}}(t, \tau), \quad (\text{C.5})$$

where K_R is the Rician K-factor. Note the similarity to the multipath MIMO radio channel equation introduced in (A.45).

We can observe that one of the biggest limitations of (C.5) to address mm-wave communication systems with characteristics as large bandwidth and high directivity is the intra-cluster resolution:

- **Zero-delay spread clusters:** there is no distinction in the TDoA of each sub-path within each cluster n .
- **Equal sub-path power distribution:** each sub-path has the same power $P_{m,n} = P_n/M$.
- **Equal CPR per sub-path:** $|\gamma_{n,m}^{\theta\theta}|^2 = |\gamma_{n,m}^{\phi\phi}|^2$. This is unlikely to happen within clusters since usually reflection coefficients are different for the distinct polarizations as shown

in Fig. A.2. We analyse measurements and simulations and introduce novel modelling methodology in Chapter 7.

- **Fix intra-cluster angular offset:** with higher angular resolution, the intra-cluster angular distribution becomes more relevant.

Part of this problematic is addressed in the 3GPP TR 38.901 Release 15 [4], which recommends the following extensions to deal with large bandwidths and antenna arrays in stochastic channels.

Extensions for Large Bandwidths and Large Antenna Arrays: Modification on the Channel Equation

Under the assumption of large bandwidths and antenna arrays, each ray within a given cluster has a unique TDoA. Hence, (C.2) can be extended as

$$H_{u,s,n,m}^{\text{NLOS}}(t, \tau) = \sqrt{P_{n,m}} \cdot \mathbf{g}_{R,u}(\theta_{A,n,m}, \phi_{A,n,m})^T \cdot \mathbf{\Gamma}_{n,m} \cdot \mathbf{g}_{T,s}(\theta_{D,n,m}, \phi_{D,n,m}) \cdots \\ \cdots e^{j \frac{2\pi}{\lambda(f)} \mathbf{p}_{T,s}^T \cdot \mathbf{\Omega}_{D,n,m}} \cdot e^{j \frac{2\pi}{\lambda(f)} \mathbf{p}_{R,u}^T \cdot \mathbf{\Omega}_{A,n,m}} \cdot e^{\frac{2\pi}{\lambda_0} \mathbf{p}_{R,u}^T \cdot \mathbf{v}t} \delta(\tau - \tau_{n,m}). \quad (\text{C.6})$$

When the bandwidth and array size become critical, the delay between the antenna elements become significant, and $\tau_{n,m}$ in (C.6) is replaced by

$$\tau_{u,s,n,m} = \tau_{n,m} - \frac{1}{c} \mathbf{p}_{R,u}^T \cdot \mathbf{\Omega}_{A,n,m} - \frac{1}{c} \mathbf{p}_{R,s}^T \cdot \mathbf{\Omega}_{D,n,m}. \quad (\text{C.7})$$

We have introduced in [126] and in [127] an analysis of the influence of bandwidth and array size on hybrid beam-forming at mm-wave in indoor scenarios using RT simulations. We have shown that there is a degradation on performance when the channel model considers the influence of the delays between the antenna elements. Neglecting these intra-array delays results in an overestimation of the achievable capacities.

Extensions for Large Bandwidths and Large Antenna Arrays: Modelling of Intra-cluster Angular and Delay Spreads

With higher temporal and angular resolution, there are three parameters per cluster n that need to be generated with more details: offset angles, relative delay of the m^{th} sub-path, and the sub-path power.

In (C.5), each sub-path had equal power distribution, which is unlikely to happen if we are able to isolate or resolve, each sub-path. [4] recommends to calculate the power of each

sub-path using $P_{n,m} = P_n \cdot \frac{\hat{P}_{n,m}}{\sum_{m=1}^M \hat{P}_{n,m}}$, where

$$\hat{P}_{n,m} = e^{-\frac{\tau_{n,m}}{DS_n}} \cdot e^{-\frac{\sqrt{2}|\alpha_{AoA,n,m}|}{ASA_n}} \cdot e^{-\frac{\sqrt{2}|\alpha_{AoD,n,m}|}{ASD_n}} \cdot e^{-\frac{\sqrt{2}|\alpha_{EoA,n,m}|}{ESA_n}} \cdot e^{-\frac{\sqrt{2}|\alpha_{ESD,n,m}|}{ESD_n}}, \quad (\text{C.8})$$

where DS_n , ASA_n , ESA_n , ASD_n , and ESD_n are the per cluster DS, ASA, ESA, ASD, and ESD, respectively. Furthermore, $\alpha_{n,m,\{AoA,AoD,EoA,EoD\}} \sim \text{unif}(-2,2)$ is the intra-cluster angle offset.

The intra-cluster delays are generated as

$$\hat{\tau}_{n,m} = \hat{\tau}'_{n,m} - \min \left(\left\{ \hat{\tau}'_{n,i} \right\}_{i=1}^M \right),$$

where n is the current cluster index, and $\hat{\tau}'_{n,m} \sim \text{unif}(0, 2 \cdot DS_n)$. Finally, $\tau_{n,m} = \tau_n + \hat{\tau}_{n,m}$ in (C.6).

This recommendation also addresses the possibility of different number of sub-paths M per cluster, that depends on a sparsity index, and a custom variable to select a trade-off between simulation complexity and accuracy, since at the end, each MPC has a different TDoA, DoA, and DoD. More details can be found in [4].

Explicit Ground Reflection

As we have already addressed in Section D.3, the ground reflection is a component that can be deterministically estimated based on the location of the terminals. The latest 3GPP recommendation considers the explicit inclusion of the ground reflection as an additional modelling component [4]. Similarly, measurements and modelling aspects on GR within the QuaDRiGa model can be found in [128]. An analysis based on the measurements presented in this work is addressed in Section 6.3.1. Regarding multi-band modelling, the relative permittivity of the ground material $\epsilon_{GR} \in \mathbb{C}$ is frequency dependent.

Correlation Modelling for Multi-frequency Simulations

In the 3GPP SCMs in [4], the extension for the correlated multi-band models is addressed as an additional modelling component. In this model, the LSPs are synthesized from distributions with mean and standard deviation modelled as a frequency dependent function. As an example, the DS in UMi Street Canyon scenarios in NLOS is calculated as

$$\begin{aligned} \mu_{\text{lgDS}}(f_c) &= -0.24 \log_{10}(1 + f_c) - 6.83 \\ \sigma_{\text{lgDS}}(f_c) &= 0.16 \log_{10}(1 + f_c) - 0.28, \end{aligned} \quad (\text{C.9})$$

where f_c is the carrier frequency. The multi-band correlated LSPs are calculated then as

$$DS(f_c) = 10^{x \cdot \sigma_{\text{lgDS}}(f_c) + \mu_{\text{lgDS}}(f_c)}, \quad (\text{C.10})$$

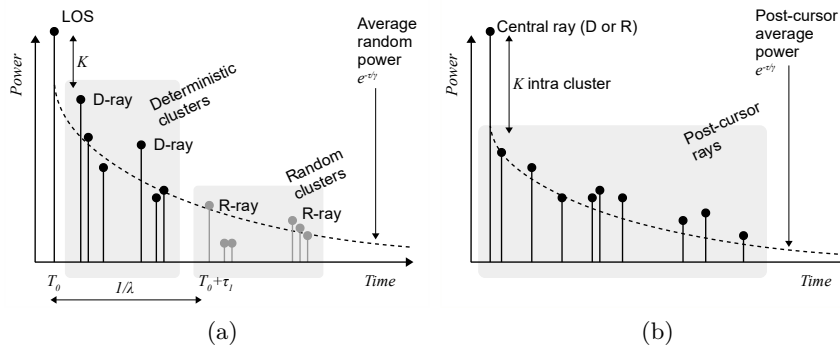


Figure C.4: Structure of the CIR in the quasi-deterministic model MiWEBA: (a) complete CIR, and (b) intra-cluster detail.

where the same $x \sim \mathcal{N}(0,1)$ is used for all the frequencies. This introduces a full-correlation of the LSPs over frequency. Differently, we propose in Chapter 6 an approach based on the measured correlations over frequency.

The delays, directions of arrival and departure are generated only once, based on the LSPs calculated from the lowest f_c . Afterwards, the power of the different clusters are calculated from the LSPs over the different frequencies, but referenced to the LSPs of the lowest f_c . More details on the implementation can be found in [4].

C.4.2 Quasi-deterministic Spatial Channel Modelling

In this sub-section we make a summary of this modelling approach taking as a reference the MiWEBA model from [99]. This model consists of a pre-defined set of deterministic clusters and random clusters depending on the different scenarios.

Channel Impulse Response Equation

The CIR equation is defined from the 802.11ad channel modelling document [129],

$$\begin{aligned}
 h(t, \phi_{\text{TX}}, \theta_{\text{TX}}, \phi_{\text{RX}}, \theta_{\text{RX}}) &= \sum_i A_i C_i(t - T_i, \phi_{\text{TX}} - \Phi_{\text{TX},i}, \theta_{\text{TX}} - \Theta_{\text{TX},i}, \dots \\
 &\quad \dots \phi_{\text{RX}} - \Phi_{\text{RX},i}, \theta_{\text{RX}} - \Theta_{\text{RX},i}) \\
 C_i(t, \phi_{\text{TX}}, \theta_{\text{TX}}, \phi_{\text{RX}}, \theta_{\text{RX}}) &= \sum_k \alpha_{i,k} \delta(\tau - \tau_{i,k}) \delta(\phi_{\text{TX}} - \phi_{\text{TX},i,k}) \dots \\
 &\quad \dots \delta(\theta_{\text{TX}} - \theta_{\text{TX},i,k}) \delta(\phi_{\text{RX}} - \phi_{\text{RX},i,k}) \delta(\theta_{\text{RX}} - \theta_{\text{RX},i,k}), \quad (\text{C.11})
 \end{aligned}$$

As shown in Fig. C.4, this approach considers different kind of clusters C_i according to the nature of the cursor rays.

Deterministic rays (D-rays)

These paths are calculated explicitly based on the geometry of the scenario and propagation conditions. Depending on the scenario, there are a pre-defined set of deterministic rays, which include ground reflections, reflections on walls, and double wall-ground reflections. The delay and direction of these rays are calculated using the method of images and the amplitude and polarization with Fresnel equations. In addition, the roughness of the surface is also considered using the Rayleigh criterion.

Random rays (R-rays)

These are low power paths from irregular objects or high order reflections. The cluster's time of arrival follow a Poisson distribution and the paths are exponentially distributed. The DoA and DoD are uniformly distributed within pre-defined ranges that depend on the scenarios. More details can be found in [99]. While the paths amplitudes are drawn from i.i.d. Rayleigh random variables, the phases are from uniform random variables. Polarization is also treated stochastically, being the amplitude of the co-polarized components drawn from truncated log-normal distributions, and the cross-polarized from uniform distributions in the interval $[-0.1, 0.1]$.

Intra-cluster Properties

As Fig. C.4b shows, clusters are composed of a central D- or R-ray $\alpha_{i,0}$ followed by K post-cursor rays $\alpha_{i,1}, \dots, \alpha_{i,K}$, where k depends on the cluster and scenario. The post-cursors have a time of arrival following a Poisson distribution with arrival rate λ . The power of the post-cursor rays decay exponentially with a decay time γ . On the other hand, due to limited experimental results available during the modelling phase, intra-cluster angular spreads are modelled as independent normally distributed variables with $\mathcal{N}(0, 5^\circ)$.

C.5 Summary of the State of the Art in mm-wave and Multi-band Channel Modelling

mm-wave communications at 60 GHz were already standardized in 2012 in the frame of the IEEE 802.11ad working group. In such a context, channel models were demanding extensions to consider wider bandwidths and higher intra-cluster resolutions, being the quasi-deterministic approach introduced by [130] one of the first approaches toward more deterministic models within stochastic frameworks.

Since then, different projects have developed their own channel model based on their understanding of necessities and applications. Between the most relevant and widely spread mm-wave channel models we can mention:

- **mmMAGIC 5GPP¹** is a SCM based on the guidelines in [4] with additional features covering a frequency range from 6 to 100 GHz. Since it is based on the 3GPP TR 38.901, this model addresses the intra-cluster characteristics mentioned in Section C.4.1. The main focus is the modelling of frequency dependent large-scale parameters, ground reflection effects, cluster, and sub-paths, small-scale fading, blockage, building penetration among others. This model covers a wide range of application scenarios, from shopping malls to street canyon, [51].
- **NYU Wireless:** this is a statistical spatial channel model SSCM developed using time clusters and spatial lobes. Based on multiple measurements at different frequencies ranging from 28 GHz to 73 GHz, it generates multi-path parameters for omnidirectional and directional CIRs with their corresponding PAPs. It supports multiple scenarios as urban-micro (UMi), urban-macro (UMa), and rural-macro (RMa) [131].
- **METIS:** this channel model is based on the WINNER/3GPP and has three modelling approaches: map-based (ray tracing), stochastic (GBSCM), and a hybrid model. The Supported frequencies range is from 0.45 GHz to 70 GHz, and the bandwidth from 100 MHz for a carrier up to 6 GHz, and 1 GHz for higher frequencies. However, intra-cluster spreads are not addressed in the stochastic model, keeping the zero-delay spread clusters legacy from WINNER and 3GPP. The scenarios depend on the selected model. The models parameters were derived from measurements and simulations.
- **QuaDRiGa:** it is based on WINNER and the 3GPP SCMs, with quasi-deterministic extensions to support spatial consistency and tracking of users. It has been parametrized from extensive measurement campaigns in multiple frequency bands from sub-6 GHz to the mm-wave spectrum.
- **MiWEBA²:** it is based on a quasi-deterministic (Q-D) channel model [130], that combines a geometry-based approach for a limited number of deterministic multi-path components and a stochastic approach. The CIR consists of few strong Q-D rays, a moderate number of relatively weak random rays (R-rays) and flashing rays (F-rays). This model includes intra-cluster spreads. The clusters are modelled having a strong component called cursor, and then following an exponential decay. MiWEBA only addresses the 60 GHz channel and the scenarios are classified as access (open area, street canyon and Indoor), backhaul/front haul (above roof top, street canyon), and D2D (open area, street canyon and Indoor), among others, [119]. The model parameters were derived from measurements and extensive RT simulations.

¹We have contributed to this project providing measurements and analysis of intra-cluster fading properties.

²Without directly participating in this initiative, we have contributed to the parametrization of this model within the frame of the IEEE 802.11 Next Generation 60GHz (NG60) Study Group by providing intra-cluster DSs from measurements in a large hall scenario (IEEE 802.11-16/0668r0).

D Miscellaneous

Overview

This chapter collects several mathematical proofs, simulations, and empirical validations of ray-tracing models addressed in the main body of this work.

D.1 Identification of the Channel Impulse Response using M-sequences

M-sequences are a sub-class of PRBS, also known as PN sequences, with the particularity that they are periodic and reproduce every possible binary sequence that can be generated using a shift register. Furthermore, the amount of ones and zeros in the binary sequence is the same, and as shown later, it leads to a flat spectrum. The length N of the PN-sequence is related to the length M of the register by $N = 2^M - 1$.

Let us represent an ideal discrete bipolar M-sequence with amplitude V as

$$s(t) = V \cdot \overbrace{\text{rect}\left(\frac{t}{T_0}\right)}^{\text{pulse shape } s_0(t)} * \underbrace{\sum_{n=0}^{N-1} b_n \cdot \delta(t - nT_0)}_{\text{binary sequence } b(t)}, \quad (\text{D.1})$$

where $T_0 = \frac{1}{f_0}$ is the length of a single chip, f_0 the clock frequency, and $b_n \in \mathcal{U}\{-1, +1\}$ is the uniform bipolar distributed signal indicating the amplitude of the n^{th} chip. The total length of the sequence is $T_N = NT_0$.

The binary sequence $b(t)$ has the following autocorrelation properties [132]

$$R_{b,b}(nT_0) = \frac{1}{N} \sum_{m=0}^{N-1} b(t) \cdot b^*(t + nT_0) = \begin{cases} 1 & \text{if } n = 0 \\ -\frac{1}{N} & \text{if } 0 < n < N \end{cases} \quad (\text{D.2})$$

where the ratio $1/\frac{1}{N} = N$ defines the peak to side-lobes amplitude, which increases directly proportional to the length of the sequence. The autocorrelation of the binary sequence with the pulse shape introduced in (D.1) can be calculated as the convolution with a time inverted copy of it self

$$\begin{aligned} R_{s,s}(t) &= s(t) * s^*(-t), \\ &= b(t) * \underbrace{s_0(t) * s_0^*(-t)}_{V^2 \cdot \text{tri}\left(\frac{t}{T_0}\right)} * b^*(-t), \\ &= V^2 \cdot \text{tri}\left(\frac{t}{T_0}\right) * R_{b,b}(t), \\ &= V^2 \left(\frac{N+1}{N}\right) \cdot \text{tri}\left(\frac{t}{T_0}\right) - \frac{V^2}{N}, \end{aligned} \quad (\text{D.3})$$

The power spectral density (PSD) of the sequence is related to the autocorrelation by its Fourier transform (under the assumption of an ergodic process) $\text{PSD}_s(f) \bullet \text{---} \circ R_{s,s}(t)$:

$$\text{PSD}_s(f) = V^2 \left(\frac{N+1}{N}\right) \cdot \text{sinc}^2(T_0 f). \quad (\text{D.4})$$

Let us consider a LTI system described by its impulse response $h(t)$ representing a multi-path propagation channel as described in Section A.2. The input signal to the system is a sounding m-sequence $s(t)$ as described in (D.1). The RX signal $x(t)$ is represented as the convolution between the channel and the TX signal $s(t)$:

$$x(t) = h(t) * s(t). \quad (\text{D.5})$$

At the RX, we convolve the RX signal $x(t)$ with a time inverted complex conjugated copy $\tilde{s}(t)$ of the TX sequence $s(t)$, which results in the cross-correlation $C_{x,\tilde{s}}(t)$:

$$\begin{aligned} C_{x,\tilde{s}}(t) &= x(t) * \tilde{s}^*(-t), \\ &= h(t) * \underbrace{s(t) * \tilde{s}^*(-t)}_{R_{s,\tilde{s}}(t)} + \underbrace{n(t) * \tilde{s}^*(-t)}_{\text{noise term } \tilde{n}(t)}, \end{aligned} \quad (\text{D.6})$$

where $n(t)$ is AWGN. Under the assumption that $s(t) = \tilde{s}(t)$, $R_{s,\tilde{s}}(t)$ tends to a Kronecker delta function, hence the convolution in (D.6) becomes the recovered CIR $h(t)$:

$$C_{x,\tilde{s}}(t) = h(t) * \left(\underbrace{V^2 \cdot \text{tri}\left(\frac{t}{T_0}\right)}_{\rightarrow V^2 \cdot \delta(t)} + \underbrace{\frac{V^2}{N} \cdot \text{tri}\left(\frac{t}{T_0}\right) - \frac{V^2}{N}}_{\rightarrow 0} \right) + \tilde{n}(t) \approx \overbrace{V^2 \cdot h(t)}^{\text{measured CIR}} + \underbrace{\tilde{n}(t)}_{\text{measured noise}}. \quad (\text{D.7})$$

The complete process also benefits the CIR estimation with an auto-correlation gain of V^2 . Furthermore, under the assumption of $h(t)$ being uncorrelated to the measurement noise $\tilde{n}(t) \sim \mathcal{N}(0, \sigma_N^2)$, the measurement SNR can be increased by taking N_{avg} snapshots per measurement and averaging. Since AWGN is a zero mean Gaussian random process, the noise in the averaged output will be reduced by a factor of N_{avg} . Hence, with $N_{avg} = 1024$ snapshots, the SNR is increased by 1024 times (≈ 30 dB).

The length of the M-sequence defines also the un-ambiguity measurement range: if copies of the sequence are received after a complete period given by T_N , the autocorrelation is wrapped around and it is impossible to identify absolute delays¹. Assuming a bandwidth BW equal to the clock frequency $f_0 = 6.75$ GHz, the measurement distance is then limited to $d_{\max} = c \cdot 1/BW = 181.87$ m for the $M = 12$ bit sequence, and to $d_{\max} = 1455.30$ m for the $M = 15$ bit sequence.

¹In some cases, the wrap around effect can be counteracted by performing directive scans and counting with a good knowledge of the environment. The wrapped around reflections usually arrive from different directions and can be isolated in the directional scan domain and re-aligned relative to the absolute delay.

D.2 Influence of Bandwidth in Band-limited Channels

Let us consider a CIR as the summation of L MPCs

$$h(\tau) = \sum_L \gamma_l \delta(\tau - \tau_l), \quad (\text{D.8})$$

where $\gamma_l \in \mathbb{C}$ is the complex gain of the l^{th} path. The frequency transfer function of the channel $H(f)$ is calculated as the Fourier transform

$$\begin{aligned} H(f) &= \int h(\tau) e^{-j2\pi f\tau} d\tau, \\ &= \int \sum_L \gamma_l \delta(\tau - \tau_l) e^{-j2\pi f\tau} d\tau, \\ &= \sum_L \gamma_l \int \delta(\tau - \tau_l) e^{-j2\pi f\tau} d\tau, \\ &= \sum_L \gamma_l \int e^{-j2\pi f\tau_l} d\tau, \\ &= \sum_L \gamma_l e^{-j2\pi f\tau_l}. \end{aligned} \quad (\text{D.9})$$

The sampling process introduces a band limitation on the frequency domain, given by the sampling frequency f_s . Therefore, after sampling, $\tilde{H}(f)$ is calculated as

$$\tilde{H}(f) = \text{rect}\left(\frac{f}{f_s}\right) H(f), \quad (\text{D.10})$$

where $f_s = 2B = \frac{1}{\Delta\tau}$ is the sampling frequency, and B the bandwidth

$$\text{rect}\left(\frac{f}{f_s}\right) = \begin{cases} 1 & \text{if } |f| < f_s/2 \\ 0 & \text{if } |f| > f_s/2 \end{cases} \bullet \circ \frac{1}{\Delta\tau} \cdot \text{sinc}\left(\frac{\tau}{\Delta\tau}\right). \quad (\text{D.11})$$

The band-limited CIR $\tilde{h}(\tau)$ is then calculated as the inverse Fourier transform of $\tilde{H}(f)$

$$\begin{aligned} \tilde{H}(f) = \text{rect}\left(\frac{f}{f_s}\right) H(f) \bullet \circ \tilde{h}(\tau) &= \frac{1}{T} \cdot \text{sinc}\left(\frac{\tau}{\Delta\tau}\right) * h(\tau), \\ &= \frac{1}{\Delta\tau} \cdot \text{sinc}\left(\frac{\tau}{\Delta\tau}\right) * \sum_L \gamma_l \delta(\tau - \tau_l), \\ &= \frac{1}{\Delta\tau} \cdot \sum_L \gamma_l \cdot \text{sinc}\left(\frac{\tau - \tau_l}{\Delta\tau}\right). \end{aligned} \quad (\text{D.12})$$

Let us now consider the discrete sampled signal $\hat{h}(\tau) = \sum_k \tilde{h}(k\Delta\tau) \delta(\tau - k\Delta\tau)$. The sampled channel consists of the real channel convolved with a “sinc” function. Therefore, considering that $\text{sinc}\left(\frac{\tau}{\Delta\tau}\right) = 0 \forall \tau = n\Delta\tau$ with $n \in \mathbb{Z}$, then $\hat{h}(\tau) = h(\tau)$ only if $\tau_l = n\Delta\tau$. This is very unlikely to happen. Hence, $\hat{h}(\tau)$ will be, at each delay sample $k\Delta\tau$, the scaled summation of

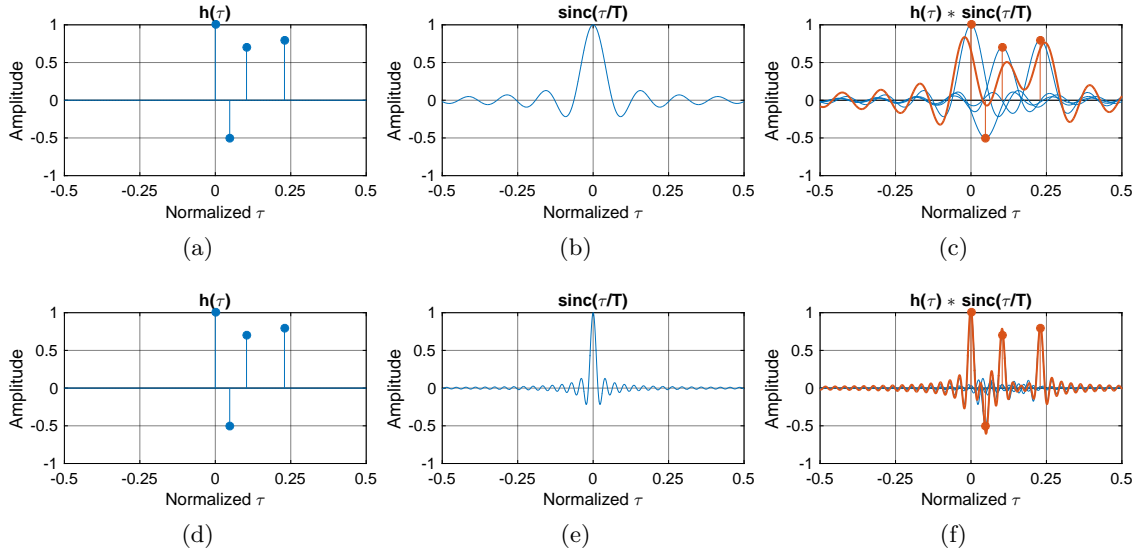


Figure D.1: CIR (a) and (d), sinc function with different bandwidths (b) and (e), and the band-limited measured CIR with different bandwidths (c) and (f).

shifted *sinc* functions:

$$\hat{h}(\tau) = \sum_k \frac{1}{\Delta\tau} \sum_l \gamma_l \cdot \text{sinc}\left(\frac{k\Delta\tau - \tau_l}{\Delta\tau}\right) \delta(\tau - k\Delta\tau). \quad (\text{D.13})$$

The complete process is depicted with two examples in Fig. D.1. An arbitrary CIR is presented in Fig. D.1a and Fig. D.1d, the *sinc* function with two different bandwidths in Fig. D.1b and Fig. D.1e, and the result of the convolution in Fig. D.1c and Fig. D.1f. We can observe that the influence of subsequent paths is larger when the bandwidth is shorter, $\Delta\tau \rightarrow 0$, since the width of *sinc* is broader. On the other hand, with larger bandwidths, each path is isolated in the delay domain, and the influence of the side-lobes of the *sinc* function is also reduced.

D.3 Analysis of the Influence of Directivity and Bandwidth using the Deterministic Two-rays Ground-reflection Model

Let us now analyse the influence of multipath propagation on path-loss and fading, and then the influence of system aspects as directivity and bandwidth using the two-ray ground-reflection analytical model shown in Fig. D.2. This model accounts for the interference of a direct LOS and a specular reflected path from the ground. Let us describe the stationary two-rays ground-reflection radio channel model using (A.39) as

$$\tilde{h}(\tau) = \sum_{l=1}^2 \underbrace{\mathbf{g}_R^T(\boldsymbol{\Omega}_{A_l}) \boldsymbol{\Gamma}_l \mathbf{g}_T(\boldsymbol{\Omega}_{D,l})}_{a_l} \delta(\tau - \tau_l), \quad (\text{D.14})$$

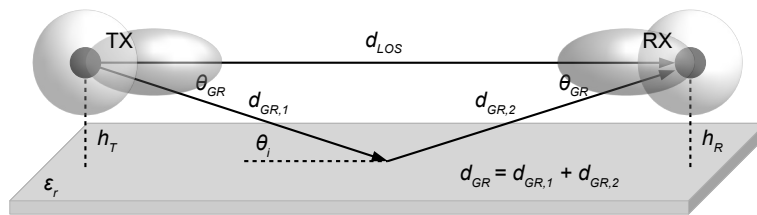


Figure D.2: Components of the two-rays ground-reflection model.

where the path $l = 1$ is the LOS and $l = 2$ is the ground reflection. The narrowband RX power at a TX-RX distance d is calculated using (B.4)

$$P_R(d) = P_T \left(\frac{c}{4\pi f_c} \right)^2 \cdot \left| \underbrace{\frac{\sqrt{g(\phi_{\text{LOS}}, \theta_{\text{LOS}})}}{d_{\text{LOS}}}}_{\text{LOS path}} + \Gamma(\theta_i) \underbrace{\frac{\sqrt{g(\phi_{\text{GR}}, \theta_{\text{GR}})}}{d_{\text{GR}}}}_{\text{Reflected path}} \cdot e^{-j2\pi \frac{\Delta d}{\lambda_c}} \right|^2, \quad (\text{D.15})$$

where d_{LOS} and d_{GR} are the propagation distance of the LOS and ground reflection paths, respectively, $\Delta d/\lambda_c = (d_{\text{GR}} - d_{\text{LOS}})/\lambda_c$ is the difference of phase between the two components, $g(\cdot)$ is the gain of the antennas, and $\Gamma(\cdot)$ is the ground reflection coefficient that depends on the polarization and complimentary incident angle $\theta_i = \theta_{\text{GR}}$:

$$\Gamma(\theta_i) = \frac{\sin(\theta_i) - X_{H/V}}{\sin(\theta_i) + X_{H/V}}, \quad (\text{D.16})$$

where

$$X_V = \frac{\sqrt{\epsilon_r - \cos^2(\theta_i)}}{\epsilon_r}, \text{ and } X_H = \sqrt{\epsilon_r - \cos^2(\theta_i)}. \quad (\text{D.17})$$

Fig. D.3b shows the effects of multi-path on fading, generating locations with higher and lower power than the FSPL, displayed in red. The reflection coefficient for concrete ($\epsilon_r = 4.5$) for different distances can be observed in Fig. D.3a. At short distances there is a change on the phase, meaning that at the same position there will be a constructive and destructive interference in the different polarizations, as shown in the detailed Fig. D.3b. The use of polarization diversity could reduce the effects of fading, since the strongest polarizations could be chosen in the different positions. The model in (D.15) is narrowband, valid only for a single frequency $f_c = \frac{c}{\lambda_c}$. However, the extension to larger bandwidths is straightforward. The received power is then calculated as the sum of the power of each sub-carrier. Furthermore, if we add directivity to the antenna, the influence of the interfering path at shorter TX-RX distances is diminished reducing fading, as shown in Fig. D.4. More on fading is addressed in the following chapter.

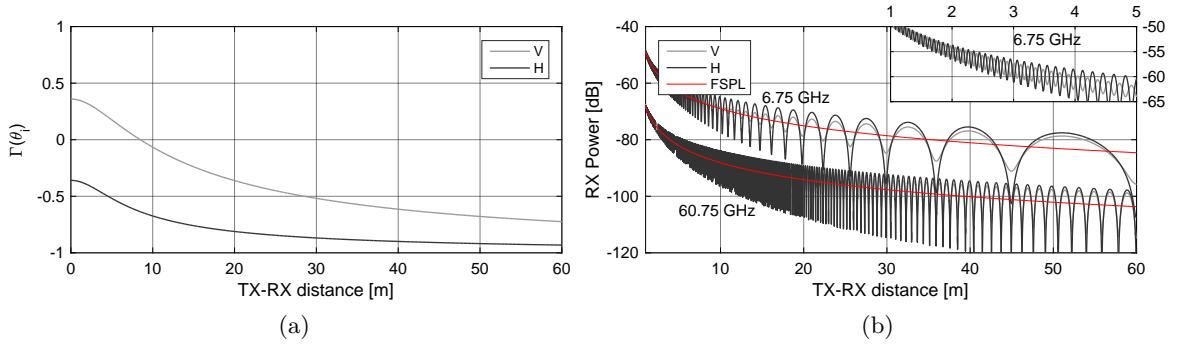


Figure D.3: (a) Ground reflection coefficients (polarimetric) for concrete and (b) simulated RX power with the two-rays with ground-reflection model for different polarizations with isotropic antennas at 6.75 GHz and 60.75 GHz.

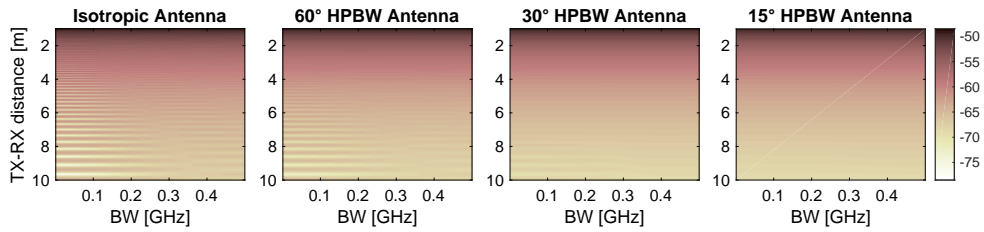


Figure D.4: Influence of bandwidth and directivity in the RX power for the two-rays ground-reflection model with horizontal polarization at 60.75 GHz.

D.4 Simulative Analysis of the Influence of Directivity and Bandwidth in Small-scale Fading

Similarly to Appendix D.2, let's define a test scenario with $L = 3$ (signal sources) located as indicated in Fig. D.5a and a RX with an isotropic antenna, which moves away from the scatterers in the direction $\phi_\nu = 0$ and $\theta_\nu = 0$.

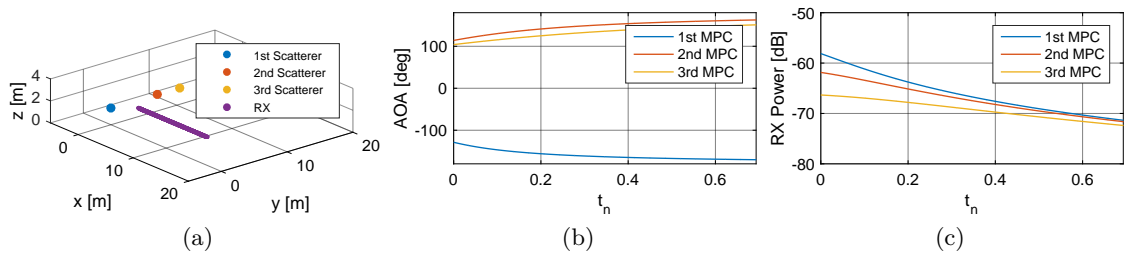


Figure D.5: Simulation set-up: (a) scenario, (b) AOA, and (c) RX power.

The baseband digitized RX signal in the frequency domain is calculated as²

$$\hat{H}(t_n, f_k) = \sum_{l=1}^L \gamma_l e^{-j2\pi f_k \tau_l} e^{j2\pi \nu_l t_n}, \quad (\text{D.18})$$

where $t_n = \{0, \dots, \Delta t, \dots, (N-1)\Delta t\}$ are the different time instances. The sampling time is selected in order to have 4 samples per wavelength $\lambda_c = \frac{c}{f_c}$ in space, with $f_c = 6$ GHz. Hence, with a constant velocity $v = 5 \text{ km h}^{-1}$, $\Delta t = \frac{\lambda_c/4}{v}$. In total, $N = 1000$ samples were simulated in the time domain. On the other hand, $f_k = \left\{ -\frac{(K-1)}{2}\Delta f, \dots, \frac{(K-1)}{2}\Delta f \right\}$ are the baseband frequency components, with a total of $K = 10000$ samples, and $\Delta f = B$, $\gamma_l = \frac{1}{4\pi f_c \tau_l}$ is the amplitude of each path (assumed to be only FSPL), τ_l is the delay and $\nu_l = \frac{v}{\lambda_c} \cdot \mathbf{r}_{\text{RX},l}^T \mathbf{v}$ the Doppler signature of each MPC, with

$$\begin{aligned} \mathbf{r}_{\text{RX},l}^T &= [\cos \theta_{\text{AOA},l} \cos \phi_{\text{AOA},l} \quad \cos \theta_{\text{AOA},l} \sin \phi_{\text{AOA},l} \quad \sin \theta_{\text{AOA},l}], \\ \mathbf{v}^T &= [\cos \theta_\nu \cos \phi_\nu \quad \cos \theta_\nu \sin \phi_\nu \quad \sin \theta_\nu]. \end{aligned} \quad (\text{D.19})$$

The other domains are related by the direct and inverse Fourier transform, as introduced in Section A.2.1, and the marginal profiles are calculated by integrating in the corresponding dimension, as discussed in Section A.2.1. Regarding the independent variables, the Doppler domain is related to time by $\nu = \left\{ -\frac{1}{\Delta t/2}, \dots, \frac{1}{\Delta t/2} \right\}$, and the delay domain to the frequency by $\tau_k = \{0, \dots, \Delta \tau, \dots, (k-1)\Delta \tau\}$, with $\Delta \tau = \frac{1}{B}$.

The AoAs and RX power of each MPC over time is displayed in Fig. D.5b and Fig. D.5c, respectively.

Let's analyse the case of $L = 1$ and $L = 3$ MPCs. The first case emulates only the filtering effect of the antenna (we don't account for the gain in the direction of the selected MPC). The channel that the system observes with the different bandwidths is depicted in Fig. D.6. We can see that since we have a single MPC, we have a frequency flat channel, independently from the bandwidth.

In addition, Fig. D.7 shows the Doppler PSD with different number of MPCs and bandwidths. It can be observed the widening of the spectrum (spreading) with the increasing number of MPCs.

On the other hand, the channel that the system observes with the different bandwidths and $L = 3$ MPCs is shown in Fig. D.8. Firstly, with more paths, the channel is frequency-flat or selective depending on the bandwidth and different positions. With a short bandwidth, when all the MPCs can't be resolved, the channel is, independently from the number of MPCs, frequency flat, as shown in Fig. D.9a. On the other hand, with a larger bandwidth, if the channel is flat or selective, depends on the number of MPCs, as seen in Fig. D.9b and Fig. D.9c.

²This already accounts the band limitation effects discussed in Appendix D.2.

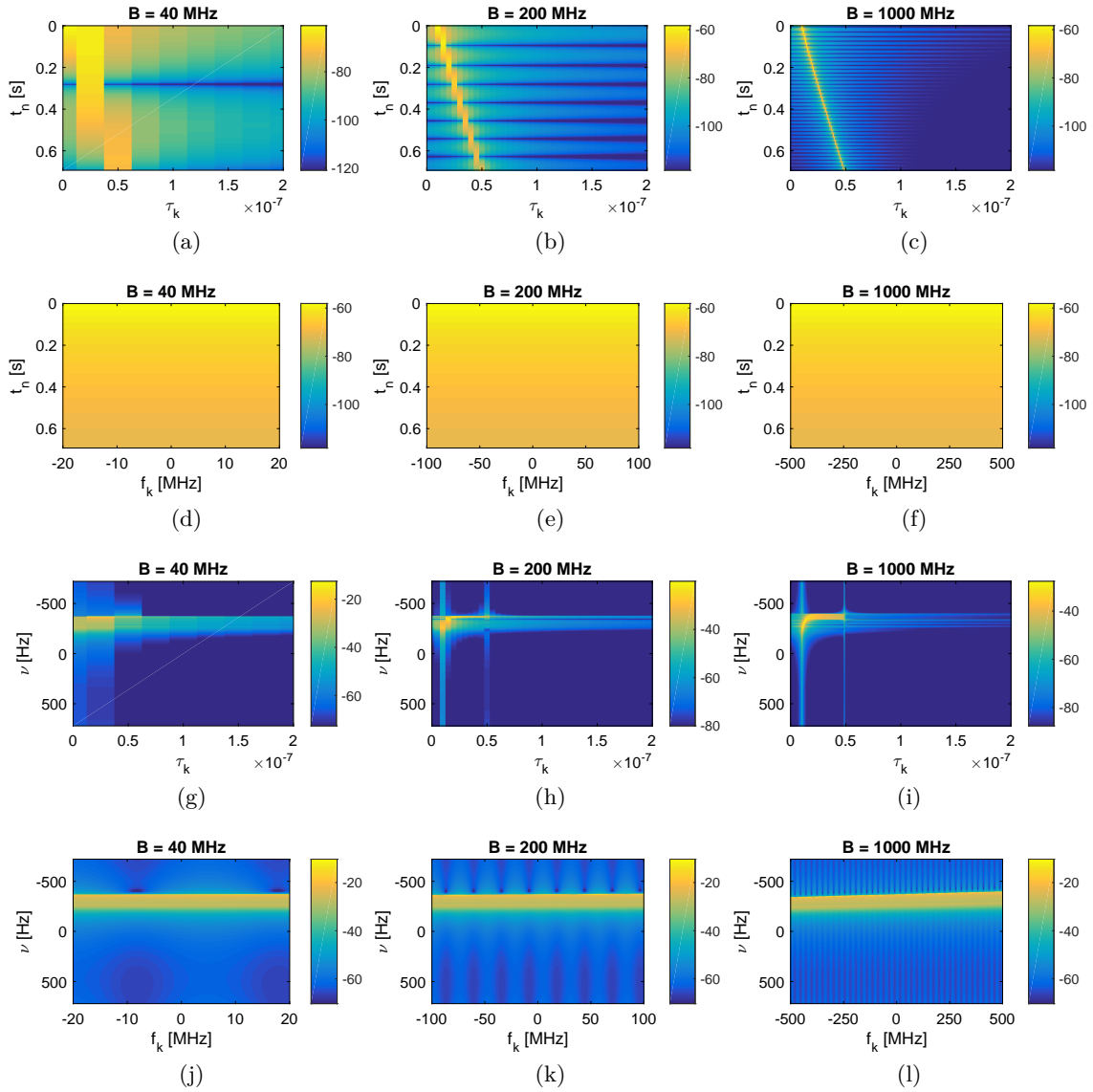


Figure D.6: Single-path channel in the different domains with different bandwidths (a)-(c) delay-time, (d)-(f) frequency-time, and (g)-(i) frequency-Doppler.

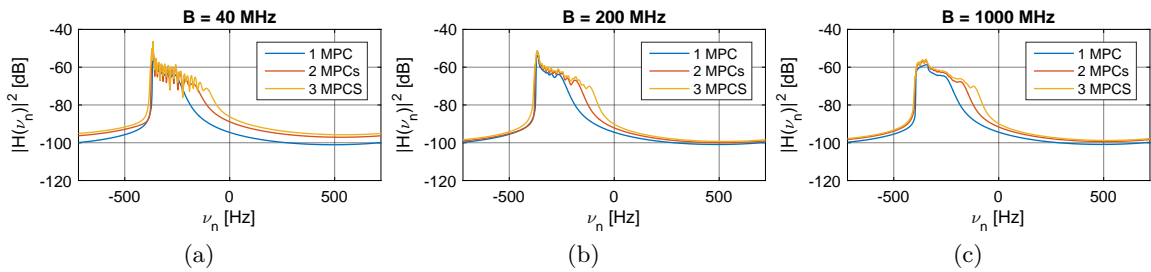


Figure D.7: Doppler power spectrum density for different bandwidths and number of MPCs within the channel.

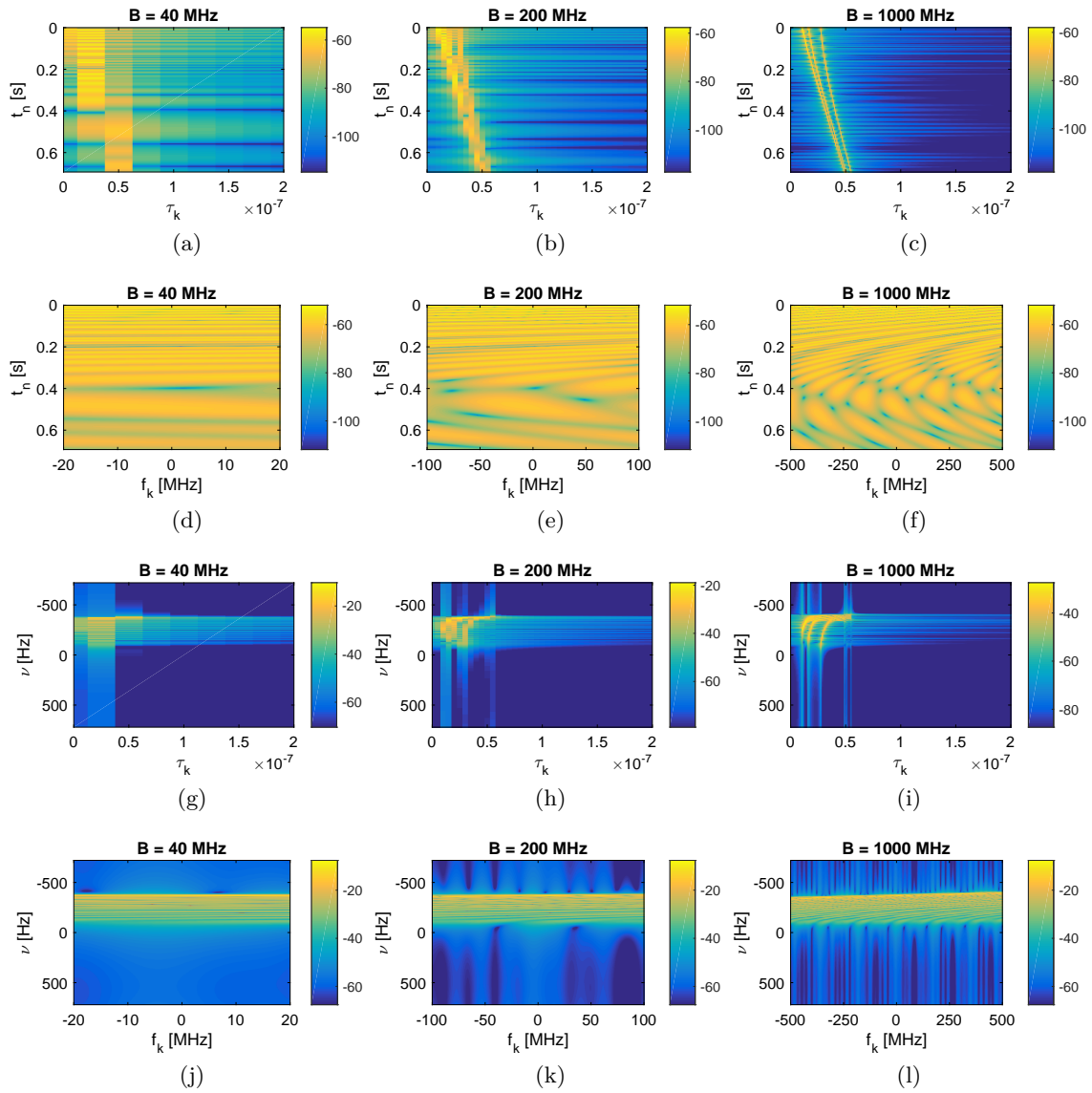


Figure D.8: Three-paths channel in the different domains with different bandwidths (a)-(c) delay-time, (d)-(f) frequency-time, and (g)-(i) frequency-Doppler.

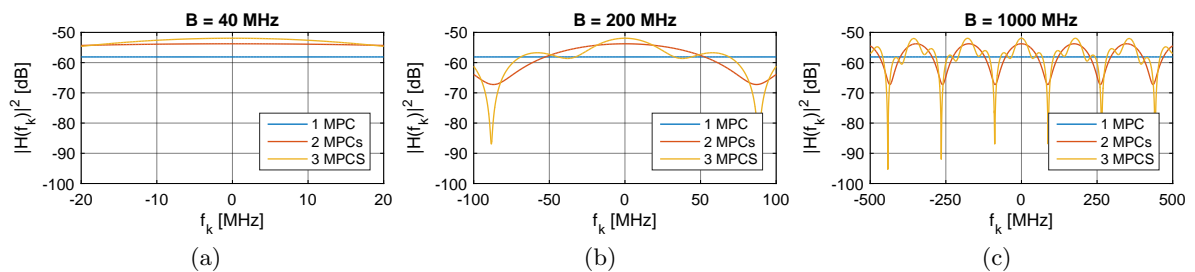


Figure D.9: Power spectrum density for different bandwidths and number of MPCs within the channel.

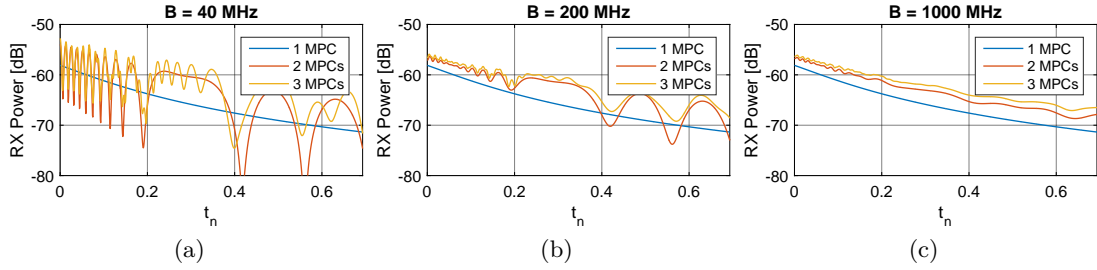


Figure D.10: Averaged RX power during displacement for different bandwidths and number of MPCs.

The averaged RX power over frequency in the different positions is calculated as

$$\bar{P}_{\text{RX}}(t_n) = \frac{1}{K} \sum_{f_k} |\hat{H}(t_n, f_k)|^2, \quad (\text{D.20})$$

and displayed in Fig. D.10 for different bandwidths and number of MPCs. We can observe that in the same scenario, fading depends on the directivity (number of MPCs within the channel) and bandwidth (possibility to resolve the different MPCs within the channel). With a larger bandwidth, the MPCs are resolved in time, and they do not “interact” in the delay domain. On the other hand, with a shorter bandwidth, these MPCs are not resolved in delay any more and their combination generates larger variations on the amplitude of the RX signal, as displayed in Fig. D.10.

D.5 Parametrization of Ray-Tracing simulations

The RT tool used for the propagation simulations along this work is ProMan v14.0, a software unit belonging to the Winprop software suite (Altair, www.altair.com). The scenarios have been created either manually (conference room scenario) with the software tool WallMan (a CAD design tool) or with point clouds from 3D laser scans measurements (large corridor scenario). More information on the validation of this model can be found in Appendix D.6.

The computation of the signal level along the propagation paths is based on Fresnel coefficients for transmission and reflection, and GTD/UTD for diffractions³, and is calculated based on the permittivity, permeability, conductivity, and thickness of the materials defined in the database provided by the software.

D.6 Validation of RT Model: Zusebau Building

We have performed two measurement campaigns to validate the RT simulations in the Zusebau building at the Technische Universität Ilmenau: a cluster level and a complete 3D double

³More information about RT can be found in Appendix C.3.

Table D.1: RT parameters for the simulations in the different scenarios.

Num. of Paths	DR (dB)	Transmissions	Reflections	Diffractions	Reflections and Diffractions	Scattering
100	100	3	5	1	2	Yes ^a

^aScatterer resolution tiles of 10 m.

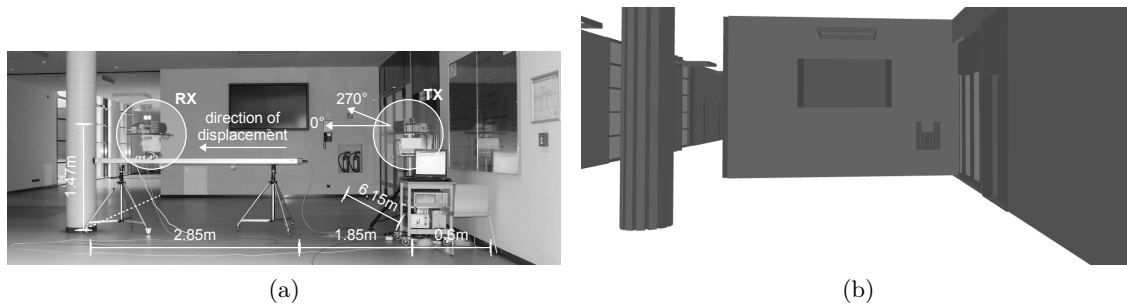


Figure D.11: (a) Picture and (b) RT model of the cluster-level measurement.

directional campaign. The complete scenario was scanned using the Leica BLK 360 3D laser scan⁴. A CAD model with high resolution and details was generated from the resulting point cloud and parametrized with a list of materials with their corresponding electromagnetic properties, [133]. This model has been later used for the simulations with the WinProp RT tool in the different scenarios presented along this work.

D.6.1 Cluster Level Ray-tracing Validation from Measurements

Dual-polarized high gain lens antennas with 2° HPBW were mounted over positioners at the TX and RX. While the TX was static over a tripod, the RX was mounted over a rail parallel to a wall as shown in Fig. D.11a. The channel was measured every 0.2 m, and at each measurement position, the azimuth was scanned with 2° steps at the TX from 270° to 322° and from 270° to 218° at the RX.

As shown in Fig. D.11b, the same wall was isolated to compare the simulation results with the measurements. The measured and simulated power bi-azimuth profile during the displacement of the RX over the rail are shown in Fig. D.12. There is a good match between the simulations and measurements in the directional domain. Two strong scatterers were identified along the displacement of the RX: a specular reflection in the wall/monitor and a reflection on the fire extinguisher.

Furthermore, the antenna patterns calculated from analytical equations were embedded and the rotating scanning procedure was emulated on the RT simulations. The co-polarized RX power of the specular reflection in the different positions along the rail is displayed in

⁴The digitization of the environment with the 3D laser scan and the generation of the CAD model was made by Mr. Han Niu.

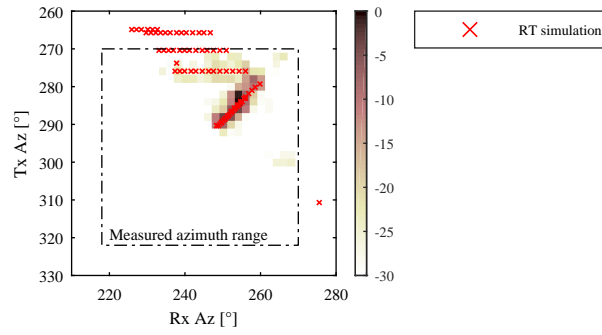


Figure D.12: Cluster-level measured and simulated bi-azimuth profile: average over the different positions in the rail.

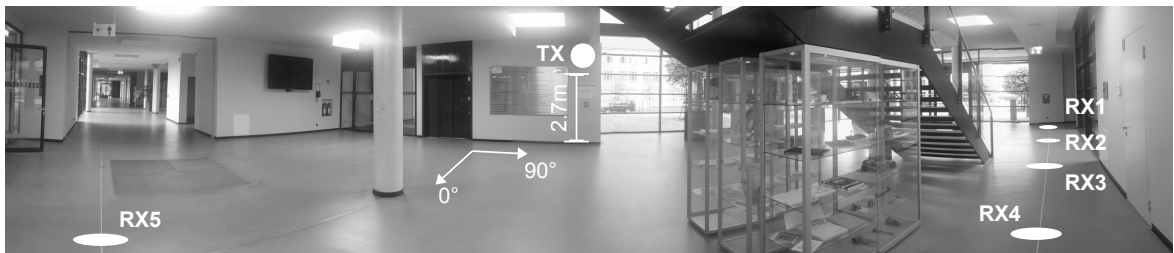


Figure D.13: View of the complete hall with the TX and RXs locations in the measurements for the scenario validation.

Fig. D.14. The power and polarization follows the same trend as the measurements, being in most of the cases the $\phi\phi$ (HH) combination weaker than the $\theta\theta$ (VV), as discussed in Appendix A.1, and shown in other measurements in similar conditions in Section 4.1.2 and Section 4.3.5.

D.6.2 Complete Ray-tracing Scenario Validation from Measurements

As shown in Fig. D.13, in this case the TX was located at 2.7 m height emulating an access point and the RX in 5 different positions at 1.3 m height in LOS and OLOS visibility con-

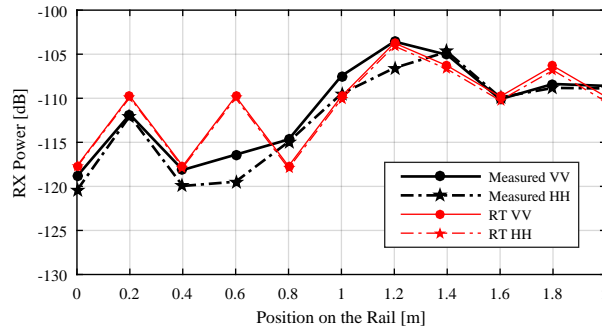


Figure D.14: Measured and RT simulated RX power of the specular reflection for the different co-polarized components.

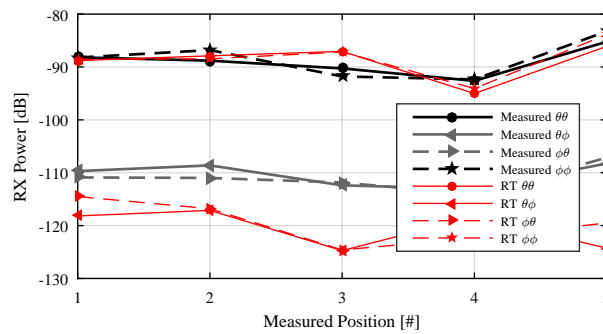


Figure D.15: Synthetic omni-directional RX power from for the different polarizations: measurements and simulations.

ditions. Dual-polarized 30° HPBW antennas were used at the TX and RX to scan with 30° steps the azimuth from 270° to 90° and the elevation from -30° to 30° at the TX, and from 0° to 360° , and from -30° to 30° at the RX.

The measured and simulated RX power for the different polarizations can be observed in Fig. D.15. A good matching can be observed on the values and trends. However, the cross-polarized power is higher in the measurements due to the limited XPD of the antennas (no more than 20 dB). This also reflects the limitations on estimating the XPRs ratios from measurements [102].

D.7 Parameters for the Deterministic Clusters Simulations

Similarly to the MIWEBA model [98], the power of the deterministic components is calculated as follows. The LOS component:

$$P_{\text{LOS}} = 20 \log_{10} \left(\frac{c_0}{f_0} \frac{1}{4\pi d_{\text{LOS}}} \right), \quad (\text{D.21})$$

where c_0 is the propagation speed of light in vacuum, f_0 is the carrier frequency, and d_{LOS} is the TX - RX distance. In the case of the ground reflection:

$$\begin{aligned} P_{\text{GR}} = & 20 \log_{10} \left(\frac{c_0}{f_0} \frac{1}{4\pi d_{\text{GR}}} \right) + \dots \\ & 20 \log_{10} \left(\frac{\sin(\theta_{\text{GR}}) - \sqrt{B}}{\sin(\theta_{\text{GR}}) + \sqrt{B}} \right) + \dots \\ & 20 \log_{10} \left(\exp \left(-\frac{1}{2} \left(4\pi \sin(\theta_{\text{GR}}) \sigma_{\text{GR}} \frac{f_0}{c_0} \right)^2 \right) \right), \end{aligned} \quad (\text{D.22})$$

where d_{GR} and $\theta_{A,\text{GR}}$ are the propagation distance and elevation of arrival angle of the GR component, respectively, calculated with (6.1) and (6.2). The side walls reflections are:

$$P_{\text{SRR/SRL}} = 20 \log_{10} \left(\frac{c_0}{f_0} \frac{1}{4\pi d_{\text{SRR/SRL}}} \right) + \dots$$

$$\begin{aligned}
& 20 \log_{10} \left(n \frac{\sin(\phi_{\text{SRR/SRL}}) - \sqrt{B}}{\sin(\phi_{\text{SRR/SRL}}) + \sqrt{B}} \right) + \dots \\
& 20 \log_{10} \left(\exp\left(-\frac{1}{2} \left(4\pi \sin(\phi_{\text{SRR/SRL}}) \sigma_{\text{SRR/SRL}} \frac{f_0}{c_0}\right)^2\right) \right), \quad (\text{D.23})
\end{aligned}$$

where $d_{\text{SRR/SRL}}$ and $\phi_{A,\text{SRR/SRL}}$ are the propagation distance and azimuth of arrival angle of the reflections on the side walls, respectively, calculated with (6.4) and (6.7). The parameter $n \in \mathcal{N}$ represents the reflection order. The back reflections are calculated as

$$\begin{aligned}
P_{\text{BR}} &= 20 \log_{10} \left(\frac{c_0}{f_0} \frac{1}{4\pi d_{\text{BR}}} \right) + \dots \\
& 20 \log_{10} \left(\frac{\sin(\phi_{\text{BR}}) - \sqrt{B}}{\sin(\phi_{\text{BR}}) + \sqrt{B}} \right) + \dots \\
& 20 \log_{10} \left(\exp\left(-\frac{1}{2} \left(4\pi \sin(\phi_{\text{BR}}) \sigma_{\text{BR}} \frac{f_0}{c_0}\right)^2\right) \right), \quad (\text{D.24})
\end{aligned}$$

where d_{BR} and $\phi_{A,\text{BR}}$ are the propagation distance and azimuth of arrival angle of the reflections on the back walls, respectively, calculated with (6.4) and (6.7). Finally, the diffuse scatterers are calculated as

$$\begin{aligned}
P_{\text{DS}} &= 20 \log_{10} \left(\frac{c_0}{f_0} \frac{1}{4\pi d_{\text{DS}}} \right) + \dots \\
& 20 \log_{10} \left(\frac{\sin(\phi_{\text{DS}}) - \sqrt{B}}{\sin(\phi_{\text{DS}}) + \sqrt{B}} \right) + \dots \\
& 10 \log_{10} \left(\exp\left(-\frac{1}{2} \left(4\pi \sin(\phi_{\text{DS}}) \sigma_{\text{DS}} \frac{f_0}{c_0}\right)^2\right) \right), \quad (\text{D.25})
\end{aligned}$$

where d_{DS} and $\phi_{A,\text{DS}}$ are the propagation distance and azimuth of arrival angle. The propagation distance and azimuth or arrival are calculated as a single reflection.

The parameter B for the horizontal polarization is

$$B = \epsilon_r - \cos^2(\phi_{\text{SRL/SRR/BR/DS}}), \quad (\text{D.26})$$

and for the vertical polarization

$$B = \frac{\epsilon_r - \cos^2(\phi_{\text{SRL/SRR/BR/DS}})}{\epsilon_r^2}. \quad (\text{D.27})$$

All the parameters for these simulations are summarized in Table D.2. In addition, the global parameters in the **street canyon scenario in Tokyo** are:

- Street width: $w = 7.75$ m.
- Coordinate of the TX: $(x, y, z) = (0.1, 0, 17)$.
- Coordinate of the RX: $(x, y, z) = (30.8 : 5 : 95.8, \frac{w}{2}, 1.6)$.

Table D.2: Parameter for the deterministic clusters simulations.

	Scatterer	Name	Coordinates (x,y) (m)	ϵ	σ
Street canyon scenario	Side reflection (left)	SRL	$(0, y)$	$2.7 + 0.2j$	0.0005
	Side reflection (right)	SRR	$(7.75, y)$	$6.25 + 0.3j$	0.0005
	Ground reflection	GR	-	$2.1 + 0.2j$	0.0001
	Back reflections	BR 1	$(107, 0)$	$6.25 + 0.3j$	0.00008
		BR 2	$(108, 0)$	$6.25 + 0.3j$	0.0005
	Diffuse scattering	DS 1	$(94, 0)$	2.15	0.000005
		DS 2	$(82, 0)$	2.1	0.0005
		DS 3	$(64, 0)$	2.1	0.00005
		DS 4	$(52, 0)$	3	0.00005
	Large corridor scenario	Side reflection (left)	SRL	$(0, y)$	$2.7 + 0.2j$
Side reflection (right)		SRR	$(5, y)$	$2.5 + 0.2j$	0.002
Ground reflection		GR	-	$2.1 + 0.2j$	0.0002
Back reflections		BR 1	$(58, 0)$	$2.3 + 0.2j$	0.000675
		BR 2	$(60, 0)$	$2.3 + 0.2j$	0.000675
		BR 3	$(61, 0)$	$2.3 + 0.2j$	0.000675
		BR 4	$(67.5, 0)$	$2.75 + 0.2j$	0.0012
		BR 5	$(75, 0)$	$2.75 + 0.2j$	0.0005
		BR 6	$(84, 0)$	$2.75 + 0.2j$	0.0005
		BR 7	$(85, 0)$	$2.75 + 0.2j$	0.0005
Diffuse scattering		DS 1	$(19, 0, H_{TX})$	$2.3 + 0.2j$	0.000875
		DS 2	$(24, 0)$	$2.3 + 0.2j$	0.000875
		DS 3	$(29, 0)$	$2.3 + 0.2j$	0.000875
		DS 4	$(34.5, 0)$	$2.3 + 0.2j$	0.000875
		DS 5	$(39, 0)$	$2.3 + 0.2j$	0.000875
		DS 6	$(44, 0)$	$2.3 + 0.2j$	0.000875
		DS 7	$(49, 0)$	$2.3 + 0.2j$	0.000875
		DS 8	$(54, 0)$	$2.3 + 0.2j$	0.000875
		DS 9	$(63.5, 0)$	$2.3 + 0.2j$	0.000675

- Maximum reflection order: $n = 3$.

On the other hand, the global parameters in the **large corridor scenario** are:

- Corridor width: $w = 5$ m.
- Coordinate of the TX: $(x, y, z) = (0, 2, 1.6)$.
- Coordinate of the RX: $(x, y, z) = (9.24 : 2 : 57.24, 2, 1.6)$.
- Maximum reflection order: $n = 3$.

Table D.3: List of antennas.

Band	HPBW	Polarization	Designation
6.75 GHz	30°	Dual	QRH20
	30°	Dual	QRH40
	Omni	Single	Custom
30 GHz	30°	Dual	QWH-DL-18-40-K-SG-R
	30°	Dual	QRH40
	Omni	Single	Custom
60 GHz	2°	Dual	SAG-5836833503-15-S1
	30°	Dual	SAC-1430-141-C2
	Omni	Single	MD249-AA
70 GHz	15°	Dual	QWH-ECCROOZ125
190 GHz	15°	Dual	Custom

D.8 List of Antennas used During the Measurements

The antennas used during the different measurements can be found in Table D.3. A custom omni-directional antennas covering from 1 GHz to 40 GHz was used as a single antenna for the measurements simultaneously at 6.75 GHz and 30 GHz.

The QHR40 antenna is also used as a single antenna for the simultaneous measurements in the 6.75 GHz and 30 GHz bands.

E List of Own Publications, Patents, and Recognitions

“I thought I was the only one, but I am not even one of them.”

An Argentinian writer.

Overview

This chapter summarizes all the publications in which I have participated that are related to this thesis. I have separated them into the ones in which I have been the first author, and the ones in which I have contributed with measurement results or analysis of data.

E.1 Publications as First Author

E.1.1 Journals and Magazines

D. Dupleich, R. Müller, M. Landmann, E. Shinwasusin, K. Saito, J. Takada, J. Luo, R. S. Thomä, and G. Del Galdo, “**Multi-band Propagation and Radio Channel Characterization in Street Canyon Scenarios for 5G and Beyond,**” in *IEEE Access*, vol. 7, pp. 9724-9735, 2019.

Radio access at mm-waves has been subject of intensive research in the latest years. However, within the initial deployment of 5G, mm-waves are still relegated and there is a generalized idea that the mm-wave channel for radio access, in comparison to the sub-6 GHz channel, is not only sparse but also troublesome for outdoor applications. In the present paper we introduce simultaneous multi-band measurements comparing the sub-6 GHz with the mm-waves channel at 30 GHz and 60 GHz in street canyon scenarios using the same measurement equipment in Germany and Japan. An analysis on the propagation and radio channel characteristics shows that mm-waves channel offers similar opportunities as the sub-6 GHz. Consequently, the challenge relies on the design of an adequate radio interface matching the channel characteristics. In that regard, aspects as the location of clusters and spatial consistency gain importance within geometry-based stochastic channel models (GBSCMs). The analysis of the large-scale parameters (LSPs) has shown a large influence of the geometry of the scenario on the channel, encouraging the introduction of deterministic modelling components within GBSCMs targeting these scenarios.

D. Dupleich, E. Schäfer, G. Del Galdo, and R. S. Thomä, “**Influence of Spatial-wideband Effects in Evaluation of mm-Wave Communications,**” in *IET Microwaves, Antennas and Propagation*, vol. 13, no. 13, pp. 2200-2206, 30 10 2019, doi: 10.1049 / iet-map.2018.6160.

Hybrid, mixed analogue/digital beam-forming architectures are a central research topic for the development of mm-wave communication for fifth generation. Most approaches are based on phase shifters in the analogue part, which are inherently narrowband. In this study, the authors evaluate the effects and performance of narrowband beam-steering on wideband signals using two different modelling approaches: spatial-narrowband model, in which the inter-antenna element delays are neglected, and spatial-wideband model, in which the inter-antenna element delays are considered. They show that neglecting the spatial-wideband effects on channel models overestimates the focusing of beam-forming, the expected delay spread reduction, and achievable data-rate with an increasing number of antennas and bandwidth. These effects are quantised by simulations using a realistic ray-tracing scenario at 60 GHz.

D. Dupleich, N. Iqbal, C. Schneider, S. Häfner, R. Müller, S. Skoblikov, J. Luo, G. Del Galdo, and R. S. Thomä, “**Influence of System Aspects on Fading at mm-Waves,**” in *IET Microwaves, Antennas and Propagation*, vol. 12, no. 4, pp. 516-524, 28 3 2018.

This contribution presents propagation measurements at 60 GHz in indoor non-line of sight scenarios. Besides analysing the measurements, the authors have considered several system

aspects, such as bandwidth and directivity in order to investigate the small-scale behaviour of the radio channel after beam-forming. The results show that due to the high resolution in the angular and time domain achievable by large antenna arrays and wideband signals, the fading is significantly reduced and the equivalent transmission channel becomes more sparse and deterministic. These insights represent an essential source of information for future systems design and the ongoing channel modelling activities for systems operating at mm-waves.

E.1.2 Conferences

D. Dupleich, H. Abbas Mir, C. Schneider, G. Del Galdo and R. Thomä, “**On the Modelling of the NLOS First Multi-path Component in Stochastic Spatial Channel Models,**” *2021 15th European Conference on Antennas and Propagation (EuCAP)*, 2021, pp. 1-5, doi: 10.23919 / EuCAP51087.2021.9411142.

Positioning and localization is one of the key features in the 5G and beyond wireless networks. Since accuracy strongly depends on the channel conditions, channel models are of special importance for the testing and development of such applications. While several localization methods are based on the time of arrival (ToA) and time-difference of arrival (TDoA), stochastic spatial channel models (SCMs) as the 3GPP don't consider absolute values on the delays of the non-line of sight (NLOS) multi-path components (MPCs), making these models not appropriate for these applications. Therefore, we investigate the time and angular characteristics of the first multi-path component (FMPC) using multi-band ray tracing (RT) simulations in order to extend stochastic SCMs to support localization applications in NLOS.

D. Dupleich, R. Müller and R. Thomä, “**Practical Aspects on the Noise Floor Estimation and Cut-off Margin in Channel Sounding Applications,**” *2021 15th European Conference on Antennas and Propagation (EuCAP)*, 2021, pp. 1-5, doi: 10.23919 / EuCAP51087.2021.9411409.

The characterization of propagation at mm-waves and THz is obtaining relevance since they are expected to be the frequency bands of the future wireless generations. Hence, measurements conducted all around the world with different equipments need to be comparable by establishing common methodologies and best-practice guidelines. As an example, all measurements are affected by noise, but its estimation and removal are not standardized. Therefore, in the present paper we define a methodology on the estimation of the noise floor and the cut-off margin for its subsequent removal. We firstly analyse the influence of the channel sounder noise floor on the estimation of different propagation parameters directly from the measured channel impulse responses (CIRs), showing the need of its removal before any processing of the measurements. Later, we introduce an algorithm to estimate the noise floor in the presence of signal, and the cut-off margin. Finally, we evaluate its performance empirically with measurements.

D. Dupleich, R. Müller, M. Landmann, J. Luo, G. D. Galdo and R. S. Thomä, “**Multi-band Characterization of Propagation in Industry Scenarios,**” in *14th European Conference on Antennas and Propagation (EuCAP)*, Copenhagen, Denmark, 2020, pp. 1-5, doi: 10.23919 / EuCAP48036.2020.9135630.

Industry 4.0 is the scenario in which the 5G and beyond networks are expected to show all their potential. However, while propagation at sub-6 GHz has been widely investigated in industry environments, mm-waves propagation and channel modelling in those scenarios is still under early research. Therefore, we introduce novel simultaneous multiband ultra-wideband measurements at 6.75 GHz and 30 GHz in LOS and NLOS with RX below and above clutter level. This unique set-up allows a direct comparison between the sub-6 GHz and mm-wave channel. Results have shown larger specular to dense multi-path components power ratio and shorter large-scale parameters at mm-waves.

D. Dupleich, R. Müller, S. Skoblikov, M. Landmann, G. D. Galdo and R. Thomä, “**Characterization of the Propagation Channel in Conference Room Scenario at 190 GHz,**” in *14th European Conference on Antennas and Propagation (EuCAP)*, Copenhagen, Denmark, 2020, pp. 1-5, doi: 10.23919 / EuCAP48036.2020.9135404. **Nominated to Best Paper Award in Propagation.**

In the present paper we introduce unique double directional dual-polarized measurements at 190 GHz in a conference room with the aim of characterizing propagation for channel modelling and beam-forming applications. Assisted by ray-tracing, multiple scatterers have been identified, showing a rich multi-path environment. Investigations have shown that polarization diversity increases spatial diversity and a more deterministic modelling approach in polarization is needed to avoid overestimating polarization diversity gains.

D. Dupleich, R. Müller, C. Schneider, S. Skoblikov, J. Luo, M. Boban, G. Del Galdo, and R. Thomä, “**Multi-band Vehicle to Vehicle Channel Measurements from 6 GHz to 60 GHz at “T” Intersection,**” in *90th IEEE Vehicular Technology Conference*, Honolulu, Hawaii (USA), 2019.

We introduce simultaneous multi-band ultra-wideband double-directional measurements at 6.75 GHz, 30 GHz, and 60 GHz in a corner scenario at a “T” intersection in an urban environment. We analyse the influence of the dynamics from LOS to NLOS on the large-scale parameters, showing that the propagation channel offers similar scattering opportunities at the sub-6 GHz and the mm-wave bands. In addition, we discuss the possibility of utilizing the directional information from sub-6 GHz to steer beams in the mm-waves bands.

D. Dupleich, R. Müller, S. Skoblikov, J. Luo, G. Del Galdo, R. S. Thomä, “**Multi-band Double-directional 5G Street Canyon Measurements in Germany,**” in *European Conference on Networks and Communications (EuCNC)*, Valencia, 2019, pp. 1-5.

In the present paper we introduce the results of simultaneous multi-band ultra-wideband measurements at 6.75, 30, and 60 GHz in a street canyon scenario under LOS in Germany. This is the first part of a street canyon measurements series using the same channel sounder in different parts of the world. The aim of these measurements is to analyse and compare the propagation characteristics with multi-band channel modelling in view. We show that from the propagation perspective, mm-waves offer very similar opportunities than the well-known and exploited sub-6 GHz bands.

D. Dupleich, R. Müller, N. Han, S. Häfner, C. Schneider, J. Luo, G. Del Galdo, and R. S. Thomä, “**Polarization in Spatial Channel Models at mm-Waves: a Correlation Based**

Approach,” in *13th European Conference on Antennas and Propagation (EuCAP)*, Krakow, 2019, pp. 1-5.

Polarization diversity at mm-waves is under consideration for the new 3GPP release. Since mm-waves systems have higher resolution in the time and angular domain, more accurate intra-cluster models are needed, in which path properties as polarization becomes more deterministic. In the present paper we discuss the limitations of the current modelling of the polarimetric matrix in spatial channel models (SCMs) and we propose a new modelling approach including correlation between the different coefficients through the cross-polarization ratios (XPRs) and co-polarization ratios (CPRs). Since path-level information is necessary for this analysis, and due to the lack of high-resolution parameter estimation (HRPE) at mm-waves, we have performed 60 GHz cluster level measurements to validate ray-tracing simulations that were later used to derive the model parameters.

D. Dupleich, R. Müller, S. Skoblikov, C. Schneider, J. Luo, G. Del Galdo, and R. S. Thomä, **“Multi-band Indoor Propagation Characterization by Measurements from 6 to 60 GHz,”** in *13th European Conference on Antennas and Propagation (EuCAP)*, Krakow, 2019, pp. 1-5.

We introduce simultaneous multi-band ultra-wideband directional measurements at 6.75 GHz, 30 GHz, and 60 GHz in an indoor environment with different visibility conditions. Large scale parameters and path-loss has been analysed for the different bands considering the propagation channel, and later the influence of the system aspects in the radio channel. We have observed that the major differences between bands are introduced by the characteristics of the targeted system.

D. Dupleich, R. Müller, S. Skoblikov, C. Schneider, J. Luo, M. Boban, G. Del Galdo, and R. S. Thomä, **“Multi-band Characterization of Path-loss, Delay, and Angular Spread in V2V Links,”** in *IEEE 29th Annual International Symposium on Personal, Indoor and Mobile Radio Communications (PIMRC)*, Bologna, 2018, pp. 85-90, doi: 10.1109 / PIMRC.2018.8580797.

We perform simultaneous vehicle-to-vehicle (V2V) multi-band double-directional measurements at 6.75 GHz, 30 GHz, and 60 GHz in a street canyon environment. We analyse both line-of-sight channels and those obstructed by vehicle blocker. For the different bands, we analyse delay spread, angular spread, vehicle blockage loss, and path loss. Finally, we discuss how the system aspects influence the radio channel.

D. Dupleich, R. Müller, S. Skoblikov, C. Schneider, M. Boban, J. Luo, G. Del Galdo, and R. S. Thomä, **“Multi-band Spatio-Temporal Characterization of a V2V Environment Under Blockage,”** in *12th European Conference on Antennas and Propagation (EuCAP)*, London, 2018, pp. 1-5.

In the present paper we introduce novel simultaneous multi-band double-directional ultra-wideband measurements at 6.75 GHz, 30 GHz, and 60 GHz in an urban V2V scenario. The objective is to characterize propagation differences between the measured bands in view of correlated multi-band channel models. Furthermore, we investigate the impact of other vehicles blocking the V2V link by performing measurements with different blocker sizes (specifically, a passenger car and a large van). The shadowing effects and the correlation between intra-cluster delay spreads and large-scale parameters are investigated in the different bands.

D. Dupleich, E. Schäfer, G. Del Galdo, and R. S. Thomä, “**Influence of System Aspects in Propagation Based Evaluation of Beam-forming at mm-Waves,**” in *12th European Conference on Antennas and Propagation (EuCAP)*, London, 2018, pp. 1-5. **Nominated to Best Paper Award in Antennas.**

In the present paper we analyse the system performance and effects of narrowband beam-steering on the equivalent channel at mm-waves considering aspects as bandwidth and number of antennas. Using ray-tracing at 60 GHz, we show that neglecting the spatial-wideband effects on the channel models overestimates the delay spread reduction and achievable data-rate with increasing number of antennas and bandwidth.

D. Dupleich, S. Häfner, R. Müller, C. Schneider, J. Luo, and R. S. Thomä, “**Real-field Performance of Hybrid MISO Time Reversal Multi-beam Beam-former at mm-Waves,**” in *11th European Conference on Antennas and Propagation (EuCAP)*, Paris, 2017, pp. 448-452. doi: 10.23919 / EuCAP.2017.7928225

In the present paper we evaluate the performance of a hybrid digital/analog multi-beam beam-forming architecture with polarization and delay compensation using time reversal (TR). Double-directional, ultra wideband dual-polarized channel measurements at 70 GHz in a conference room have been used to emulate the channel. The use of multiple beams to mitigate human shadowing has been evaluated and the temporal and spatial focusing of time-reversal to reduce inter-user interference.

D. Dupleich, N. Iqbal, C. Schneider, S. Häfner, R. Müller, S. Skoblikov, J. Luo, and R. S. Thomä, “**Investigations on Fading Scaling with Bandwidth and Directivity at 60 GHz,**” in *11th European Conference on Antennas and Propagation (EuCAP)*, Paris, 2017, pp. 3375-3379. doi: 10.23919 / EuCAP.2017.7928451 **Granted with the Best Paper Award in Propagation. Granted with the “Publikationspreis der TU Ilmenau 2018” in the “Ingenieurwissenschaften” category.**

In the present paper we analyse small-scale fading of reflections at 60 GHz using different antennas and bandwidths. The aim is to investigate the deterministic property of the channel in view of modelling and deployment of systems with larger bandwidths and higher directivity. We have investigated the scattering effect of a reflection on a wall emulating a beam-former in a NLOS condition. The results show that the distribution of the amplitudes fit better with a Rician than a Rayleigh distribution. Furthermore, we show that an increasing bandwidth and directivity increases the K-factor, supporting the idea of deterministic paths apart from the LOS.

D. Dupleich, S. Häfner, R. Müller, C. Schneider, R. S. Thomä, J. Luo, E. Schulz, X. Lu, and G. Wang, “**Real-field Performance of Multiple-beam Beam-former with Polarization Compensation,**” in *10th European Conference on Antennas and Propagation (EuCAP)*, Davos, 2016, pp. 1-5.

In the present paper we introduce the architecture of a hybrid digital/analog beam-forming with polarization compensation. To evaluate the performance of this architecture we use double-directional, ultra-wideband dual-polarized channel measurements at 70 GHz that have been carried out in a small-office environment scenario at the TU Ilmenau. Different

positions of Tx and Rx have been measured using horn antennas. The channel impulse responses (CIR) have been processed to emulate a communication system with analog beam-forming capabilities. A single data stream adopting single beam and multi-beam beam-forming strategies has been tested with the measured data, showing an improvement in performance achieved by adopting such an architecture.

D. Dupleich, J. Luo, S. Häfner, R. Müller, C. Schneider, and R. S. Thomä, “**A Hybrid Polarimetric Wide-Band Beam-former Architecture for 5G mm-Wave Communications,**” in *20th International ITG Workshop on Smart Antennas*, Munich, Germany, 2016, pp. 1-8.

Beam-forming at millimeter wave frequencies (mm-wave) is a key technology to fulfill the fifth generation (5G) high data rate requirements. In this paper, we describe a novel hybrid architecture for mm-wave beam-forming, which addresses the mm-wave specific propagation channel characteristics that are identified in recent measurement campaigns. This architecture leverages baseband processing both in analog and digital domain. By enabling multi-beam beam-forming and compensating the polarization mismatch, delay difference (of different beams) and optionally the Doppler shifts (depending on mobility) of the beams at the Tx, a coherent summation of the signals in different beams can be realized, allowing to maximize the signal-to-noise ratio (SNR) and reduce the Rx complexity. Simulations based on measured channels in a typical large indoor scenario have been used to sustain the effectiveness of the proposed beam-forming architecture.

D. Dupleich, S. Häfner, C. Schneider, R. Müller, R. S. Thomä, J. Luo, N. Iqbal, E. Schulz, X. Lu, and G. Wang, “**Double-directional and Dual-polarimetric Indoor Measurements at 70 GHz,**” in *IEEE 26th Annual International Symposium on Personal, Indoor, and Mobile Radio Communications (PIMRC)*, Hong Kong, 2015, pp. 2234-2238, doi: 10.1109 / PIMRC.2015.7343669.

Double-directional, ultra wideband dual-polarized channel measurements at 70 GHz have been carried out in a small-office environment. The aim of these measurements is to study the temporal, directional, and polarization properties of the channel for modelling purposes of the future wireless communication systems at mm-waves. A highly deterministic behaviour of the channel and the environment has been identified, as well as the limitations of only parameterizing channel models as WINNER for the new mm-wave channel models.

D. Dupleich, F. Fuschini, R. Mueller, E. Vitucci, C. Schneider, V. Degli Esposti, and R. S. Thomä, “**Directional Characterization of the 60 GHz Indoor-office Channel,**” in *XXXIth URSI General Assembly and Scientific Symposium (URSI GASS)*, Beijing, 2014, pp. 1-4.

Directional, dual-link, quad-polarized 60GHz channel measurements have been carried out in a small-office environment. Purpose of the measurements is to study the directional properties of the channel in view of future multi-gigabit system adopting beam-forming or macro-diversity solutions. The impact of polarization on the characteristics of the channel is also addressed in the study.

D. Dupleich, M. Grimm, F. Schlembach and R. S. Thomä, “**Practical aspects of a digital feedforward approach for mitigating non-linear distortions in receivers,**” *2013 11th International Conference on Telecommunications in Modern Satellite, Cable and Broadcasting*

Services (TELSIKS), Nis, 2013, pp. 170-177. doi: 10.1109 / TELSIS.2013.6704914

This paper addresses the mitigation of non-linearly induced interference in reconfigurable wideband direct down-conversion receivers using digital signal processing techniques. Multi-mode and multi-band transceivers are widely used nowadays. However, due to their aim to be flexible and reconfigurable, they lack of high selectivity and are more sensitive to non-linear distortions beside other RF impairments. The case of blocking through out of band interferer signals is found in practice, where the receiver tries to demodulate a weak signal from a far base station, but a high power wideband signal from a near base station in a different frequency-slot induces the receiver to work in a non-linear region. The spectral regrowth of the interferer signal that falls above the desired one deteriorates the bit error rate performance. In the receiver, the automatic gain control attenuates the interferer, but also reduces the power of the desired signal, thereby decreasing the dynamic range of the receiver. A feedforward algorithm based on a reference model and adaptive filters has been analysed under fading channel conditions in MATLAB and later tested in the lab in a realtime implementation in the FPGA of a software-defined radio device. Results show an enhancement in the bit error rate by reducing the interference and an increase in the dynamic range of the receiver.

E.1.3 White Papers, Temporary Documents, and Technical Documents in Standardization

D. Dupleich, Alexander Ebert, Robert Müller, Giovanni Del Galdo, and Reiner Thomä, **“Verification of Dual-Polarized Ultra-Wideband Channel Sounder for THz Applications,”** in *3rd Post IRACON Meeting*, Online, 2021.

The lower THz bands are foreseen as candidates to achieve the data-rates demanded in the sixth generation (6G) of wireless communications. Hence, multiple measurements for characterization of propagation at these frequencies in different scenarios are being conducted all around the world. This also impulses activities on standardization of measurement equipment and methodologies to define common practices and make measurements from different actors comparable. Therefore, in the present paper we investigate the accuracy of a dual-polarized ultra-wideband channel sounder in the time, angular, and polarization domains by means of a verification methodology based on interferometry.

D. Dupleich, R. Müller, C. Schneider, S. Skoblikov, J. Luo, M. Boban, G. Del Galdo, and R. S. Thomä, **“Multi-band Vehicle to Vehicle Channel Measurements from 6 GHz to 60 GHz at “T” Intersection,”** in *11th MC and Technical Meeting IRACON*, Gdansk, Poland, 2019.

We introduce simultaneous multi-band ultra wide-band double-directional measurements at 6.75 GHz, 30 GHz, and 60 GHz in a corner scenario at a “T” intersection in an urban environment. We analyse the influence of the dynamics from LOS to NLOS on the large-scale parameters, showing that the propagation channel offers similar scattering opportunities at the sub-6 GHz and the mm-wave bands. In addition, we discuss the possibility of utilizing the directional information from sub-6 GHz to steer beams in the mm-waves bands.

D. Dupleich, R. Müller, S. Skoblikov, M. Landmann, G. Del Galdo, and R. S. Thomä, **“Indoor Double-directional 3D Measurements at 190 GHz for 5G and Beyond,”** in *10th MC and Technical Meeting IRACON*, Oulu, Finland, 2019.

In the present paper we introduce double-directional 3D measurements at 190 GHz in a conference room with the aim of characterizing propagation for channel modelling and beam-forming applications. Multiple scatterers have been identified with the assistance of ray-tracing, showing a rich multi-path environment. Furthermore, investigations into polarization have shown that a more deterministic modelling approach is needed for polarization.

D. Dupleich, R. Müller, S. Skoblikov, J. Luo, G. Del Galdo, and R. S. Thomä, **“Multi-band Double-directional 5G Street Canyon Measurements in Germany,”** in *9th MC and Technical Meeting IRACON*, Dublin, Ireland, 2019.

In the present paper we introduce the results of simultaneous multi-band ultra-wideband measurements at 6.75, 30, and 60 GHz in a street canyon scenario under LOS in Germany. This is the first part of a street canyon measurements series using the same channel sounder in different parts of the world. The aim of these measurements is to analyse and compare the propagation characteristics with multi-band channel modelling in view. We show that from the propagation perspective, mm-waves offer very similar opportunities than the well known and exploited sub-6 GHz bands.

D. Dupleich, R. Müller, S. Skoblikov, C. Schneider, J. Luo, G. Del Galdo, and R. S. Thomä, **“Simultaneous Multi-band Indoor Measurements from 6 to 60 GHz - a Study on System Influence on Channel Modelling,”** in *7th MC and Technical Meeting IRACON*, Cartagena, Spain, 2018.

In the present paper we introduce simultaneous multi-band ultra wideband directional measurements at 6.75 GHz, 30 GHz, and 60 GHz in an indoor environment with different visibility conditions. Large scale parameters and path-loss has been analysed for the different bands considering the propagation channel, and later the influence of the system aspects in the radio channel. We have observed that the major differences between bands are introduced by the characteristics of the targeted system.

D. Dupleich, S. Häfner, R. Müller, C. Schneider, J. Luo, E. Schulz, X. Lu, G. Wang, and R. S. Thomä, **“Real-field Performance of Multiple-beam Beam-former with Polarization Compensation,”** in *NEWCOM/COST Workshop on Wireless Communications JNCW 2015*, Barcelona, Spain, 2015.

Double-directional, ultra wideband dual-polarized channel measurements at 70 GHz have been carried out in a small-office environment scenario at the TU Ilmenau. Different positions of Tx and Rx have been measured using horn antennas, sweeping the angular domain at both ends. The measured data has been processed to emulate a communication system with analog beam-forming capabilities. Different polarimetric single datastream beam-forming and multi-beam beam-forming strategies have been adopted and analysed with the measured data, showing an improvement in performance achieved by adopting such an architecture.

D. Dupleich, S. Häfner, R. Müller, C. Schneider, J. Luo, E. Schulz, and R. S. Thomä,

“Double-directional Dual-polarimetric Ultra-wideband Measurements at 70 GHz in a Small Office Scenario,” in *13th MC and Scientific Meeting IC1004*, Valencia, Spain, 2015.

Double-directional, ultra wideband dual-polarized channel measurements at 70GHz have been carried out in a small-office environment at the TU Ilmenau. Different positions of Tx and Rx have been measured using horn antennas and sweeping the angular domain at both ends. The aim of these measurements is to study the directional and polarization properties of the channel in view of the future wireless communication systems adopting beam-forming at mm-waves and for channel modelling purposes.

D. Dupleich, C. Schneider, F. Fuschini, R. Müller, E. M. Vitucci, V. Degli Esposti, and R. S. Thomä, **“Polarimetric wide-band directional characterization at mm-Wave in a small office scenario,”** in *10th MC and Technical Meeting IC1004*, Aalborg, Denmark, 2014.

Directional, dual-link, quad-polarized 60GHz channel measurements have been carried out in a small-office environment. Purpose of the measurements is to study the directional properties of the channel in view of future multi-gigabit system adopting beam-forming or macro-diversity solutions. The impact of polarization on the characteristics of the channel is also addressed in the study.

E.2 Contributions

E.2.1 Books

“THz COMMUNICATIONS: Paving the way towards wireless Tbps,” 2021, *Springer Nature*. ISBN: 978-3-030-73737-5.

This book describes the fundamentals of THz communications, spanning the whole range of applications, propagation and channel models, RF transceiver technology, antennas, base-band techniques, and networking interfaces. The requested data rate in wireless communications will soon reach from 100 Gbit/s up to 1 Tbps necessitating systems with ultra-high bandwidths of several 10s of GHz which are available only above 200 GHz. In the last decade, research at these frequency bands has made significant progress, enabling mature experimental demonstrations of so-called THz communications, which are thus expected to play a vital role in future wireless networks. In addition to chapters by leading experts on the theory, modeling, and implementation of THz communication technology, the book also features the latest experimental results and addresses standardization and regulatory aspects. This book will be of interest to both academic researchers and engineers in the telecommunications industry.

“Radio Propagation Measurements and Channel Modeling: Best Practices for Millimeter-Wave and Sub-Terahertz Frequencies,” 2021, *John Wiley and Sons* - To be published.

E.2.2 Journals and Magazines

C. Gentile, A. F. Molisch, J. Chuang, D. Michelson, A. Bodi, A. Bhardwaj, O. Ozdemir, W. Khawaja, I. Guvenc, Z. Cheng, F. Rottenberg, T. Choi, R. Müller, N. Han, and D. Dupleich, “**Methodology for Benchmarking Radio-Frequency Channel Sounders through a System Model**,” in *IEEE Transactions on Wireless Communications*, doi: 10.1109

Development of a comprehensive channel propagation model for high-fidelity design and deployment of wireless communication networks necessitates an exhaustive measurement campaign in a variety of operating environments and with different configuration settings. As the campaign is time-consuming and expensive, the effort is typically shared by multiple organizations, inevitably with their own channel sounder architectures and processing methods. Without proper benchmarking, it cannot be discerned whether observed differences in the measurements are actually due to the varying environments or to discrepancies between the channel sounders themselves. The simplest approach for benchmarking is to transport participant channel sounders to a common environment, collect data, and compare results. Because this is rarely feasible, this paper proposes an alternative methodology – which is both practical and reliable – based on a mathematical system model to represent the channel sounder. The model parameters correspond to the hardware features specific to each system, characterized through precision, in situ calibration to ensure accurate representation; to ensure fair comparison, the model is applied to a ground-truth channel response that is identical for all systems. Five worldwide organizations participated in the cross-validation of their systems through the proposed methodology. Channel sounder descriptions, calibration procedures, and processing methods are provided for each organization as well as results and comparisons for 20 ground-truth channel responses.

S. Salous, F. Tufvesson, K. Turbic, L. M. Correia, T. Kürner, D. Dupleich, C. Schneider, D. Czaniera, and B. Montenegro Villacieros, “**IRACON Propagation Measurements and Channel Models for 5G and Beyond**,” in *ITU Journal: ICT Discoveries-Special issue-Radio wave propagation*, 2019.

Several frequency bands and system architectures are proposed for 5G and beyond to meet the higher data rates for point-to-point communication and point to area coverage. In this paper, we present radio propagation studies and models developed in typical scenarios for massive antenna deployment and body area networks, in frequency bands below 6 GHz, building entry loss and clutter loss and vehicular communication, in the millimeter wave bands, and models in the Terahertz for 5G and beyond.

R. He, C. Schneider, B. Ai, G. Wang, Z. Zhong, D. Dupleich, R. S. Thomä, M. Boban, J. Luo, and Y. Zhang, “**Propagation Channels of 5G millimetre-wave Vehicle-To-Vehicle Communications: Recent Advances and Future Challenges**,” in *IEEE Vehicular Technology Magazine*. doi: 10.1109 / MVT.2019.2928898.

Wireless vehicular communications and sensing technologies are key to enabling more advanced intelligent transportation systems (ITSs) with improved safety and efficiency. Within the realm of wireless communication, millimeter-wave (mm-wave) technology has recently received much attention, providing rich spectrum resources to support the timely transmis-

sion of large amounts of data. This is especially important for vehicular applications because the number of sensors on modern vehicles is rapidly increasing and thus generating large amounts of data. To fully exploit this potential, understanding mm-wave vehicle-to-vehicle (V2V) propagation channels is crucial. In this article, we review the state of the art in mm-wave V2V channel measurements and modeling, describe recent directional V2V channel measurements performed in the 60-GHz band, and discuss future challenges to be addressed in mm-wave V2V channel measurements and modeling.

N. Iqbal, J. Luo, C. Schneider, D. Dupleich, R. Müller, S. Häfner, and R. S. Thomä, “**Investigating Validity of Wide-Sense Stationary Assumption in Millimeter Wave Radio Channels,**” in *IEEE Access*, vol. 7, pp. 180073-180082, 2019, doi: 10.1109 / ACCESS.2019.2957949.

In this paper, impact of antenna directivity and bandwidth on the small scale fading statistics have been analyzed for millimeter-wave (mmWave) radio channels. For this purpose, small-scale fading measurements at the mmWave frequency band (58-62 GHz) are carried out using transmit and receive antennas with different antenna directivities (emulated beamforming gains). Measurements emulate a non line-of-sight scenario when the communication between transmit and receive antennas is possible only through a single multipath cluster. In order to compare results, measurements in a line-of-sight scenario with omni-directional antennas are also carried out for reference purpose. Considering two main mmWave system features i.e., high antenna directivity and higher system bandwidth, we report the following results: 1) Randomness/fading in the received signal magnitude vanishes with an increase in bandwidth. 2) The channel impulse response $h(t, \tau)$ does not remain a wide-sense stationary (WSS) random process in the slow-time domain i.e., along t , where, the fast-time domain refers to the dimension along τ . 3) Measured channels are WSS in the frequency domain and the coherence bandwidth increases when propagation channels are illuminated with high gain antennas.

N. Iqbal, J. Luo, R. Müller, G. Steinböck, C. Schneider, D. Dupleich, S. Häfner, and R. S. Thomä, “**Multipath Cluster Fading Statistics and Modeling in Millimeter-Wave Radio Channels,**” in *IEEE Transactions on Antennas and Propagation*, vol. 67, no. 4, pp. 2622-2632, April 2019.

The second-order statistics of indoor directional channels are investigated using millimeter-wave (mmWave) band (30.4-37.1 GHz) ultrawideband (UWB) channel measurements. Considering two main mmWave system assumptions (high bandwidth and high beamforming gain), this paper aims to investigate the validity of the Rayleigh-Rice fading models for the cluster fading envelope. The results from the mmWave band study are compared to an already well-studied lower frequency FCC band (3.4-10.1 GHz). During the measurements, only selective objects (emulated multipath clusters in the propagation channel) are illuminated in a small lecture room. The experiments show that for both UWB channels, the complex received (Rx) signal is a circularly symmetric non-Gaussian random variable with highly correlated inphase (I) and quadrature (Q) components. These properties demonstrate that the intracluster multipath components (MPCs) structure is sparse. Consequently, modeling the cluster fading envelope with Rayleigh-Rice distribution is not realistic. Therefore, the sum-of-cisoids principle is used for intracluster multipath modeling which inherently considers a correlation between I and Q components. It has been established that a reasonably good approximation of the cluster fading envelope can be obtained with $N = 3-6$ equal amp-

litude cisoids. However, we remark that Rayleigh–Rice models may become realistic cluster fading envelopes for narrowband mmWave systems.

M. Boban, D. Dupleich, N. Iqbal, J. Luo, C. Schneider, R. Müller, Z. Yu, D. Steer, T. Jämsä, J. Li, and R. S. Thomä, “**Multi-band Vehicle-to-Vehicle Channel Characterization in the Presence of Vehicle Blockage,**” in *IEEE Access*, vol. 7, pp. 9724–9735, 2019.

Vehicle-to-Vehicle (V2V) channels exhibit unique properties, due to the highly dynamic environment and low elevation of the antennas at both ends of the link. Of particular importance for the behavior of V2V channels, and consequent reliability of the communication link, is the severity and dynamics of blockage of both line-of-sight (LOS) and other multipath components (MPCs). The characteristics of blockage become more important as the carrier frequency increases and the ability of the signal to penetrate through objects diminishes. To characterize the effects of vehicle blockage, we performed V2V channel measurements in four different frequency bands (6.75, 30, 60, and 73 GHz) in urban and highway scenarios. We analysed the impact of the blocker size and position on the received power and fast fading parameters, as well as the frequency dependency of these parameters under blockage. Our results show there is a strong influence of the size of the blocking vehicle on the blockage loss and the angular/delay spread. The position of the blocker relative to the transmitter and receiver also plays an important role. On the other hand, the frequency dependency is quite limited, with the blockage loss increasing slightly and the number of scattered MPCs reducing slightly as frequency increases. The main conclusion of this study is that V2V communication will be possible in high (millimeter wave) frequencies, even in the case of blockage by other vehicles.

C. Ling, X. Yin, R. Müller, S. Häfner, D. Dupleich, C. Schneider, J. Luo, H. Yan, and R. S. Thomä, “**Double-Directional Dual-Polarimetric Cluster-Based Characterization of 70–77 GHz Indoor Channels,**” in *IEEE Transactions on Antennas and Propagation*, vol. 66, no. 2, pp. 857–870, Feb. 2018.

This paper presents 70–77 GHz wideband channel characteristics of delay, spatial, and polarimetric domains for small office and entrance hall scenarios. Based on measured multi-dimensional power spectra of delay, and directions (i.e., azimuth and elevation) of departure and of arrival, multipath clusters were detected using the K-means, threshold-based, and Gaussian-mixture-model clustering algorithms. The spatial positions and directions of clusters, including the first- and last-hop scatterers, are determined using a measurement-based ray tracer method. Our experimental analysis reveals that the composite and cluster-level channel behaviors are considerably dependent on the geometry of environments, the interaction/bouncing order between a wave and objects, the position of transmitter and receiver, the underlying antenna type, and the polarimetric combination. The angular spread of arrival is observed larger than that of departure, and the characteristics for the horizontal polarization are comparable with those for vertical polarization. Our results also manifest the merits of threshold-based clustering algorithm in terms of clusters’ compactness, separation, and exclusiveness. We further find that the identified interaction points exhibit excellent agreement with real physical objects existing in the environment. Based on these results, an indoor stochastic channel model is established not only for the composite parameters and cluster characteristics, but also for the first- and last-hop scatterers’ position, direction, and their dispersive statistics. This model can be used to generate channel realizations of

reasonable spatial consistency.

S. Salous, V. Degli Esposti, F. Fuschini, R. S. Thomä, R. Müller, D. Dupleich, K. Haneda, J. M. Molina Garcia-Pardo, J. P. Garcia, D. P. Gaillot, S. Hur, and M. Nekovee, “**Millimeter-Wave Propagation Characterization and modeling toward fifth-generation systems. [Wireless Corner]**,” in *IEEE Antennas and Propagation Magazine*, vol. 58, no. 6, pp. 115-127, Dec. 2016.

New radio interface technologies such as massive arrays will render basic assumptions for statistical channel models obsolete. In this issue’s “Wireless Corner” column, the authors present an extensive and rigorous review of the propagation characterization and modeling of wave propagation in the millimeter-wave frequency range. An overview of propagation modeling including path loss, shadowing, stochastic, and ray-tracing models is presented. Aspects such as channel sounding techniques and standardization are also tackled. The article considers not only the well-studied 60-GHz frequency band but other bands with potential for future indoor/outdoor communications. The main challenges related to the use of these bands in future wireless systems are carefully discussed.

Fuschini et al., “**Item Level Characterization of mm-Wave Indoor Propagation,**” in *EURASIP Journal on Wireless Communications and Networking*, 2016.

According to the current prospect of allocating next generation wireless systems in the underutilized millimetre frequency bands, a thorough characterization of mm-wave propagation represents a pressing necessity. In this work, an “item level” characterization of radiowave propagation at 70 GHz is carried out. The scattering properties of several, different objects commonly present in indoor environment are investigated by means of measurements carried out in an anechoic chamber. The measured data have been also exploited to tune some parameters of a 3D ray tracing model.

V. Degli-Esposti, F. Fuschini, E. M. Vitucci, M. Barbiroli, M. Zoli, L. Tian, X. Yin, D. Dupleich, R. Müller, C. Schneider, and R. S. Thomä, “**Ray-Tracing-Based mm-Wave Beamforming Assessment,**” in *IEEE Access*, vol. 2, pp. 1314-1325, 2014.

The use of large-size antenna arrays to implement pencil-beam forming techniques is becoming a key asset to cope with the very high throughput density requirements and high path-loss of future millimeter-wave (mm-wave) gigabit-wireless applications. Suboptimal beamforming (BF) strategies based on search over discrete set of beams (steering vectors) are proposed and implemented in present standards and applications. The potential of fully adaptive advanced BF strategies that will become possible in the future, thanks to the availability of accurate localization and powerful distributed computing, is evaluated in this paper through system simulation. After validation and calibration against mm-wave directional indoor channel measurements, a 3-D ray tracing model is used as a propagation-prediction engine to evaluate performance in a number of simple, reference cases. Ray tracing itself, however, is proposed and evaluated as a real-time prediction tool to assist future BF techniques.

E.2.3 Conferences

H. Niu, D. Dupleich, R. Müller, S. Skoblikov, C. Schneider, G. Del Galdo, and R. S. Thomä, “**Hybrid Ray Tracing Method for Millimeter Wave Propagation Simulation in Large Indoor Scenarios,**” in *23rd International ITG Workshop on Smart Antennas*, Vienna, Austria, 2019, pp. 1-6.

In this paper, a novel three dimensional (3D) hybrid ray tracing (HRT) method for wave propagation simulation for large indoor and small cell urban environment is proposed. HRT combines two image based ray tracing (RT) methods: “standard” ray tracing (i.e., the rigorous and conventional image ray tracing) with high accuracy and “intelligent” ray tracing (i.e., visibility tree based image ray tracing) with less time consuming. To establish the accuracy of HRT, its simulation results were compared with millimeter wave (mmWave) measurements in a large indoor scenario under different visibility conditions. It shows that good predictions can be provided by HRT in many aspects, such as path loss, temporal characteristics, evolution of channel, etc. Meanwhile, mismatch and difference between measurement and simulation will be shown and be analyzed as well.

N. Iqbal, J. Luo, D. Dupleich, S. Häfner, R. Müller, C. Schneider, and R. S. Thomä, “**Second-order Statistical Characterization of the 60 GHz Cluster Fading Channels,**” in *29th IEEE Annual International Symposium on Personal, Indoor and Mobile Radio Communications (PIMRC)*, Bologna, 2018, pp. 241-245.

The small scale fading measurements at the 60 GHz frequency band are carried out to investigate the second-order statistics of a fading multipath cluster. The cluster is illuminated with different gain antennas (emulated beamforming gains). The analysis reveals that the measured channel impulse response (CIR) is approximately circular (or circularly symmetric) with correlated inphase (I) and quadrature (Q) components. These properties correspond to the sparse multipath channels and are different from the Rayleigh/Rician fading channels which assume that the I and Q components are mutually uncorrelated colored Gaussian variates. These differences prevent the application of the Rayleigh/Rice fading models in the intra-cluster multipath modeling.

N. Iqbal, D. Dupleich, C. Schneider, J. Luo, R. Müller, S. Häfner, G. Del Galdo, and R. S. Thomä, “**Modeling of Intra-cluster Multipaths for 60 GHz Fading Channels,**” in *12th European Conference on Antennas and Propagation (EuCAP)*, London, 2018, pp. 1-5, doi: 10.1049 / cp.2018.0873. **Nominated to Best Paper Award in Propagation.**

Using Sum-Of-Cisoids (SOC) principle along with a deterministic parameter computation method, this paper provides studies on modeling of the intra-cluster number of scattered multi-path components (MPC) N and their amplitudes c_n . Modeling objective is to ensure that the fading statistics of the receive (Rx) signal magnitude of the measured beam-formed channels for an emulated cluster; match precisely with the deterministic samples (channel snapshots) of the simulation model. It has been found that measured Rx signal magnitude can be excellently approximated with $N = 2-6$ subpaths/sinusoids which is much lower than 3GPP assumed number i.e. $N = 20$.

E. Schäfer, C. Steinmetz, R. Zetik, J. König, D. Dupleich, G. Del Galdo, and R. S. Thomä, **“Interference Mitigation in mm-Wave Backhaul Networks with Limited Channel-State Information,”** in *IEEE International Conference on Microwaves, Antennas, Communications and Electronic Systems (COMCAS)*, Tel-Aviv, 2017, pp. 1-5.

Our goal is to identify if limited channel-state information is sufficient to mitigate interferences between the stations of a wireless mobile backhaul network, which is especially of great importance if the network employs full-duplex operation or terrestrial and satellite links sharing the same spectrum. We analyze and compare the signal-to-interference-and-noise ratio of plain beam steering and zero-forcing beam steering for a millimeter-wave backhaul network with limited channel-state information where only the positions of the stations are known, while buildings and other possible sources of multi-path components are unknown. Numerical analyses based on raytracing in a realistic urban scenario reveal that zero-forcing beam steering outperforms plain beam steering by about 12 dB. Furthermore, we compare the steering approaches to block diagonalization with full channel-state information as a reference. For situations with low signal-to-noise ratio as in wide-band communications, zero-forcing beam steering can achieve a similar signal-to-noise-and-interference ratio to block diagonalization. We conclude that knowing the positions of wireless backhaul stations obviates the need for expensive channel estimation.

N. Iqbal, C. Schneider, J. Luo, D. Dupleich, R. Müller, S. Häfner, and R. S. Thomä, **“On the Stochastic and Deterministic Behavior of mmWave Channels,”** in *11th European Conference on Antennas and Propagation (EUCAP)*, Paris, 2017, pp. 1813-1817, doi: 10.23919 / EuCAP.2017.7928665.

A wireless channel is always composed of both deterministic and stochastic multi-path components. A high Rician K-factor increases the contribution of deterministic channel components, thereby reducing the significance of stochastic parts of a channel. This paper focus at the investigative analysis of K-factor and fading depth to analyze the deterministic behavior of a channel under a certain bandwidth. In this paper, 4 different propagation setups have been studied including a LOS, reflections from black board and wall are considered due to their different surface roughness and double bounce reflections from both surfaces. It has been observed that in all propagation cases, small scale fading depth asymptotically converges towards zero dB whereby K-factor increases with bandwidth. Results also show that the de-polarization of a signal increases its amplitude fading. This effect is much more significant at lower bandwidths but an increase in bandwidth reduces the difference in fade depths between polarized and depolarized signals. These observations lead to a conclusion that channel tend to be more deterministic at higher bandwidths.

N. Iqbal, J. Luo, C. Schneider, D. Dupleich, S. Häfner, R. Müller, and R. S. Thomä, **“Frequency and Bandwidth Dependence of Millimeter Wave Ultra-wide-band Channels,”** in *11th European Conference on Antennas and Propagation (EUCAP)*, Paris, 2017, pp. 141-145, doi: 10.23919 / EuCAP.2017.7928850.

If a channel is frequency dependent then Uncorrelated Scattering (US) (a narrow-band assumption) don't hold. This has a significant impact at the considered channel modeling methodology as delay and angular dispersion of waves can no longer be studied independently because the small scale fading of individual multipath components become correlated.

In this paper, we investigate the frequency dependence of the 30 GHz millimeter-Wave (mm-Wave) Ultra-Wide band (UWB) channel. Our indoor small lecture room measured channel results show that both delay and angular spreads vary significantly for different frequencies within a measured UWB channel. This is due to different interactions with objects in the environment due to significant difference in the comparative wavelengths. Therefore, we stress that mmWave-UWB channel modeling methodology must take into account the frequency dependence of channel parameters. In order to support its significance, we have also provided an evidence from mmWave system architecture point of view.

N. Iqbal, J. Luo, C. Schneider, D. Dupleich, R. Müller, S. Häfner, and R. S. Thomä, “**Stochastic/deterministic Behavior of Cross-polarization Discrimination in mmWave Channels,**” in *IEEE International Conference on Communications (ICC)*, Paris, 2017, pp. 1-5, doi: 10.1109 / ICC.2017.7996409.

Large absolute channel bandwidths at millimeter wave (mmWave) frequencies and more directional antenna gains may lead to quasi-deterministic (less random) channel fading behavior. Randomness in the cross polarization discrimination (XPD) is an attribute related to the channel fading behavior. In narrow-band channels, it is usually modeled as a log-normal random variable. From channel modeling perspectives, XPD power level in a particular propagation environment and its degree of randomness are of fundamental interest. In this paper, XPD behavior is characterized as a function of bandwidth in 4 different propagation setups including line of sight (LOS), reflections from black board, a rough wall and double bounce reflections from both surfaces. It has been observed that in all cases, the coefficient of variation of XPD around its mean value reduces exponentially with an increase in channel bandwidth demonstrating an evolution towards quasi-deterministic channel behavior. Additionally, a 5-10 dB difference in XPD values has also been observed between narrow-band and UWB channels in the considered propagation setups.

N. Iqbal, C. Schneider, J. Luo, D. Dupleich, R. Müller, and R. S. Thomä, “**Modeling of Directional Fading Channels for Millimeter Wave Systems,**” in *IEEE 86th Vehicular Technology Conference (VTC-Fall)*, Toronto, ON, 2017, pp. 1-5, doi: 10.1109 / VTCFall.2017.8288375.

In this paper, directional small scale fading measurements are used to extract the fading statistics of the received signal magnitude and the parameters of the underlying stochastic (Rayleigh/Rician) model. After that sum-of-cisoids (SOC) principle is used to model the deterministic samples (channel snapshots) of the stochastic model with a special focus on the number of sinusoids/scatterers and their weights. It has been established that theoretical and simulated results of the SOC fading channel simulator provide an excellent approximation of the measured received signal magnitude per cluster with a small number of sinusoids i.e. = 4.

R. Müller, S. Häfner, D. Dupleich, R. S. Thomä, G. Steinböck, J. Luo, E. Schulz, X. Lu, and G. Wang, “**Simultaneous Multi-Band Channel Sounding at mm-Wave Frequencies,**” in *10th European Conference on Antennas and Propagation (EuCAP)*, Davos, 2016, pp. 1-5.

The vision of multi Gbit/s data rates in future mobile networks requires the change to millimeter wave (mm-Wave) frequencies for increasing bandwidth. As a consequence, new technologies have to be deployed to tackle the drawbacks of higher frequency bands, e.g. increased

path loss. Development and verification of those novel technologies required an understanding of the propagation effects at mm-Wave which enabled by channel sounding measurements and analysis. Due to the variety of considered frequency bands and the necessity of spatial resolved measurements for e.g. testing of beamforming approaches, measurement duration and comparability becomes problematic. This paper presents multi-band channel sounder architectures, usable to measure up to four frequency bands simultaneously. Furthermore, we present a measurement campaign, featuring full polarimetric and directional resolved dual-band measurements, which comprises the microwave band at 10 GHz and the mm-Wave band at 30 GHz. Preliminary analysis results are presented.

S. Häfner, D. Dupleich, R. Müller, J. Luo, E. Schulz, C. Schneider, R. S. Thomä, X. Lu, and T. Wang, “**Characterisation of Channel Measurements at 70GHz in Indoor Femtocells,**” in *81st IEEE Vehicular Technology Conference (VTC Spring)*, Glasgow, 2015, pp. 1-5.

A wideband, fully polarimetric and directional radio channel sounding campaign conducted at 70 GHz is presented. Measurement site was chosen as an entrance hall, featuring femtocell size. Transmitter and receiver were placed according to an access-point scenario. Initial large-scale parameters like excess-delay, delay-spread and angular spread are derived for channel characterisation. It is not the paper’s goal to describe a new channel model. The main focus is the identification of propagation effects and characteristics, which have to be considered in future modelling. It was found, that first more specular than diffuse components occur and second the channel is spatially sparse.

R. Müller, R. Herrmann, D. Dupleich, C. Schneider, and R. S. Thomä, “**Ultrawideband Multichannel Sounding for mm-Wave,**” in *8th European Conference on Antennas and Propagation (EuCAP)*, The Hague, 2014, pp. 817-821, doi: 10.1109 / EuCAP.2014.6901887.

Owing to the increasing data rates, future 5G mobile networks will need to operate at higher frequencies and bandwidths. To investigate new techniques for those networks, channel sounding is essential for measuring and analysing the multipath propagation in single and multi-user situations under time-variant shadowing environments. This requires a challenging design of the millimeter-wave (mm-wave) channel sounder (CS) - it must provide ultrawideband (UWB) real-time operation with multiple antennas and a high dynamic range. In addition, polarimetric information is needed to fully characterise the wireless channel, e.g. for cases of polarisation misalignment at the mobile device. This paper presents a novel UWB dual-polarised mm-wave channel sounder architecture for real time measurements in 5G mobile networks and motivates the need for polarimetric measurements with experimental data collected at 60 GHz.

V. Degli-Esposti, F. Fuschini, E. M. Vitucci, M. Barbiroli, M. Zoli, D. Dupleich, R. Müller, C. Schneider, and R. S. Thomä, “**Polarimetric Analysis of mm-Wave Propagation for Advanced Beamforming Applications,**” in *9th European Conference on Antennas and Propagation (EuCAP)*, Lisbon, 2015, pp. 1-4.

Pencil-beam forming techniques based on large antenna arrays are becoming a crucial asset to cope with the very high throughput density requirements and high path-loss constraints of future millimeter-wave gigabit-wireless applications. Directional, polarimetric 60 GHz indoor measurements are used in the present work to modify and calibrate a 3D ray tracing

model and in particular to tune the embedded effective-roughness diffuse scattering model. The potential of polarimetric beamforming is then evaluated through system simulation in simple, reference cases using the ray tracing model as a propagation-prediction engine.

R. Müller, S. Hafner, D. Dupleich, J. Luo, E. Schulz, R. Herrmann, C. Schneider, R. S. Thomä, X. Lu, and T. Wang, “**Ultra-Wideband Channel Sounder for Measurements at 70 GHz,**” in *IEEE 81st Vehicular Technology Conference (VTC Spring)*, Glasgow, 2015, pp. 1-5, doi: 10.1109 / VTCSpring.2015.7146143.

Owing to the limitation in bandwidth of currently used frequency bands, future fifth generation (5G) mobile networks will need to operate at higher frequencies. However, one important step in the research activities for the next generation of mobile networks is the broadband fully polarimetric analysis of the multipath propagation in dynamic single and multiuser scenarios under time-variant shadowing environments in millimetre-wave (mm-wave) channels. This paper presents a channel sounding campaign at 70 GHz in an urban outdoor scenario focusing on broadband channel characteristic at mmwave. For the measurements a novel dual-polarized (DP) ultrawideband (UWB) multi-channel sounder (DP-UMCS) architecture, developed at the TU Ilmenau for propagation measurements in cellular networks, was used to study the directional and polarization properties of the channel in view of the future wireless communication systems.

R. Müller, D. Dupleich, C. Schneider, R. Herrmann, and R. S. Thomä, “**Ultrawideband 3D mmWave Channel Sounding for 5G,**” in *XXXIth URSI General Assembly and Scientific Symposium (URSI GASS)*, Beijing, 2014, pp. 1-4, doi: 10.1109 / URSIGASS.2014.6929647.

Increasing data rates in mobile networks require new technologies for the next generation of mobile communication systems such as massive MIMO, device-centric architectures, smarter devices, machine-2-machine communication etc. However, one important step to reach the goal of 100 GBit/s will be use of higher bandwidth. Owing to the limitation in bandwidth of currently used frequency bands, future fifth generation (5G) mobile networks will need to operate at higher frequencies. Analysis of the multipath propagation in dynamic single and multi-user scenarios under time-variant shadowing environments with high bandwidth requires a millimetre-wave (mm-wave) channel sounder (CS). It must provide ultra-wideband (UWB) real-time operation with multiple antennas and a high dynamic range. In addition, polarimetric information is needed to fully characterise the wireless channel, e.g. for cases of polarisation misalignment at the mobile device. This paper presents a novel UWB dual-polarised (DP) mm-wave channel sounder architecture for real time measurements in 5G mobile networks to overcome these requirements. We also show measurement data to motivate the need for polarimetric double-directional measurements.

E.2.4 White Papers and Temporary Documents

S. Salous et al., “**COST IC1004 White Paper on Channel Measurements and Modeling for 5G Networks in the Frequency Bands above 6 GHz**”.

E.3 Patents

J. Luo, R. S. Thomä, D. Dupleich, M. Röding, S. Häfner, R. Müller, C. Schneider, and D. Schulz, “**Analog beamforming devices,**” *Patent number: 10432290*, U.S., 2018.

An analog beamforming transmitter includes: a plurality of beamforming transmission circuits coupled in parallel between a signal input and an array of antenna ports, wherein the signal input is configured to receive an analog complex-valued communication signal having an in-phase and a quadrature component, wherein each antenna port of the array of antenna ports is configured to provide a dual-polarized antenna signal having a first polarization component and a second polarization component, wherein each beamforming transmission circuit is coupled between the signal input and a respective antenna port of the array of antenna ports, wherein each beamforming transmission circuit comprises a first coefficient input for receiving a first analog complex-valued beamforming coefficient a set of first analog complex-valued beamforming coefficients and a second coefficient input for receiving a second analog complex-valued beamforming coefficient of a set of second analog complex-valued beamforming coefficients.

F Declaration of Authorship

Anlage 1

Erklärung

Ich versichere, dass ich die vorliegende Arbeit ohne unzulässige Hilfe Dritter und ohne Benutzung anderer als der angegebenen Hilfsmittel angefertigt habe. Die aus anderen Quellen direkt oder indirekt übernommenen Daten und Konzepte sind unter Angabe der Quelle gekennzeichnet.

Bei der Auswahl und Auswertung folgenden Materials haben mir die nachstehend aufgeführten Personen in der jeweils beschriebenen Weise entgeltlich/unentgeltlich¹⁾ geholfen:

- 1.
- 2.
- 3.

Weitere Personen waren an der inhaltlich-materiellen Erstellung der vorliegenden Arbeit nicht beteiligt. Insbesondere habe ich hierfür nicht die entgeltliche Hilfe von Vermittlungs- bzw. Beratungsdiensten (Promotionsberater oder anderer Personen) in Anspruch genommen. Niemand hat von mir unmittelbar oder mittelbar geldwerte Leistungen für Arbeiten erhalten, die im Zusammenhang mit dem Inhalt der vorgelegten Dissertation stehen.

Die Arbeit wurde bisher weder im In- noch im Ausland in gleicher oder ähnlicher Form einer Prüfungsbehörde vorgelegt.

Ich bin darauf hingewiesen worden, dass die Unrichtigkeit der vorstehenden Erklärung als Täuschungsversuch bewertet wird und gemäß § 7 Abs. 10 der Promotionsordnung den Abbruch des Promotionsverfahrens zur Folge hat.

(Ilmenau, 01.06.2021)

(Unterschrift)

¹⁾ Unzutreffendes bitte streichen.